July 2019

ForskEL project no. 12150/EUDP 64018-003

Final report: Flexible use of biomass on PF Fired power plants

Appendix A. Journal paper: Laxminarayan Y., Jensen P.A., Wu H., Frandsen F.J., Sander B., Glarborg P. Deposit Shedding in Biomass-Fired Boilers: Shear Adhesion Strength Measurements. Energy Fuels 2017, 31, 8733–41.

1. Department of Chemical and Biochemical Engineering
Technical University of Denmark
Søltofts Plads, Building 229, DK-2800, Kgs. Lyngby, Denmark
2. Ørsted Bioenergy & Thermal power,
Kraftværksvej 53, DK-7000, Fredericia, Denmark

CHEC no. R19??

energy&fuels
Article
pubs.acs.org/EF

Deposit Shedding in Biomass-Fired Boilers: Shear Adhesion Strength Measurements

Yashasvi Laxminarayan,*,† Peter Arendt Jensen,† Hao Wu,† Flemming Jappe Frandsen,† Bo Sander,‡ and Peter Glarborg†

†Department of Chemical and Biochemical Engineering, Technical University of Denmark, Søltofts Plads 229, 2800 Kgs. Lyngby, Denmark

‡DONG Energy A/S, Kraftsværksvej 53, Skærbæk, DK-7000, Fredericia, Denmark

ABSTRACT: Ash deposition on boiler surfaces is a major problem encountered in biomass combustion. Timely removal of ash deposits is essential for optimal boiler operation. In order to improve the understanding of deposit shedding in boilers, this study investigates the adhesion strength of biomass ash from full-scale boilers, as well as model fly ash deposits containing KCl, K_2SO_4, CaO, $CaSO_4$, SiO_2, K_2CO_3, Fe_2O_3, $K_2Si_4O_9$, and KOH. Artificial biomass ash deposits were prepared on superheater tubes and sintered in an oven with temperatures ranging from 500 to 1000 °C. Subsequently, the deposits were sheared off by an electrically controlled arm, and the corresponding adhesion strength was measured. The effect of sintering temperature, sintering time, deposit composition, thermal shocks on the deposit, and steel type was investigated. The results reveal that the adhesion strength of ash deposits is dependent on two factors: ash melt fraction, and corrosion occurring at the deposit−tube interface. Adhesion strength increases with increasing sintering temperature, sharply increasing at the ash deformation temperature. However, sintering time, as well as the type of steel used, does not have a significant effect under the investigated conditions. Addition of compounds which increase the melt fraction of the ash deposit, typically by forming a eutectic system, increases the adhesion strength, whereas addition of inert compounds with a high melting point decreases the adhesion strength. Furthermore, the study indicated that sulfation of ash deposits leads to an increase in adhesion strength, while cooling down the deposits after sintering decreases the adhesion strength. Finally, it was observed that adhesion strength data follow a log-normal distribution.

■ INTRODUCTION

One of the major operational problems encountered in biomass-fired boilers is the formation of ash deposits on boiler surfaces. Ash deposition hinders the efficiency of heat transfer to the steam cycle[1] and may completely block flue gas channels in severe cases, causing expensive unscheduled boiler shutdowns. Furthermore, ash deposits may cause severe corrosion of boiler surfaces.[2] Therefore, timely and effective removal of ash deposits is essential for optimal boiler operation.

Natural as well as artificially induced shedding of ash deposits may be caused by several mechanisms including erosion, debonding, molten slag flow, and thermal and mechanical stresses in the deposits.[3] Full-scale investigations have revealed that debonding is the dominant mechanism for shedding of dense and hard deposits in biomass boilers,[4] occurring when the generated stress (e.g., by soot-blowing or due to the inherent weight of the deposit) exceeds the adhesion strength at the deposit−tube interface.[1] Hence, quantification of the adhesion strength of ash deposits is crucial for understanding deposit shedding, and for optimizing artificial removal of deposits (e.g., by soot-blowing or application of thermal shocks). Sootblowing in boilers produces both lateral (lift) and longitudinal (drag) forces on deposits,[5] highlighting the importance of understanding the shear as well as tensile adhesion strength of ash deposits. Additionally, the adhesion strength at the interface is dependent on the contact area between the steel tube and the innermost layer of the ash deposit.[5] The innermost layer of biomass ash deposits is primarily formed by heterogeneous condensation, or homogeneous/heterogeneous nucleation and subsequent thermophoretic deposition of alkali salts,[6,7] with their composition typically dominated by KCl and K_2SO_4.[8]

Previous studies have investigated the adhesion strength of deposits for coal ash[9−11] as well as ash from kraft recovery boilers.[5] Other studies have tried to quantify the inherent compression and bend strength of sintered ash deposits.[12−16] However, there is a lack of understanding of the adhesion strength of biomass ash deposits to boiler surfaces. The literature lacks a detailed investigation, describing the effect of various parameters, such as sintering temperature, chemical composition, and sintering time, on the adhesion strength of biomass ash deposits.

The present work quantifies the shear adhesion strength of biomass ash and salt rich deposits in a laboratory oven, in order to determine the effect of gas and steel surface temperature, deposit chemical composition, sintering duration, steel type, and thermal shocks brought about by a rapid change in sintering temperature. The study simulates the conditions present at the deposit−tube interface, under different deposit properties and boiler conditions. Apart from providing a better fundamental understanding of deposit shedding, the outcome of this study may facilitate boiler operation by recommending boiler conditions for minimizing the formation of strong

Received: May 7, 2017
Revised: July 6, 2017
Published: July 11, 2017

ACS Publications

DOI: 10.1021/acs.energyfuels.7b01312
Energy Fuels 2017, 31, 8733−8741

deposits. Furthermore, the data obtained from this study may be used to optimize soot-blowing in boilers.

■ EXPERIMENTAL SECTION

Materials. Experimental analysis was carried out using fly ash obtained from the electrostatic precipitator/bag filter of a straw-fired grate boiler (Avedøreværket unit 2, 100 MW_{th}), a wood-fired suspension boiler (Avedøreværket unit 2, 800 MW_{th}), and a straw + wood cofired suspension boiler (Amagerværket unit 1, 350 MW_{th}). The fly ash properties are provided in Table 1. While the straw fly ash is rich in K and Cl, the wood fly ash and the straw + wood cofired fly ash are rich in Ca and Si. As a result, the ash deformation temperature,[17] which is the temperature at which the ash first softens and therefore becomes sticky,[18] of straw fly ash is low (640 °C), whereas the ash deformation temperature of wood fly ash and straw + wood cofired fly ash is rather high (1240 and 1220 °C). Additionally, model fly ash deposits were prepared using mixtures of KCl (Sigma-Aldrich, CAS number: 7447-40-7), K_2SO_4 (Sigma-Aldrich, CAS number: 7778-80-5), K_2CO_3 (Sigma-Aldrich, CAS number: 584-08-7), CaO (Sigma-Aldrich, CAS number: 1305-78-8), $CaSO_4$ (Alfa Aesar, CAS number: 7778-18-9), SiO_2 (Sigma-Aldrich, CAS number: 60676-86-0), Fe_2O_3 (Sigma-Aldrich, CAS number: 1309-37-1), $K_2Si_4O_9$ (Alfa Aesar, CAS number: 1312-76-1), and KOH (Sigma-Aldrich, CAS number: 1310-58-3), in order to understand the effect of different components constituting a typical biomass fly ash. The melting point/eutectic point/glass transition temperature of the model fly ash compounds is provided in Table 2. Each of the different components was milled and sieved individually to obtain a particle size distribution bounded by 32 and 90 μm. However, it should be noted that fly ash in boilers typically form a bimodal particle size distribution, consisting of submicron particles, as well as larger particles (~10–200 μm).[1,6] Although the deposits prepared in this study do not contain any submicron particles, it is ensured that the particle size lies within the second peak of the characteristic bimodal size distribution. Since KCl and K_2SO_4 are the major species found in the inner layer of typical biomass ash deposits,[8] all investigated model fly ash deposits contained KCl and K_2SO_4.

Table 1. Composition, Particle Size, and Melting Point Analysis of the Investigated Fly Ashes

elemental composition (wt %, dry basis)	straw fly ash, grate fired	straw + wood cofired fly ash, suspension fired	wood fly ash, suspension fired
Al	–	2	2.13
Ca	1.3	20	20.8
Cl	19	1.3	0.2
Fe	0.044	1.4	1.73
K	43	9.1	6.26
Mg	0.12	3.3	3.22
Na	0.9	0.9	0.43
P	–	1.4	1.09
S	7.9	1.5	1.08
Si	1.1	12	17.7
Ti	–	0.14	–
Mn	0.059	–	–
deformation temperature[17] (°C)	640	1240	1220
hemispherical temperature[17] (°C)	640	1250	1230
fluid temperature[17] (°C)	760	1260	1240
median particle size (μm)	51.7	44.5	34.7

Experiments were carried out using three different types of steel, TP347HFG (Salzgitter Mannesmann), 316SS (Sandvik), and 3R69BT (Sandvik), as well as tubes made from pure iron. The tubes had an outer diameter of 38 mm and a thickness of 5 mm. The chemical composition of the steel tubes is provided in Table 3. The addition of Cr, Mo, and Mn in steel reduces oxide scale growth,[19,20] improving overall corrosion resistance,[21] while Ni acts as a deterrent for Cl induced corrosion.[22] Preoxidation of steel tubes is beneficial for hindering corrosion[23,24] and provides superior replication of operational boiler tubes.[25,26] Thermogravimetric analysis of the steel tubes at 600 °C revealed that the majority of the oxidation occurs in the first few hours, after which the rate of oxidation significantly slows down (see Figure 1). Therefore, the tubes were preoxidized for 24 h at 600 °C prior to conducting experiments.

Table 2. Eutectic Temperature/Melting Point/Glass Transition Temperature of the Investigated Model Fly Ash Compounds[a]

Composition	Eutectic temperature[†]melting point[‡]/glass transition temperature[§] (°C)
KCl[‡]	770
KCl + K_2SO_4[†]	690
KCl + K_2SO_4 + CaO[†]	690
KCl + K_2SO_4 + $CaSO_4$[†]	644
KCl + K_2SO_4 + SiO_2[†]	690
KCl + K_2SO_4 + K_2CO_3[†]	580
KCl + K_2SO_4 + Fe_2O_3[†]	577
KCl + K_2SO_4 + $K_2Si_4O_9$[§]	650
KCl + K_2SO_4 + KOH[†]	288

[a] Data obtained from multiple sources.[8,37,38,67]

Table 3. Composition of the Investigated Steel Tubes

Steel type	Cr (wt %)	Ni (wt %)	Fe (wt %)	Others (wt %)
Iron			100	
316SS	16–18	10–14	balance	C = 0.08, Si = 0.75, Mn = 2, P = 0.045, S = 0.03, Mo = 2.5
TP347HFG	17–20	9–13	balance	C = 0.08, Si = 0.75, Mn = 2, P = 0.04, S = 0.03, Nb + Ta = 1
3R69BT	17.5	12.5	balance	C = 0.03, Si = 0.4, Mn = 1.7, P = 0.03, S = 0.015, Mo = 2.2

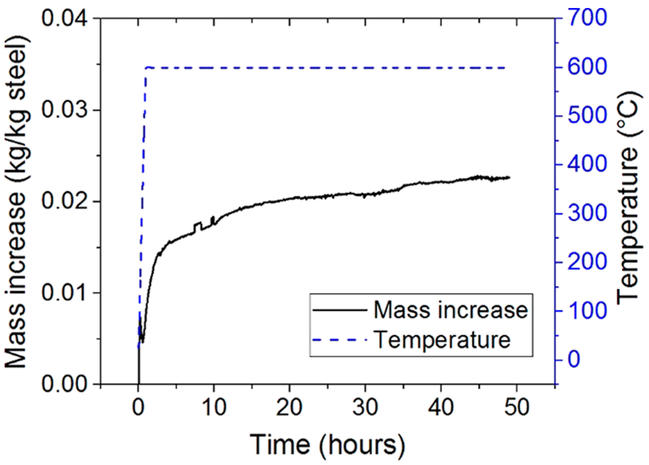

Figure 1. Thermogravimetric analysis of steel used (TP347HFG), exposed to air at 600 °C. Most of the oxidation occurs within the first few hours, after which the oxidation rate significantly slows down. Sample mass of 2059 mg, heating rate of 10 K/min.

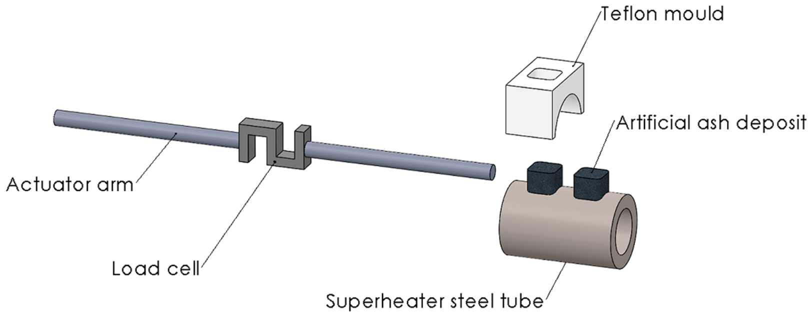

Figure 2. Experimental setup for adhesion strength measurements. The superheater steel tube is placed inside the oven while the load cell is outside the oven. The actuator arm shears off the artificial ash deposit and the load cell measures the corresponding adhesion strength. Image not to scale.

Sample Preparation. In order to obtain tightly packed and adherent deposits, the ash particles were mixed with a 50% isopropanol solution to prepare a thick slurry and molded into a cubical shaped deposit on the surface of the tube, using a Teflon mold (see Figure 2). The deposits were 15 mm × 15 mm × 10 mm, (W × D × H) in size, leading to a contact surface area of 223 mm^2. The use of deposit slurries is in accordance with EU guidelines[2,27,28] for high temperature corrosion testing, providing a better representation of deposits in power plants. However, it should be noted that the deposit formation process and the typical particle size distribution of fly ash in boilers are different from the case of the samples prepared in this study.[1,6,8]

Deposit Sintering and Adhesion Strength Measurement. The deposits were heated up and sintered inside an oven for a fixed duration. A purge air flow of 15 NL/min was injected into the oven, to protect the oven heating elements from corrosion.

After sintering, the deposits were cooled down to the required measurement temperature at a rate of 15 °C/min, subsequently followed by shear adhesion strength measurements. An electrically controlled arm was used to debond the artificial ash deposit from the superheater tube, as shown in Figure 2. The arm was controlled using a linear actuator, and the corresponding force applied on the ash deposit was measured using a load cell. Shear adhesion strength was calculated by dividing the measured force by the contact area between the deposit and the superheater tube. Standard experiments were performed by sintering the deposits at 650 °C for 4 h, while the adhesion strength was measured at 600 °C. These parameters were chosen providing consideration for typical sintering temperatures of the inner layers of the deposit,[8] typical boiler steam temperatures,[29−32] temperature gradients across the steel tube, resulting in the steel surface temperature to be 20−50 °C higher than the steam temperature,[8,33,34] a reasonable experimental time, and the deposit formation process.[6,31] In order to account for the scatter observed while measuring adhesion strength, measurements were conducted on at least four deposit samples for each instance of experimental conditions.

Selected samples were analyzed using scanning electron microscopy to observe the deposit−tube interface. The steel tubes, along with deposits, were cast in epoxy and polished, without any exposure to water, thereby preventing any dissolution, recrystallization, and removal of salts.

■ RESULTS AND DISCUSSION

Effect of Sintering Temperature. Figure 3 shows the effect of sintering temperature on adhesion strength. Experiments were performed with pure KCl, as well as three different boiler fly ashes (see Table 1). It can be observed that adhesion strength increases with increasing temperature, with a sharp increase near the melting point/ash deformation temperature,[17] i.e., 640 °C for straw fly ash, and 770 °C for KCl.

A sharp increase in adhesion strengths for wood fly ash and the straw + wood cofired fly ash has not been observed in this study, due to their high ash deformation temperatures, 1220 and 1240 °C respectively (see Figure 3). Furthermore, it should be noted that increasing the temperature of the oven to temperatures significantly higher than the melting point (or ash deformation temperature) led to completely molten deposits, whose adhesion strength could not be measured.

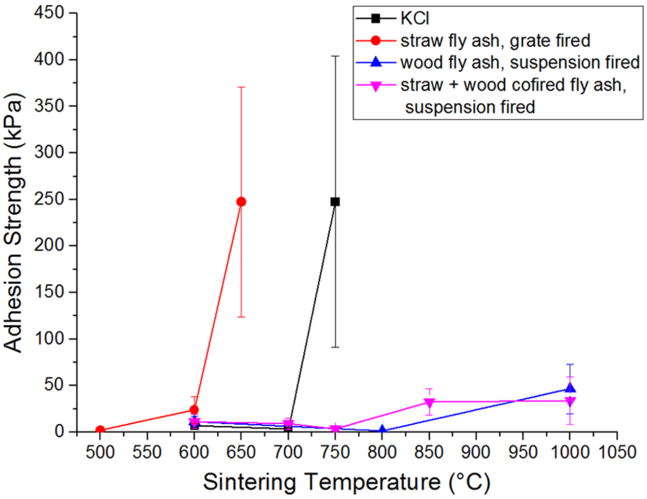

Figure 3. Effect of sintering temperature on shear adhesion strength for KCl and biomass fly ashes. Shear adhesion strength increases sharply near the melting point/ash deformation temperature.[17] Deposits sintered for 4 h, measured at 600 °C, TP347HFG steel preoxidized for 24 h, average of 4 data points.

Effect of Eutecticity. The constituents of fly ash typically form eutectic systems,[3,35] leading to melt formation at temperatures lower than the melting point of the individual components. The aforementioned results seem to indicate that the adhesion strength of an ash deposit is dependent on its melting point. Previous studies in literature have indicated that the melt fraction of the deposit, especially at the deposit−tube interface, influences its adhesion strength.[4,5] In order to better understand this phenomenon, experiments were performed with model fly ash compounds containing KCl and K_2SO_4. KCl and K_2SO_4, with individual melting points of 770 and 1069 °C, form a eutectic system with a eutectic temperature of 690 °C. The eutectic temperature was calculated using the software, FactSage.[36,37] However, other experimental studies have identified melt formation at 683 °C for a 50 wt % KCl−K_2SO_4 system.[38] In the experiments, the amount of K_2SO_4 in KCl was varied at 650 °C, and the corresponding results are shown in Figure 4, along with the KCl−K_2SO_4 phase diagram. The phase diagram was obtained using FactSage.

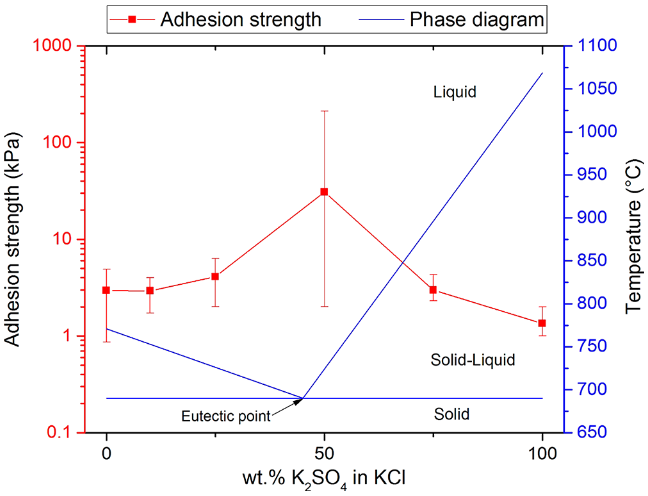

Figure 4. Effect of varying concentration of K_2SO_4 in KCl on shear adhesion strength. Deposits sintered at 650 °C for 4 h, measured at 600 °C, TP347HFG steel preoxidized for 24 h, average of 4 data points (24 for 50 wt %). Mixing of KCl and K_2SO_4 causes an increase in adhesion strength.

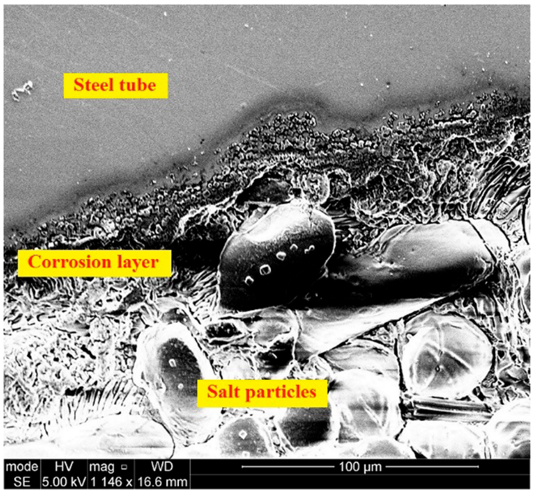

Figure 5. SEM image of deposit−tube interface. KCl−K_2SO_4 (50 wt %) deposit, sintered at 650 °C for 4 h, TP347HFG steel preoxidized for 24 h. Partially molten corrosion layer observed at the deposit−tube interface.

The results indicate that while pure substances do not have much adhesion strength at 650 °C, mixing of the components causes a large increase in the adhesion strength. Since KCl and K_2SO_4 form a eutectic system, mixing of the two components leads to an increase in the melt fraction of the deposit. Therefore, it can be inferred that a higher melt fraction at the deposit−tube interface leads to a higher adhesion strength. However, the experiments were carried out at 650 °C, which is lower than the eutectic temperature of the KCl−K_2SO_4 system. This indicates the presence of a secondary phenomenon influencing deposit adhesion strength, which has been explored in the following section by conducting a SEM analysis of the deposit−tube interface.

SEM Analysis of the Deposit−Tube Interface. In order to determine the morphology of the deposits at the deposit−tube interface, SEM analysis of the interface was carried out for the model fly ash deposit containing KCl and K_2SO_4 (50 wt %). The analysis revealed the formation of a dense, partially molten layer at the interface, as seen in Figure 5. As the temperature increases, corrosion starts to occur at the interface. As a result, corrosion products, such as Fe/Cr chlorides, oxides, chromates, etc., are formed.[2,39−43] Most of the corrosion products form a complex eutectic system with the components present in the deposit.[44,45] This leads to a lower eutectic temperature at the interface, compared to the outer layers of the deposit. The partially molten layer causes increased surface wetting and adsorption,[46] leading to high surface adhesion.

It should be noted that debonding always occurred in the corrosion layer throughout all experiments, exposing a fresh layer of steel tube after deposit removal.

Effect of Composition. Experiments were conducted with model fly ash deposits to understand the role of different components present in a typical biomass fly ash. The model fly ash deposits were made up of particles larger than 32 μm and smaller than 90 μm.

The results highlight the effect of sulfation on adhesion strength, as seen in Figure 6. The deposit containing KCl and K_2SO_4 (50 wt %) exhibited much higher adhesion strength compared to a deposit containing pure KCl. Similarly, the deposit containing KCl, K_2SO_4, and $CaSO_4$ (33 wt % each) showed a higher adhesion strength than the deposit containing KCl, K_2SO_4, and CaO.

The increase in adhesion strength of deposits containing sulfur can be attributed to the fact that KCl−K_2SO_4 and KCl−K_2SO_4−$CaSO_4$ form a eutectic system (see Table 2). Therefore, sulfation lowers the eutectic/deformation temperature of the ash deposit, increasing melt fraction, and thereby increasing adhesion strength.

In boilers, KCl can undergo sulfation in the gas phase prior to deposition,[47] or in solid phase after deposition on boiler surfaces.[48] While gas phase sulfation is faster than solid phase sulfation, the deposit is exposed to the flue gas for a longer period of time,[48] making both sulfation mechanisms relevant. Similarly, CaO can undergo sulfation to form $CaSO_4$.[49,50]

Sulfation of KCl in deposits can occur as a gas−solid or gas−liquid reaction by SO_2[51] or SO_3,[52] as shown in the following equations.

$$2KCl + SO_2 + \frac{1}{2}O_2 + H_2O \rightarrow K_2SO_4 + 2HCl$$

$$2KCl + SO_3 + H_2O \rightarrow K_2SO_4 + 2HCl$$

Iron oxide may catalytically convert SO_2 to SO_3,[45,53] or react with SO_2 to form Fe(III) sulfites or sulfates,[54,55] thereby catalyzing the overall sulfation reaction and increasing the concentration of K_2SO_4 near the steel surface.

The present results provide evidence that sulfation may result in an increase in adhesion strength at the investigated conditions. However, these results are not conclusive, since sulfate-forming reactions occurring inside the deposit have not been explored in the conducted experiments. Further investigation of deposit sulfation is required to completely understand the influence of the overall sulfation process on deposit adhesion strength. Nevertheless, it is speculated that reactions occurring between the deposit and the flue gas may contribute to adhesion strength variations in boilers.

Furthermore, the results portray the effect of CaO, SiO_2, K_2CO_3, Fe_2O_3, $K_2Si_4O_9$, and KOH (see Figure 6). While Ca and Si are widely present in biomass ash deposits, the presence of K_2CO_3 has been identified in only a few studies in literature.[56,57] The addition of CaO to a model fly ash deposit

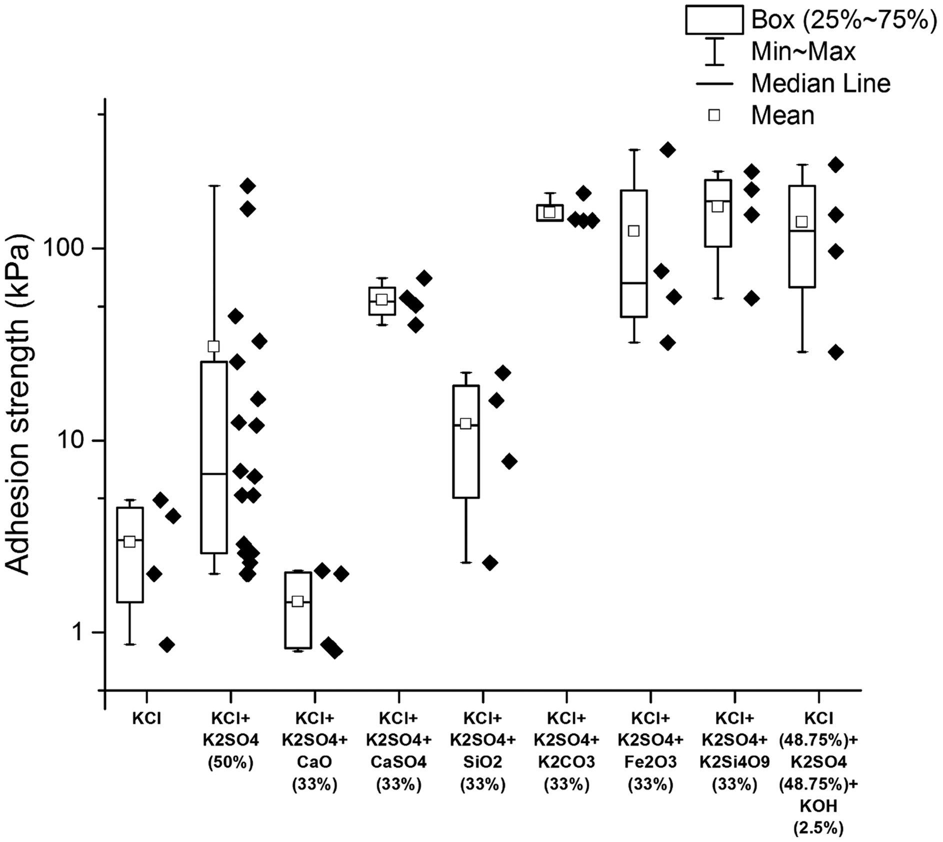

Figure 6. Effect of composition on adhesion strength using model fly ash compounds. Deposits sintered at 650 °C for 4 h, measured at 600 °C, TP347HFG steel preoxidized for 24 h, 4 data points (24 for KCl + K_2SO_4). All compositions in weight %.

containing KCl−K_2SO_4 decreased its adhesion strength. CaO does not form a eutectic melt with the KCl−K_2SO_4 system, effectively reducing the melt fraction, and thereby decreasing the adhesion strength. However, the addition of SiO_2 does not seem to significantly affect the adhesion strength under the conditions examined.

The addition of K_2CO_3 to the model fly ash deposit containing KCl and K_2SO_4 considerably increased the adhesion strength. Addition of K_2CO_3 decreases the eutectic temperature of the KCl−K_2SO_4 system (see Table 2), increasing the melt fraction of the ash deposit at 650 °C, and thereby increasing the adhesion strength. Furthermore, K_2CO_3 may react with the steel, leading to the formation of a potassium−chromium compound, most likely K_2CrO_4,[41,58,59] which forms a low-temperature melt with KCl,[60] further increasing the melt fraction at the deposit−tube interface.

Moreover, the addition of Fe_2O_3 significantly increased the adhesion strength of the ash deposits, bolstering the aforementioned theory correlating corrosion with high adhesion strength. Apart from decreasing the melting point of the mixture (see Table 2), the presence of Fe_2O_3 in the deposit may cause increased formation of corrosion intermediates, such as $FeCl_2$ or $FeCl_3$, according to the following proposed reaction. The reaction mechanism has been verified using Factsage.[37]

$$Fe_2O_3 + 6KCl \rightleftharpoons 2FeCl_3 + 3K_2O$$

Moreover, in full-scale boilers, where HCl present in the flue gas may be oxidized to Cl_2, the following reaction may occur, leading to the formation of $FeCl_2$.[22,61,62]

$$Fe_2O_3 + 2Cl_2 \rightleftharpoons 2FeCl_2 + 1.5O_2$$

Since $FeCl_2$, as well as $FeCl_3$, forms a eutectic system with the ash deposit, the corresponding increase in melt fraction results in an increase in adhesion strength.

A similar increase in adhesion strength is observed when $K_2Si_4O_9$ is added to the KCl−K_2SO_4 system. The presence of alkali silicates has been identified in mature and sintered deposits in straw-fired boilers.[8] $K_2Si_4O_9$ is known to form a glass phase at high temperatures, gradually decreasing in viscosity with increasing temperature.[63] Analysis of the $K_2Si_4O_9$ samples using differential scanning calorimetry revealed that $K_2Si_4O_9$ has a glass transition temperature of 650 °C (see Figure 7). The formation of a semimolten glass phase causes an increase in surface wetting and increased adhesion of the deposit to the steel tube.

The presence of KOH in deposits has been postulated in a few studies in literature.[56,62] In the present study, it was observed that even the addition of a small amount of KOH (2.5 wt %) to the model fly ash deposit causes a large increase in adhesion strength. This can directly be attributed to the low melting point of KOH (360 °C) and the formation of a eutectic system with KCl−K_2SO_4 (see Table 2), causing increased melt formation and adhesion strength.

From this section, it can be concluded that addition of compounds which increase the melt fraction of the ash deposit, usually by forming a eutectic system, increases the adhesion strength. However, addition of inert compounds with a high melting point, such as CaO (melting point of 2572 °C), decreases the adhesion strength.

DOI: 10.1021/acs.energyfuels.7b01312
Energy Fuels 2017, 31, 8733−8741

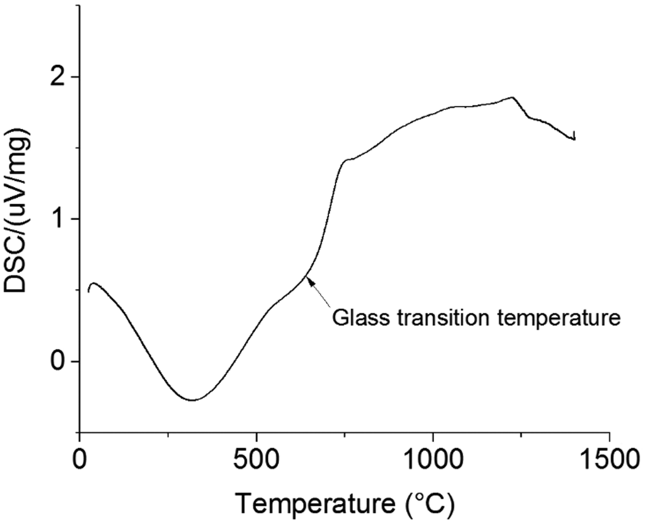

Figure 7. Differential scanning calorimetry analysis of $K_2Si_4O_9$. The silicate forms a glassy phase, with a glass transition temperature of 650 °C. Sample mass of 10.5 mg, heating rate of 10 K/min.

Effect of Sintering Time. The sintering time seems to have a negligible effect on adhesion strength up to 24 h at the investigated conditions, as seen in Figure 8. It should be noted that the all experiments are subjected to an additional 30 min of heating time prior to sintering, and 5 min for strength measurement after sintering.

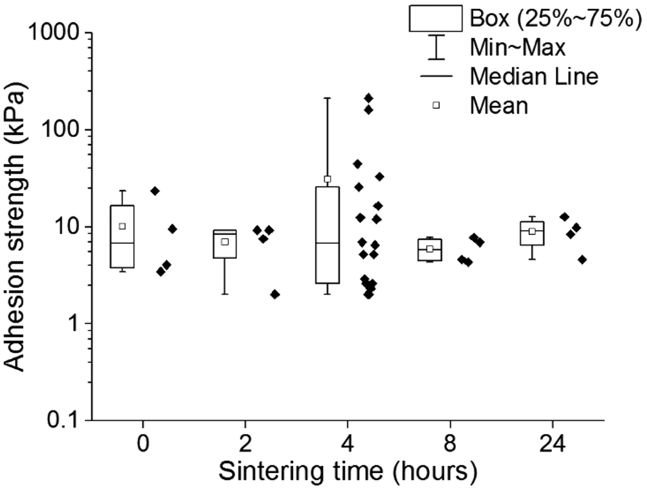

Figure 8. Effect of sintering time on adhesion strength. KCl−K_2SO_4 (50 wt %) deposit, sintered at 650 °C, measured at 600 °C, TP347HFG steel preoxidized for 24 h, 4 data points (24 for 4 h).

The results suggest that the initial, partially molten corrosion layer is formed rather quickly, and significant changes in adhesion strength do not occur after the formation of the initial corrosion layer at the interface within 24 h. Several studies in literature indicate that the onset of corrosion is typically within a few minutes, and the rate of corrosion decreases exponentially over time.[2,39,64] The marginal change in melt fraction due to increasing corrosion is not significant enough to observe reliable changes in adhesion strength. However, further investigation is required prior to arriving at conclusions, especially considering that sintering in boilers may occur for longer durations.

Nevertheless, an increase in deposit adhesion strength may be observed in boilers due to sintering caused by reactions occurring in the deposit, e.g., sulfation,[65] which have not been investigated in this study. Sulfation does not occur in the experimental setup, due to the absence of SO_2 in the gas stream.

Effect of Thermal Shocks. Application of thermal shocks to induce deposit shedding is a technique commonly used to remove heavily sintered deposits from superheater tubes.[13,66] This study further investigates the effect of thermal shocks by cooling down the deposit after sintering. Deposits were cooled down at a rate of 15 °C/min.

As seen in Figure 9, cooling down the deposits results in a decrease in adhesion strength. Thermal stresses are induced at the deposit−tube interface, owing to differences in the thermal expansion coefficients between the deposit/corrosion layer and the steel tube.[66] As a result, cracks may develop at the interface, leading to a decrease in adhesion strength.

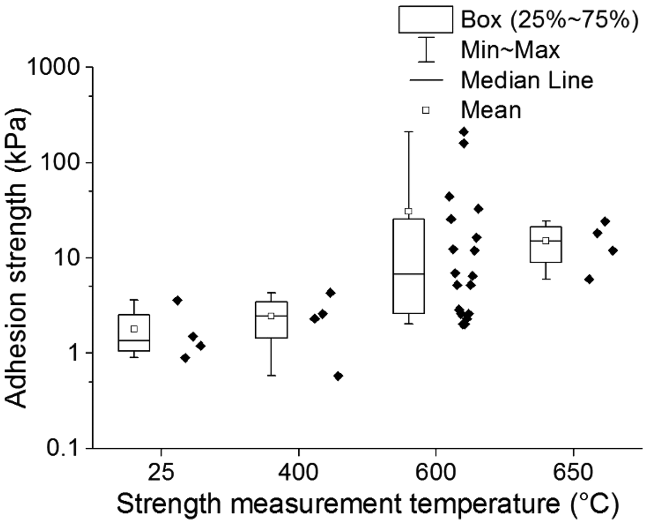

Figure 9. Effect of strength measurement temperature on adhesion strength. KCl−K_2SO_4 (50 wt %) deposit, sintered at 650 °C for 4 h, TP347HFG steel preoxidized for 24 h, 4 data points (24 for 600 °C).

Effect of Steel Type. In order to understand the effect of the type of steel used, experiments were carried out using a model fly ash deposit containing KCl−K_2SO_4 (50 wt %) on three different types of steel as well as pure iron tubes (see Table 3). Experiments were carried out for 4 h at 650 °C.

The results indicate that the type of steel used does not have a strong influence on the adhesion strength at the investigated conditions, considering the scatter in data (see Figure 10). Previous studies have shown that KCl induces corrosion at the steel surface, irrespective of the type of steel,[58] although the depth of the corrosion layer might be different. The results seem to indicate that while the presence of corrosion causes high adhesion strength, the depth of the corrosion layer is not a major factor influencing adhesion strength, especially considering that the onset of the corrosion layer is typically within a few minutes.[2,39,64]

However, the adhesion strength of deposits to pure iron tubes appears to be slightly higher, when compared to the investigated steels, indicating that the presence of corrosion inhibiting elements in steel might play a role in influencing adhesion strength. Further investigation, spanning over a larger range of steel types, is required prior to arriving at conclusions.

DOI: 10.1021/acs.energyfuels.7b01312
Energy Fuels 2017, 31, 8733−8741

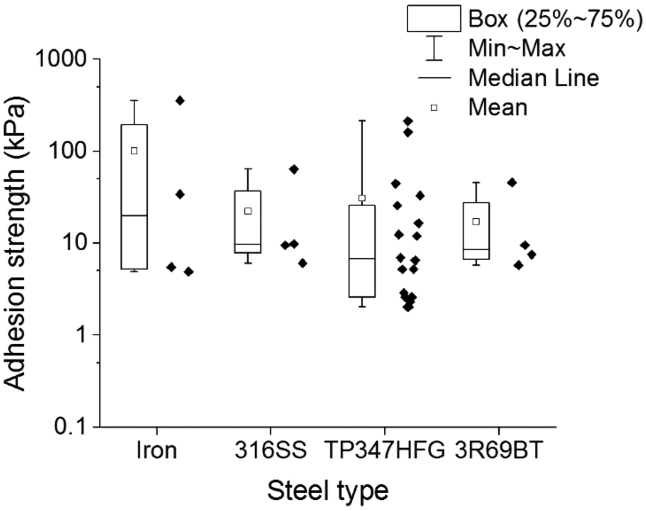

Figure 10. Effect of steel type on adhesion strength. KCl–K_2SO_4 (50 wt %) deposit, sintered at 650 °C for 4 h, measured at 600 °C, steels preoxidized for 24 h, 4 data points (24 for TP347HFG).

Analysis of Scatter in Adhesion Strength Data. In order to better understand the significant scatter observed in the data, 24 experiments were conducted using KCl–K_2SO_4 (50 wt %) deposits. The experiments reveal that adhesion strength data roughly follow a log-normal distribution, as seen in Figure 11. This is similar to observations made using deposits from kraft recovery boilers.[5] Moreover, experiments conducted in full-scale biomass-fired boilers indicate similar trends.[4]

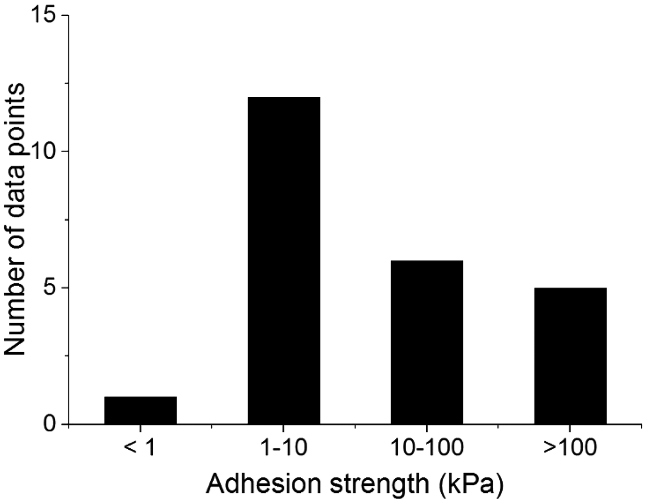

Figure 11. Log-normal distribution of adhesion strength data. KCl–K_2SO_4 (50 wt %) deposit, sintered at 650 °C for 4 h, measured at 600 °C, TP347HFG steel preoxidized for 24 h, 24 data points.

The stochastic nature of debonding has significant implications on deposit shedding in boilers. The results suggest that even though soot-blowing may remove the majority of the deposits, the strongly adherent deposits might not be removed. Subsequent accumulation of strong deposits probably results in the eventual fouling of boiler surfaces.[5]

The adhesion strength of biomass ash deposits observed in this study is comparable in magnitude to coal ash deposits from lab-scale investigations,[9−11] as well as biomass ash deposits from full-scale studies,[4] as shown in Table 4. However, previous lab-scale investigations indicate that deposits from kraft recovery boilers are more strongly adherent, when compared to biomass and coal ash deposits.[5]

Table 4. Adhesion Strength of Different Types of Deposits

deposit type	adhesion strength (kPa)
biomass ash deposits, current lab-scale investigation	1−350
biomass ash deposits, full-scale investigations[4]	20−250
coal ash deposits, lab-scale investigations[9−11]	35−350
deposits from kraft recovery boilers, lab-scale investigations[5]	1000−16000

Practical Application of the Study. The results allow a better understanding of the process of deposit shedding, both qualitatively and quantitatively. Furthermore, the obtained data may be used to develop a tool for analyzing the effect of fuel composition on adhesion strength, and suggesting boiler operating conditions to prevent the formation of strong deposits. For example, the study identifies that maintaining steel temperatures below the ash deformation temperature results in the formation of weaker deposits. Furthermore, the study quantifies the degree of thermal shocks needed to weaken the strongly adherent deposits. Moreover, the study analyzes the effect of composition of the fly ash, which could be used to estimate fuel quality. However, further work is required prior to arriving at conclusions.

Additionally, the obtained data may be used to optimize soot-blowing in boilers by recommending soot-blowing frequencies and pressures based on the fuel and operating conditions. This may be done by modeling the log-normal distribution of adhesion strength data, incorporating the effect of deposit composition, flue gas temperature, and steam temperature. However, further experimental work is required for the development of a detailed model.

■ CONCLUSIONS

This study investigated the shear adhesion strength of biomass ash deposits from full-scale boilers, as well as model fly ash deposits containing KCl, K_2SO_4, CaO, $CaSO_4$, SiO_2, K_2CO_3, Fe_2O_3, $K_2Si_4O_9$, and KOH. Deposits were prepared on superheater tubes and sintered in a laboratory oven. The effects of sintering temperature, sintering time, deposit composition, thermal shocks on the deposit, and steel type were investigated.

Increasing sintering temperatures resulted in higher adhesion strengths, with a sharp increase observed near the ash deformation temperature/melting point. Sintering time did not significantly affect adhesion strengths up to 24 h at 650 °C, using a model fly ash deposit containing KCl–K_2SO_4 (50 wt %). Furthermore, it was substantiated that cooling down the deposit after sintering reduces the adhesion strength, due to thermal stresses induced at the deposit–tube interface.

Deposits containing sulfates showed increased adhesion strengths, indicating that sulfation may cause the formation of stronger deposits. The addition of K_2CO_3, Fe_2O_3, $K_2Si_4O_9$, and KOH to the model fly ash deposit increased the ash melt fraction at the deposit–tube interface, thereby increasing the adhesion strength, whereas the addition of CaO decreased the ash melt fraction, thereby decreasing the adhesion strength.

Furthermore, the type of steel used did not seem to have a considerable effect on the adhesion strength. Finally, experiments revealed that adhesion strength data roughly follow a log-normal distribution.

This study identified that the adhesion strength of ash deposits is dependent on two factors: ash melt fraction, and corrosion occurring at the deposit−tube interface. A higher ash melt fraction at the deposit−tube interface leads to an increase in adhesion strength. Corrosion occurring at the interface leads to the formation of corrosion products, which form a eutectic system with the inner layer of deposit and increase the local melt fraction, thereby increasing the adhesion strength.

AUTHOR INFORMATION

Corresponding Author

*E-mail: ylax@kt.dtu.dk.

ORCID

Yashasvi Laxminarayan: 0000-0002-8976-0326
Hao Wu: 0000-0003-0462-2491
Peter Glarborg: 0000-0002-6856-852X

Notes

The authors declare no competing financial interest.

ACKNOWLEDGMENTS

This work is part of the project, 'Flexible use of Biomass on PF fired power plants', funded by Energinet.dk through the ForskEL program, DONG Energy and DTU.

REFERENCES

(1) Zbogar, A.; Frandsen, F.; Jensen, P. A.; Glarborg, P. *Prog. Energy Combust. Sci.* **2009**, *35*, 31−56.
(2) Okoro, S. C.; Montgomery, M.; Frandsen, F. J.; Pantleon, K. *Energy Fuels* **2014**, *28*, 6447−6458.
(3) Frandsen, F. *Ash Formation, Deposition and Corrosion When Utilizing Straw for Heat and Power Production*; Technical University of Denmark, Department of Chemical Engineering, 2010.
(4) Bashir, M. S.; Jensen, P. A.; Frandsen, F.; Wedel, S.; Dam-Johansen, K.; Wadenbäck, J. *Energy Fuels* **2012**, *26*, 5241−5255.
(5) Kaliazine, A.; Cormack, D.; Ebrahimi-Sabet, A.; Tran, H. *J. Pulp Paper Sci.* **1999**, *25*, 418−424.
(6) Zhou, H.; Jensen, P. A.; Frandsen, F. J. *Fuel* **2007**, *86*, 1519−1533.
(7) Baxter, L. L. *Biomass Bioenergy* **1993**, *4*, 85−102.
(8) Jensen, P. A.; Frandsen, F. J.; Hansen, J.; Dam-Johansen, K.; Henriksen, N.; Hörlyck, S. *Energy Fuels* **2004**, *18*, 378−384.
(9) Moza, A. K.; Austin, L. G. *Fuel* **1981**, *60*, 1057−1064.
(10) Moza, A.; Shoji, K.; Austin, L. *J. Inst. Energy* **1980**, *53*, 17−19.
(11) Raask, E. *VGB Kraftwerkstech* **1973**, *53*, 248−254.
(12) Attig, R.; Barnhart, D. A laboratory method of evaluating factors affecting tube bank fouling in coal-fired boilers. In *The Mechanism of Corrosion by Fuel Impurities*; Johnson, H. R., Littler, D. J., Eds.; Butterworth: London, 1963; p 173.
(13) Conn, R.; Jones, M. Comparison of low-rank coal ash sintering characteristics with pilot plant ash fouling tendencies. In *Third Engineering Foundation Conference on Slagging and Fouling Due to Impurities in Combustion Gases*; Barrett, R. E., Ed.; Copper Mountain: CO, 1984; pp 207−228.
(14) Cumming, I.; Joyce, W.; Kyle, J. *J. Inst. Energy* **1985**, *58*, 169−175.
(15) Yilu, S. Evaluating fouling and slagging characteristics of different Chinese coal ashes. In *Third Engineering Foundation Conference on Slagging and Fouling Due to Impurities in Combustion Gases*; Barrett, R. E., Ed.; Copper Mountain: CO, 1984; pp 557−592.
(16) Piroozmand, F.; Tran, H.; Kaliazine, A.; Cormack, D. Strength of recovery boiler fireside deposits at high temperatures. *Tappi Proceedings*; 1998; pp 169−179.
(17) European Committee for Standardization. *Solid biofuels - Method for the determination of ash melting behaviour - Part 1: Characteristic temperatures method, CEN/TS 15370−1:2006*.
(18) Gupta, S.; Wall, T.; Creelman, R.; Gupta, R. *Fuel Process. Technol.* **1998**, *56*, 33−43.
(19) Hamzah, M.; Yeo, W.; Fry, A.; Inayat-Hussain, J.; Ramesh, S.; Purbolaksono, J. *Eng. Failure Anal.* **2013**, *35*, 380−386.
(20) Schmidt, D.; Schütze, M. *Mater. Sci. Forum* **2011**, *696*, 330−335.
(21) Yukitoshi, T.; Yoshikawa, K.; Daikoku, T.; Masuyama, F. *J. Mater. Energy Syst.* **1982**, *4*, 99−109.
(22) Zahs, A.; Spiegel, M.; Grabke, H. J. *Corros. Sci.* **2000**, *42*, 1093−1122.
(23) Okoro, S. C.; Kvisgaard, M.; Montgomery, M.; Frandsen, F. J.; Pantleon, K. *Surf. Eng.* **2017**, *33*, 428−432.
(24) Israelsson, N.; Engkvist, J.; Hellström, K.; Halvarsson, M.; Svensson, J.; Johansson, L. *Oxid. Met.* **2015**, *83*, 29−53.
(25) Sabau, A.; Wright, I.; Shingledecker, J. *Mater. Corros.* **2012**, *63*, 896−908.
(26) Rizzi, M.; Guerrini, E.; Trasatti, S. *Metall. Ital.* **2012**, *2*, 29−35.
(27) Coleman, K.; Simms, N.; Kilgallon, P.; Oakey, J. *Mater. Sci. Forum* **2008**, *595-598*, 377−386.
(28) Grabke, H. J.; Meadowcroft, D. *A Working Party Report on Guidelines for Methods of Testing and Research in High Temperature Corrosion*; European Federation of Corrosion: Belgium, 1995.
(29) Bashir, M. S.; Jensen, P. A.; Frandsen, F.; Wedel, S.; Dam-Johansen, K.; Wadenbäck, J.; Pedersen, S. T. *Fuel Process. Technol.* **2012**, *97*, 93−106.
(30) Wu, H.; Shafique Bashir, M.; Jensen, P. A. *Full-Scale Ash Deposition Measurements at Avedøre Power Plant Unit 2 during Suspension-Firing of Wood with and without Coal Ash Addition*; Technical University of Denmark, Department of Chemical Engineering: 2012.
(31) Hansen, S. B. *Model for Deposition Build-up in Biomass Boilers*; Technical University of Denmark: 2015.
(32) Montgomery, M.; Jensen, S.; Borg, U.; Biede, O.; Vilhelmsen, T. *Mater. Corros.* **2011**, *62*, 593−605.
(33) Lindberg, D.; Niemi, J.; Engblom, M.; Yrjas, P.; Laurén, T.; Hupa, M. *Fuel Process. Technol.* **2016**, *141*, 285−298.
(34) Montgomery, M.; Karlsson, A.; Larsen, O. H. *Mater. Corros.* **2002**, *53*, 121−131.
(35) van Lith, S. C. *Release of Inorganic Elements during Wood-Firing on a Grate*; Technical University of Denmark: 2005.
(36) Bale, C.; Bélisle, E.; Chartrand, P.; Degterov, S.; Eriksson, G.; Hack, K.; Jung, I.; Kang, Y.; Melançon, J.; Pelton, A. *CALPHAD: Comput. Coupling Phase Diagrams Thermochem.* **2009**, *33*, 295−311.
(37) Bale, C.; Chartrand, P.; Degterov, S.; Eriksson, G.; Hack, K.; Mahfoud, R. B.; Melançon, J.; Pelton, A.; Petersen, S. *CALPHAD: Comput. Coupling Phase Diagrams Thermochem.* **2002**, *26*, 189−228.
(38) Arvelakis, S.; Jensen, P. A.; Dam-Johansen, K. *Energy Fuels* **2004**, *18*, 1066−1076.
(39) Sui, J.; Lehmusto, J.; Bergelin, M.; Hupa, M. *Oxid. Met.* **2014**, *82*, 437−456.
(40) Shinata, Y.; Nishi, Y. *Oxid. Met.* **1986**, *26*, 201−212.
(41) Pettersson, J.; Asteman, H.; Svensson, J.; Johansson, L. *Oxid. Met.* **2005**, *64*, 23−41.
(42) Spiegel, M. *Mater. Corros.* **1999**, *50*, 373−393.
(43) Lee, S. Y.; McNallan, M. J. *Corrosion* **1991**, *47*, 868−874.
(44) Viklund, P.; Hjörnhede, A.; Henderson, P.; Stålenheim, A.; Pettersson, R. *Fuel Process. Technol.* **2013**, *105*, 106−112.
(45) Nielsen, H. P.; Frandsen, F. J.; Dam-Johansen, K. *Energy Fuels* **1999**, *13*, 1114−1121.
(46) Packham, D. E. Theories of fundamental adhesion In *Handbook of Adhesion Technology*; da Silva, L. F. M., Öchsner, A., Adams, R. D., Eds.; Springer: Berlin, 2011; pp 9−38.
(47) Iisa, K.; Lu, Y.; Salmenoja, K. *Energy Fuels* **1999**, *13*, 1184−1190.

DOI: 10.1021/acs.energyfuels.7b01312
Energy Fuels 2017, 31, 8733−8741

(48) Sengeløv, L. W.; Hansen, T. B.; Bartolomé, C.; Wu, H.; Pedersen, K. H.; Frandsen, F. J.; Jensen, A. D.; Glarborg, P. *Energy Fuels* **2013**, *27*, 3283−3289.
(49) Borgwardt, R. H.; Bruce, K. R. *AIChE J.* **1986**, *32*, 239−246.
(50) Marsh, D.; Ulrichson, D. *Chem. Eng. Sci.* **1985**, *40*, 423−433.
(51) Henriksson, M.; Warnqvist, B. *Ind. Eng. Chem. Process Des. Dev.* **1979**, *18*, 249−254.
(52) Fielder, W.; Stearns, C.; Kohl, F. *J. Electrochem. Soc.* **1984**, *131*, 2414−2417.
(53) Jørgensen, T. L.; Livbjerg, H.; Glarborg, P. *Chem. Eng. Sci.* **2007**, *62*, 4496−4499.
(54) Fu, H.; Wang, X.; Wu, H.; Yin, Y.; Chen, J. *J. Phys. Chem. C* **2007**, *111*, 6077−6085.
(55) Baltrusaitis, J.; Cwiertny, D. M.; Grassian, V. H. *Phys. Chem. Chem. Phys.* **2007**, *9*, 5542−5554.
(56) Wu, H.; Bashir, M. S.; Jensen, P. A.; Sander, B.; Glarborg, P. *Fuel* **2013**, *113*, 632−643.
(57) Blomberg, T. *Mater. Corros.* **2006**, *57*, 170−175.
(58) Kiamehr, S.; Dahl, K. V.; Montgomery, M.; Somers, M. A. *Mater. Corros.* **2015**, *66*, 1414−1429.
(59) Lehmusto, J.; Skrifvars, B.; Yrjas, P.; Hupa, M. *Fuel Process. Technol.* **2013**, *105*, 98−105.
(60) Ishitsuka, T.; Nose, K. *Corros. Sci.* **2002**, *44*, 247−263.
(61) Okoro, S. C.; Kiamehr, S.; Montgomery, M.; Frandsen, F. J.; Pantleon, K. *Mater. Corros.* **2017**, *68*, 499−514.
(62) Folkeson, N.; Jonsson, T.; Halvarsson, M.; Johansson, L.; Svensson, J. *Mater. Corros.* **2011**, *62*, 606−615.
(63) Dickinson, J. E.; Scarfe, C. M.; McMillan, P. *J. Geophys. Res.* **1990**, *95*, 15675−15681.
(64) Karlsson, S.; Jonsson, T.; Hall, J.; Svensson, J.; Liske, J. *Energy Fuels* **2014**, *28*, 3102−3109.
(65) Hurley, J. P.; Benson, S. A. *Energy Fuels* **1995**, *9*, 19−30.
(66) Raask, E. *Mineral Impurities in Coal Combustion: Behavior, Problems, and Remedial Measures*; Hemisphere Pub. Corp.: WA, 1985.
(67) Janz, G. J.; Allen, C. B.; Downey, J. R.; Tomkins, R. *Physical Properties Data Compilations Relevant to Energy Storage. I. Molten salts: Eutectic Data*; Rensselaer Polytechnic Institute: New York, 1978.

DOI: 10.1021/acs.energyfuels.7b01312

July 2019

ForskEL project no. 12150/EUDP 64018-003

Final report: Flexible use of biomass on PF Fired power plants

Appendix B. Journal paper: B. Laxminarayan Y., Nair A.B., Jensen P.A., Wu H., Frandsen F.J., Sander B., Glarborg P. Tensile Adhesion Strength of Biomass Ash Deposits: Effect of Temperature Gradient and Ash Chemistry. Energy Fuels 2018, 32, 4432-4441.

1. **Department of Chemical and Biochemical Engineering**
Technical University of Denmark
Søltofts Plads, Building 229, DK-2800, Kgs. Lyngby, Denmark
2. **Ørsted Bioenergy & Thermal power,**
Kraftværksvej 53, DK-7000, Fredericia, Denmark

CHEC no. R1902

energy&fuels
Article
Cite This: Energy Fuels 2018, 32, 4432−4441
pubs.acs.org/EF

Tensile Adhesion Strength of Biomass Ash Deposits: Effect of the Temperature Gradient and Ash Chemistry

Yashasvi Laxminarayan,*,[†] Akhilesh Balachandran Nair,[†] Peter Arendt Jensen,[†] Hao Wu,[†] Flemming Jappe Frandsen,[†] Bo Sander,[‡] and Peter Glarborg[†]

[†] Department of Chemical and Biochemical Engineering, Technical University of Denmark (DTU), Søltofts Plads 229, 2800 Kongens Lyngby, Denmark

[‡] Ørsted Bioenergy & Thermal Power A/S, Kraftsværksvej 53, Skærbæk, 7000 Fredericia, Denmark

ABSTRACT: Replacing coal with biomass in power plants is a viable option for reducing net CO_2 emissions and combating climate change. However, biomass combustion in boilers may exacerbate problems related to ash deposition and corrosion, demanding effective deposit removal. The tensile adhesion strength of model biomass ash deposits, containing mixtures of KCl, K_2SO_4, CaO, $CaSO_4$, and $K_2Si_4O_9$, has been investigated in this study. The deposits were prepared on superheater steel tubes and sintered in an oven. The superheater steel tube was cooled by air, incorporating a temperature gradient across the deposits. After sintering, the deposits were removed using an electrically controlled arm and the corresponding tensile adhesion strength was measured. The influence of the flue gas temperature (500−700 °C), steel surface temperature (500−650 °C), and deposit composition were investigated. The results revealed that increasing the flue gas temperature as well as the steel surface temperature led to a sharp increase in the tensile adhesion strength of the model deposits. The sharp increase was typically observed near the melting temperature (or deformation temperature) of the investigated model deposits. Furthermore, migration of molten/vapor species from the outer layer of the deposit to the deposit−tube interface, causing liquid-state sintering, was observed at high flue gas temperatures, leading to an increase in the tensile adhesion strength. Varying the ash chemistry of the model deposits revealed that the melt fraction of the deposit was highly influential in determining the deposit adhesion strength. The addition of compounds that increased the melt fraction of the deposit increased the tensile adhesion strength, whereas the addition of inert compounds with a high melting point, such as CaO, decreased the tensile adhesion strength. Moreover, the results suggested that the adhesion strength of the deposits was influenced by the corrosion occurring at the deposit−tube interface.

INTRODUCTION

Following the Paris Agreement at COP21,[1] global efforts to mitigate climate change have accelerated. Being a CO_2-neutral fuel, biomass can potentially replace coal for providing flexible electricity and heat production. Globally, the supply of biomass for energy has been growing at 2.5% every year since 2010, with bioenergy contributing 10.5% of the global primary energy consumption.[2] With Denmark aiming to replace coal with biomass in pulverized fuel power plants by 2030,[3] biomass firing and co-firing are gaining increased importance. However, biomass-fired boilers encounter numerous operational challenges, several of which are related to the critical volatile ash-forming elements, such as K and Cl, causing severe ash deposition and corrosion on boiler surfaces.[4,5] Deposit formation in boilers may occur through several mechanisms, including diffusion and condensation of vapors, thermophoresis, convective diffusion, and inertial impaction.[6,7] Ash deposition on boiler surfaces hinders heat transfer to the steam cycle, thereby reducing boiler efficiency.[8] Moreover, ash deposition may completely block the flue gas channels in severe cases, resulting in expensive boiler shutdowns. Therefore, timely and effective deposit removal are essential for maximizing boiler efficiency and availability.

Shedding of ash deposits in boilers may occur naturally, without any operational influence, or may be induced artificially (e.g., using soot blowing or load changes). Deposit shedding may occur through several mechanisms, including erosion, debonding, molten slag flow, and thermal and mechanical stresses within the deposits.[5] Erosion occurs when sharp-edged fly ash particles collide with non-molten deposits, resulting in deposit removal through chipping or repeated deformation. Debonding occurs when the generated stress (e.g., by soot blowing or as a result of the weight of the deposit) exceeds the adhesion strength at the deposit−tube interface, resulting in deposit removal from the tube surface. If the temperature of the outer layer of the deposit is sufficiently high for the formation of low-viscosity slags, molten phases may flow off the deposit. Thermal shocks caused by temperature changes in the boiler may induce deposit shedding due to differences among the thermal expansion coefficients of the tube, the corrosion layer, and the deposit. Full-scale investigations have identified that debonding is the dominant mechanism for deposit shedding in suspension-fired biomass boilers.[9] Hence, quantification of the adhesion strength of ash deposits is essential for understanding deposit shedding and for optimizing artificial removal of

Special Issue: 6th Sino-Australian Symposium on Advanced Coal and Biomass Utilisation Technologies

Received: October 13, 2017
Revised: January 19, 2018
Published: January 23, 2018

DOI: 10.1021/acs.energyfuels.7b03114
Energy Fuels 2018, 32, 4432−4441

deposits (e.g., by soot blowing) in boilers. Since soot blowing in boilers may produce both lateral (lift) and longitudinal (drag) forces on deposits,[10] it is important to quantify both the shear and tensile adhesion strength of ash deposits.

The adhesion strength of coal ash deposits[11−13] and deposits in kraft recovery boilers[10] has been investigated in previous studies, while a few studies have quantified the compression and bend strength of ash deposits.[14−17] The authors have previously investigated the shear adhesion strength of biomass ash deposits to superheater steel tubes, describing the influence of the sintering temperature, sintering time, deposit composition, thermal shocks on the deposit, and steel type.[18] However, the majority of studies investigating the adhesion strength of ash deposits have been performed under isothermal conditions. While a few studies have incorporated temperature gradients across the deposit layer to understand the effect of corrosion,[19−21] the effect of temperature gradients on the adhesion strength of ash deposits has not been investigated previously, to the best knowledge of the authors.

The temperature difference across deposits in full-scale boilers can be greater than 200 °C.[19,22] Previous studies have indicated that the physical and chemical properties of the deposit may be influenced by the presence of a temperature gradient across the deposit.[19,22] Differences in temperature across the deposit may cause variations in temperature-dependent sintering and vaporization and condensations of alkali- and chlorine-rich species within the deposit. Furthermore, the Soret effect may be observed, where a concentration gradient across the deposit is induced by a temperature gradient.[23] Therefore, incorporation of a temperature gradient across the deposit is essential for a realistic simulation of operational boiler conditions.

In this study, the tensile adhesion strength of salt-rich biomass ash deposits was investigated, under the influence of a temperature gradient across the deposits. Artificial biomass fly ash deposits were prepared from mixtures of KCl, K_2SO_4, CaO, $CaSO_4$, and $K_2Si_4O_9$ on air-cooled superheater steel tubes and sintered in an oven. After sintering, the deposits were removed using an electrically controlled arm, and the corresponding tensile adhesion strength was measured. The influence of the flue gas temperature, steel surface temperature, and deposit composition was investigated.

■ EXPERIMENTAL SECTION

Materials. Artificial biomass ash deposits were prepared using mixtures of KCl (CAS Registry Number 7447-40-7, Sigma-Aldrich), K_2SO_4 (CAS Registry Number 7778-80-5, Sigma-Aldrich), CaO (CAS Registry Number 1305-78-8, Sigma-Aldrich), $CaSO_4$ (CAS Registry Number 7778-18-9, Alfa Aesar), and $K_2Si_4O_9$ (CAS Registry Number 1312-76-1, Alfa Aesar). The materials were milled and sieved individually to obtain a particle size distribution in the range of 32−90 μm. However, it should be noted that fly ash particles in biomass boilers typically form a bimodal size distribution, containing sub-micrometer particles as well as larger particles with sizes up to 200 μm.[6,24] Accurately reproducing the typical bimodal size distribution of fly ash for the experiments is a tedious process. Therefore, a fixed particle size distribution in the range of 32−90 μm was adopted for comparing the influence of ash chemistry. The materials were mixed in different combinations to create model deposits, as shown in Table 1, along with their eutectic temperature/glass transition temperature.[25]

Table 1. Eutectic Temperature/Glass Transition Temperature of the Investigated Model Deposits[a]

composition	eutectic temperature/glass transition temperature (°C)
KCl + K_2SO_4[b]	690
KCl + K_2SO_4 + CaO[b]	690
KCl + K_2SO_4 + $CaSO_4$[b]	644
KCl + K_2SO_4 + $K_2Si_4O_9$[c]	650

[a] Eutectic data obtained from Janz et al.[25] [b] Eutectic temperature. [c] Glass transition temperature.

Furthermore, an experiment was performed using straw fly ash obtained from the baghouse filter of the grate-fired boiler in Avedøreværket unit 2.[5,26] The steam cycle of the 100 MW_{th} boiler was operated at 580 °C and 300 bar, with approximately 25 tons/h of wheat straw used at full load. Straw was fed to the boiler on a vibrating grate, and primary air was supplied through the grate, whereas secondary air was injected in the freeboard.[5] The fly ash composition and ash-melting analyses[27] are provided in Table 2. The fly ash was rich in KCl and K_2SO_4, with an ash deformation temperature of 640 °C, slightly lower than the eutectic temperature of the KCl−K_2SO_4 system (690 °C). The particle size distribution of the fly ash is provided in Figure 1. It should be noted that sub-micrometer particles were not detected in the investigated fly ash, probably as a result of the agglomeration occurring during storage.

Table 2. Composition, Particle Size, and Ash-Melting Analyses of the Investigated Straw Fly Ash, Obtained from a Grate-Fired Boiler

element	composition (wt %, dry basis)
Al	–
Ca	1.3
Cl	19
Fe	0.044
K	43
Mg	0.12
Na	0.9
P	–
S	7.9
Si	1.1
Ti	–
Mn	0.059
deformation temperature[27] (°C)	640
hemispherical temperature[27] (°C)	640
fluid temperature[27] (°C)	760
median particle size (μm)	51.7

The deposits were prepared on a superheater steel tube (TP347HFG, Salzgitter Mannesmann), with an outer diameter of 38 mm, a thickness of 5 mm, and a length of 200 mm. The chemical composition of the tube can be found in previously published literature.[18] TP347HFG is characterized by its high Cr, Mn, and Ni contents. The presence of Cr and Mn in steel reduces oxide scale growth by forming Cr−Mn spinels,[28,29] improving the overall corrosion resistance,[30] while Ni deters Cl-induced corrosion.[31]

Apart from hindering corrosion, preoxidation of steel tubes provides a more accurate replication of operational boiler tubes.[32−35] Thermogravimetric analysis of the steel tubes at 600 °C in a previous investigation[18] has indicated that the majority of the oxidation occurs rapidly in the first 10 h, with the oxidation rate slowing down significantly after 24 h. Therefore, the steel tubes were preoxidized for 24 h at 600 °C prior to sample preparation.

Sample Preparation. The required components constituting the model deposit were mechanically mixed with a 50% isopropanol solution to prepare a uniform slurry. The use of slurries to prepare ash deposits is in accordance with European Union (EU) guidelines.[36−38] The slurry was molded into eight cubical-shaped deposits on the superheater steel tube using a Teflon mold, as shown in Figure 2. The superheater steel tube was placed inside the mold, and the mold was securely closed using clamps. During the molding process, hooks used

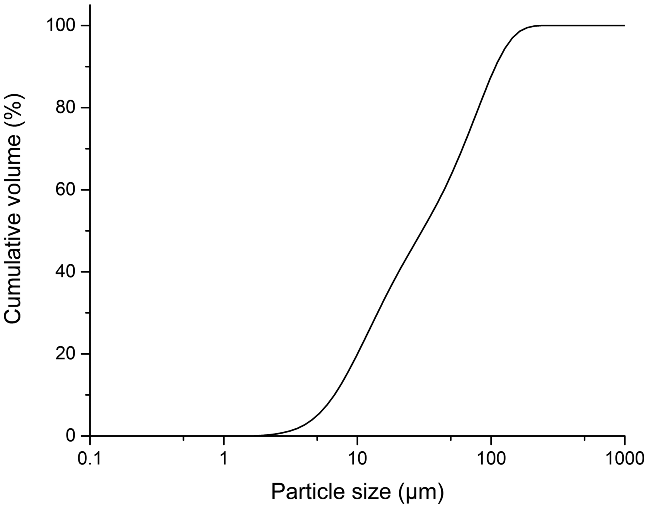

Figure 1. Particle size distribution of the investigated straw fly ash, obtained using a Malvern Mastersizer 3000. D_{10} = 8.01 μm; D_{50} = 51.7 μm; and D_{90} = 142 μm.

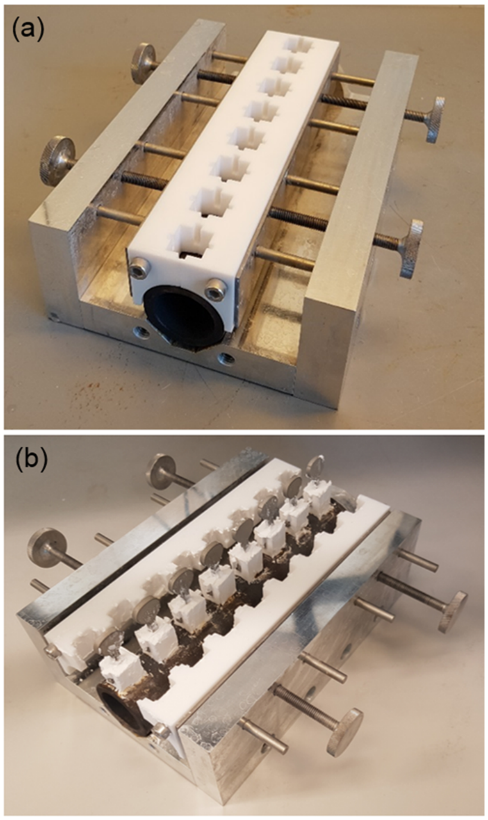

Figure 2. Teflon mold used for sample preparation. (a) After the superheater steel tube was positioned, the hooks were inserted into the mold, followed by injection of the deposit slurry. (b) Subsequently, the deposits and superheater steel tube were removed, by opening the Teflon mold.

for tensile strength measurements were inserted into the mold to allow the deposit to be debonded perpendicular to the steel tube. Subsequently, the deposit slurry was injected into the mold and shaped into cubical pellets, with sides of 15 mm each, leading to a contact surface area of 223 mm^2. Thereafter, the Teflon mold was opened, leaving the superheater steel tube with eight deposits.

It should be noted that the deposit formation process in boilers is different from the samples prepared in this study.[6,22]

Deposit Sintering. The superheater steel tube containing the deposits was placed around a double annular cooling probe in an oven, and the deposit hooks were connected to the corresponding strength measurement arms, as shown in Figure 3. Air flowed through the channels of the cooling probe, with the primary air flowing in through the innermost channel and flowing out through the outermost channel, while the secondary air flowed through the annular region of the cooling probe, as shown in Figure 4a.

The following nomenclature has been used to refer to the different measured temperatures in the experimental setup (see Figure 4a):

- Flue gas temperature is the gas temperature in the oven heating chamber (oven temperature).
- Cooling probe temperature is the temperature at the outer surface of the cooling probe (and the inner surface of the superheater steel tube), measured at the axial centerpoint of the superheater steel tube. The flow rate of the primary air was controlled electronically, such that the cooling probe temperature is maintained at a desired value. The cooling probe could be maintained at a temperature of up to 200 °C lower than that of the flue gas (oven temperature). The cooling probe temperature in the experimental setup is analogous to the steam temperature in boilers.
- Steel surface temperature is the temperature at the outer surface of the superheater steel tube, measured at the centerpoint of the deposit–tube interface. Eight deposits correspond to eight steel surface temperatures. The steel surface temperatures were higher than the cooling probe temperatures as a result of the presence of a vertical temperature gradient (ΔT_v) across the steel tube. Furthermore, the steel surface temperature varied along the length of the superheater steel tube as a result of the presence of a horizontal temperature gradient (ΔT_h).

The secondary air allowed for additional cooling and reduced ΔT_h. The flow rate of the secondary air was controlled manually using a rotameter and was optimized to minimize ΔT_h. It was identified that a secondary air flow rate of 50 NL/min, which was the maximum possible flow rate, resulted in minimum temperature gradients across the steel tube, advocating the use of 50 NL/min of secondary air throughout all experiments.

The steel surface temperatures were measured by mounting six thermocouples on the outer surface of the superheater steel tube. The temperature gradients along the steel tube at a flue gas temperature of 650 °C and cooling probe temperatures of 450–650 °C are shown in Figure 4b. It was observed that a horizontal temperature gradient of up to 64 °C existed along the steel surface (ΔT_h = 0–64 °C). It should be noted that the air supply to the cooling probe was shut off for the measurement, corresponding to a cooling probe temperature of 650 °C, resulting in isothermal conditions. Furthermore, the mean steel surface temperature was up to 88 °C higher than the cooling probe temperature (ΔT_v = 0–88 °C). Both ΔT_h and ΔT_v decreased with an increasing cooling probe temperature. Previous studies in full-scale boilers have identified that the steel surface temperature is typically around 20–50 °C higher than the steam temperature.[22,39]

It should be noted that the measurements to quantify the steel surface temperatures were performed in the absence of the deposits. The presence of the deposits might result in slight differences. Furthermore, the steel surface temperature was measured at six locations, whereas the superheater steel tube contained eight deposits. The steel surface temperatures at the center of the deposits were interpolated linearly, wherever required, using the measured data.

After the superheater steel tube with the deposits was placed around the cooling probe, the oven was heated to the required temperature at a uniform heating rate of 10 °C/min. Subsequently, the deposits were allowed to sinter for 2 h. A purge air flow of 25 NL/min, acting as the flue gas, was injected into the oven, to protect the heating elements from corrosion. Baseline experiments were performed with a flue gas temperature of 650 °C and a cooling probe temperature of 500 °C, using a model deposit containing KCl and K_2SO_4 (50 wt %). Typical steam temperatures in biomass boilers range from 440 to 580 °C,

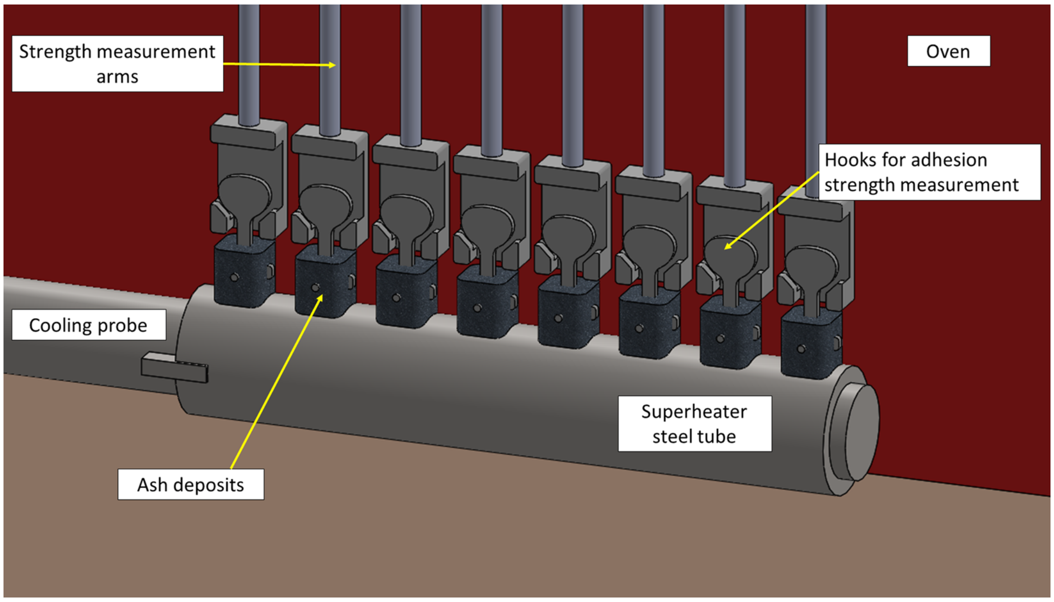

Figure 3. Experimental setup for adhesion strength measurements. The superheater steel tube with the deposits was placed around the air-cooled probe inside the oven, and the deposits were connected to the strength measurement arms.

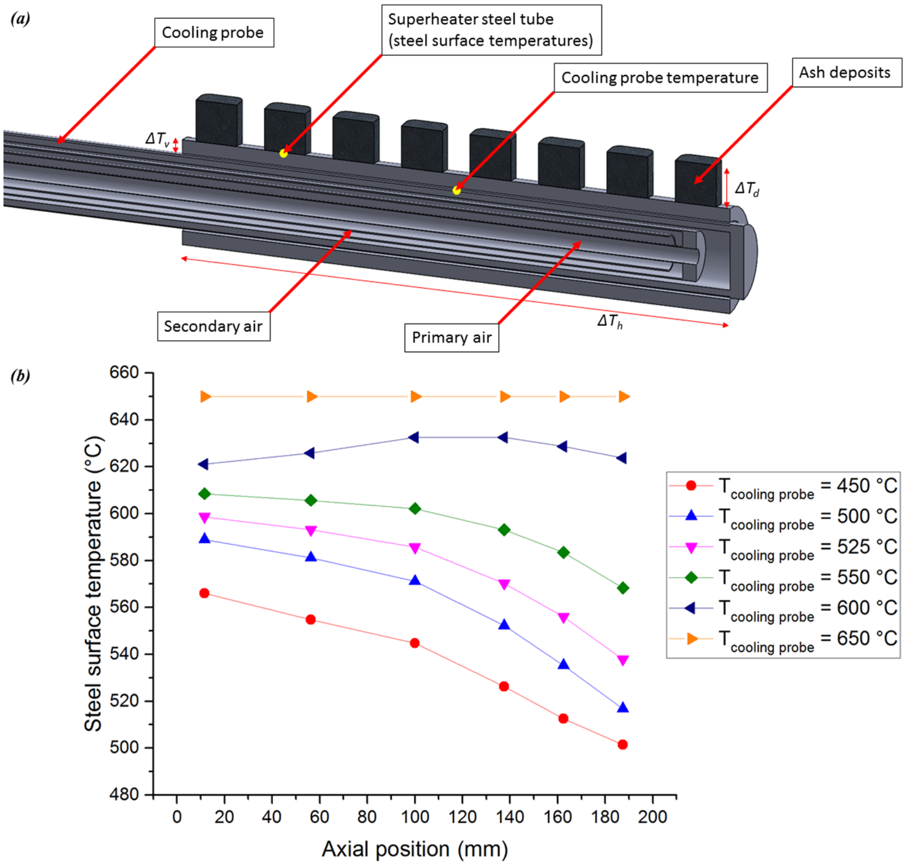

Figure 4. (a) Cross-sectional view of the mounted air-cooled probe. The cooling probe temperature was measured on the outer surface of the cooling probe (and the inner surface of the superheater steel tube) at the axial centerpoint of the superheater steel tube. Steel surface temperatures refer to the temperatures at the outer surface of the superheater steel tube. Horizontal and vertical temperature gradients exist along/across the superheater steel tube and the deposits. (b) Temperature along the outer surface of the superheater steel tube, with a flue gas temperature of 650 °C. The axial position was measured from the left edge of the superheater steel tube.

while typical flue gas temperatures in the superheater/tube bank region range from 580 to 1300 °C.[4,26,39,40]

Measurement of the Tensile Adhesion Strength. After sintering, tensile adhesion strength measurements were performed using a movable actuator and load cell system mounted on the frame of the oven. For each measurement, the actuator was connected to the required strength measurement arm, pulling it slowly at a speed of 2.5 mm/s to debond the deposit, while the corresponding force was measured using the load cell. The tensile adhesion strength was calculated by dividing the measured force by the contact area between the deposit and steel tube.

The strength measurement arms were directed through an air-cooled plate heat exchanger, installed in the outer shell of the oven, for protecting the heat-sensitive actuator and the load cell.

Statistical Data Analysis Using Welch's t Test. Two-tail Welch's t test[41] for unpaired data with unequal variances was performed on the experimental data to analyze the statistical difference between two data sets. The test compared the two data sets, calculating the t value (T) as shown below

$$T = \frac{\mu_1 - \mu_2}{\sqrt{\frac{\sigma_1^2}{N_1} + \frac{\sigma_2^2}{N_2}}}$$

where μ and σ are the mean and standard deviation of the data sets, and N represents the sample size. Subsequently, the p value (p) was calculated, as shown below

$$p = P(|T| \leq t_{1-\alpha/2,\nu})$$

$t_{1-\alpha/2,\nu}$ is the critical value of the t distribution, where ν represents the degree of freedom and α is the significance level. A typical value of 0.05 was chosen for the significance level, corresponding to a confidence level of 95%, indicating that the data sets in consideration are significantly different if $p \leq 0.05$. Previous studies[10,18] have indicated that the adhesion strength data for boiler deposits typically follow a log-normal distribution. Because Welch's t test requires that the data follow a normal distribution, the t test was performed using the logarithmic values of the measured adhesion strength.

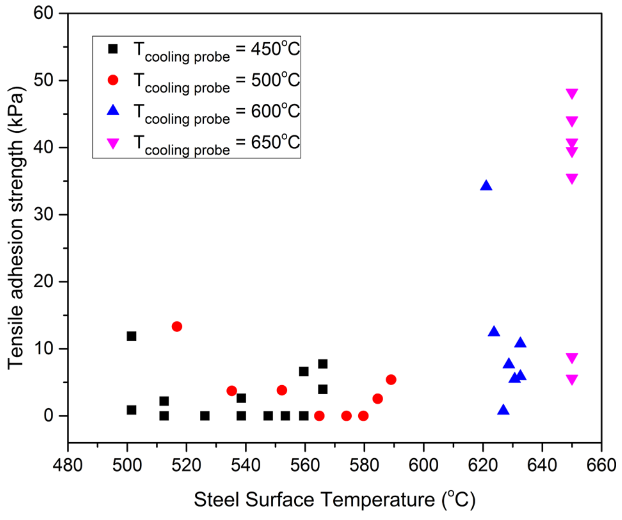

Figure 5. Effect of the steel surface temperature on tensile adhesion strength. KCl−K_2SO_4 (50 wt %) deposits were sintered with a flue gas temperature of 650 °C for 2 h. Superheater steel (TP347HFG) was preoxidized for 24 h.

RESULTS AND DISCUSSION

Effect of the Steel Surface Temperature. Figure 5 shows the effect of the steel surface temperature on the tensile adhesion strength of the investigated model deposits, containing KCl and K_2SO_4 (50 wt %), which was sintered for 2 h with a flue gas temperature of 650 °C. The cooling probe temperature was varied from 450 to 650 °C, resulting in the corresponding steel surface temperatures varying from 501 to 650 °C. The experiments revealed that the tensile adhesion strength of the model deposits was low (<12 kPa) at steel surface temperatures below 600 °C at the investigated conditions. Several deposits did not adhere to the steel tube, resulting in zero adhesion strength. However, the adhesion strength increased sharply at a steel surface temperature of 650 °C, with a mean tensile adhesion strength of 31.79 kPa.

Two-tail Welch's t test[41] for unpaired data with unequal variances was performed on the experimental data, as shown in Table 3. The results revealed that a statistically significant difference did not exist between cooling probe temperatures of 450−500 and 500−600 °C. However, adhesion strength data at a cooling probe temperature of 650 °C was significantly different from adhesion strength data at 600 and 450 °C, with p values of 0.0425 and 0.0019, respectively. The results from the t test substantiate the sharp increase in adhesion strength at 650 °C.

Previous investigations have shown that corrosion leads to the formation of a partially molten layer at the deposit−tube interface, resulting in a sharp increase in adhesion strength.[18] Corrosion occurs at the deposit−tube interface, resulting in the formation of Fe/Cr chlorides, oxides, chromates, etc. with increasing steel surface temperatures, causing a higher degree of corrosion.[18,36,42,43] Because most of the corrosion products form a complex eutectic system with the KCl−K_2SO_4 model deposit,[44,45] a partially molten layer was formed at the deposit−tube interface, even below the eutectic temperature of the KCl−K_2SO_4 system (690 °C). The partially molten layer increased the physical contact area between the deposit and the tube on a molecular scale, thereby increasing adsorption. Furthermore, the corrosion reactions occurring between the deposit and the steel tube may have increased surface adhesion.[46] Visual observations of the deposit−tube interface after debonding indicated the presence of a thick corrosion layer at a steel surface temperature of 650 °C.

It should be noted that debonding always occurred at the deposit−tube interface for the aforementioned experiments. The results concur with previous lab-scale investigations,[18] where a sharp increase in the adhesion strength was observed near the melting temperature/ash deformation temperature of the ash deposit, as well as full-scale deposit probe investigations,[9] where deposits formed on a steel tube at higher steel surface temperatures required larger soot-blowing peak impact pressures to be removed. Furthermore, the mean tensile adhesion strength of the KCl−K_2SO_4 (50 wt %) deposits measured in this study at 650 °C and isothermal conditions (31.79 kPa) is similar in magnitude to the mean shear adhesion strength of KCl−K_2SO_4 (50 wt %) deposits at 650 °C (30.82 kPa) measured in a previous study.[18]

A high degree of scatter was observed in the present experimental data. Previous lab-scale[10,18] and full-scale[9] studies have also indicated that adhesion strength data for boiler deposits display a high degree of scatter, typically following a log-normal distribution.

Effect of the Flue Gas Temperature. To investigate the effect of the flue gas temperature on the tensile adhesion strength of ash deposits, experiments were carried out with model deposits containing KCl and K_2SO_4 (50 wt %). The deposits were sintered for 2 h with the cooling probe temperature maintained at 500 °C, while the flue gas temperature was varied from 500 to 700 °C.

Table 3. Statistical Analysis of Data Sets with Varying Cooling Probe Temperatures[a]

compared data sets				
cooling probe temperature, mean steel surface temperature (°C)	cooling probe temperature, mean steel surface temperature (°C)	T	$p = P(\lvert T\rvert \leq t_{1-\alpha/2,\nu})$	data significantly different? ($p \leq 0.05$?)
450, 538	500, 562	−0.5281	0.6089	no
500, 562	600, 628	−0.7199	0.4881	no
600, 628	650, 650	−2.2932	0.0425	yes
450, 538	650, 650	−3.9671	0.0019	yes

[a] Two-tail Welch's t test for unpaired data with unequal variances, with α = 0.05. KCl−K_2SO_4 (50 wt %) deposits were sintered with a flue gas temperature of 650 °C for 2 h.

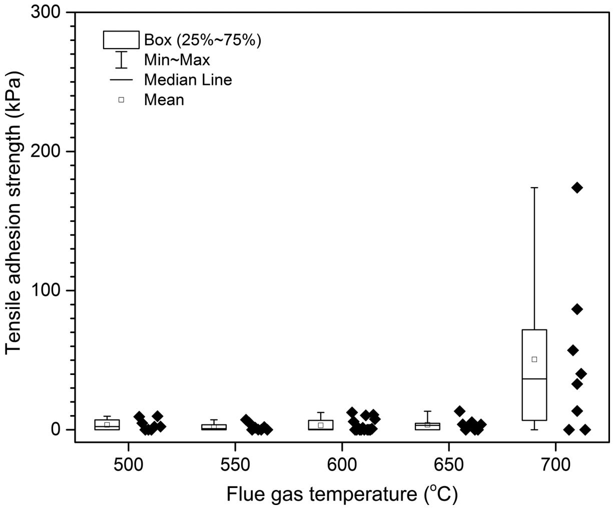

Figure 6. Effect of the flue gas temperature on the tensile adhesion strength. KCl−K_2SO_4 (50 wt %) deposits were sintered with a cooling probe temperature of 500 °C for 2 h. Mean steel surface temperatures varied from 500 to 576 °C. Superheater steel (TP347HFG) was preoxidized for 24 h.

As seen in Figure 6, it was observed that the tensile adhesion strength of the model deposits did not change significantly with flue gas temperatures of 500−650 °C at the investigated conditions. The mean steel surface temperature varied from 500 to 558 °C, when the flue gas temperature was varied from 500 to 650 °C. However, when the flue gas temperature was increased to 700 °C, a sharp increase in the tensile adhesion strength was observed. At a flue gas temperature of 700 °C and a cooling probe temperature of 500 °C, the steel surface temperature was 576 °C. Statistical analysis of the obtained experimental data using Welch's t test (see Table 4) confirmed that the data set corresponding to a flue temperature of 700 °C was significantly different from the data set corresponding to 650 °C, whereas no statistically significant difference could be observed from 500 to 650 °C.

To understand the increase in tensile adhesion strength at a flue gas temperature of 700 °C, the corresponding deposit was analyzed using scanning electron microscopy and energy-dispersive X-ray spectroscopy (SEM−EDS). The debonded deposit was cast in epoxy and polished, without any exposure to water, thereby preventing any dissolution, recrystallization, and removal of salts. The images revealed the presence of a thick molten layer at the deposit−tube interface, as shown in Figure 7b. K_2SO_4 particles were suspended in the KCl−K_2SO_4 melt, where the composition of KCl in the melt was 8 wt %. However, KCl particles could be identified in the outer layer of the deposit (see Figure 7a).

The high molten content at the deposit−tube interface may be attributed to several factors. At a flue gas temperature of 700 °C, the outer layer of the KCl−K_2SO_4 model deposit became partially molten, because KCl and K_2SO_4 form a eutectic system with a eutectic temperature of 690 °C (see Table 1). As a result, the molten outer layer probably trickled down through the pores of the deposit due to capillary and gravitational forces, solidifying at lower temperatures near the deposit−tube interface. This phenomenon is observed in full-scale boilers in the form of liquid-state sintering,[5,47,48] resulting in the formation of hard and strongly adherent deposits, and has been observed in previous experimental investigations.[19,49,50]

Sintering increases the bulk density and thermal conductivity of the deposits,[51] thereby increasing the temperature of the deposit over time and further increasing the molten content at the deposit−tube interface. Furthermore, significant gas-phase migration may have occurred within the deposit, where species on the outer layer of the deposit vaporized, diffused through the pores of the deposit, and eventually condensed near the deposit−tube interface.[50] Therefore, the high molten/condensed content at the deposit−tube interface increased the surface wetting and, therefore, increased the tensile adhesion strength.

It should be noted that the dissolution of KCl and K_2SO_4 in the 50% isopropanol solution during sample preparation may have increased the molten content at the deposit−tube interface. Furthermore, corrosion occurring at the deposit−

Table 4. Statistical Analysis of Data Sets with Varying Flue Gas Temperatures[a]

compared data sets				
flue gas temperature (°C)	flue gas temperature (°C)	T	$p = P(\lvert T\rvert \leq t_{1-\alpha/2,\nu})$	data significantly different? ($p \leq 0.05$?)
500	550	1.2965	0.2514	no
550	600	−1.1280	0.3024	no
600	650	−0.3018	0.7684	no
650	700	−2.5395	0.0294	yes

[a] Two-tail Welch's t test for unpaired data with unequal variances, with α = 0.05. KCl−K_2SO_4 (50 wt %) deposits were sintered with a cooling probe temperature of 500 °C for 2 h. Mean steel surface temperatures varied from 500 to 576 °C.

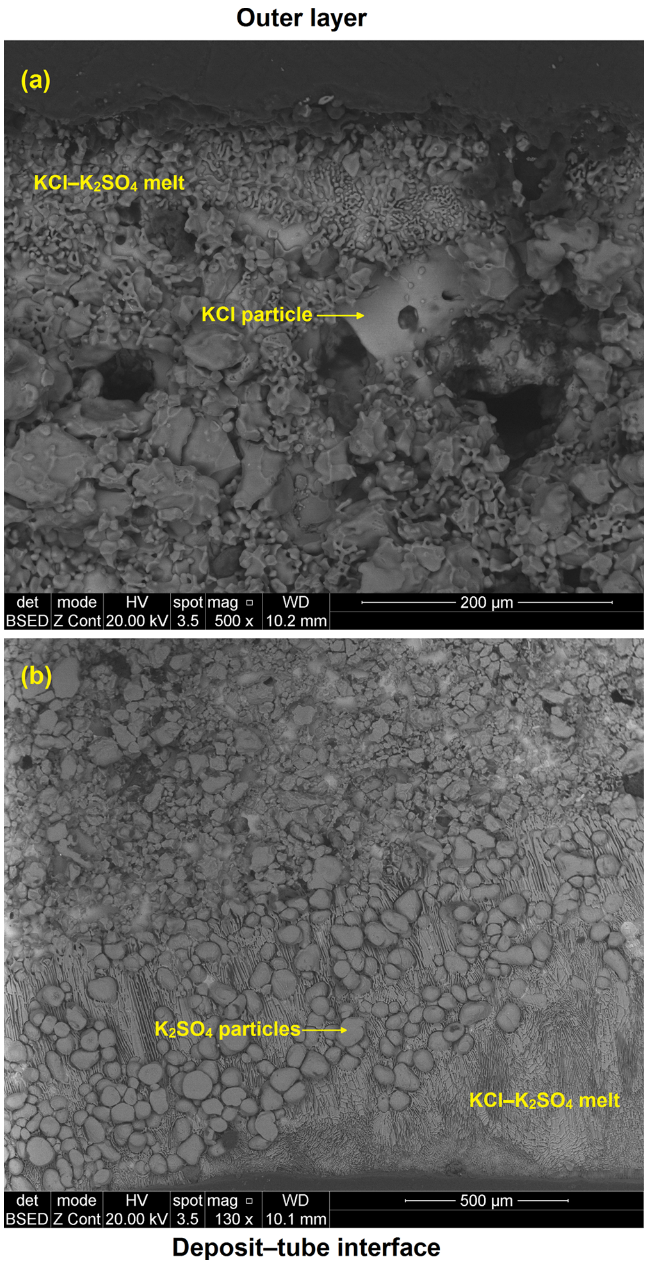

Figure 7. SEM image of a KCl−K_2SO_4 (50 wt %) deposit, sintered with a flue gas temperature of 700 °C and a steel surface temperature of 576 °C (cooling probe temperature of 500 °C) for 2 h at the (a) outer layer of the deposit, in contact with the flue gas, and (b) inner layer of the deposit, in contact with the superheater steel tube.

tube interface may have contributed toward the formation of the molten layer.[18] However, with a steel surface temperature of 576 °C, the corrosion layer is not expected to cause a significant increase in the tensile adhesion strength, as suggested by the results described in Figure 5.

Increasing the flue gas temperature to 750 °C led to a high degree of molten content, which severely reduced the deposit thickness, such that the adhesion strength could not be measured.

The results suggest that a temperature gradient across the deposit may induce migration of molten/vapor species from the outer layer of the deposit to the deposit−tube interface, causing liquid-state sintering and possibly leading to an increase in deposit adhesion strength. However, a further investigation spanning over a larger range of flue gas temperatures and time is required to completely understand the effect of sintering on the adhesion strength.

Effect of the Deposit Composition. To understand the effect of different components present in ash deposits, the composition of the model deposits was varied by adding CaO, $CaSO_4$, and $K_2Si_4O_9$ to the KCl−K_2SO_4 model deposit. Furthermore, experiments were conducted with the straw fly ash obtained from the Avedøreværket grate-fired boiler (see Table 2 for fly ash properties and Figure 1 for particle size distribution).

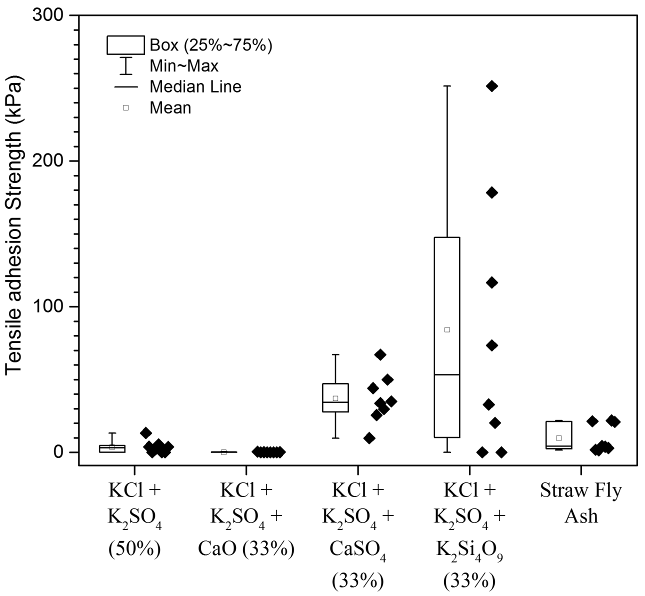

Figure 8. Effect of the deposit composition on the tensile adhesion strength. Deposits were sintered with a flue gas temperature of 650 °C, a cooling probe temperature of 500 °C, and a mean steel surface temperature of 562 °C for 2 h. Superheater steel (TP347HFG) was preoxidized for 24 h.

Figure 8 shows the effect of the deposit composition on the tensile adhesion strength. The addition of CaO to the model deposit containing KCl and K_2SO_4 considerably decreased the adhesion strength at the investigated conditions, with several deposits not adhering to the steel tubes. In comparison of the adhesion strength data of the model deposit containing KCl and K_2SO_4 (50 wt %) to the model deposit containing KCl, K_2SO_4, and CaO (33 wt %) using Welsh's *t* test, the obtained *p* value was 0.0011 (see Table 5), implying that the difference in the data sets is statistically significant.

Calcium is widely present in deposits formed in coal and wood-fired boilers, primarily as oxides and sulfates.[22,52] Because CaO does not form a eutectic melt with the KCl−K_2SO_4 system, the addition of CaO reduced the melt fraction, thereby decreasing adhesion strength.[18]

However, as shown in Figure 8, the addition of $CaSO_4$ significantly increased the adhesion strength of the model deposit containing KCl and K_2SO_4. The increase in adhesion strength, which was determined to be statistically significant (see Table 5), can be attributed to the fact that KCl−K_2SO_4−$CaSO_4$ forms a eutectic system, with a eutectic temperature of 644 °C (see Table 1). As a result, a molten layer at the outer surface of the deposit was formed, which probably trickled down through the deposit pores to induce liquid-state sintering

DOI: 10.1021/acs.energyfuels.7b03114
Energy Fuels 2018, 32, 4432−4441

Table 5. Statistical Analysis of Data Sets with Varying Deposit Compositions[a]

compared data sets				
composition (wt %)	composition (wt %)	T	$p = P(\lvert T\rvert \leq t_{1-\alpha/2,\nu})$	data significantly different? ($p \leq 0.05$?)
KCl + K_2SO_4 (50%)	KCl + K_2SO_4 + CaO (33%)	6.7866	0.0011	yes
KCl + K_2SO_4 + CaO (33%)	KCl + K_2SO_4 + $CaSO_4$ (33%)	−12.4072	0.0002	yes
KCl + K_2SO_4 (50%)	KCl + K_2SO_4 + $K_2Si_4O_9$ (33%)	−5.7502	0.0003	yes
KCl + K_2SO_4 (50%)	straw fly ash	−0.3627	0.7237	no

[a] Two-tail Welch's t test for unpaired data with unequal variances, with $\alpha = 0.05$. Deposits were sintered with a flue gas temperature of 650 °C, a cooling probe temperature of 500 °C, and a mean steel surface temperature of 562 °C for 2 h.

and, therefore, increased the tensile adhesion strength of the deposits. Furthermore, corrosion occurring at the deposit–tube interface may have resulted in an increased melt fraction at the interface, because the corrosion products form a complex eutectic system with KCl, K_2SO_4, and $CaSO_4$.[25]

CaO in boilers may react with SO_2 or SO_3 in the flue gas to undergo sulfation, forming $CaSO_4$.[53−55] Sulfation may occur in the gas phase prior to deposition or in the solid phase after deposition on boiler surfaces.[18] Furthermore, iron oxide in the steel may catalytically convert SO_2 to SO_3,[45,56] thereby catalyzing the overall sulfation reaction and increasing the concentration of $CaSO_4$ near the steel surface.

Replacing CaO with $CaSO_4$ in the model deposit resulted in an increase in deposit adhesion strength, indicating that sulfation of Ca in boilers may result in the formation of strongly adherent deposits. Previous investigations have also indicated that sulfation of ash deposits may increase their adhesion strength.[18] However, further investigation is required to completely understand the effect of sulfation on ash deposits.

The presence of silicates has been identified in slagging deposits and in sintered biomass ash deposits.[5,22,57] The addition of $K_2Si_4O_9$ to the model deposit containing KCl and K_2SO_4 increased its adhesion strength, as shown in Figure 8. The increase in the tensile adhesion strength was statistically significant (see Table 5). Differential scanning calorimetry (DSC) analysis of $K_2Si_4O_9$ in a previous investigation[18] has revealed the formation of a glass phase at 650 °C. The formation of a glass phase probably caused deposit sintering and increased the contact area between the deposit and the tube, thereby increasing the tensile adhesion strength of the deposits.

The tensile adhesion strength of deposits prepared from straw fly ash was similar in magnitude to model deposits containing KCl and K_2SO_4 (50 wt %). Statistical analysis using Welch's t test indicated that a significant statistical difference between the corresponding two data sets did not exist (see Table 5). This can be attributed to the composition of the straw fly ash, which is dominated by KCl and K_2SO_4 (approximately 50 wt % each). The results further suggest that the difference in the particle size distribution of the straw fly ash and the model deposit did not significantly influence the tensile adhesion strength.

The tensile adhesion strength of biomass ash deposits investigated in this study is similar in magnitude to the shear adhesion strength of biomass ash deposits, as seen from a comparison to previous lab-scale investigations[18] (1−350 kPa) and full-scale investigations (20−250 kPa)[9] as well as coal ash deposits from lab-scale investigations (35−350 kPa).[11−13] However, the deposits from kraft recovery boilers possess a higher adhesion strength, as seen from lab-scale investigations (1000−16 000 kPa).[10]

The present results allow for a better understanding of deposit shedding in boilers and recognize the influence of the melt fraction at the deposit−tube interface, corrosion, and sintering on the deposit adhesion strength in boilers.

CONCLUSION

The tensile adhesion strength of model deposits containing KCl, K_2SO_4, CaO, $CaSO_4$, $K_2Si_4O_9$, and straw fly ash obtained from a grate-fired boiler was investigated in this study. Artificial ash deposits were prepared on superheater steel tubes and sintered in an oven under the influence of a temperature gradient across the deposits. The influence of the flue gas temperature, steel surface temperature, and deposit composition were investigated.

The results revealed that the tensile adhesion strength of the model deposits containing KCl and K_2SO_4 (50 wt %) was low (<12 kPa) at steel surface temperatures below 600 °C, with several deposits not adhering to the steel tube. However, the tensile adhesion strength increased sharply at a steel surface temperature of 650 °C at the investigated conditions, with a mean value of 31.79 kPa. Corrosion products created at the deposit−tube interface formed a eutectic system with the deposit constituents at 650 °C, thereby forming a partially molten layer at the deposit−tube interface and increasing the adhesion strength.

Furthermore, the results showed that varying the flue gas temperature from 500 to 650 °C did not have a significant effect on the adhesion strength of the model deposits. However, at a flue gas temperature of 700 °C, a sharp increase in the tensile adhesion strength was observed. The temperature gradient across the deposits, at a flue gas temperature of 700 °C, induced migration of molten/vapor species from the outer layer of the deposit to the deposit−tube interface, causing liquid-state sintering and, thereby, increasing the tensile adhesion strength.

Variation of the chemistry of the model deposits revealed that the melt fraction of the ash deposit is an important parameter for determining the deposit adhesion strength. The addition of compounds that increased the melt fraction of the deposit increased the tensile adhesion strength, whereas the addition of inert compounds with a high melting point, such as CaO, decreased the tensile adhesion strength. Furthermore, the tensile adhesion strength of the deposits prepared using straw fly ash was similar in magnitude to model deposits containing KCl and K_2SO_4.

AUTHOR INFORMATION

Corresponding Author

*E-mail: ylax@kt.dtu.dk.

ORCID

Yashasvi Laxminarayan: 0000-0002-8976-0326

Hao Wu: 0000-0003-0462-2491
Peter Glarborg: 0000-0002-6856-852X

Notes

The authors declare no competing financial interest.

■ ACKNOWLEDGMENTS

This work is part of the project “Flexible Use of Biomass on PF Power Plants” funded by Energinet, through the ForskEL program, Ørsted Bioenergy & Thermal Power A/S, and DTU.

■ REFERENCES

(1) United Nations Framework Convention on Climate Change (UNFCCC). *Adoption of the Paris Agreement*; UNFCCC: New York, 2015; Report FCCC/CP/2015/L.9/Rev.1.

(2) REN21 Secretariat. *Renewables 2017: Global Status Report*; REN21 Secretariat: Paris, France, 2017; ISBN: 978-3-9818107-6-9.

(3) Danish Government. *Our Future Energy*; Danish Government: Copenhagen, Denmark, 2011; ISBN: 978-87-7844-915-3.

(4) Wu, H.; Bashir, M. S.; Jensen, P. A.; Sander, B.; Glarborg, P. *Fuel* **2013**, *113*, 632−643.

(5) Frandsen, F. *Ash Formation, Deposition and Corrosion When Utilizing Straw for Heat and Power Production*; Department of Chemical and Biochemical Engineering, Technical University of Denmark (DTU): Kongens Lyngby, Denmark, 2010; ISBN: 978-87-92481-40-5.

(6) Zhou, H.; Jensen, P. A.; Frandsen, F. J. *Fuel* **2007**, *86* (10−11), 1519−1533.

(7) Hansen, S. B. Model for Deposition Build-up in Biomass Boilers. Ph.D. Thesis, Technical University of Denmark (DTU), Kongens Lyngby, Denmark, 2015.

(8) Zbogar, A.; Frandsen, F.; Jensen, P. A.; Glarborg, P. *Prog. Energy Combust. Sci.* **2009**, *35* (1), 31−56.

(9) Bashir, M. S.; Jensen, P. A.; Frandsen, F.; Wedel, S.; Dam-Johansen, K.; Wadenbäck, J. *Energy Fuels* **2012**, *26* (8), 5241−5255.

(10) Kaliazine, A.; Cormack, D. E.; Ebrahimi-Sabet, A.; Tran, H. *J. Pulp Pap. Sci.* **1999**, *25* (12), 418−424.

(11) Moza, A. K.; Austin, L. G. *Fuel* **1981**, *60* (11), 1057−1064.

(12) Moza, A. K.; Shoji, K.; Austin, L. G. *J. Inst. Energy* **1980**, *53* (414), 17−19.

(13) Raask, E. *VGB Kraftwerkstech.* **1973**, *53* (4), 248−254.

(14) Attig, R. C.; Barnhart, D. H. In *The Mechanism of Corrosion by Fuel Impurities*; Johnson, H. R., Littler, D. J., Eds.; Butterworth: London, U.K., 1963; p 173.

(15) Conn, R. E.; Jones, M. L. *Proceedings of the Third Engineering Foundation Conference on Slagging and Fouling Due to Impurities in Combustion Gases*; Barrett, R. E., Ed.; Copper Mountain, CO, July 29−Aug 3, 1984; pp 207−228.

(16) Cumming, I. W.; Joyce, W. I.; Kyle, J. H. *J. Inst. Energy* **1985**, *58*, 169−175.

(17) Yilu, S. *Proceedings of the Third Engineering Foundation Conference on Slagging and Fouling Due to Impurities in Combustion Gases*; Barrett, R. E., Ed.; Copper Mountain, CO, July 29−Aug 3, 1984; pp 557−592.

(18) Laxminarayan, Y.; Jensen, P. A.; Wu, H.; Frandsen, F. J.; Sander, B.; Glarborg, P. *Energy Fuels* **2017**, *31* (8), 8733−8741.

(19) Lindberg, D.; Niemi, J.; Engblom, M.; Yrjas, P.; Laurén, T.; Hupa, M. *Fuel Process. Technol.* **2016**, *141*, 285−298.

(20) Kawahara, Y. *Mater. Corros.* **2006**, *57* (1), 60−72.

(21) Brossard, J. M.; Diop, I.; Chaucherie, X.; Nicol, F.; Rapin, C.; Vilasi, M. *Mater. Corros.* **2011**, *62* (6), 543−548.

(22) Jensen, P. A.; Frandsen, F. J.; Hansen, J.; Dam-Johansen, K.; Henriksen, N.; Hörlyck, S. *Energy Fuels* **2004**, *18* (2), 378−384.

(23) Chipman, J. *J. Am. Chem. Soc.* **1926**, *48* (10), 2577−2589.

(24) Pagels, J.; Strand, M.; Rissler, J.; Szpila, A.; Gudmundsson, A.; Bohgard, M.; Lillieblad, L.; Sanati, M.; Swietlicki, E. *J. Aerosol Sci.* **2003**, *34* (8), 1043−1059.

(25) Janz, G. J.; Allen, C. B.; Downey, J. R., Jr.; Tomkins, R. P. T. *Physical Properties Data Compilations Relevant to Energy Storage. I. Molten Salts: Eutectic Data*; National Standard Reference Data System (NSRDS): Washington, D.C., 1978; NSRDS-NBS 61.

(26) Bashir, M. S.; Jensen, P. A.; Frandsen, F.; Wedel, S.; Dam-Johansen, K.; Wadenbäck, J.; Pedersen, S. T. *Fuel Process. Technol.* **2012**, *97*, 93−106.

(27) European Committee for Standardization (CEN). *Solid Biofuels—Method for the Determination of Ash Melting Behaviour—Part 1: Characteristic Temperatures Method*; CEN: Brussels, Belgium, 2006; CEN/TS 15370-1:2006.

(28) Hamzah, M. Z.; Yeo, W. H.; Fry, A. T.; Inayat-Hussain, J. I.; Ramesh, S.; Purbolaksono, J. *Eng. Failure Anal.* **2013**, *35*, 380−386.

(29) Schmidt, D.; Schütze, M. *Mater. Sci. Forum* **2011**, *696*, 330−335.

(30) Yukitoshi, T.; Yoshikawa, K.; Daikoku, T.; Masuyama, F. *J. Mater. Energy Syst.* **1982**, *4* (2), 99−109.

(31) Zahs, A.; Spiegel, M.; Grabke, H. J. *Corros. Sci.* **2000**, *42* (6), 1093−1122.

(32) Okoro, S. C.; Kiamehr, S.; Montgomery, M.; Frandsen, F. J.; Pantleon, K. *Mater. Corros.* **2017**, *68* (5), 499−514.

(33) Israelsson, N.; Engkvist, J.; Hellström, K.; Halvarsson, M.; Svensson, J. E.; Johansson, L. G. *Oxid. Met.* **2015**, *83* (1−2), 29−53.

(34) Sabau, A. S.; Wright, I. G.; Shingledecker, J. P. *Mater. Corros.* **2012**, *63* (10), 896−908.

(35) Rizzi, M.; Guerrini, E.; Trasatti, S. P. *Metall. Ital.* **2012**, *2*, 29−35.

(36) Okoro, S. C.; Montgomery, M.; Frandsen, F. J.; Pantleon, K. *Energy Fuels* **2014**, *28* (10), 6447−6458.

(37) Coleman, K. E.; Simms, N. J.; Kilgallon, P. J.; Oakey, J. E. *Mater. Sci. Forum* **2008**, *595−598*, 377−386.

(38) Grabke, H. J.; Meadowcroft, D. B. *A Working Party Report on Guidelines for Methods of Testing and Research in High Temperature Corrosion*; European Federation of Corrosion: London, U.K., 1995; ISBN: 1907625828.

(39) Montgomery, M.; Karlsson, A.; Larsen, O. H. *Mater. Corros.* **2002**, *53* (2), 121−131.

(40) Montgomery, M.; Jensen, S. A.; Borg, U.; Biede, O.; Vilhelmsen, T. *Mater. Corros.* **2011**, *62* (7), 593−605.

(41) Welch, B. L. *Biometrika* **1947**, *34* (1), 28−35.

(42) Sui, J.; Lehmusto, J.; Bergelin, M.; Hupa, M. *Oxid. Met.* **2014**, *82* (5−6), 437−456.

(43) Spiegel, M. *Mater. Corros.* **1999**, *50* (7), 373−393.

(44) Viklund, P.; Hjörnhede, A.; Henderson, P.; Stålenheim, A.; Pettersson, R. *Fuel Process. Technol.* **2013**, *105*, 106−112.

(45) Nielsen, H. P.; Frandsen, F. J.; Dam-Johansen, K. *Energy Fuels* **1999**, *13* (6), 1114−1121.

(46) Packham, D. E.Theories of Fundamental Adhesion. In *Handbook of Adhesion Technology*; da Silva, L. F. M., Öchsner, A., Adams, R. D., Eds.; Springer: Berlin, Germany, 2011; pp 9−38, DOI: 10.1007/978-3-642-01169-6_2.

(47) Raask, E. *Mineral Impurities in Coal Combustion: Behavior, Problems, and Remedial Measures*; Hemisphere Publishing Corporation: Washington, D.C., 1985.

(48) Zhang, D.; Jackson, P. J.; Vuthaluru, H. B. Low-Rank Coal and Advanced Technologies for Power Generation. In *Impact of Mineral Impurities in Solid Fuel Combustion*; Gupta, R., Wall, T., Baxter, L., Eds.; Kluwer Academic Publishers: Cambridge, MA, 2002; pp 45−64, DOI: 10.1007/0-306-46920-0_4.

(49) German, R. M.; Suri, P.; Park, S. J. *J. Mater. Sci.* **2009**, *44* (1), 1−39.

(50) Niemi, J.; Lindberg, D.; Engblom, M.; Hupa, M. *Chem. Eng. Sci.* **2017**, *173*, 196−207.

(51) Zbogar, A.; Frandsen, F. J.; Jensen, P. A.; Glarborg, P. *Prog. Energy Combust. Sci.* **2005**, *31* (5−6), 371−421.

(52) Raask, E. *Prog. Energy Combust. Sci.* **1982**, *8*, 261−276.

(53) Anthony, E. J.; Granatstein, D. L. *Prog. Energy Combust. Sci.* **2001**, *27* (2), 215−236.

(54) Borgwardt, R. H.; Bruce, K. R. *AIChE J.* **1986**, *32* (2), 239−246.

(55) Marsh, D. W.; Ulrichson, D. L. *Chem. Eng. Sci.* **1985**, *40* (3), 423−433.

(56) Jørgensen, T. L.; Livbjerg, H.; Glarborg, P. *Chem. Eng. Sci.* **2007**, *62* (16), 4496−4499.

(57) Hansen, L. A.; Nielsen, H. P.; Frandsen, F. J.; Dam-Johansen, K.; Hørlyck, S.; Karlsson, A. *Fuel Process. Technol.* **2000**, *64* (1), 189−209.

July 2019

ForskEL project no. 12150/EUDP 64018-003

Final report: Flexible use of biomass on PF Fired power plants

Appendix C. Journal paper: C. Laxminarayan Y., Jensen P.A., Wu H., Frandsen F.J., Sander B., Glarborg P. Biomass fly ash deposition in an entrained flow reactor. Proc. Combust. Inst 2019. 37, 2689 - 2696.

1. Department of Chemical and Biochemical Engineering
Technical University of Denmark
Søltofts Plads, Building 229, DK-2800, Kgs. Lyngby, Denmark
2. Ørsted Bioenergy & Thermal power,
Kraftværksvej 53, DK-7000, Fredericia, Denmark

CHEC no. R1902

Available online at www.sciencedirect.com

ScienceDirect

Proceedings of the Combustion Institute 37 (2019) 2689–2696

Proceedings of the Combustion Institute

www.elsevier.com/locate/proci

Biomass fly ash deposition in an entrained flow reactor

Yashasvi Laxminarayan [a,*], Peter Arendt Jensen [a], Hao Wu [a], Flemming Jappe Frandsen [a], Bo Sander [b], Peter Glarborg [a]

[a] *Department of Chemical and Biochemical Engineering, Technical University of Denmark, Søltofts Plads 229, 2800 Kgs. Lyngby, Denmark*

[b] *Ørsted Bioenergy & Thermal Power A/S, Kraftsværksvej 53, Skærbæk, DK-7000 Fredericia, Denmark*

Received 30 November 2017; accepted 3 June 2018
Available online 23 June 2018

Abstract

Fly ash deposition on boiler surfaces is a major operational problem encountered in biomass-fired boilers. Understanding deposit formation, and developing modelling tools, will allow improvements in boiler efficiency and availability. In this study, deposit formation of a model biomass ash species ($K_2Si_4O_9$) on steel tubes, was investigated in a lab-scale Entrained Flow Reactor. $K_2Si_4O_9$ was injected into the reactor, to form deposits on an air-cooled probe, simulating deposit formation on superheater tubes in boilers. The influence of flue gas temperature (589 – 968°C), probe surface temperature (300 – 550°C), flue gas velocity (0.7 – 3.5 m/s), fly ash flux (10,000 – 40,000 g/m^2h), and probe residence time (up to 60 min) was investigated. The results revealed that increasing flue gas temperature and probe surface temperature increased the sticking probability of the fly ash particles, thereby increasing the rate of deposit formation. However, increasing flue gas velocity resulted in a decrease in the deposit formation rate, due to increased particle rebound. Furthermore, the deposit formation rate increased with probe residence time and fly ash flux. Inertial impaction was the primary mechanism of deposit formation, forming deposits only on the upstream side of the steel tube. A mechanistic model was developed for predicting deposit formation in the reactor. Deposit formation by thermophoresis and inertial impaction was incorporated into the model, and the sticking probability of the ash particles was estimated by accounting for energy dissipation due to particle deformation. The model reasonably predicted the influence of flue gas temperature and fly ash flux on the deposit formation rate.

Keywords: Biomass; Fly ash; Deposit formation; Fouling; Ash sticking probability

1. Introduction

Combustion of biomass for electricity and heat production is a promising solution for reducing net CO_2 emissions. Denmark is planning to phase out coal by 2030, with intentions to replace it with biomass in pulverized fuel-fired power plants [1]. However, the inorganic content in biomass causes several operational problems, including increased deposition of chemically aggressive ash species on boiler surfaces. Ash deposits hinder heat transfer to the steam cycle, thereby reducing boiler efficiency, causing corrosion of boiler surfaces, and blocking flue gas channels in severe

---

* Corresponding author.
E-mail address: ylax@kt.dtu.dk (Y. Laxminarayan).

https://doi.org/10.1016/j.proci.2018.06.039

cases, causing unscheduled boiler shut-downs [2]. Therefore, reducing deposit formation is essential for maximizing boiler efficiency and availability.

Inorganic species in the flue gas may occur as vapors, submicron aerosol particles, and larger fly ash particles. The vapor species may undergo heterogeneous condensation on heat transfer surfaces. Deposition of submicron aerosol particles may occur via thermophoresis, Brownian motion or eddy diffusion [3]. Deposition of larger fly ash particles primarily occurs via inertial impaction, and subsequent particle sticking, which is dependent on the collision efficiency and sticking probability of the fly ash particles to boiler surfaces [3]. However, quantification of sticking probability has been a challenge.

Simple sticking models correlate the sticking probability with the viscosity of the particles and the deposit surface [4]. When the ash composition is dominated by alkali salts, the sticking probability may be expressed as a function of the melt fraction of the particle/deposit surface [3]. In the low temperature region of the boilers, where the ash predominantly exists as viscoelastic particles, deposition can be described using detailed models, accounting for energy dissipation due to particle deformation [5]. Such models define a critical velocity of the incoming particle, such that deposition occurs if the particle velocity is lower than the critical velocity. A comprehensive review of ash sticking and rebound criteria may be found in literature [6].

Several experimental investigations quantifying deposit formation in full-scale grate-fired [7,8] and suspension-fired [9–12] boilers, as well as pilot-scale and lab-scale studies [13–18], have been reported. However, a comprehensive fundamental investigation, quantifying the effect of operating conditions and ash chemistry on deposit build-up, at well-defined conditions relevant for biomass-fired boilers, is lacking.

In this study, ash deposition on steel tubes in a laboratory Entrained Flow Reactor (EFR) was quantified, at conditions simulating full-scale biomass-fired boilers. Model biomass fly ash, comprised of $K_2Si_4O_9$, was injected into the reactor, to form deposits on an air-cooled probe. The influence of flue gas temperature, probe surface temperature, flue gas velocity, fly ash flux, and probe residence time was investigated. Furthermore, a mechanistic model was developed to predict deposit formation in the reactor.

2. Experimental section

2.1. Materials

Experiments were carried out with amorphous $K_2Si_4O_9$ (Alfa Aesar, CAS number: 1312-76-1). The majority of biomass fly ashes and deposits contain significant quantities of amorphous materials [10,19,20], including silicates [2,21], characterized by their viscoelastic behavior, justifying the use of $K_2Si_4O_9$ for experimental analysis. Additionally, biomass fly ash deposits may contain alkali metal compounds such as KCl and K_2SO_4 [21]. The influence of fly ash composition on deposit formation has been investigated in a subsequent study [22].

The $K_2Si_4O_9$ had a volume-median particle diameter (D_{50}) of 62.3 μm ($D_{10} = 7.31$ μm, $D_{90} = 272$ μm, dry basis). Further details on the particle size distribution may be found in the supplemental material (Fig. S.1). However, it should be noted that fly ash in boilers typically forms a bimodal particle size distribution, containing submicron particles, as well as larger particles [3]. $K_2Si_4O_9$ was subjected to Differential Scanning Calorimetry (DSC), revealing that $K_2Si_4O_9$ forms a glass phase at 650°C, after which the viscosity of $K_2Si_4O_9$ decreases with increasing temperature [23].

2.2. Experimental setup

The EFR setup consisted of a gas supply system, a screw feeder for injecting solids, a gas preheater, a 2 m long electrically heated furnace (inner diameter = 80 mm), and a fly ash deposition system comprising of a steel tube mounted on an air-cooled probe. A schematic representation of the setup is shown in Fig. 1. A detailed description of the EFR may be found in previously published literature [22,24,25].

$K_2Si_4O_9$ particles were mixed with primary air, and fed into the furnace, together with preheated secondary air. The walls of the furnace could be heated up to 1450°C. It should be noted that the particle and gas temperatures in the furnace might be slightly lower than the temperature of the furnace walls.

After the furnace, the entrained flow entered a bottom chamber, where the $K_2Si_4O_9$ particles formed deposits on a steel tube (type 316), simulating deposit formation on the first row of platen superheater tubes in boilers. For each experiment, the steel tubes were used as received, without any pre-oxidization. The steel tube, with an outer diameter of 10 mm, a thickness of 1 mm, and a length of 140 mm, was mounted on a retractable annular cooling probe (diameter of 8 mm), as shown in Fig. 2.

The temperature measured between the outer surface of the cooling probe and the inner surface of the steel tube, at the axial centerline of the reactor (referred to as probe surface temperature, see Fig. 2), was controlled electronically. The cooling probe surface temperature is analogous to steam temperature in boilers. A horizontal temperature gradient (ΔT, see Fig. 2), of typically 50°C, was present along the cooling probe. The bottom chamber of the EFR was water-cooled, resulting in a decrease in the flue gas temperature.

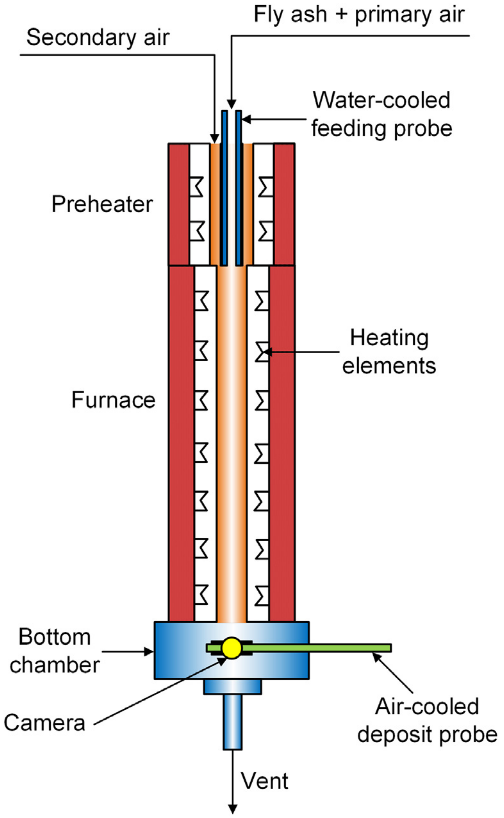

Fig. 1. Schematic representation of the Entrained Flow Reactor.

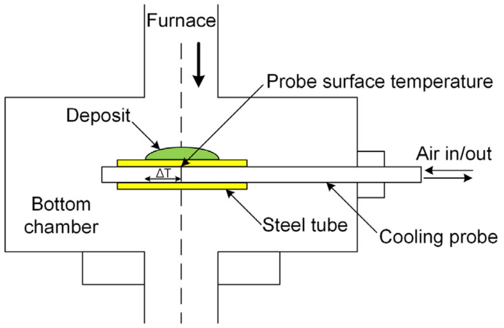

Fig. 2. Bottom chamber of the EFR. Deposits are formed on the steel tube mounted on the probe.

Therefore, the flue gas temperature in the bottom chamber was measured by replacing the cooling probe with a suction pyrometer.

The fly ash deposition process was recorded by a high-speed camera, mounted on a port in the bottom chamber (see Fig. 1). After deposit formation for a specified duration, the probe was retracted, and the deposit was removed and weighed.

2.3. Experimental conditions

Baseline experiments were performed at a furnace temperature of 1100°C, resulting in a flue gas temperature of 781°C near the probe, a probe surface temperature of 475°C, a flue gas velocity of 1 m/s (at the furnace temperature), a fly ash flux of 20,400 g/m^{2}h, corresponding to a fly ash concentration of 26.57 g/Nm^3, using pure $K_2Si_4O_9$ for 15 min. In other experiments, the flue gas temperature was varied from 589 to 968°C, the probe surface temperature from 300 to 550°C, the flue gas velocity from 0.7 to 3.5 m/s, the fly ash flux from 10,000 to 40,000 g/m^{2}h, with probe residence times of up to 60 min.

Typical superheater steam temperatures in biomass-fired boilers range from 440 – 580°C, while the flue gas temperatures in the superheater/tube bank region range from 580 – 1300°C [9,20,26,27]. The flue gas velocity in full-scale boilers ranges from 4 – 8 m/s [3,9]. However, lower gas velocities were adopted during the experiments in order to maintain a similar Stokes number (≈ 1). The typical fly ash flux in biomass boilers varies from 10,000 to 60,000 g/m^{2}h [20]. However, the corresponding fly ash concentrations in the experiments (13 – 53 g/Nm^3), are higher than the typical fly ash concentrations in full-scale biomass-fired boilers (1 – 6 g/Nm^3).

3. Deposit formation model

A mechanistic deposit formation model was developed to simulate deposit formation in the reactor. The model incorporated deposit formation by thermophoresis and inertial impaction of $K_2Si_4O_9$ particles, while deposit formation by condensation was neglected due to the absence of vapor species in the gas phase.

$$\frac{dm(t,\theta)}{dt} = \dot{T}(t,\theta) + \dot{I}(t,\theta) \qquad (1)$$

where m is the mass of the deposit (kg), t is the time (s), and θ is the angular position (radians).

The rate of deposit formation by thermophoresis ($\dot{T}(t,\theta)$) was described using Eq. (2) [28].

$$\dot{T}(t,\theta) = u_T(\theta)\cdot C\cdot s(\theta) \qquad (2)$$

where u_T is the thermophoretic velocity (m/s), C is the concentration of $K_2Si_4O_9$ (kg/m^3), and $s$is the surface area of the deposit (m^2).

The rate of deposit formation by inertial impaction $\dot{I}(t,\theta)$ was described using Eq. (3) [3].

$$\dot{I} = u_g\cdot C\cdot \eta_I(\theta)\cdot \eta_s(\theta)\cdot s(\theta) \qquad (3)$$

where u_g is the gas velocity (m/s), η_I is the local collision efficiency of each particle, and η_s is the sticking probability of the ash particles. Since the $K_2Si_4O_9$ particles are viscoelastic in nature, the sticking probability of ash particles was estimated by accounting for energy dissipation due to particle deformation. The critical velocity of the incoming particles ($u_{p,\ crit}$) was calculated [5], such that

$$\eta_s = \begin{cases} 0 & u_p \cdot \sin\left(\alpha_{impact}\right) > u_{p,crit} \\ 1 & u_p \cdot \sin\left(\alpha_{impact}\right) \leq u_{p,crit} \end{cases} \tag{4}$$

where u_p is the particle velocity (m/s) and α_{impact} is the angle of impaction (radians).

The critical velocity of the incoming particle is a function of the particle diameter (d_p), particle density (ρ_p), interface energy (surface tension) (Γ) and equivalent Young's modulus (E) [29].

$$u_{p,crit} = \frac{\left(\frac{2\Gamma}{d_p}\right)^{5/6}}{\left(\rho_p^3 E^2\right)^{1/6}} \tag{5}$$

$$\frac{1}{E} = \frac{1 - \upsilon_{particle}^2}{E_{particle}} + \frac{1 - \upsilon_{deposit}^2}{E_{deposit}} \tag{6}$$

where υ is the Poisson's ratio. The Young's modulus was estimated as $E = A \cdot \exp(-BT)$, where A and B are empirical constants obtained from literature [30].

Furthermore, the model incorporated heat transfer across the deposit layer and the steel tube, as described by Eq. (7).

$$\frac{k_{tube}}{\delta_{tube}}\left(T_{tube} - T_{probe}\right) = \frac{k_{deposit}}{\delta_{deposit}}\left(T_{deposit} - T_{tube}\right)$$
$$= h_{gd}\left(T_{gas} - T_{deposit}\right) + \varepsilon\sigma\left(T_{gas}^4 - T_{deposit}^4\right) \tag{7}$$

T_{gas} is the gas temperature, whereas $T_{deposit}$, T_{tube}, and T_{probe} are the temperatures at the surface of the deposit, steel tube and probe (K). k, δ, h, ε, and σ refer to the thermal conductivity (W/mK), thickness (m), heat transfer coefficient (W/m^{2}K^1), emissivity, and Stefan Boltzmann constant (W/m^{2}K).

The particles were assumed to be isothermal, with the corresponding heat transfer equation described in Eq. (8).

$$\rho_p\left(\frac{\pi}{6}d_p^3\right)C_p\frac{dT_{particle}}{dt'} = h_{gp}\left(\pi d_p^2\right)\left(T_{gas} - T_{particle}\right)$$
$$+ \varepsilon\sigma\left(\pi d_p^2\right)\left(T_{gas}^4 - T_{particle}^4\right) \tag{8}$$

ρ_p, C_p, d_p, $T_{particle}$ and t' refer to the particle density (kg/m^3), specific heat capacity (J/kgK), diameter (m), temperature (K) and residence time (s).

It was assumed that the particles in the furnace were perfectly entrained in the gas flow, resulting in equal particle and gas velocities. The terminal velocity of the $K_2Si_4O_9$ particles was estimated to be 2% of the gas velocity, using the Wen and Yu drag model [31], justifying the aforementioned assumption.

Further details on the model, and equations used for estimating physical properties, may be found in the supplemental material and previously published literature [5,19,22].

4. Results and discussion

4.1. *Effect of flue gas temperature*

The effect of flue gas temperature on deposit formation rate is shown in Fig. 3. It was observed that the deposit formation rate increased with increasing flue gas temperature at the investigated conditions. Visual observations of the formed deposits (see Fig. 3) revealed that deposits were formed only on the upstream side of the steel tube, suggesting that $K_2Si_4O_9$ deposition occurred primarily via inertial impaction. Studies on deposit formation in full-scale pulverized biomass-fired boilers have also identified inertial impaction as the primary mechanism of deposit formation [3,9,21]. Increasing the flue gas temperature decreased the viscosity/Young's modulus of the $K_2Si_4O_9$ particles, thereby resulting in stickier particles, and increasing deposit formation via inertial impaction. The experimental results were reproducible with a relative standard error of 4%, based on 5 repetitions of baseline experiments.

The experimental results agree with full-scale investigations [9], where increasing flue gas temperatures led to increased deposit formation. Furthermore, it was observed that increasing the flue gas temperature in the experiments resulted in increased adhesion strength of the deposits to the steel tube, as indicated by previous studies [23]. Deposit shedding was not observed in any of the reported experiments.

The deposit formation model was able to predict the influence of flue gas temperature on the observed deposit formation rates with an accuracy (R^2) of 94% (see Fig. 3), suggesting a fairly accurate representation of the sticking probability of the fly ash particles.

4.2. *Effect of probe surface temperature*

Figure 3 also shows the effect of probe surface temperature on the deposit formation rate. It was observed that increasing the probe surface temperature from 300°C to 450°C increased the deposit formation rate at the investigated conditions. However, increasing the probe surface temperature from 450 – 550°C did not influence the rate of deposit formation significantly.

Increasing the probe surface temperature increased the temperature at the surface of the deposit, thereby decreasing the corresponding viscosity/Young's modulus. This resulted in an increased sticking probability of the deposit surface, causing increased deposit formation. However, quantification of the temperature at the surface of the deposit would aid in understanding the observed effect of probe surface temperature on the rate of deposit formation.

The results suggest that increasing steam temperatures in boilers might increase deposit

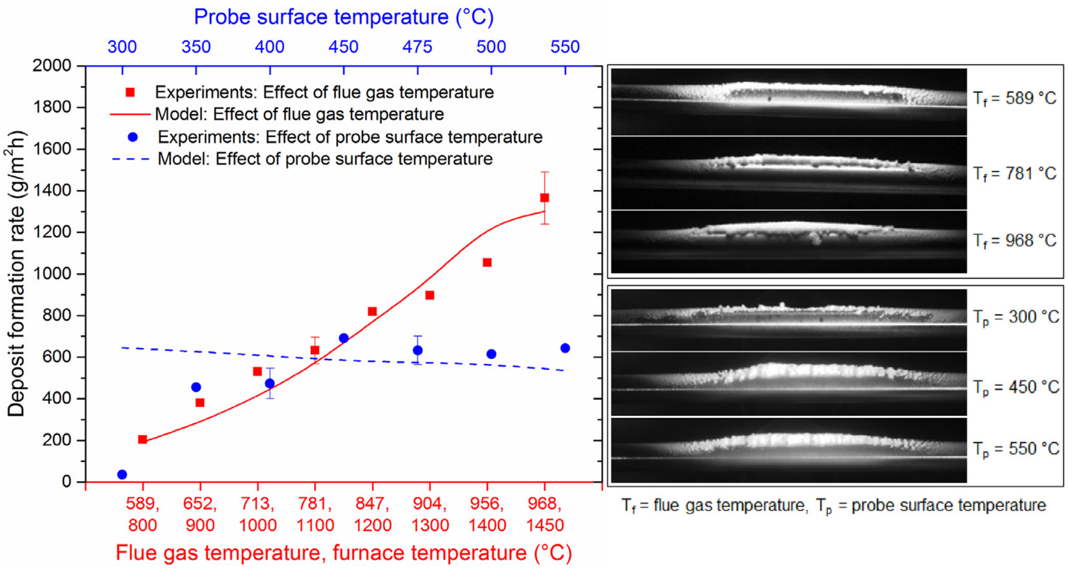

Fig. 3. Effect of flue gas temperature and probe surface temperature on the deposit formation rate. Experiments performed with $K_2Si_4O_9$ with a median particle size of 62.3 µm, mean gas velocity of 1 m/s, fly ash flux of 20,400 g/m^{2}h for 15 min. Flue gas temperature during variation of probe surface temperature = 781°C. Probe surface temperature during variation of flue gas temperature = 475°C. Images captured at the end of the experiments.

formation. However, above a certain steam temperature, determined by the thermal properties of the deposit, a further increase in the steam temperature might not influence the rate of deposit formation. The results concur with a previous investigation [14], where varying probe surface temperatures from 475 – 650°C had a negligible effect on the deposition rate of peat and straw. Nevertheless, it should be noted that high steam temperatures might lead to severe corrosion of the superheater tubes in boilers [27].

The model was unable to accurately predict the influence of probe surface temperature (see Fig. 3), especially from 300 – 400°C, suggesting that the sticking probability of the deposit surface requires a more accurate representation in the model. Furthermore, the deviations may have emanated from the heat transfer equations in the model, which do not account for the decrease in local gas temperatures induced by the cooling probe, especially when the probe surface temperature is maintained at 300°C. CFD simulations of the deposit formation process in the EFR may provide more accurate model predictions. The model predicted a relatively linear decrease in the deposit formation rate with increasing probe surface temperature, due to a decrease in the estimated thermophoretic deposition with reducing temperature gradients in the thermal boundary layer.

4.3. *Effect of mean flue gas velocity*

Figure 4 shows the effect of mean flue gas velocity on the deposit formation rate for flue gas temperatures of 781 and 968°C. At a flue gas temperature of 781°C, it was observed that increasing the flue gas velocity from 0.7 – 3 m/s reduced the deposit formation rate, with a sharp decrease observed between 1 – 1.6 m/s. However, at a flue gas temperature of 968°C, the deposit formation rate remained relatively constant from 1 – 3 m/s, and decreased in value from 3 – 3.5 m/s. Furthermore, it was observed that the thickness of the formed deposits decreased with increasing mean flue gas velocity (see Fig. 4).

Increasing the flue gas velocity, and thereby the particle velocity, increases the kinetic energy of the impacting particles. If the particle velocity exceeds the critical velocity of impaction, the particle is unable to dissipate its kinetic energy, and rebounds from the deposit after impaction. The critical velocity is a function of the particle size and temperature-dependent particle properties. Nevertheless, a relatively sharp decrease in the deposit formation rate with increasing gas velocity was observed, which may be attributed to the fact that the particles with the largest diameter and mass have the lowest critical velocity. Furthermore, the experimental observations suggest that the critical velocity of the $K_2Si_4O_9$ particles increased with increasing temperature at the investigated conditions.

The model predicted a gradual decrease in the deposit formation rate with increasing flue gas velocity (see Fig. 4), with an accuracy (R^2) of 38%. However, the model was unable to predict the sharp decrease in deposit formation rate at 1 m/s and 781°C, and at 3 m/s and 968°C, probably because the model assumed a uniform plug flow

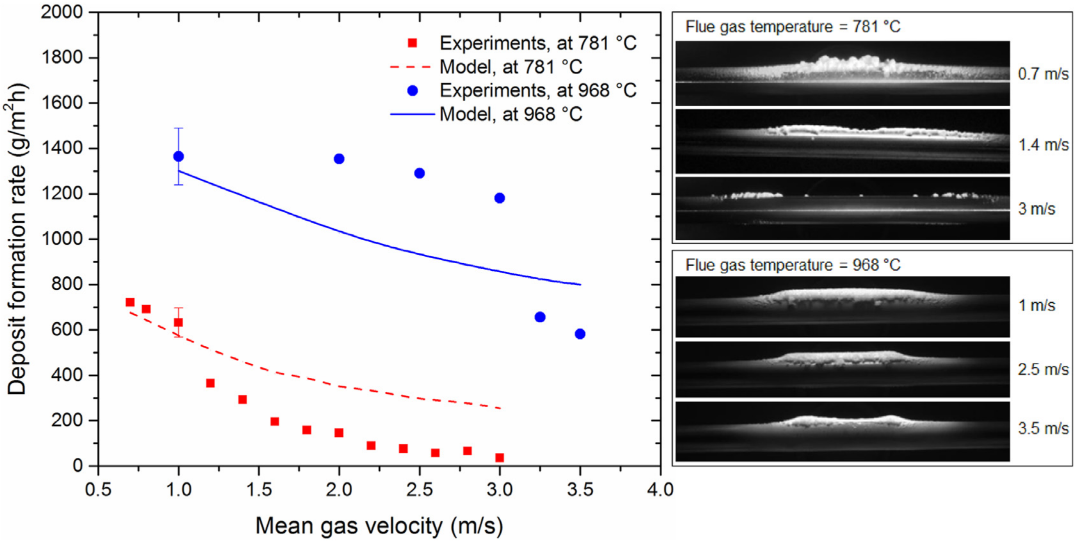

Fig. 4. Effect of mean gas velocity on the deposit formation rate. Experiments performed with $K_2Si_4O_9$ with a median particle size of 62.3 μm, probe surface temperature of 475°C, fly ash flux of 20,400 g/m^{2}h for 15 min. Images captured at the end of the experiments.

in the furnace. Furthermore, agglomeration of particles in the furnace/screw feeder have not been accounted for in the model.

At baseline conditions, the critical velocity predicted by the model varied from 0.23 – 1.4 m/s for particle diameters from 10 – 100 μm. These values agree with previous investigations, where the critical velocity varied from 0.1 – 1.2 m/s for particle diameters from 10 – 100 μm [32–35].

4.4. Effect of probe residence time

The effect of probe residence time on deposit formation rate can be seen in Fig. 5. The deposit formation rate increased with time up to 30 min, at the investigated conditions. However, further increase in time did not significantly influence the deposit formation rate.

As the deposit grew in size, the temperature at the surface of the deposit increased, thereby increasing the sticking probability of the deposit surface. Therefore, the fraction of impacting particles undergoing deposition increased over time. However, the growth rate of the deposit remained constant after 30 min of deposition. Further investigation, quantifying the temperature history of the deposit surface, is required to completely understand the deposit formation process. Nevertheless, the results highlight the importance of a sticky surface for deposit build-up via inertial impaction. The results are consistent with the experiments in Section 4.2, suggesting that the deposit formation rate may not further increase above a certain temperature at the surface of the deposit.

The model predicted a relatively linear increase in the deposit formation rate with time (see Fig. 5), with an accuracy (R^2) of 39%. This increase may be attributed to the increasing local collision efficiency of the incoming particles with increasing deposit thickness. However, the model is not able to predict the saturation in deposit formation rate after 30 min, probably due to an inaccurate representation of the sticking probability of the deposit surface and/or the heat transfer model.

Due to the high temperatures at the deposit surface, sintered deposits could be observed for experiments performed longer than 30 min. Furthermore, natural shedding events were observed only when experiments longer than 60 min were conducted. The large deposits were unstable, breaking away from the steel tube at the deposit-tube interface. A video of deposit formation and shedding on the steel tube can be found in the supplemental material (Video S1), or accessed at youtu.be/gLSHd8fAZo0. The results concur with previous investigations [12,23], establishing debonding as the dominant mechanism of deposit shedding in boilers.

4.5. Effect of fly ash flux

The effect of fly ash flux on deposit formation rate can be observed in Fig. 5. The deposit formation rate increased linearly with increasing ash flux at the investigated conditions. Increasing ash flux increased the total number of particles impacting the steel tube, thereby resulting in a corresponding increase in the deposit formation rate. The results agree with previous full-scale in-

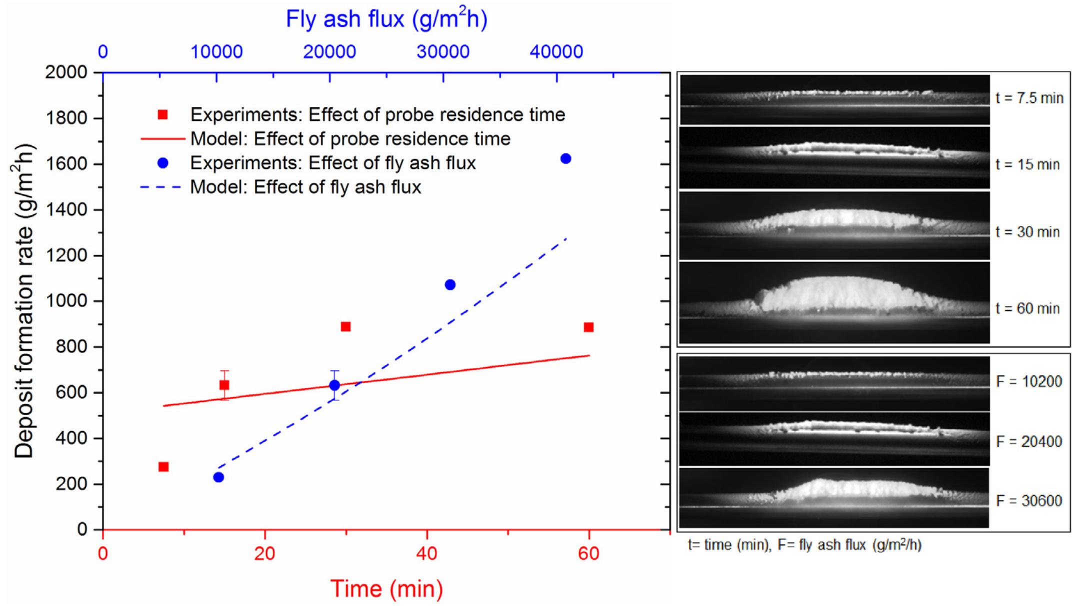

Fig. 5. Effect of time and fly ash flux on the deposit formation rate. Experiments performed with $K_2Si_4O_9$ with a median particle size of 62.3 µm, flue gas temperature of 781°C, probe surface temperature of 475°C, and mean gas velocity of 1 m/s. Fly ash flux during variation of time = 20,400 g/m^{2}h. Time during variation of fly ash flux = 15 min. Images captured at the end of the experiments.

vestigations [7], which indicated a linear increase in the rate of deposit formation via inertial impaction with increasing ash flux.

The model was able to predict the increase in deposit formation rate with increasing ash flux, with an accuracy (R^2) of 86%. However, the slightly smaller slope of the model predictions may be attributed to an inaccurate representation of the sticking probability of the deposit surface.

5. Conclusions

The deposit formation of $K_2Si_4O_9$ on an air-cooled steel tube was investigated in a laboratory-scale Entrained Flow Reactor.

The results revealed that increasing the flue gas temperature from 589 – 968°C, and the probe surface temperature from 300 – 450°C, increased the deposit formation rate. However, varying the probe surface temperature from 450 – 550°C did not influence the deposit formation rate significantly, at the investigated conditions. Furthermore, increasing flue gas velocity from 0.7 – 3.5 m/s resulted in a decrease in the rate of deposit formation.

The deposit formation rate increased with probe residence time. However, the growth rate of the deposit was constant after 30 min at the investigated conditions. Furthermore, increasing fly ash flux resulted in a linear increase in the deposit formation rate. Inertial impaction was observed to be the primary mechanism of deposit formation, forming deposits only on the upstream side of the steel tube.

A mechanistic model was developed to predict deposit formation in the reactor. The model was able to reasonably predict the influence of flue gas temperature and fly ash flux, suggesting that accounting for energy dissipation due to particle deformation, for predicting the sticking probability of incoming ash particles, seems to be fairly successful in predicting the influence of changes in local conditions on the deposit formation process. However, the model was unable to accurately predict the influence of probe surface temperature, gas velocity and probe residence time. Improvements in the prediction of the sticking probability of the deposit surface, as well as CFD simulations of the deposit formation process in the reactor, are desirable to improve model predictions.

The obtained results provide an improved understanding of $K_2Si_4O_9$ deposit formation in boilers, describing the influence of operating conditions on deposit growth. Furthermore, the experimental data may be used to develop novel sticking criteria to predict deposit growth in full-scale boilers.

Acknowledgements

This work is part of the project, ‘Flexible use of Biomass on PF fired power plants’, funded by

Energinet through the ForskEL program, Ørsted and DTU.

Supplementary materials

Supplementary material associated with this article can be found, in the online version, at doi: 10.1016/j.proci.2018.06.039.

References

[1] The Danish Government, *Our Future Energy* (2011) ISBN: 978-87-7844-915-3.

[2] F. Frandsen, Ash Formation, Deposition and Corrosion When Utilizing Straw for Heat and Power Production, Technical University of Denmark, Lyngby, Denmark, 2010, p. 341.

[3] H. Zhou, P.A. Jensen, F.J. Frandsen, *Fuel* 86 (10–11) (2007) 1519–1533.

[4] P.M. Walsh, A.N. Sayre, D.O. Loehden, L.S. Monroe, J.M. Beér, A.F. Sarofim, *Prog. Energy Combust. Sci.* 16 (4) (1990) 327–345.

[5] S.B. Hansen, P.A. Jensen, F.J. Frandsen, B. Sander, P. Glarborg, *Energy Fuels* 31 (3) (2017) 2771–2789.

[6] U. Kleinhans, C. Wieland, F.J. Frandsen, H. Spliethoff, *Prog. Energy Combust. Sci.* 68 (2018) 65–168.

[7] P.A. Jensen, M. Stenholm, P. Hald, *Energy Fuels* 11 (5) (1997) 1048–1055.

[8] A. Žbogar, P.A. Jensen, F.J. Frandsen, J. Hansen, P. Glarborg, *Energy Fuels* 20 (2) (2006) 512–519.

[9] M.S. Bashir, P.A. Jensen, F. Frandsen, S. Wedel, K. Dam-Johansen, *J. Wadenbäck, Fuel Process. Technol.* 97 (2012) 93–106.

[10] D. Nordgren, H. Hedman, N. Padban, D. Boström, M. Öhman, *Fuel Process. Technol.* 105 (2013) 52–58.

[11] B.J. Skrifvars, T. Laurén, M. Hupa, R. Korbee, P. Ljung, *Fuel* 83 (10) (2004) 1371–1379.

[12] M.S. Bashir, P.A. Jensen, F. Frandsen, S. Wedel, K. Dam-Johansen, J. Wadenbäck, *Energy Fuels* 26 (4) (2012) 2317–2330.

[13] M. Theis, B.J. Skrifvars, M. Hupa, H. Tran, *Fuel* 85 (7–8) (2006) 1125–1130.

[14] M. Theis, B.J. Skrifvars, M. Zevenhoven, M. Hupa, H. Tran, *Fuel* 85 (14–15) (2006) 2002–2011.

[15] S.S. Lokare, J.D. Dunaway, D. Moulton, D. Rogers, D.R. Tree, L.L. Baxter, *Energy Fuels* 20 (3) (2006) 1008–1014.

[16] G. Li, S. Li, X. Xu, Q. Huang, Q. Yao, *Energy Fuels* 28 (1) (2014) 219–227.

[17] R. Shenassa, H. Tran, D.C.S. Kuhn, *Pulp Pap. Can.* 100 (10) (1999) 56–62.

[18] A.L. Robinson, H. Junker, L.L. Baxter, *Energy Fuels* 16 (2) (2002) 343–355.

[19] S.B. Hansen, *Model for Deposition Build-up in Biomass Boilers,* PhD thesis, Technical University of Denmark, Lyngby, Denmark, 2015.

[20] H. Wu, M.S. Bashir, P.A. Jensen, B. Sander, P. Glarborg, *Fuel* 113 (2013) 632–643.

[21] P.A. Jensen, F.J. Frandsen, J. Hansen, K. Dam-Johansen, N. Henrisken, S. Hörlyck, *Energy Fuels* 18 (2) (2004) 378–384.

[22] Y. Laxminarayan, *Formation, Sintering and Removal of Biomass Ash Deposits,* PhD thesis, Technical University of Denmark, Lyngby, Denmark, 2018.

[23] Y. Laxminarayan, P.A. Jensen, H. Wu, F.J. Frandsen, B. Sander, P. Glarborg, *Energy Fuels* 31 (8) (2017) 8733–8741.

[24] H. Wu, P. Glarborg, F.J. Frandsen, K. Dam-Johansen, P.A. Jensen, *Energy Fuels* 25 (7) (2011) 2862–2873.

[25] Y. Zheng, P.A. Jensen, A.D. Jensen, B. Sander, H. Junker, *Fuel* 86 (7–8) (2007) 1008–1020.

[26] M. Montgomery, S.A. Jensen, U. Borg, O. Biede, T. Vilhelmsen, *Mater. Corros.* 62 (7) (2011) 593–605.

[27] M. Montgomery, A. Karlsson, O.H. Larsen, *Mater. Corros.* 53 (2) (2002) 121–131.

[28] C. He, G. Ahmadi, *Aerosol Sci. Technol.* 29 (6) (1998) 525–546.

[29] C. Thornton, Z. Ning, *Powder Technol.* 99 (2) (1998) 154–162.

[30] W. Ai, J.M. Kuhlman, *Energy Fuels* 25 (2) (2011) 708–718.

[31] C.Y. Wen, Y.H. Yu, *Chem. Eng. Prog. Symp. Ser.* 62 (1966) 100–111.

[32] M. Dong, S. Li, J. Xie, J. Han, *Energies* 6 (7) (2013) 3245–3262.

[33] L.N. Rogers, J. Reed, *J. Phys. D Appl. Phys.* 17 (4) (1984) 677–689.

[34] N.A. Esmen, P. Ziegler, R. Whitfield, *J. Aerosol Sci.* 9 (6) (1978) 547–556.

[35] H.-C. Wang, W. John, Particles on Surfaces 1, Springer, 1988, pp. 211–224. ISBN: 978-1461595335.

July 2019

ForskEL project no. 12150/EUDP 64018-003

Final report: Flexible use of biomass on PF Fired power plants

Appendix D. Journal paper: Wang G., Jensen P.A., Wu H., Frandsen F.J., Sander B., Glarborg P. Potassium Capture by Kaolin, Part 1: KOH. Energy & Fuel 2018, 32, 1851-1862.

1. **Department of Chemical and Biochemical Engineering**
Technical University of Denmark
Søltofts Plads, Building 229, DK-2800, Kgs. Lyngby, Denmark
2. **Ørsted Bioenergy & Thermal power,**
Kraftværksvej 53, DK-7000, Fredericia, Denmark

CHEC no. R1902

energy&fuels Article
Cite This: Energy Fuels 2018, 32, 1851−1862 pubs.acs.org/EF

Potassium Capture by Kaolin, Part 1: KOH

Guoliang Wang,*[,†] Peter Arendt Jensen,[†] Hao Wu,[†] Flemming Jappe Frandsen,[†] Bo Sander,[‡] and Peter Glarborg[†]

[†]Department of Chemical and Biochemical Engineering, Technical University of Denmark, Søltofts Plads, Building 229, DK-2800 Lyngby, Denmark

[‡]Ørsted Bioenergy & Thermal Power A/S, Kraftværksvej 53, 7000 Fredericia, Denmark

Supporting Information

ABSTRACT: The reaction of gaseous KOH with kaolin and mullite powder under suspension-fired conditions was studied by entrained flow reactor (EFR) experiments. A water-based slurry containing kaolin/mullite and KOH was fed into the reactor and the reacted solid samples were analyzed to quantify the K-capture level. The effect of reaction temperature, K-concentration in the flue gas, and, thereby, molar ratio of K/(Al+Si) in reactants, gas residence time, and solid particle size on K-capture reaction was systematically investigated. Corresponding equilibrium calculations were conducted with FactSage 7.0. The experimental results showed that kaolin reached almost full conversion to K-aluminosilicates under suspension-fired conditions at 1100−1450 °C for a residence time of 1.2 s and a particle size of D_{50} = 5.47 μm. The amount of potassium captured by kaolin generally followed the equilibrium at temperatures above 1100 °C, but lower conversion was observed at 800 and 900 °C. Crystalline kaliophilite ($KAlSiO_4$) was formed at higher temperatures (1300 and 1450 °C), whereas, amorphous K-aluminosilicate was formed at lower temperatures. Coarse kaolin (D_{50} = 13.48 μm) captured KOH less effectively than normal (D_{50} = 5.47 μm) and fine (D_{50} = 3.51 μm) kaolin powder at 1100 and 1300 °C. The difference was less significant at 900 °C. Mullite generated from kaolin captured KOH less effectively than kaolin at temperatures below 1100 °C. However, at 1300 and 1450 °C, the amount of potassium captured by mullite became comparable to that of kaolin.

1. INTRODUCTION

Suspension-combustion boilers (also called pulverized fuel combustion boilers) are increasingly used for the production of power and heat from biomass.[1,2] Combustion of biomass in suspension-fired boilers can produce renewable, CO_2-neutral electricity with a higher electrical efficiency, compared with that of grate-fired boilers.[3] However, during the combustion process of biomass, significant amounts of K-species, such as KOH, KCl, and K_2SO_4, are released to the gas phase in the boiler chamber, and this leads to deposit formation and corrosion,[4−12] as well as deactivation of SCR (selective catalytic reduction) catalysts.[13−18] Ash deposition and corrosion problems may be mitigated by reducing the super heater temperature. However, this will cause a reduced electrical efficiency of power plants.[3,19−22]

To minimize the ash-related problems in biomass combustion, different treatments and processing technologies have been developed, including the use of alkali scavenging additives,[23−30] co-combustion with other biofuels or fossil fuels that are rich in Si or Al,[31−35] utilizing effective deposit removal techniques,[36] and a combination of different thermochemical processes.[37,38] Among these, using additives is a promising option, primarily because of its high effectiveness and the low requirements for boiler.

The basic principle of additive use is that the additives are injected into boilers to react with the problematic gaseous K-salts (such as KOH and KCl), forming K-species (such as K-aluminosilicates) with low corrosivity and high melting temperatures.[2,23,26,27,29,39−46] Biomass firing additives can generally be categorized into Al−Si-based, S-based, P-based, and Ca-based, according to the major elements present in the additives.[2,42,47−50]

Kaolin[51−55] and coal fly ash[52] are typical Al−Si-based additives for biomass combustion and they have been studied in laboratory-scale experiments. In addition, coal fly ash has been commercially utilized in full-scale biomass suspension-firing boilers in Denmark, and has been shown to have the capacity to significantly remedy deposition and corrosion problems.[29,40] The mineralogical composition of coal fly ash is complex, including mainly mineral phases such as quartz, mullite, kaolinite, illite, siderite, etc.[56,57] Among these mineral phases, kaolinite has been shown to be one of the most effective one for K-capture.[58] Kaolinite is a layered aluminosilicate mineral with chemical formula of $Al_2Si_2O_5(OH)_4$. Kaolin is a type of clay that is rich in kaolinite. Investigating the K-capture reaction by kaolin is important for obtaining an improved understanding of K-capture by coal fly ash.

Kaolin undergoes complex transformation when being heated up. Above 450 °C, kaolin transfers into metakaolin via a dehydroxylation reaction as shown in reaction R1.[51]

$$\begin{aligned} &Al_2Si_2O_5(OH)_4 \text{ (kaolin)} \\ &\rightarrow Al_2O_3\cdot 2SiO_2 \text{ (metakaolin)} + 2H_2O(g) \end{aligned} \qquad \text{(R1)}$$

Metakaolin is a type of amorphous aluminosilicate that reacts effectively with gaseous K-salts.[51] Metakaolin further transforms

Received: November 22, 2017
Revised: January 15, 2018
Published: January 17, 2018

to a spinel structure and amorphous SiO_2 when it is heated to temperatures above 980 °C (see reaction R2).

$$Al_2O_3{\cdot}2SiO_2\ (\text{metakaolin}) \rightarrow Al_2O_3{\cdot}SiO_2\ (\text{spinel}) + SiO_2\ (\text{amorphous}) \tag{R2}$$

Mullite starts to form at ~1100 °C, and its amount increases with temperature and time, according to reaction R3.[59]

$$3(Al_2O_3{\cdot}SiO_2)\ (\text{spinel}) + 3SiO_2\ (\text{amorphous}) \rightarrow 3Al_2O_3{\cdot}2SiO_2\ (\text{mullite}) + 4SiO_2\ (\text{amorphous}) \tag{R3}$$

At temperatures above 1400 °C, needle-shaped mullite grains are formed, and the size and the aspect ratio of the mullite grains increase with increasing calcination temperature.[59] Generally, compared to metakaolin, mullite is believed to be less reactive for alkali capture.[52] Thus, the transformation of kaolin at high temperatures may influence the K-capture reaction. To achieve the best K-capture results, kaolin should be injected into boilers at an optimal temperature window.

Alkali capture, especially the Na-capture reaction by kaolin, has been widely studied, primarily because of its application for cleaning Na-species from hot flue gases in combined cycle gas turbine (CCGT) power plants[60−62] and for dealing with ash-related problems in combustion of Na-rich low rank coals in power plant boilers.[28,63−65] However, when it comes to biomass combustion, K-capture reaction is of greater concern, but it has been studied to a less extent.[51]

Gas-phase release and speciation of potassium are dependent on many factors, including combustion conditions, fuel ash transformation chemistry, etc. In the combustion of biomass with high K content but low Cl and S contents, KOH(*g*) is the dominant K-species in the high-temperature flue gas.[66,67] When S and Cl are available, KCl and K_2SO_4 would be formed during the combustion process, but at high temperature, KCl and K_2SO_4 can also transfer into KOH in the presence of water.[51]

KOH is a troublesome K-species and the main reactions involved for kaolin/metakaolin to capture KOH are shown in reactions R4 and R5.[66]

$$Al_2O_3{\cdot}2SiO_2\ (\text{metakaolin}) + 2KOH \rightarrow 2KAlSiO_4\ (\text{kalsilite}) + H_2O \tag{R4}$$

$$Al_2O_3{\cdot}2SiO_2\ (\text{metakaolin}) + 2KOH + 2SiO_2 \rightarrow 2KAlSi_2O_6\ (\text{leucite}) + H_2O \tag{R5}$$

The two main products are kalsilite ($KAlSiO_4$) and leucite ($KAlSi_2O_6$), with melting temperatures above 1600 and 1500 °C, respectively. Therefore, the melt-induced slagging and corrosion in biomass-fired boilers could be significantly mitigated by the use of kaolin.[3,22,68] However, the kinetics and detailed knowledge on the KOH-capture reaction by kaolin is still limited, especially, for suspension combustion.

To the authors' knowledge, the only literature available on alkali capture by dispersed kaolin particles under suspension-fired conditions is the experimental study by Wendt and co-workers[63,69,70] done in a 17 kW down-flow combustor, which simulated the conditions in suspension-fired boilers. A sodium acetate solution was injected into the reactor to produce a sodium vapor. The effects of temperature and residence time, as well as the presence of sulfur and chlorine, on the Na-capture reaction were studied. Results showed that the rate of NaOH adsorption was higher than that of NaCl, and they proposed that NaOH is the only reacting species in both cases. However, whether the kinetics of Na and K capture by kaolin are the same has not been established.[52]

Gaseous KOH capture by kaolin pellets (~1 mm) in a fixed bed reactor was studied by Quang and co-workers.[51,71,72] They found that kaolin captured KCl more effectively than KOH, indicating that KCl and KOH can both react directly with kaolin. The KOH concentration was very low in these studies, with a typical KOH concentration of 1.1 ppm, which is far below the K concentration in biomass suspension-fired boilers.[5]

The degree of conversion of kaolin to K-aluminosilicates may be limited by equilibrium constraints. In addition, the rate of reaction may be limited by the external and internal diffusion of the gaseous potassium species, and by the reaction kinetics. Typically, a decreased kaolin particle size and/or an increased residence time lead to an increased conversion to the products.

Under suspension-fired conditions, the reaction between gaseous KOH and dispersed kaolin particles may be affected by the local temperature, the additive particle size and composition, and the reaction time. Understanding the influence of different parameters on the K-capture reaction is crucial and helpful for providing recommendation for optimal utilization of kaolin and coal fly ash in full-scale boilers.

The objective of this work is to develop a method to study the K-capture reactions by solid additives under well-controlled suspension-fired conditions, and to systematically investigate the impact of different parameters on the K-capture reaction by solid additives, such as reaction temperature, K concentration/molar ratio of K/(Al+Si) in the reactant, kaolin particle size, gas residence time, and the high-temperature transformation of kaolin. This paper is Part 1 of a series of two papers studying the potassium capture by kaolin. This paper focuses on the KOH capture by kaolin; the second one focuses on the K-capture reaction by kaolin using KCl, K_2CO_3, and K_2SO_4.

2. EXPERIMENTAL SECTION

2.1. Materials. Kaolin powders of three different particle sizes and a mullite powder were utilized in this study. The particle size distribution (PSD) of the materials was analyzed with a Malvern 3000 particle size distribution analyzer. Based on the PSD, the three kaolin powders are named as normal kaolin powder (D_{50} = 5.47 μm), fine kaolin powder (D_{50} = 3.51 μm), and coarse kaolin powder (D_{50} = 13.48 μm). The normal kaolin powder was purchased from VWR Chemicals, and the fine kaolin powder was generated by grinding the normal kaolin powder in a ball mill. The coarse kaolin powder was obtained by grinding kaolin stones purchased from Ward's Science. Mullite powder was generated by heat treatment of the normal kaolin powder (D_{50} = 5.47 μm) at 1100 °C for 24 h.[59] The calcinated mullite sample was regrinded, to break the agglomerated blocks, and to get a D_{50} of 5.90 μm, which is similar to that of the normal kaolin powder (D_{50} = 5.47 μm).

The materials were analyzed by ICP-OES (inductively coupled plasma atomic emission spectroscopy) and XRD (X-ray diffraction), for elemental composition and mineralogical composition. The elemental composition of the three kaolin samples was similar, as shown in Table 1. The molar (Na+K)/(Si+Al) ratio of the three kaolin samples is ~0.02, indicating that a large fraction of Al and Si are available for K-capture through reactions R4 and R5. The molar Si/Al ratio of the normal and the coarse kaolin powder is 1.12 and 1.17, respectively, which is higher than the theoretical molar Si/Al ratio of kaolinite ($Al_2Si_2O_5(OH)_4$). This is due to the presence of quartz (SiO_2), confirmed by the XRD spectrum of the kaolin powder shown in Figure 1.

As shown in Table 1, the BET surface area of the normal kaolin is 12.70 m^2/g. The BET surface area of the fine and coarse kaolin is

Table 1. Characteristics of the Solid Additives

	fine kaolin	normal kaolin	coarse kaolin	mullite
O (wt %, dry)	56.9	56.9	55.88	51.30
S (wt %, dry)	0.02	0.02	0.03	0.02
Si (wt %, dry)	22.0	22.0	23.0	24.8
Al (wt %, dry)	19.0	19.0	19.0	21.4
Fe (wt %, dry)	0.47	0.47	0.46	0.53
Ca (wt %, dry)	0.1	0.1	0.1	0.11
Mg (wt %, dry)	0.14	0.14	0.12	0.16
Na (wt %, dry)	0.1	0.1	0.1	0.1
K (wt %, dry)	1.1	1.1	1.2	1.2
Ti (wt %, dry)	0.02	0.02	0.01	0.02
P (wt %, dry)	0.05	0.05	0.05	0.06
Cl (wt %, dry)	0.1	0.1	0.05	0.11
D_{50} (μm)	3.51	5.47	13.48	5.90
BET surface area(m^2/g)	13.02	12.70	11.83	5.30

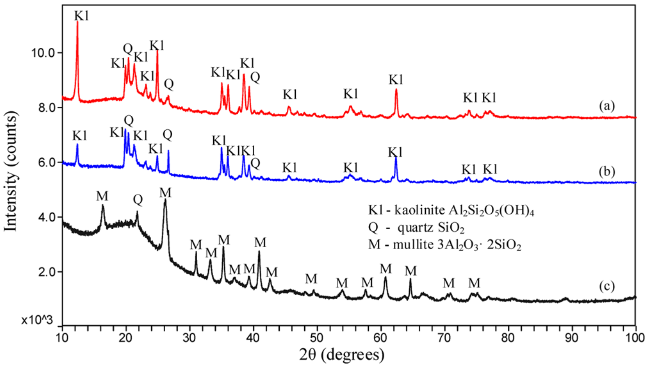

Figure 1. XRD spectra of the kaolin and mullite: (a) normal kaolin with D_{50} = 5.47 μm and (b, c) coarse kaolin with D_{50} = 13.48 μm (panel (b)) and mullite (panel (c)).

similar to that of normal kaolin. However, the BET surface area of mullite is much smaller than that of the parental kaolin, implying a significant sintering process during the mullite preparation process.

XRD spectra of the normal kaolin, coarse kaolin, and mullite are shown in Figure 1. The XRD spectrum of the fine kaolin is the same as that of the normal kaolin and, thus, is not included. The spectra show that kaolinite ($Al_2Si_2O_5(OH)_4$) and quartz (SiO_2) are the main mineral phases in the three kaolin samples. In the mullite sample, mullite ($3Al_2O_3{\cdot}2SiO_2$) and quartz (SiO_2) are detected as the main mineral phases. No kaolinite was detected in the mullite sample, indicating a complete transformation from kaolinite to mullite during heat treatment.

2.2. Setup. Experiments were conducted in the DTU Entrained Flow Reactor (EFR), as shown in Figure 2, which can simulate the conditions in suspension-fired boilers. The EFR consists of a gas supply system, a liquid/slurry sample feeding system, a gas preheater, a vertical reactor which is electrically heated by 7 heating elements, a bottom chamber and a particle and a flue gas extraction system. The vertical reactor tube is 2 m long, and the inner diameter is 79 mm. The reactor can be heated up to 1450 °C. A 0.8 m long preheater is placed above the reactor tube for preheating the secondary gas.

To obtain a high KOH vaporization degree and a good contact of salt vapor to additives, a slurry containing KOH and kaolin was fed into the EFR, instead of feeding solid KOH and kaolin powder into the reactor directly.[73,74] The slurry was subsequently fed into the reactor, using a peristaltic pump through a water-cooled feeding probe, as shown in Figure 3. During each experiment, the slurry was stirred with a magnetic stirrer to keep it homogeneous.

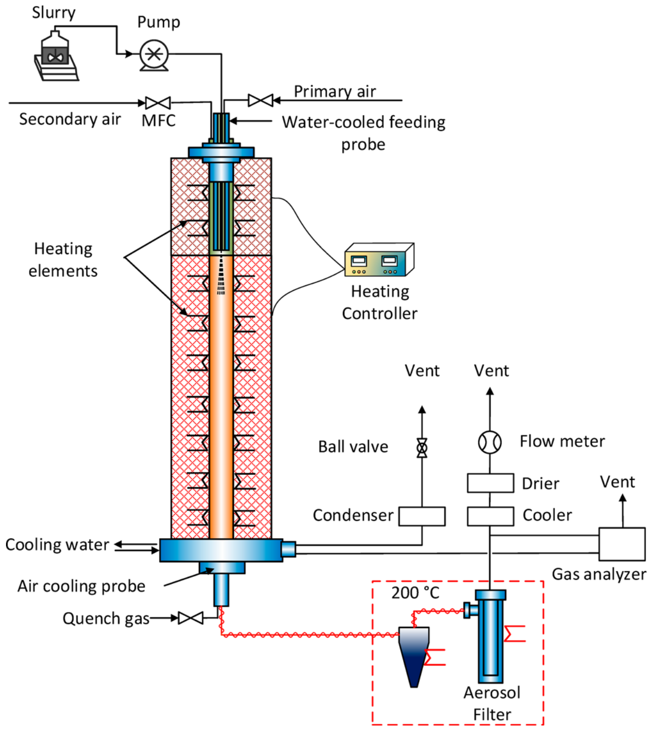

Figure 2. Schematic of the Entrained Flow Reactor (EFR).

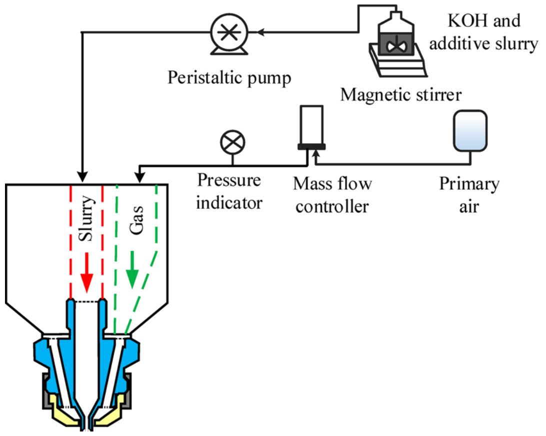

Figure 3. Slurry feeding and atomizing system of the DTU EFR.

The slurry also contained ethanol, which combusted in the reactor, producing CO_2. Therefore, the feeding rate stability can be indirectly monitored by measuring the CO_2 concentration in the flue gas. Slurry fed into the reactor was atomized, at the outlet of the water-cooled feeding probe by a 30 NL/min primary air flow, as shown in Figure 3. The atomized slurry droplets were mixed with the preheated secondary air and subsequently evaporated. KOH transferred into gas phase and reacted with solid additives (kaolin or mullite) in the reactor tube. At the outlet of the reactor, the flue gas and the entrained solid samples entered into a water-cooled bottom chamber, where the flue gas was divided into two fractions, with ~50% going to the sampling probe and subsequently to the solid sampling line, while the remaining 50% vent directly to the ventilation. The sampling probe is ~1.5 m long and air-cooled, keeping the flue gas temperature at ~300 °C. A quench gas (10 NL/min) was introduced at the inlet of the sampling probe, to quench the flue gas and the reaction. The quenching gas also helped to prevent the deposition of solid samples on the inner wall of the sampling tube. The entrained large solid particles and aerosols were captured, respectively, by a cyclone (with a cutoff diameter of 2.3 μm) and a metal filter (with a pore size of 0.8

Table 2. Conditions of Experiments in the Entrained Flow Reactor (EFR)

experimental series	additives	temp (°C)	gas residence time (s)	K concentration (ppmv)	K/(Al+Si)
(A) KOH evaporation experiments					
	no additive	800	1.2	500	no Al, Si
	no additive	900	1.2	500	no Al, Si
	no additive	1100	1.2	500	no Al, Si
	no additive	1300	1.2	500	no Al, Si
	no additive	1450	1.2	500	no Al, Si
(B) KOH capture by kaolin (impact of **K-concentration**)					
	normal kaolin (D_{50} = 5.47 μm)	1100	1.2	50	0.048
	normal kaolin (D_{50} = 5.47 μm)	1100	1.2	250	0.240
	normal kaolin (D_{50} = 5.47 μm)	1100	1.2	500	0.481
	normal kaolin (D_{50} = 5.47 μm)	1100	1.2	750	0.721
	normal kaolin (D_{50} = 5.47 μm)	1100	1.2	1000	0.961
(C) KOH-capture by kaolin (impact of **temperature**)					
	normal kaolin (D_{50} = 5.47 μm)	800	1.2	50, 500	0.048, 0.481
	normal kaolin (D_{50} = 5.47 μm)	900	1.2	50, 500	0.048, 0.481
	normal kaolin (D_{50} = 5.47 μm)	1100	1.2	50, 500	0.048, 0.481
	normal kaolin (D_{50} = 5.47 μm)	1300[a]	1.2	50, 500	0.048, 0.481
	normal kaolin (D_{50} = 5.47 μm)	1450	1.2	50, 500	0.048, 0.481
(D) KOH-capture by kaolin (impact of **residence time**)					
	normal kaolin (D_{50} = 5.47 μm)	800, 1100	0.7	500	0.481
	normal kaolin (D_{50} = 5.47 μm)		1.2	500	0.481
	normal kaolin (D_{50} = 5.47 μm)		1.5	500	0.481
	normal kaolin (D_{50} = 5.47 μm)		1.9	500	0.481
(E) KOH-capture by kaolin (impact of **kaolin particle size**)					
	fine kaolin (D_{50} = 3.51 μm)	900, 1100, 1300	1.2	500	0.481
	normal kaolin (D_{50} = 5.47 μm)	800, 900, 1100, 1300,[a] 1450	1.2	500	0.481
	coarse kaolin (D_{50} = 13.48 μm)	900, 1100, 1300	1.2	500	0.481
(F) KOH-capture by **mullite**					
	mullite (D_{50} = 5.90 μm)	800, 900, 1100, 1300, 1450	1.2	500	0.471

[a] Experiments were repeated.

μm) in the sampling line. The cyclone and filter were both heated to 200 °C, to avoid condensation of water vapor. Each experiment lasted ~60 min, and the solid samples were collected for further analysis.

In order to avoid unexpected air leakage into the EFR, the reactor was operated at a pressure slightly higher (~1.0−3.0 mbar) than atmospheric pressure, and the possible gas escaping from the reactor was captured by a shell around the reactor and pumped to ventilation.

2.3. Experimental Matrix. Two sets of experiments were conducted in the EFR: KOH evaporation experiments and KOH-capture experiments using kaolin of three different particle sizes, as well as mullite. The experimental conditions are summarized in Table 2, and more detailed information is available in Appendix I in the Supporting Information. In the KOH evaporation experiments (experiment series (A) in Table 2), KOH solution was injected into the EFR without solid additives, to study the evaporation and transformation behavior of KOH at high temperature. The concentration of KOH in the flue gas was kept at 500 ppmv. The mass of solid samples collected in the cyclone and filter were weighted to study the vaporization of KOH. In addition, the collected solid samples were analyzed via XRD to determine the transformation of KOH at high temperatures.

In the KOH-capture experiments (experiment series B−F) in Table 2), a slurry containing both KOH and kaolin/mullite was injected into the EFR. In all the KOH-capture experiments, the concentration of kaolin in the flue gas was kept constant, while the amount of KOH in the feeding slurry was adjusted. Thereby, the concentration of KOH in the flue gas was changed consequently. The KOH concentration (K concentration in Table 2) in the flue gas was changed from 50 ppmv to 1000 ppmv, and the molar ratio of K/(Al+Si) in reactants was correspondingly changed from 0.048 to 0.961.

2.4. Analytical Methods. To quantify the amount of potassium captured by kaolin, the reacted solid samples were analyzed with ICP-OES. The concentration of major elements (Al, Ca, Fe, Mg, P, S, K, Si, Na, and Ti) was determined according to Danish Standard DS/EN 15290 (Solid Biofuels—Determination of Major Elements). Danish Standard DS/EN ISO 16995 (Solid Biofuels—Determination of Water-Soluble Chloride, Sodium and Potassium) was used to determine the concentration of water-soluble potassium and chlorine. The concentration of total potassium and water-soluble potassium of product samples were both analyzed.

Two parameters were defined for quantifying the amount of potassium captured by kaolin: the K-conversion (X_K), and the K-capture level (C_K). X_K is defined as the percentage (%) of input KOH chemically captured by solid additives (kaolin/mullite) forming water-insoluble K-aluminosilicate. C_K is the mass of potassium captured by 1 g of additive (kaolin/mullite) (g K/(g additive)).

As shown in Figure 4, potassium in the reactants originated both from the salt (KOH) and the additives (kaolin/mullite). The majority

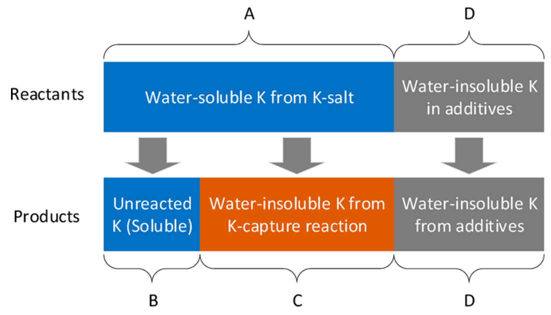

Figure 4. Potassium transformations in the K-capture reaction.

of potassium in the reactants was from KOH, which was water-soluble (part A). The remaining potassium was from additives, and it was water-insoluble (part D). During the KOH-capture reaction, part of the water-soluble K reacted with kaolin/mullite, forming water-insoluble K-aluminosilicate (part C), while the unreacted KOH remained water-soluble (part B). The K-conversion (X_K), and K-capture level (C_K) were calculated based on the ICP-OES analysis results of reacted samples, as shown in eqs 1 and 2.

$$X_K = \frac{C}{A} \times 100\% \tag{1}$$

$$C_K = \frac{n_{KOH} M_K X_K}{m_{ad}} \tag{2}$$

In eq 1, C is the amount of water-insoluble potassium formed by the K-capture reaction and A is the amount of potassium from KOH fed into the reactor, as shown in Figure 4. n_{Ksalt} (mol) is the molar amount of KOH fed into the reactor, M_K is the molar mass of K (g/mol), and m_{ad} is the mass of solid additives fed into the reactor (g). The details of the method for quantifying K-capture can be found in Appendix II of the Supporting Information.

To characterize the mineralogical composition of the reacted solid products, the collected samples were washed with deionized water at room temperature for 24 h to remove the water-soluble compounds (i.e., the K-salts in the reactant), and then filtered using 0.4 μm membranes. Subsequently, the water-washed solid samples were subjected to X-ray diffractometry (XRD) analysis. The XRD spectra were determined with a Huber diffractometer with characteristic Cu Kα radiation and operation conditions of 40 kV and 40 mA. The wavelength was 1.54056 Å. The identification of the main crystalline phase was performed with the JADE 6.0 software package (MDI, Livermore, CA) and the PDF2-2004 diffraction database.

2.5. Equilibrium Calculations. To understand the transformation of KOH at high temperature without additive injection, global equilibrium calculations under the conditions shown in experimental series A in Table 2 were conducted. To make a comparison of the experimental K-conversion (X_K) and K-capture level (C_K) relative to equilibrium, global equilibrium calculations were carried out under the conditions shown in experimental series B–F in Table 2. The calculations were performed using the Equilibrium module of the software FactSage 7.0. The databases of FactPS, FToxid, FTsalt, and FTpulp were employed for the calculations. Information about the different databases can be found in the literature.[75,76]

3. RESULTS AND DISCUSSION

3.1. Evaporation and Transformation of KOH in the EFR. Equilibrium calculations as well as EFR experiments (experimental series A in Table 2) were conducted to investigate the evaporation and transformation of KOH at high temperatures. The mass fractions of the collected solid products in cyclone and filter are shown in Figure 5A. The results of corresponding equilibrium calculations are shown in Figure 5B.

In the EFR sampling system, the large particles were collected in the cyclone, while the aerosols were collected in the filter. When the K-salts were completely vaporized in the reactor and then cooled down in the extraction probe, aerosols would form and all solid products would be collected in the filter. If some of the salt particles generated from evaporation of slurry droplets were not fully vaporized, both aerosols and some larger particles would be present, resulting in some solid material being collected also by the cyclone. The experimental data in Figure 5A indicate that a complete vaporization of KOH was obtained at 1100 °C. At 800 and 900 °C, the mass fraction of samples collected in the cyclone was 2.0% and 1.5%, respectively, indicating that a small amount of KOH had not evaporated. This is in agreement with the equilibrium calculations (Figure 5(B)), which predict that the majority of KOH appears as vapor at temperatures above 820 °C.

XRD analysis of the solid samples collected from the KOH evaporation experiments showed they consisted of $K_2CO_3 \cdot 1.5H_2O$. During cooling, gaseous or condensed KOH reacts with CO_2 to form K_2CO_3, which then absorbs moisture from the air, forming $K_2CO_3 \cdot 1.5H_2O$.

3.2. Representativeness of Solid Product Samples. The solid products from the EFR experiments, including samples from the sampling probe, cyclone, and filter, were carefully collected. For each experiment, the collected solid products corresponded to ∼58%–75% of the theoretical amount solid samples extracted by the probe. The rest were lost, mainly by deposition on the inner wall of the reactor tube.[77]

Therefore, in order to be able to determine the conversion degree of the reaction based on the collected solid product samples, the representativeness of the collected solid product samples were checked. This was done by comparing the molar

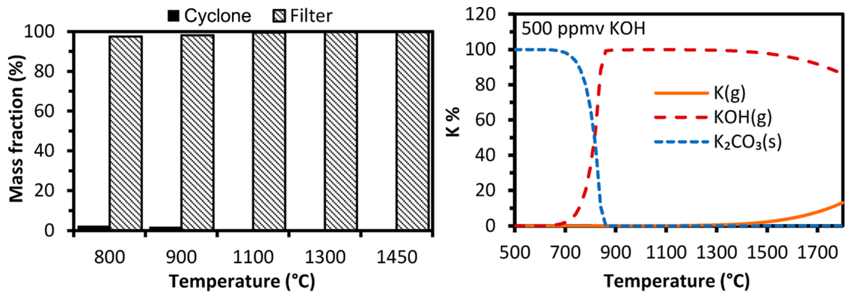

(A) EFR experiments (B) Equilibrium calculation

Figure 5. (A) Mass distribution of solid samples collected in cyclone and filter from KOH evaporation experiments; (B) equilibrium calculation results of KOH evaporation under conditions of experimental series A of Table 2.

ratio of K/(Al+Si) in the products with that of the fed reactants. The results based on ICP-OES analysis are shown in Figure 6. The molar ratios of K/(Al+Si) in the collected solid samples are almost identical to those of the reactants, implying that the solid product samples are representative.

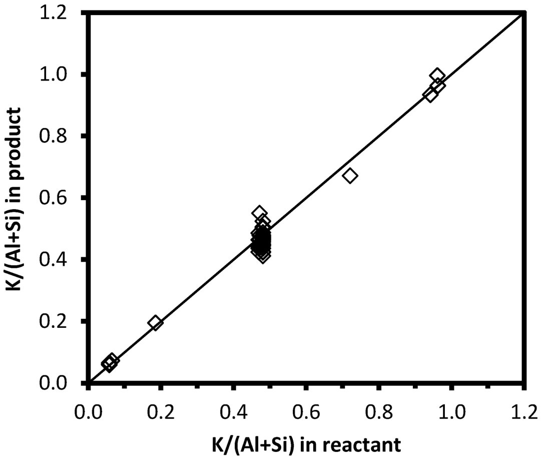

Figure 6. Comparison of K/(Al+Si) in collected solid products and that of fed reactants.

3.3. Evolution of Kaolin in the EFR. Slurries of normal kaolin (D_{50} = 5.47 μm) without and with KOH were fed into the EFR at 1300 °C, where the residence time was 1.2 s. XRD and SEM-EDX were utilized to study the mineralogical and morphological evolutions of kaolin during the reaction with KOH. The XRD spectra of the raw kaolin, the dehydroxylated kaolin (i.e., product of kaolin fed into the EFR without KOH), mullite, and the water-washed KOH-captured kaolin samples are compared in Figure 7.

The results show that only mullite and quartz were detected in the dehydroxylated kaolin (spectrum (c) in Figure 7); no kaolinite was detected. This reveals that, at 1300 °C, with a residence time of 1.2 s, all kaolinite from raw kaolin has decomposed completely. However, the peaks corresponding to mullite of the dehydroxylated kaolin are obviously weaker, compared to the peaks of the mullite powder (spectrum (b) in Figure 7). This shows that not all the decomposed kaolinite was converted to crystalline mullite, with some remaining as amorphous species, such as metakaolin and amorphous silica.[59] In the water-washed KOH-reacted kaolin (spectrum (a) in Figure 7), crystalline kaliophilite ($KAlSiO_4$) was detected, as the reaction product of kaolin and KOH at high temperatures (1300 °C) in the EFR.

The SEM images of raw kaolin, the dehydroxylated kaolin, and water-washed KOH-reacted kaolin are compared in Figure 8. It is seen that raw kaolin particles are all in the form of an irregular flaky shape, while the dehydroxylated kaolin particles are slightly more spherical but keep the original inner flaky structure. The flaky structure indicates that no significant melting occurred at 1300 °C, in agreement with the reported mullite melting point of 1830 °C.[78] For the KOH-reacted kaolin sample, some spherical particles with smooth surface were observed, showing the particles experienced melting in the EFR. Since the kaliophilite ($KAlSiO_4$) detected in the KOH-reacted solid product has a melting point of 1800 °C,[69] it is very likely that some amorphous products with low melting point also were formed.

Water-washed KOH-reacted kaolin (Figure 8C) was analyzed with SEM-EDX to get the elemental composition. The result shows that the molar ratio of K:Al:Si is 1:1.18:1.37, i.e., with extra Si compared to the chemical formula of kaliophilite ($KAlSiO_4$). This is attributed to the presence of quartz (SiO_2), which was also detected with the XRD analysis. It could also be due to the formation of some amorphous Si-species, which cannot be detected by XRD analysis.

3.4. Equilibrium Calculations. Equilibrium calculations were carried out for the same conditions as in the EFR, but with a wider temperature range (from 500 °C to 1800 °C). The influence of both the KOH concentration and thereby the molar K/(Al+Si) ratio in the reactants, and the reaction temperature, were studied by the calculations. A summary of the equilibrium calculation results is shown in Table 3. The detailed results of the calculations are shown in Appendix III in the Supporting Information.

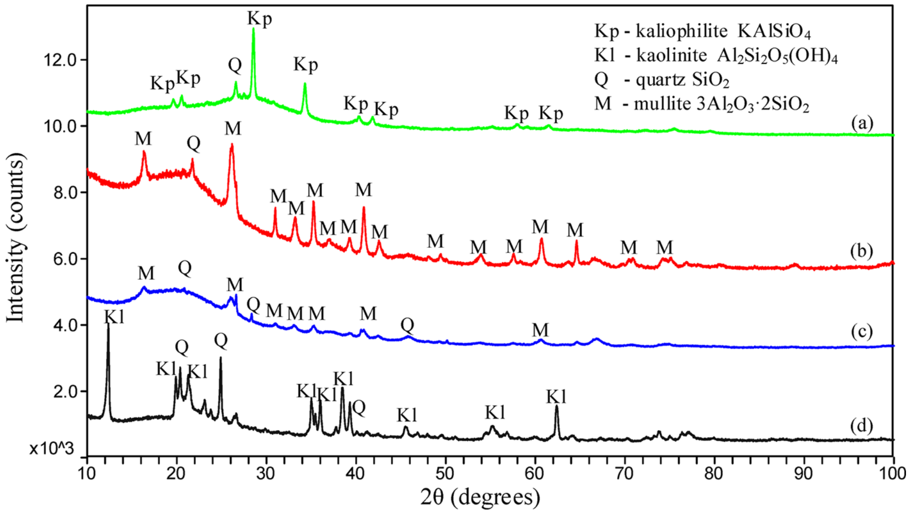

Figure 7. XRD spectra of raw, dehydroxylated, and KOH-reacted kaolin (water-washed): KOH-reacted kaolin (spectrum a), mullite obtained at 1100 °C, 24 h (spectrum b), dehydroxylated kaolin (spectrum c), and raw kaolin (spectrum d). For the samples used to obtain spectra (a) and (c), the reaction temperature in the EFR was 1300 °C, and the gas residence time was 1.2 s.

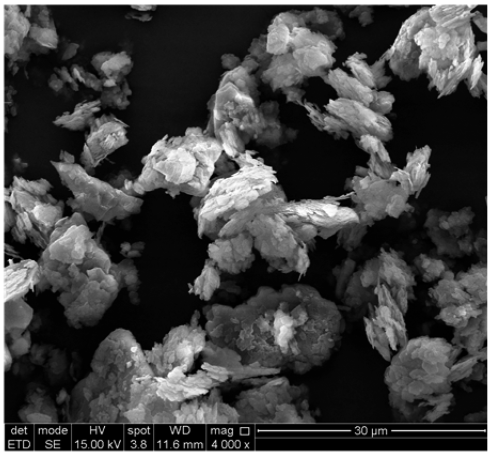

(A) Raw kaolin

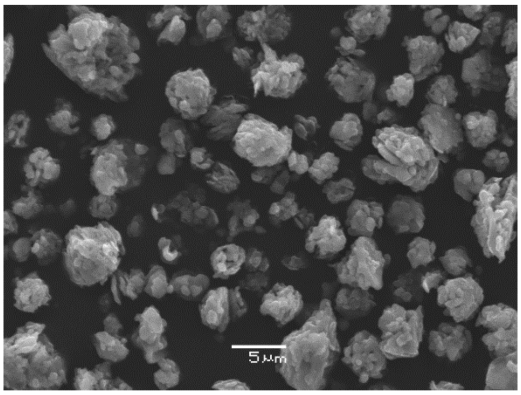

(B) Dehydroxylated kaolin

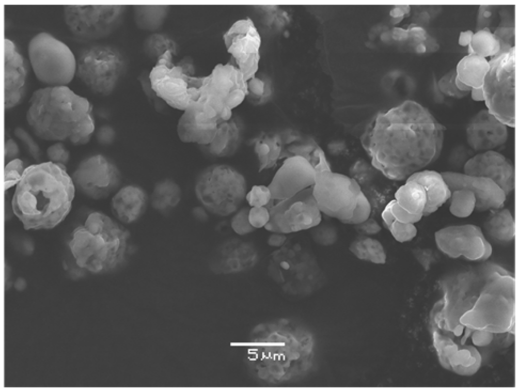

(C) KOH-reacted kaolin

Figure 8. SEM images of (A) raw kaolin, (B) dehydroxylated kaolin (without KOH fed at 1300 °C, residence time was 1.2 s), and (C) water-washed KOH-reacted kaolin (500 ppmv KOH by kaolin at 1300 °C, residence time was 1.2 s, and the K/(Al+Si) ratio in the reactant was 0.481).

The results in Table 3 indicate that the main K-aluminosilicate species formed from the reaction between KOH and kaolin varies with the molar ratio of K/(Al+Si) in the input. At 800−1450 °C, with 50 ppmv KOH, sanidine ($KAlSi_3O_8$) is the main aluminosilicate product, with K:Al:Si = 1:1:3; with 250 ppmv KOH, both sanidine ($KAlSi_3O_8$) and leucite ($KAlSi_2O_6$) are major K-aluminosilicates, whereas, with 500−1000 ppmv KOH, kaliophilite ($KAlSiO_4$) with K:Al:Si = 1:1:1 became the dominating K-aluminosilicate.

3.5. Impact of the Potassium Concentration. The experimental K-capture level (C_K) and K-conversion (X_K) are compared with the estimations from equilibrium calculations in Figure 9. The KOH concentration in the flue gas varied from 50 ppmv to 1000 ppmv, while the reaction temperature was kept constant at 1100 °C. The experimental data followed a similar trend but was always slightly lower, compared to the equilibrium prediction. When the KOH concentration increased from 50 ppmv to 500 ppmv, the C_K value for kaolin increased from 0.022 g K/(g kaolin) to 0.227 g K/(g kaolin). However, no obvious increase in C_K is observed when the KOH concentration increased further to 750 and 1000 ppmv. This is probably because the active compound in kaolin has been fully converted to K-aluminosilicates, while the increased KOH remained unreacted. The equilibrium constrain can explain the decrease in X_K. The value of X_K decreased slightly from 95.8% to 84.6% when the KOH concentration increased from 50 ppmv to 500 ppmv, while X_K decreased sharply when the KOH concentration increased from 500 ppmv to 1000 ppmv, as shown in Figure 9B.

The XRD spectra of the water-washed KOH-reacted kaolin at 50, 250, and 500 ppmv KOH are compared in Figure 10. The spectra at 750 ppmv and 1000 ppmv were similar to that at 500 ppmv and are not included. The results show that, in the 50 ppmv KOH product, only quartz and mullite were detected as the main crystalline phases. No crystalline K-aluminosilicate was detected in the sample, although sanidine ($KAlSi_3O_8$) was predicted by the equilibrium calculations shown in Table 3. This is probably because the concentration of K-aluminosilicates is low and/or they remained in an amorphous state, which cannot be detected. The 250 ppmv KOH spectrum shows that leucite ($KAlSi_2O_6$) with a molar ratio of K:Al:Si = 1:1:2 was the main K-aluminosilicate, while kaliophilite ($KAlSiO_4$) with a molar ratio of K:Al:Si = 1:1:1 became the main K-aluminosilicate at 500 ppmv KOH. The XRD analysis results generally agree with the equilibrium calculations shown in Table 3.

3.6. Impact of Reaction Temperature. The C_K and X_K obtained at different reaction temperatures (800−1450 °C) and two different KOH concentrations (50 ppmv and 500 ppmv) were compared with the equilibrium calculation results in Figure 11. Figure 11A and 11B show that, at 500 ppmv KOH, the C_K value increased from 0.166 g K/(g kaolin) to 0.241 g K/(g kaolin) by 43.6%, when the reaction temperature increased from 800 to 1300 °C. The value of X_K increased from 62.1% to 89.1%, correspondingly. However, when the temperature was increased further to 1450 °C, C_K and X_K decreased to 0.198 g K/(g kaolin) and 74.0%, respectively. This is caused by a change in the equilibrium products with a decreased amount of kaliophilite ($KAlSiO_4$) and an increased amount of leucite ($KAlSi_2O_6$) at high temperatures. At 1300 and 1450 °C, the value of C_K is close to the equilibrium calculation value. At 1100 °C and below, the C_K values are below the equilibrium levels, implying the process is kinetic-controlled.

Figures 11C and 11D show that, at 50 ppmv KOH, the K-capture level (C_K) was predicted to be 0.023 g K/(g kaolin), by the equilibrium calculations, and the predicted value of X_K was >99.2% throughout the entire temperature range. At temperatures >1100 °C, the experimental values of C_K and X_K were close to the equilibrium calculations. At 800 and 900 °C, the experimental result is slightly lower than the value predicted by the equilibrium calculations. The only K-aluminosilicate predicted by the calculations is sanidine ($KAlSi_3O_8$), with a molar ratio of K:Al:Si = 1:1:3.

The water-washed 500 ppmv KOH-reacted kaolin samples were subjected to XRD analysis, with the spectra shown in

Table 3. Summary of the Equilibrium Calculation Results of KOH Capture by Kaolin

input conditions	temp (°C)	K-species appearing	Al conc (%)	Si conc (%)	K conc (%)	K-capture (g K/g kaolin)
50 ppmv KOH, K/(Al+Si) = 0.048						
	800	100% $KAlSi_3O_8$	9	23	100	0.023
	900	100% $KAlSi_3O_8$	9	23	100	0.023
	1100	100% $KAlSi_3O_8$	9	23	100	0.023
	1300	100% $KAlSi_3O_8$	9	23	100	0.023
	1450	99% $KAlSi_3O_8$ + 1% KOH	9	23	99	0.022
250 ppmv KOH, K/(Al+Si) = 0.240						
	800	25% $KAlSi_3O_8$ + 75% $KAlSi_2O_6$	49	98	100	0.129
	900	25% $KAlSi_3O_8$ + 75% $KAlSi_2O_6$	49	98	100	0.129
	1100	24% $KAlSi_3O_8$ + 76% $KAlSi_2O_6$	49	97	100	0.129
	1300	20% $KAlSi_3O_8$ + 80% $KAlSi_2O_6$	49	96	100	0.128
	1450	22% $KAlSi_3O_8$ + 77% $KAlSi_2O_6$	49	96	99	0.128
500 ppmv KOH, K/(Al+Si) = 0.481						
	800	92% $KAlSiO_4$ + 6% $KAlSi_2O_6$	100	98	98	0.264
	900	91% $KAlSiO_4$ + 7% $KAlSi_2O_6$ + 1% KOH	100	99	98	0.264
	1100	91% $KAlSiO_4$ + 7% $KAlSi_2O_6$ + 2% KOH	100	99	98	0.263
	1300	82% $KAlSiO_4$ + 12% $KAlSi_2O_6$ + 6% KOH	95	100	94	0.252
	1450	50% $KAlSiO_4$ + 28% $KAlSi_2O_6$ + 21% KOH	79	100	78	0.209
750 ppmv KOH, K/(Al+Si) = 0.721						
	800	57% $KAlSiO_4$ + 8% $KAlO_2$ + 31% K_2SiO_3 + 3% KOH	88	78	57	0.231
	900	63% $KAlSiO_4$ + 1% $KAlO_2$ + 18% K_2SiO_3 + 16% KOH	98	87	63	0.258
	1100	65% $KAlSiO_4$ + 8% $K_2Si_2O_5$ + 27% KOH	100	89	65	0.263
	1300	57% $KAlSiO_4$ + 8% $KAlSi_2O_6$ + 35% KOH	100	100	65	0.263
	1450	57% $KAlSiO_4$ + 8% $KAlSi_2O_6$ + 35% KOH	100	100	65	0.263
1000 ppmv KOH, K/(Al+Si) = 0.961						
	800	29% $KAlSiO_4$ + 19% $KAlO_2$ + 49% K_2SiO_3 + 3% KOH	61	55	29	0.161
	900	35% $KAlSiO_4$ + 13% $KAlO_2$ + 38% K_2SiO_3 + 14% KOH	73	65	35	0.191
	1100	48% $KAlSiO_4$ + 11% K_2SiO_3 + 41% KOH	100	89	48	0.264
	1300	43% $KAlSiO_4$ + 6% $KAlSi_2O_6$ + 52% KOH	100	100	48	0.264
	1450	43% $KAlSiO_4$ + 6% $KAlSi_2O_6$ + 51% KOH + 1% K	100	100	48	0.264

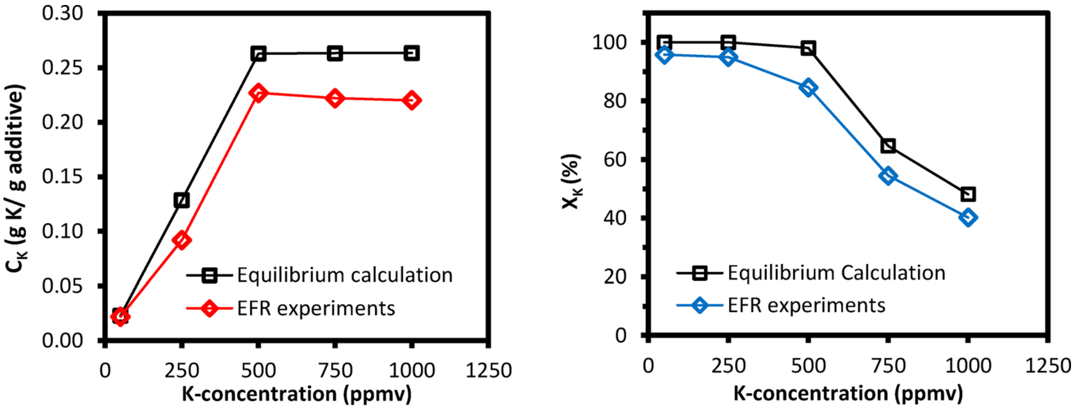

(A) K-capture level (C_K) (B) K-conversion (X_K)

Figure 9. K-capture level (C_K) and K conversion (X_K) of KOH capture by normal kaolin (D_{50} = 5.47 μm) at different KOH concentrations from 50 ppmv to 1000 ppmv (the molar K/(Al+Si) ratio in reactants varied from 0.048 to 0.961). The reaction temperature was 1100 °C, and the gas residence time was 1.2 s.

Figure 12. It shows that, with the temperature increased from 800 °C to 1450 °C, the peaks of kaliophilite ($KAlSiO_4$) increased significantly, indicating that either kaliophilite was generated in larger quantities or it became more crystalline with the increasing temperature or due to a faster cooling rate in the sampling system. No other crystalline K-aluminosilicate product was detected, although leucite ($KAlSi_2O_6$) was also predicted by the equilibrium calculations. The formation of kaliophilite was also observed in experimental studies by Steenari and her co-workers.[45] Kalsilite ($KAlSiO_4$), which is a polymorph of kaliophilite, was also widely reported in previous studies.[51,69,71,79] At 800 and 900 °C, no clear signal of K-

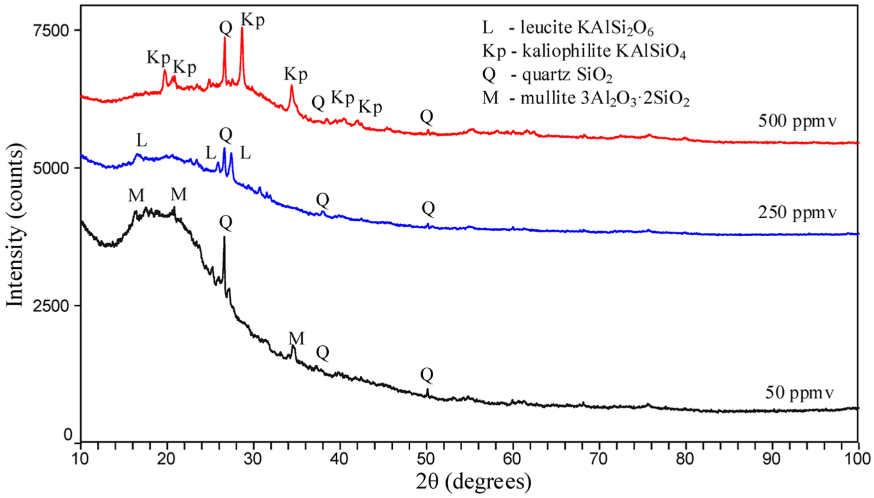

Figure 10. XRD spectra of water-washed KOH-reacted kaolin at 50, 250, and 500 ppmv KOH. The reaction temperature was 1100 °C, the molar ratios of K/(Al+Si) were 0.048, 0.240, and 0.481, and the gas residence time was 1.2 s.

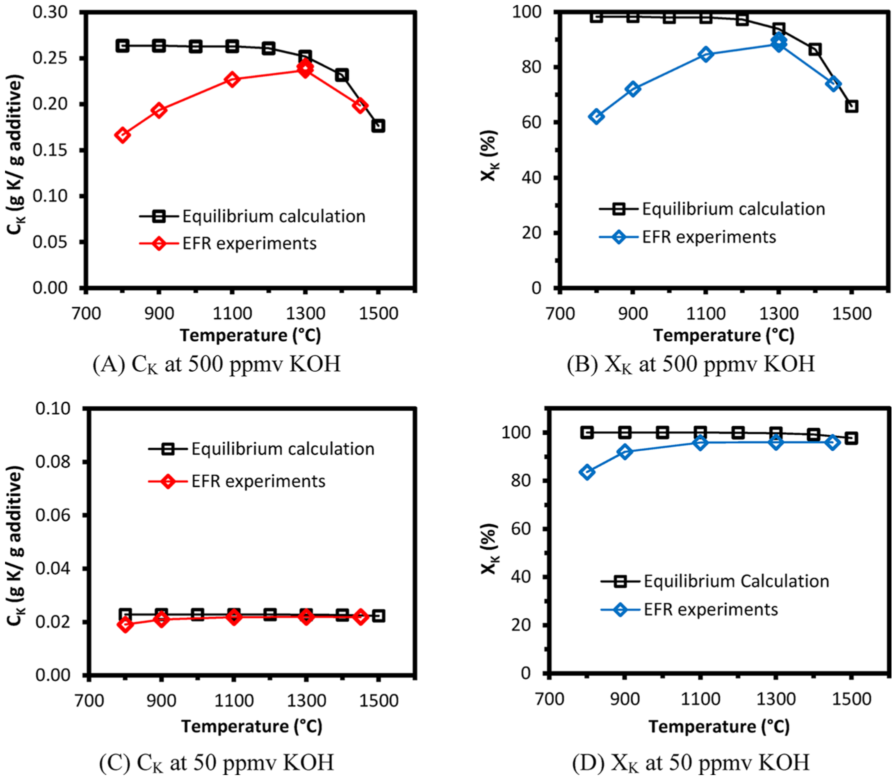

(A) C_K at 500 ppmv KOH

(B) X_K at 500 ppmv KOH

(C) C_K at 50 ppmv KOH

(D) X_K at 50 ppmv KOH

Figure 11. K-capture level (C_K) and K-conversion (X_K) of KOH capture by normal kaolin (D_{50} = 5.47 μm) at temperatures from 800 °C to 1450 °C: (A, B) the KOH concentration was 500 ppmv, and the molar K/(Al+Si) ratio was 0.481; (C, D) the KOH concentration was 50 ppmv, and the molar K/(Al+Si) ratio was 0.048. Gas residence time was 1.2 s for all experiments, and equilibrium calculation results are included for comparison.

aluminosilicate was detected by XRD. This is probably because the formed K-aluminosilicate existed in an amorphous form at lower temperatures. Kaolinite was detected in the 800 and 900 °C solid products, indicating an incomplete dehydroxylation of kaolin at temperatures below 900 °C in the EFR.

3.7. Impact of Gas Residence Time. The impact of gas residence time on the KOH-capture reaction was investigated at 800 and 1100 °C. At 800 °C, the gas residence time varied from 1.2 s to 1.9 s, while at 1100 °C, it was changed from 0.7 s to 1.7 s. In all experiments, the KOH concentration in the flue gas and the molar ratio of K/(Al+Si) in the reactants were kept constant, at 500 ppmv and 0.481, respectively. The experimental results were compared to the equilibrium calculation results in Figure 13.

At 800 °C, as shown in Figure 13A, when the gas residence time increased from 1.2 s to 1.9 s, C_K increases by 25.4% from 0.166 g K/g kaolin to 0.209 g K/g kaolin. However, at 1100 °C, when the gas residence time increased from 0.7 s to 1.2 s, C_K increased by 7.6%, from 0.211 g K/(g kaolin) to 0.227 g K/(g kaolin). When the gas residence time increased further from 1.2 s to 1.7 s, C_K increased to 0.236 by 4.1%.

In summary, the KOH-capture reaction by kaolin reached equilibrium at temperatures of 1300 and 1450 °C, with a gas residence time of 1.2 s and a kaolin particle size of D_{50} = 5.47

DOI: 10.1021/acs.energyfuels.7b03645
Energy Fuels 2018, 32, 1851−1862

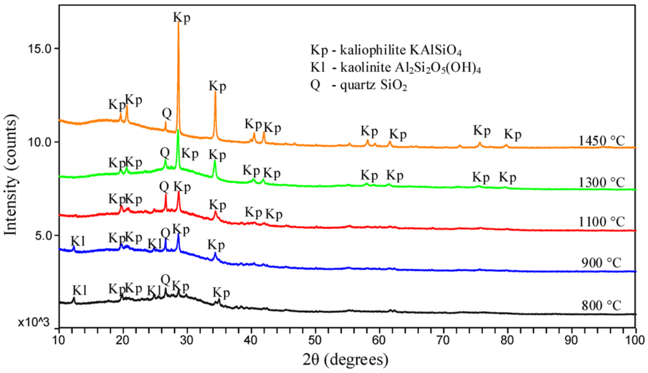

Figure 12. XRD spectra of water-washed solid samples from the experiments of KOH capture by normal kaolin (D_{50} = 5.47 μm) at different reaction temperatures, from 800 °C to 1450 °C. KOH concentration was 500 ppmv, (K/(Al+Si) = 0.481) and the gas residence time was 1.2 s.

μm. At 1100 °C with a residence time of 1.7 s, the reaction is close to the equilibrium. However, at 800 °C, C_K is obviously further away from the equilibrium, even with a longer residence time of 1.9 s, showing that the reaction is more kinetically or diffusion-controlled at 800 °C.

3.8. Impact of Kaolin Particle Size. The C_K values of fine kaolin, normal kaolin, and coarse kaolin at 800−1450 °C were compared to the equilibrium calculation results in Figure 14. Generally, the results show that, at 900−1300 °C, fine kaolin and normal kaolin behaved similarly, and C_K did not increase when the D_{50} of kaolin decreased from 5.47 μm to 3.51 μm. For coarse kaolin, the C_K value is similar to that of normal and fine kaolin at 900 °C. However, it became lower than the C_K value of normal and fine kaolin at 1100 and 1300 °C. This indicates that the conversion at 1100 and 1300 °C is partly limited by the transport processes, at least for the coarse kaolin. However, at 800 °C, the reaction appears to be kinetically limited.

3.9. KOH Capture by Mullite. The KOH capture level of mullite (D_{50} = 5.90 μm) was compared with that of normal kaolin (D_{50} = 5.47 μm) in Figure 15, at reaction temperatures of 800−1450 °C, a gas residence time of 1.2 s, and a KOH concentration of 500 ppmv. The EFR experimental results show, that at low temperatures (800−1100 °C), the C_K value of mullite is much lower than that of kaolin. This is probably partly because the BET surface area of mullite is smaller than that of kaolin (shown in Table 1) and thereby limited the internal KOH transport in the particles. On the other hand, the kinetics of the mullite−KOH reaction is probably slower than that of the kaolin−KOH reaction. At 1300 and 1450 °C, the C_K value of mullite increased significantly, and at 1450 °C, the value is close to that of the normal kaolin powder. This is probably because, at high temperatures (1300 and 1450 °C), the KOH-reacted mullite particles are melted, and the KOH diffusion mechanism changed from a slow gas−solid diffusion to a faster gas−liquid diffusion, which improved the transport of KOH inside the mullite particles. A similar phenomenon was observed by Zheng et al., when the KCl capture by mullite pellets was studied in a fixed-bed reactor.[52]

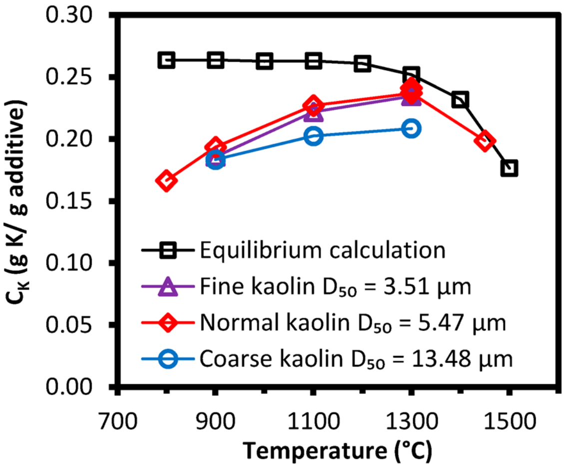

Figure 14. K-capture level (C_K) of KOH capture by kaolin of different particle size: fine kaolin (D_{50} = 3.51 μm), normal kaolin (D_{50} = 5.47 μm), and coarse kaolin (D_{50} = 13.48 μm). KOH concentration was 500 ppmv (the K/(Al+Si) molar ratio in the reactant was 0.481), and gas residence time was 1.2 s. Equilibrium calculations are included for comparison.

4. CONCLUSIONS

The impact of different parameters, including the potassium concentration in flue gas (molar ratio of K/(Al+Si) in reactants), the reaction temperature, the residence time, and

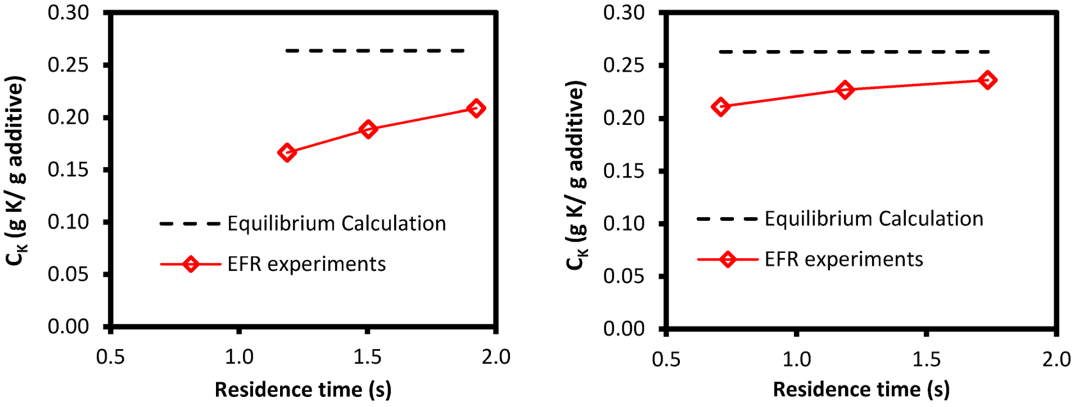

(A) 800 °C

(B) 1100 °C

Figure 13. K-capture level (C_K) of KOH capture by the normal kaolin (D_{50} = 5.47 μm) at different gas residence times. The reaction temperature was (A) 800 °C and (B) 1100 °C, and the KOH concentration was 500 ppmv (K/(Al+Si) = 0.481). Equilibrium calculation results are included for comparison.

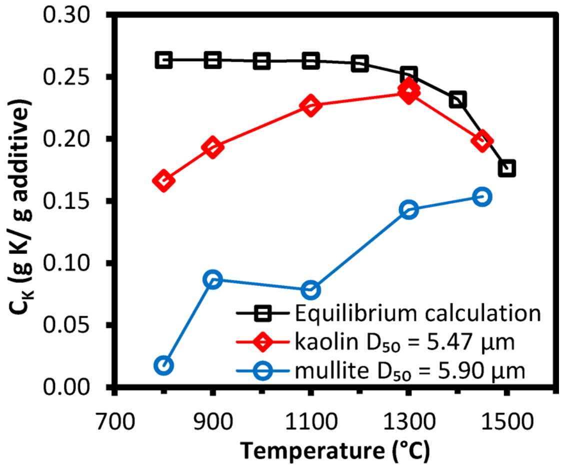

Figure 15. Comparison of K-capture level (C_K) of KOH capture by kaolin and mullite. The reaction temperature changed from 800 °C to 1450 °C. KOH concentration was 500 ppmv (K/(Al+Si) = 0.481), and gas residence time was 1.2 s. Equilibrium calculation results are included for comparison.

the kaolin particle size, as well as the high-temperature phase transformations of kaolin, on the KOH-capture reaction under suspension-fired conditions was investigated, by experiments in an entrained flow reactor and by thermodynamic equilibrium calculations.

The K-capture level (C_K) increased significantly when the KOH concentration increased from 50 ppmv to 500 ppmv, corresponding to an increase in the K/(Al+Si) molar ratio from 0.048 to 0.48, whereas no obvious increase was observed when KOH concentration increased further to 750 and 1000 ppmv. Leucite ($KAlSi_2O_6$) was formed at 250 ppmv KOH (K/(Al+Si) = 0.240), and kaliophilite ($KAlSiO_4$) was the dominant K-aluminosilicate at 500 ppmv KOH and above (K/(Al+Si) ≥ 0.481).

An almost full conversion of kaolin (D_{50} = 5.47 μm) to K-aluminosilicate was obtained without kinetic or transport limitations at temperatures above 1100 °C and the applied conditions (residence time of 1.2 s, and a KOH concentration of 500 ppmv). However, at 800 and 900 °C, the experimental data were considerably lower than the equilibrium predictions, and the K-capture level increased significantly when residence time increased, implying the reaction is probably kinetically controlled. The optimal temperature window for injecting kaolin for K-capture under suspension-fired conditions is 1100−1300 °C. At 1100 °C or above, crystalline kaliophilite ($KAlSiO_4$) was detected by XRD analysis, whereas, at 800 and 900 °C, amorphous K-aluminosilicate was formed.

Fine kaolin powder (D_{50} = 3.51 μm) and normal kaolin powder (D_{50} = 5.47 μm) behaved similarly, in terms of K-capture level (C_K), while coarse kaolin (D_{50} = 13.48 μm) showed a considerably smaller K-capture level at 1100 and 1300 °C. This is probably because KOH diffusion into the kaolin particles became a limiting factor for the coarse kaolin at 1100 °C and above. At 900 °C, where the difference was smaller, the reaction is more kinetically controlled and the additive particle size did not influence the reaction significantly with the applied particle sizes.

Mullite captured KOH less effectively, compared to kaolin at temperatures below 1100 °C. However, the C_K value of mullite increased significantly at 1300 and 1450 °C. At 1450 °C, the K-capture level of mullite is comparable to that of kaolin.

■ ASSOCIATED CONTENT

Ⓢ Supporting Information

The Supporting Information is available free of charge on the ACS Publications website at DOI: 10.1021/acs.energyfuels.7b03645.

> More-detailed experimental conditions about the EFR experiments (Appendix I); details regarding the quantification method of K-capture level (C_K) and K-conversion (X_K) (Appendix II); complete results of the equilibrium calculations of KOH capture by normal kaolin (D_{50} = 5.47 μm) (Appendix III) (PDF)

■ AUTHOR INFORMATION

Corresponding Author

*E-mail: guow@kt.dtu.dk.

ORCID

Guoliang Wang: 0000-0002-9663-5160
Hao Wu: 0000-0003-0462-2491
Peter Glarborg: 0000-0002-6856-852X

Notes

The authors declare no competing financial interest.

■ ACKNOWLEDGMENTS

This work is part of the project “Flexible Use of Biomass on PF Fired Power Plants” funded by Energinet through the ForskEL programme, Ørsted Bioenergy & Thermal Power A/S and DTU.

■ REFERENCES

(1) Hupa, M. *Energy Fuels* **2012**, *26*, 4−14.

(2) Wu, H.; Glarborg, P.; Frandsen, F. J.; Dam-Johansen, K.; Jensen, P. A. *Energy Fuels* **2011**, *25*, 2862−2873.

(3) Frandsen, F. J. Ash Formation, Deposition and Corrosion When Utilizing Straw for Heat and Power Production. Doctoral Thesis; Technical University of Denmark: Lyngby, Denmark, 2011.

(4) Andersen, K. H.; Frandsen, F. J.; Hansen, P. F. B.; Wieck-Hansen, K.; Rasmussen, I.; Overgaard, P.; Dam-Johansen, K. *Energy Fuels* **2000**, *14*, 765−780.

(5) Bashir, M. S.; Jensen, P. A.; Frandsen, F. J.; Wedel, S.; Dam-Johansen, K.; Wadenback, J.; Pedersen, S. T. Suspension-Firing of Biomass. Part 1: Full-Scale Measurements of Ash Deposit Build-up. *Energy Fuels* **2012**, *26*, 2317−2330.

(6) Hansen, L. A.; Nielsen, H. P.; Frandsen, F. J.; Dam-Johansen, K.; Hørlyck, S.; Karlsson, A. *Fuel Process. Technol.* **2000**, *64*, 189−209.

(7) Wang, G.; Shen, L.; Sheng, C. *Energy Fuels* **2012**, *26*, 102−111.

(8) Gao, X.; Yani, S.; Wu, H. *Energy Fuels* **2015**, *29*, 5171−5175.

(9) Niu, Y.; Zhu, Y.; Tan, H.; Hui, S.; Jing, Z.; Xu, W. *Fuel Process. Technol.* **2014**, *128*, 499−508.

(10) Skrifvars, B.-J.; Laurén, T.; Hupa, M.; Korbee, R.; Ljung, P. *Fuel* **2004**, *83*, 1371−1379.

(11) Wang, Q.; Yao, H.; Yu, D.; Dai, L.; Xu, M. *Energy Fuels* **2007**, *21*, 513−516.

(12) Laxminarayan, Y.; Jensen, P. A.; Wu, H.; Frandsen, F. J.; Sander, B.; Glarborg, P. *Energy Fuels* **2017**, *31*, 8733−8741.

(13) Kling, A.; Andersson, C.; Myringer, A.; Eskilsson, D.; Jaras, S. *Appl. Catal., B* **2007**, *69*, 240−251.

(14) Zheng, Y.; Jensen, A. D.; Johnsson, J. E. *Appl. Catal., B* **2005**, *60*, 253−264.

(15) Zheng, Y.; Jensen, A. D.; Johnsson, J. E.; Thøgersen, J. R. *Appl. Catal., B* **2008**, *83*, 186−194.

(16) Zheng, Y.; Jensen, A. D.; Johnsson, J. E. *Ind. Eng. Chem. Res.* **2004**, *43*, 941−947.

(17) Kling, Å.; Andersson, C.; Myringer, Å.; Eskilsson, D.; Järås, S. G. *Appl. Catal., B* **2007**, *69*, 240−251.

(18) Castellino, F.; Jensen, A. D.; Johnsson, J. E.; Fehrmann, R. *Appl. Catal., B* **2009**, *86*, 206−215.

(19) Dayton, D. C.; French, R. J.; Milne, T. A. *Energy Fuels* **1995**, *9*, 855−865.

(20) Knudsen, J. N.; Jensen, P. A.; Dam-Johansen, K. *Energy Fuels* **2004**, *18*, 1385−1399.

(21) Jappe Frandsen, F. *Fuel* **2005**, *84*, 1277−1294.

(22) Nielsen, H. P.; Frandsen, F. J.; Dam-Johansen, K. *Energy Fuels* **1999**, *13*, 1114−1121.

(23) Tobiasen, L.; Skytte, R.; Pedersen, L. S.; Pedersen, S. T.; Lindberg, M. A. *Fuel Process. Technol.* **2007**, *88*, 1108−1117.

(24) Kassman, H.; Pettersson, J.; Steenari, B.-M.; Åmand, L.-E. *Fuel Process. Technol.* **2013**, *105*, 170−180.

(25) Davidsson, K. O.; Åmand, L. E.; Steenari, B. M.; Elled, A. L.; Eskilsson, D.; Leckner, B. *Chem. Eng. Sci.* **2008**, *63*, 5314−5329.

(26) De Fusco, L.; Boucquey, A.; Blondeau, J.; Jeanmart, H.; Contino, F. *Fuel* **2016**, *170*, 16−26.

(27) Wang, L.; Hustad, J. E.; Skreiberg, Ø.; Skjevrak, G.; Grønli, M. A Critical Review on Additives to Reduce Ash Related Operation Problems in Biomass Combustion Applications. *Energy Procedia* **2012**, *20*, 20−29.

(28) Kyi, S.; Chadwick, B. L. *Fuel* **1999**, *78*, 845−855.

(29) Damoe, A. J.; Wu, H.; Frandsen, F. J.; Glarborg, P.; Sander, B. *Energy Fuels* **2014**, *28*, 3217−3223.

(30) Boström, D.; Grimm, A.; Boman, C.; Björnbom, E.; Öhman, M. *Energy Fuels* **2009**, *23*, 5184−5190.

(31) Sami, M.; Annamalai, K.; Wooldridge, M. *Prog. Energy Combust. Sci.* **2001**, *27*, 171−214.

(32) Wu, H.; Glarborg, P.; Frandsen, F. J.; Dam-Johansen, K.; Jensen, P. A.; Sander, B. *Fuel Process. Technol.* **2013**, *105*, 212−221.

(33) Wu, H.; Glarborg, P.; Frandsen, F. J.; Dam-Johansen, K.; Jensen, P. A.; Sander, B. *Fuel* **2011**, *90*, 1980−1991.

(34) Savolainen, K. *Appl. Energy* **2003**, *74*, 369−381.

(35) Wu, H. Co-combustion of Fossil Fuels and Waste. Ph.D. Thesis; Technical University of Denmark: Lyngby, Denmark, 2011.

(36) Yin, C.; Rosendahl, L. A.; Kær, S. K. *Prog. Energy Combust. Sci.* **2008**, *34*, 725−754.

(37) Jensen, P. A.; Sander, B.; Dam-Johansen, K. *Biomass Bioenergy* **2001**, *20*, 431−446.

(38) Llorente, M. J. F.; Arocas, P. D.; Nebot, L. G.; García, J. E. C. *Fuel* **2008**, *87*, 2651−2658.

(39) Si, J.; Liu, X.; Xu, M.; Sheng, L.; Zhou, Z.; Wang, C.; Zhang, Y.; Seo, Y.-C. *Appl. Energy* **2014**, *114*, 434−444.

(40) Wu, H.; Bashir, M. S.; Jensen, P. A.; Sander, B.; Glarborg, P. *Fuel* **2013**, *113*, 632−643.

(41) Wu, H.; Pedersen, M. N.; Jespersen, J. B.; Aho, M.; Roppo, J.; Frandsen, F. J.; Glarborg, P. *Energy Fuels* **2014**, *28*, 199−207.

(42) Aho, M.; Vainikka, P.; Taipale, R.; Yrjas, P. *Fuel* **2008**, *87*, 647−654.

(43) Wibberley, L. J.; Wall, T. F. *Fuel* **1982**, *61*, 93−99.

(44) Bäfver, L. S.; Rönnbäck, M.; Leckner, B.; Claesson, F.; Tullin, C. *Fuel Process. Technol.* **2009**, *90*, 353−359.

(45) Steenari, B. M.; Lindqvist, O. *Biomass Bioenergy* **1998**, *14*, 67−76.

(46) Wang, L.; Skreiberg, Ø.; Becidan, M. *Appl. Therm. Eng.* **2014**, *70*, 1262−1269.

(47) Aho, M.; Paakkinen, K.; Taipale, R. *Fuel* **2013**, *103*, 562−569.

(48) Wang, L.; Hustad, J. E.; Skreiberg, Ø.; Skjevrak, G.; Grønli, M. *Energy Procedia* **2012**, *20*, 20−29.

(49) Wang, L.; Skjevrak, G.; Hustad, J. E.; Skreiberg, Ø. *Energy Fuels* **2014**, *28*, 208−218.

(50) Turn, S. Q.; Kinoshita, C. M.; Ishimura, D. M.; Zhou, J.; Hiraki, T. T.; Masutani, S. M. A review of sorbent materials for fixed bed alkali getter systems in biomass gasifier combined cycle power generation applications. *J. Inst. Energy* **1998**, *71* (489), 163−177.

(51) Tran, K.-Q.; Iisa, K.; Steenari, B.-M.; Lindqvist, O. *Fuel* **2005**, *84*, 169−175.

(52) Zheng, Y.; Jensen, P. A.; Jensen, A. D. *Fuel* **2008**, *87*, 3304−3312.

(53) De Fusco, L.; Defoort, F.; Rajczyk, R.; Jeanmart, H.; Blondeau, J.; Contino, F. *Energy Fuels* **2016**, *30*, 8304−8315.

(54) Öhman, M.; Boström, D.; Nordin, A.; Hedman, H. *Energy Fuels* **2004**, *18*, 1370−1376.

(55) Aho, M.; Silvennoinen, J. *Fuel* **2004**, *83*, 1299−1305.

(56) Ahmaruzzaman, M. *Prog. Energy Combust. Sci.* **2010**, *36*, 327−363.

(57) Chen, Y.; Wang, G.; Sheng, C. Comparison of Particle Size Evolution during Pulverized Coal Combustion in O_2/CO_2 and O_2/N_2 Atmospheres. *Energy Fuels* **2014**, *28* (1), 136−145.

(58) Aho, M. *Fuel* **2001**, *80*, 1943−1951.

(59) Chen, C. Y.; Lan, G. S.; Tuan, W. H. *Ceram. Int.* **2000**, *26*, 715−720.

(60) Shadman, F.; Punjak, W. A. *Thermochim. Acta* **1988**, *131*, 141−152.

(61) Uberoi, M.; Punjak, W. A.; Shadman, F. *Prog. Energy Combust. Sci.* **1990**, *16*, 205−211.

(62) Escobar, I.; Oleschko, H.; Wolf, K.-J.; Müller, M. *Powder Technol.* **2008**, *180*, 51−56.

(63) Mwabe, P. O.; Wendt, J. O. L. Mechanisms governing trace sodium capture by kaolinite in a downflow combustor. In *26th Symposium on Combustion*, Napoli, Italy, 1996.

(64) Vuthaluru, H. B.; Vleeskens, J. M.; Wall, T. F. *Fuel Process. Technol.* **1998**, *55*, 161−173.

(65) Li, M.; Zhang, Z.; Wu, X.; Fan, J. *Energy Fuels* **2016**, *30*, 7763−7769.

(66) Niu, Y.; Tan, H.; Hui, S. e. *Prog. Energy Combust. Sci.* **2016**, *52*, 1−61.

(67) Wei, X.; Schnell, U.; Hein, K. *Fuel* **2005**, *84*, 841−848.

(68) Michelsen, H. P. Deposition and high-temperature corrosion in biomass-fired boilers. Ph.D. Thesis; Technical University of Denmark: Lyngby, Denmark, 1998.

(69) Mwabe, P. O. Mechanisms governing alkali metal capture by kaolinite in a downflow combustor. Ph.D. Thesis; The University of Arizona, Tucson, AZ, 1993.

(70) Gale, T. K.; Wendt, J. O. L. *Combust. Flame* **2002**, *131*, 299−307.

(71) Tran, K.-Q.; Iisa, K.; Hagström, M.; Steenari, B.-M.; Lindqvist, O.; Pettersson, J. B. C. *Fuel* **2004**, *83*, 807−812.

(72) Tran, Q. K.; Steenari, B.-M.; Iisa, K.; Lindqvist, O. *Energy Fuels* **2004**, *18*, 1870−1876.

(73) Zheng, Y.; Jensen, P. A.; Jensen, A. D. Potassium capture by kaolin and fly ash powder in an entrained flow reactor; Technical University of Denmark: Lyngby, Denmark, 2008; pp 1−51.

(74) Iisa, K.; Lu, Y.; Salmenoja, K. *Energy Fuels* **1999**, *13*, 1184−1190.

(75) Bale, C. W.; Chartrand, P.; Degterov, S. A.; Eriksson, G.; Hack, K.; Ben Mahfoud, R.; Melançon, J.; Pelton, A. D.; Petersen, S. *CALPHAD: Comput. Coupling Phase Diagrams Thermochem.* **2002**, *26*, 189−228.

(76) Bale, C. W.; Bélisle, E.; Chartrand, P.; Decterov, S. A.; Eriksson, G.; Hack, K.; Jung, I. H.; Kang, Y. B.; Melançon, J.; Pelton, A. D.; Robelin, C.; Petersen, S. *CALPHAD: Comput. Coupling Phase Diagrams Thermochem.* **2009**, *33*, 295−311.

(77) Theis, M.; Mueller, C.; Skrifvars, B.-J.; Hupa, M.; Tran, H. *Fuel* **2006**, *85*, 1970−1978.

(78) Schneider, H.; Schreuer, J.; Hildmann, B. *J. Eur. Ceram. Soc.* **2008**, *28*, 329−344.

(79) Punjak, W. A.; Shadman, F. *Energy Fuels* **1988**, *2*, 702−708.

DOI: 10.1021/acs.energyfuels.7b03645
Energy Fuels 2018, 32, 1851−1862

July 2019

ForskEL project no. 12150/EUDP 64018-003

Final report: Flexible use of biomass on PF Fired power plants

Appendix E. Journal paper: Wang G., Jensen P.A., Wu H., Frandsen F.J., Sander B., Glarborg P. Potassium Capture by Kaolin, Part 2: K_2CO_3, KCl and K_2SO_4. Energy & Fuels 2018, 32, 3566-3578.

1. **Department of Chemical and Biochemical Engineering**
Technical University of Denmark
Søltofts Plads, Building 229, DK-2800, Kgs. Lyngby, Denmark
2. **Ørsted Bioenergy & Thermal power,**
Kraftværksvej 53, DK-7000, Fredericia, Denmark

CHEC no. R1902

energy&fuels
Article
Cite This: Energy Fuels 2018, 32, 3566−3578
pubs.acs.org/EF

Potassium Capture by Kaolin, Part 2: K_2CO_3, KCl, and K_2SO_4

Guoliang Wang,*,† Peter Arendt Jensen,† Hao Wu,† Flemming Jappe Frandsen,† Bo Sander,‡ and Peter Glarborg†

†Department of Chemical and Biochemical Engineering, Technical University of Denmark, Søltofts Plads, Building 229, DK-2800 Lyngby, Denmark

‡Ørsted Bioenergy & Thermal Power A/S, Kraftværksvej 53, 7000 Fredericia, Denmark

Supporting Information

ABSTRACT: The reaction of kaolin powder with K_2CO_3, KCl, and K_2SO_4 under suspension-fired conditions was studied by entrained flow reactor experiments and equilibrium calculations. The influence of reaction temperature, K-concentration in the flue gas, molar ratio of K/(Al + Si) in the reactants, and gas residence time on the reaction was investigated. The results showed that the K-capture level (C_K) (g potassium reacted by per g kaolin available) of K_2CO_3 and KCl by kaolin generally followed the equilibrium predictions at temperatures above 1100 °C, when using a kaolin particle size of D_{50} = 5.47 μm and a residence time of 1.2 s. This revealed that a nearly full conversion was obtained without kinetic or transport limitations at the conditions applied. At 800 and 900 °C, the measured conversions were lower than the equilibrium predictions, indicating that the reactions were either kinetically or diffusion controlled. The measured C_K of K_2SO_4 by kaolin was much lower than the equilibrium predictions. Kaliophilite ($KAlSiO_4$) product was predicted by the equilibrium calculations of the K_2SO_4 capture reaction; however the XRD results revealed that leucite ($KAlSi_2O_6$) was formed. Compared with the C_K of KOH reacting with kaolin, the C_K of K_2CO_3 was similar, while the C_K values of KCl and K_2SO_4 were both lower.

1. INTRODUCTION

The Danish government plans to phase out coal from power plants by 2030, mainly through promoting wind energy and replacing coal with biomass in power plants.[1] Suspension-firing of biomass can provide CO_2-neutral electricity with higher efficiency compared to traditional grate-firing.[2] However, ash-related problems have sometimes hampered the utilization of biomass in suspension-fired power plants.

Potassium is present naturally in plant materials, and it is the main cause for most ash-related problems,[3−6] including deposition,[7−10] corrosion,[11,12] and SCR catalyst deactivation in biomass-fired boilers.[13−15] During biomass combustion, potassium is released to gas phase in different forms depending on the ash chemistry of the fuels and combustion conditions. K-species including of KOH, K_2CO_3, KCl, and K_2SO_4 have been detected in the ash from biomass-fired boilers.[3,16−22] In the combustion of woody biomass with a low fuel Cl and S content, potassium may appear as K_2CO_3 and KOH in the flue gas.[23] However, when Cl and S are available, like in the case of herbaceous biomass combustion, KCl and K_2SO_4 become the dominant K-containing compounds.[23,24] KCl and K_2SO_4 have melting temperatures of around 770 and 850 °C, respectively. The binary system of KCl and K_2SO_4 may melt at as low as 690 °C forming sticky surface on heat transfer surfaces.[25] The melted K-salts can function as a glue and accelerate the formation of ash deposit. Additionally, the deposited KCl can cause severe corrosion.[26] When the flue gas is cooled down, the condensation of KCl and K_2SO_4 forms aerosols that can poison SCR de-NO_x catalysts and thereby impede the plant NO_x removal system.[13−15] The efficiency and availability of biomass-fired boilers can be decreased due to problems caused by the potassium-rich biomass ash.[27−29]

Injecting additives to capture and transfer the volatile potassium species into less corrosive compounds with a higher melting point is an option to reduce biomass ash related challenges.[17,30−32] Kaolin and coal fly ash have been identified as effective potassium-capture additives for biomass combustion.[33,34] Kaolin is a kind of clay that is rich in a layered aluminosilicate mineral−kaolinite ($Al_2Si_2O_5(OH)_4$). Coal fly ash often contains mullite ($3Al_2O_3{\cdot}2SiO_2$) as the main mineral phase.[35] Kaolinite and mullite can react with volatile alkali species and bind alkali in alkali-aluminosilicate species.[17,36]

When kaolin is heated, it decomposes and transfers into metakaolin above 450 °C.[37,38] Metakaolin can capture gaseous potassium species such as KOH, KCl and K_2SO_4. Using KCl as an example, metakaolin react with KCl forming K-aluminosilicate, releasing HCl into the gas phase, see reaction R1 and R2.[39−41] K-aluminosilicate has a higher melting point compared to KOH, KCl and K_2SO_4 and thereby the potassium becomes less problematic for the boiler operation. Coal fly ash with mullite as the main mineral phase, can react with volatile K-species in a similar way as kaolin.[17,42−46]

$$\begin{aligned}&Al_2O_3{\cdot}2SiO_2\ (\text{metakaolin}) + 2KCl + H_2O \rightarrow\\&2KAlSiO_4\ (\text{kalsilite/kaliophilite}) + 2HCl\ (g)\end{aligned} \tag{R1}$$

$$\begin{aligned}&Al_2O_3{\cdot}2SiO_2\ (\text{metakaolin}) + 2SiO_2 + 2KCl + H_2O \rightarrow\\&2KAlSi_2O_6\ (\text{leucite}) + 2HCl\ (g)\end{aligned} \tag{R2}$$

Received: December 21, 2017
Revised: February 14, 2018
Published: February 20, 2018

DOI: 10.1021/acs.energyfuels.7b04055
Energy Fuels 2018, 32, 3566−3578

Kaolin has been tested in a large-scale CFB boilers as an additive to prevent alkali-related problems.[47] With the addition of kaolin, the amount of water-soluble K and Cl in the fly ash was significantly decreased, and the bed agglomeration temperature was increased.[47] Coal fly ash has been commercially utilized in full-scale biomass suspension-fired boilers in Denmark.[17,30,48] In order to optimize the use of these additives in biomass suspension-fired boilers, a thorough understanding of the reaction of these additives with different volatile potassium species is wanted.

Alkali capture by kaolin has been studied previously.[36,39,40,49−51] Shadman and co-workers studied the reaction of gaseous NaCl and KCl with kaolin flakes in a fixed bed reactor.[32,36,49,52,53] The results showed that kaolin captured NaCl and KCl irreversibly through chemical reaction. The reaction was diffusion-influenced under the studied conditions (800 °C, kaolin flakes with a thickness of 0.5 mm, and a residence time of 40 h). A weight increase of 26.6% of saturated kaolin flakes was observed by the NaCl-kaolin reaction.[32]

In the study by Zheng et al.,[50] the kinetics of gaseous KCl capture by kaolin pellets with a diameter of 1.5 mm was investigated in a fixed bed reactor. The influence of oxygen content (0−20%), water content (0−3 vol %), KCl concentration (0−1600 ppmv), as well as the reaction temperature (900−1500 °C) on the reaction was studied. It was shown that the diffusion of KCl inside the kaolin pellets was the rate-controlling step of the reaction at the studied conditions. The reaction temperature posed a significant impact on the KCl-capture reaction under the studied conditions. The K-capture level of kaolin decreased with exposure temperature up to 1300 °C and then increased with further increasing the exposure temperature to 1500 °C. This is because at 900−1300 °C, sintering of kaolin pellets took place, resulting in a gradual replacement of fast gas diffusion by slow condensed-state diffusion. At temperatures above 1300 °C, a partially molten phase was formed inside the pellets; as a result the liquid diffusion improved the transport of KCl.[50]

In a fixed bed study by Tran et al.,[39−41] the K-capture reaction by kaolin flakes with a diameter of 0.5−2 mm was studied in a fixed bed reactor equipped with an alkali detector. The reaction temperature was in the range of 750−950 °C. The results revealed that potassium is captured by kaolin not only via chemical adsorption but also via physical adsorption. The comparison of results using KOH, KCl, and K_2SO_4 show that the total absorption rate of KCl by kaolin was slightly higher than that of KOH, while the absorption rate of K_2SO_4 was significantly lower than that of KOH and KCl at the studied conditions.

The studies mentioned above were all conducted in fixed bed reactors where kaolin was present in the form of pellets or flakes, and the reaction time was as long as hours. The reaction conditions differ significantly from those in suspension fired boilers, where kaolin particles are well dispersed and the reaction time is only a few seconds.[30,54] Additionally, alkali species and kaolin may be exposed to flame temperature as high as 1700 °C.[27,54] The reaction of K-species with kaolin at suspension-firing conditions takes place between condensed-phase kaolin particles (solid or melted) and the gaseous potassium species.[55,56] The reaction may be influenced by external and internal diffusion, kinetic limitations and chemical equilibrium.[39,50] To the authors' knowledge, quantitative study on K-capture by kaolin at suspension-fired conditions is not available, and no previous study is published where the influence of alkali species (KCl, KOH, K_2CO_3, and K_2SO_4) on the reaction with kaolin at suspension-fired conditions is investigated and compared.

Wendt and co-workers studied the gaseous sodium capture reaction by kaolin at suspension fired conditions using a 17 kW down flow combustor. The results showed that the capture rate of NaOH was obviously higher than that of NaCl. They proposed that NaOH was the only reacting species in both cases.[51,57] However, whether the kinetics of Na-species and K-species capture by kaolin are the same has not been established.

In paper 1 of this paper series,[58] we have investigated the reaction between KOH and kaolin at suspension-fired conditions in the temperature range of 800−1450 °C. It was shown that 1g kaolin reacting with gas phase KOH can capture up to 0.22 g of K in the temperature range of 1100−1300 °C, with a kaolin particle size of D_{50} = 5.47 μm and a residence time of 1.2 s. At the applied conditions, the KOH conversion could be reasonably predicted by equilibrium calculations at temperatures above 1100 °C.[58]

This is paper 2 of this paper series, investigating the reaction of kaolin with different K-species. The aim of this work is to get a thorough understanding of the K-capture reaction by kaolin under suspension-firing conditions so as to minimize or avoid ash-related problems caused by K-species during combustion of K-rich biomass fuels. More specifically, the objective of this work is to understand the influences of the molar ratio of K/(Al + Si) in reactants, K-concentration, reaction temperature, and K-species type on the K-capture reaction using kaolin at suspension-firing conditions.

2. EXPERIMENTAL SECTION

2.1. Materials. Kaolin powder purchased from VWR Chemicals was utilized in this study. The characteristics of the kaolin powder including elemental composition, particle size and BET surface area are listed in Table 1. It is seen that the molar (Na + K)/(Si + Al) ratio of the kaolin is 0.02, indicating a large fraction of Al and Si is available for K-capture. Additionally, the kaolin sample was analyzed by XRD (X-ray diffraction), and the results showed that kaolinite ($Al_2Si_2O_5(OH)_4$) was the main mineral phase with also some quartz (SiO_2).

Table 1. Characteristics of Kaolin Powder

properties	kaolin
O (wt %, dry)	56.9
S (wt %, dry)	0.02
Si (wt %, dry)	22.0
Al (wt %, dry)	19.0
Fe (wt %, dry)	0.47
Ca (wt %, dry)	0.1
Mg (wt %, dry)	0.14
Na (wt %, dry)	0.1
K (wt %, dry)	1.1
Ti (wt %, dry)	0.02
P (wt %, dry)	0.05
Cl (wt %, dry)	0.1
D_{50} (μm)	5.47
BET surface area (m^2/g)	12.70

2.2. Setup. Experiments were carried out in the DTU entrained flow reactor (EFR), which can simulate the conditions in suspension-fired boilers. A schematic figure of the EFR can be found in paper 1 of this series.[58] The vertical reactor tube of the EFR is 2 m long, with an inner diameter of 79 mm. The reactor can be electrically heated up to 1450 °C by 7 heating elements. A 0.8 m long preheater is above the vertical reactor tube for preheating the secondary gas. The potassium species (including K_2CO_3, KCl, and K_2SO_4) and kaolin were mixed with deionized water, to make a homogeneous slurry. The slurry was pumped

Table 2. Experimental Conditions of the EFR experiments

experimental series	K-species	additives	temp/°C	gas residence time/s	K in gas/ppmv	K/(Al + Si)
(A) K-salt vaporization experiments						
	K_2CO_3	no additive	800	1.2	500	no Al, Si
	KCl	no additive	900	1.2	500	no Al, Si
	K_2SO_4	no additive	1100	1.2	500	no Al, Si
		no additive	1300	1.2	500	no Al, Si
		no additive	1450	1.2	500	no Al, Si
(B) K_2CO_3-capture by kaolin (impact of K-concentration)						
	K_2CO_3	kaolin	1100	1.2	500	0.481
	K_2CO_3	kaolin	1100	1.2	1000	0.961
(C) K_2CO_3-capture by kaolin (impact of temperature)						
	K_2CO_3	kaolin	800	1.2	500	0.481
	K_2CO_3	kaolin	900	1.2	500	0.481
	K_2CO_3	kaolin	1100	1.2	500	0.481
	K_2CO_3	kaolin	1300	1.2	500	0.481
	K_2CO_3	kaolin	1450	1.2	500	0.481
(D) KCl-capture by kaolin (impact of K-concentration)						
	KCl	kaolin	1300	1.0−1.2	50[a]	0.048
	KCl	kaolin	1300	1.0−1.2	250[a]	0.240
	KCl	kaolin	1300	1.0−1.2	500[a]	0.481
	KCl	kaolin	1300	1.0−1.2	750	0.721
	KCl	kaolin	1300	1.0−1.2	1000	0.961
(E) KCl-capture by kaolin (impact of temperature)						
	KCl	kaolin	900	1.0−1.2	50, 500	0.048, 0.481
	KCl	kaolin	1100	1.0−1.2	50, 500	0.048, 0.481
	KCl	kaolin	1300[a]	1.0−1.2	50, 500	0.048, 0.481
	KCl	kaolin	1450	1.0−1.2	50, 500	0.048, 0.481
(F) KCl-capture by kaolin (impact of residence time)						
	KCl	kaolin	1100, 1300	0.6	500	0.481
	KCl	kaolin	1100, 1300	0.8	500	0.481
	KCl	kaolin	1100, 1300	1.2	500	0.481
	KCl	kaolin	1100, 1300	1.9	500	0.481
(G) K_2SO_4-capture by kaolin (impact of K-concentration)						
	K_2SO_4	kaolin	1100	1.2	50	0.048
	K_2SO_4	kaolin	1100	1.2	500	0.481
	K_2SO_4	kaolin	1100	1.2	1000	0.961
(H) K_2SO_4-capture by kaolin (impact of temperature)						
	K_2SO_4	kaolin	800	1.2	500	0.481
	K_2SO_4	kaolin	900	1.2	500	0.481
	K_2SO_4	kaolin	1100	1.2	500	0.481
	K_2SO_4	kaolin	1450	1.2	500	

[a] Note: Experiments were repeated.

into the EFR and subsequently atomized by the preheated secondary gas. The potassium species vaporized and reacted with kaolin in the reactor tube, and the solid products were collected by a cyclone (cutoff diameter of 2.3 μm) and a metal filter (pore size of 0.8 μm). Detailed information about the reactor can be found in paper 1 of this paper series.[58]

2.3. Experimental Matrix. Two series of experiments were conducted in the EFR: K-salt vaporization experiments and K-salt capture experiments using kaolin. The experimental conditions are summarized in Table 2. In the K-salt vaporization experiments (series A in Table 2), solutions of K_2CO_3, KCl and K_2SO_4 respectively were fed into the EFR without kaolin, to study the vaporization and transformation of K_2CO_3, KCl and K_2SO_4 at high temperatures. The concentration of KCl was kept at 500 ppmv, while K_2CO_3 and K_2SO_4 were kept at 250 ppmv to maintain the same K-concentration in the flue gas. The solid samples in the cyclone and filter were carefully collected, weighted and stored for further analysis.

In the K-capture experiments (series B−H in Table 2), KCl, K_2CO_3, and K_2SO_4 were fed into the EFR together with kaolin, respectively. The impact of K-concentration, molar ratio of K/(Al + Si) in reactants, reaction temperature, and gas residence time on the K-capture reaction was investigated. In the K-capture experiments, the concentration of kaolin in the flue gas inside the EFR was kept constant. While the concentration of K-salts in the flue gas was varied, and the molar K/(Al +

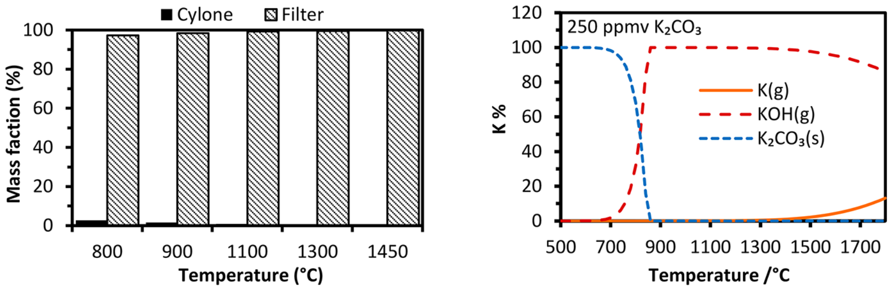

(A) K_2CO_3 vaporization in EFR (D) Equilibrium calculation (K_2CO_3)

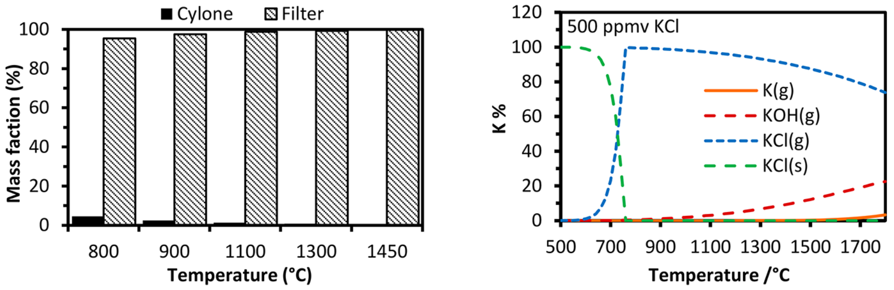

(B) KCl vaporization in EFR (E) Equilibrium calculation (KCl)

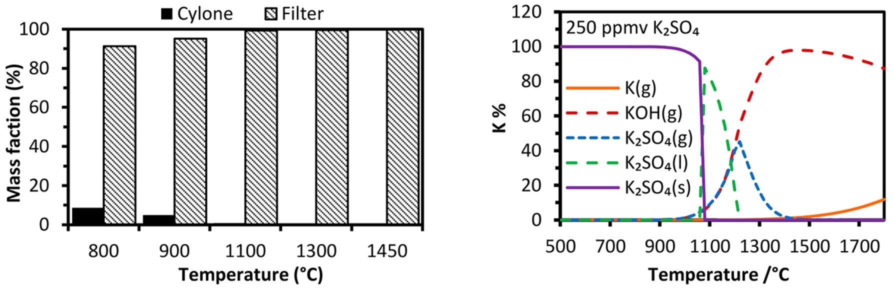

(C) K_2SO_4 vaporization in EFR (F) Equilibrium calculation (K_2SO_4)

Figure 1. Mass distribution of solid samples collected in the cyclone and filter from K-salt vaporization experiments for (A) K_2CO_3, (B) KCl, and (C) K_2SO_4, and corresponding equilibrium calculation results for (D) K_2CO_3, (E) KCl, and (F) K_2SO_4.

Si) ratio in the reactants changed consequently. The K-concentration in the flue gas was varied from 50 ppmv to 1000 ppmv, and the molar K/(Al + Si) ratio in the reactants changed from 0.048 to 0.961 correspondingly. For each experiment, solid products were carefully collected from the cyclone and filter. The representativeness of the collected solid samples was examined by comparing the molar ratios of K/(Al + Si) in collected solid samples with that of the fed reactants.

2.4. Analytical Methods. The reacted solid samples from the K-capture experiments were analyzed with ICP-OES (Inductively Coupled Plasma Atomic Emission Spectroscopy) to determine the amount of potassium captured by kaolin. Two parameters were defined for the quantification: X_K (K-conversion), and C_K (K-capture level). X_K is defined as the percentage (%) of potassium in the input potassium species chemically captured by kaolin forming water-insoluble K-aluminosilicate. C_K is the mass of potassium captured by 1 g of additive (kaolin) (g K/g additive). The details about the calculation methods can be found in paper 1 of this series of study.[58]

To characterize the mineralogical composition of the reacted solid products, water-washed solid products were subjected to X-ray diffractometry (XRD) analysis. The XRD patterns were determined with a Huber diffractometer with characteristic Cu Kα radiation and operation conditions of 40 kV and 40 mA. The identification of main crystalline phases was performed with the JADE 6.0 software package (MDI Livermore, CA) and diffraction database of PDF2−2004.

2.5. Equilibrium Calculation. To better understand the K-capture reaction by kaolin, equilibrium calculations were carried out using Factsage 7.0. The databases of FactPS, FToxid, FTsalt, and FTpulp were employed for the calculations. Information about the different databases can be found in literature,[59,60] and a detailed description of the equilibrium calculation is available in appendix II of the Supporting Information.

3. RESULTS AND DISCUSSION

3.1. Vaporization and Transformation of K-Salts. The vaporization and transformation of K_2CO_3, KCl, and K_2SO_4 at high temperatures may affect the K-capture reaction, and it was studied at the conditions shown in series A of Table 2. K-species (K_2CO_3, KCl and K_2SO_4) entered into the EFR in a form of slurry droplets. When water in these droplets evaporated, condensed phase K-salts were formed, which could be vaporized to gas phase or stay as condensed phase in the reactor. If all the K-salts are vaporized, aerosols will be formed and captured only by the filter. If the K-salts are not fully vaporized, the condensed K-salts can generate some larger particles being collected by the cyclone. The mass fraction of the solid samples collected in the cyclone and filter is shown in Figure 1A−C. Results of corresponding equilibrium calculations were shown in Figure 1D−F.

For K_2CO_3, the experimental results reveal that, at temperatures ≥1100 °C, all solid samples were captured by the filter, implying that a complete vaporization was obtained. At 800 and 900 °C, 1.6% and 2.7% of the product samples was captured by the cyclone, respectively. An increase of CO_2 concentration by 262 ppmv in flue gas was observed at 1100 °C and above, corresponding to a complete decomposition of K_2CO_3, forming KOH and CO_2. This also indicates that the formation of K_2CO_3

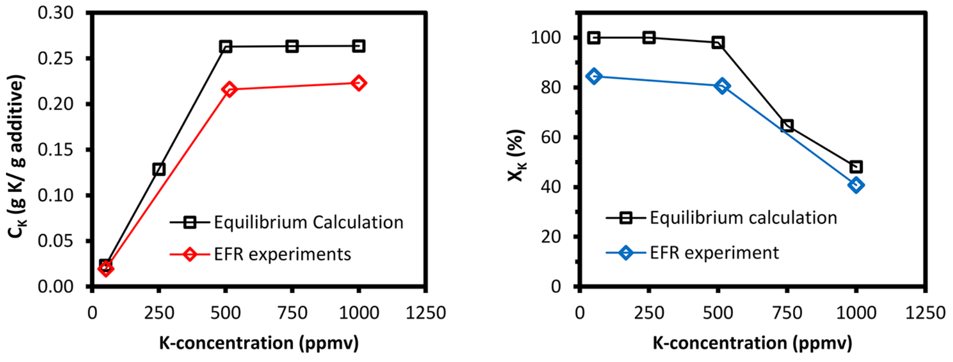

(A) K-capture level (C_K) (B) K-conversion (X_K)

Figure 2. K-capture level (C_K) and K conversion (X_K) of K_2CO_3-capture by kaolin at K_2CO_3 concentration varied from 25 ppmv to 500 ppmv (molar ratio of K/(Al + Si) in reactants changed from 0.048 to 0.961). Reaction temperature was 1100 °C. Gas residence time was 1.2 s. Equilibrium calculation results were included for comparison.

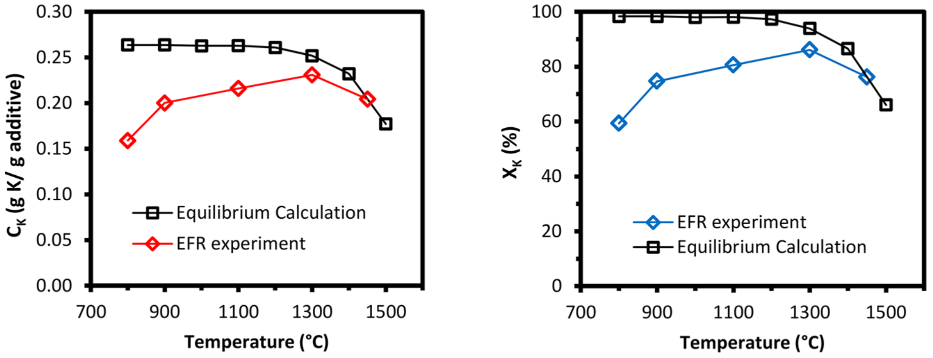

(A) K-capture level (C_K) (B) K-conversion (X_K)

Figure 3. K-capture level (C_K) and K-conversion (X_K) of K_2CO_3 capture by kaolin at different temperatures (800−1450 °C). K_2CO_3 concentration was 250 ppmv, molar ratio of K/(Al + Si) in reactants was 0.481, and residence time was 1.2 s. Equilibrium calculation results are included for comparison.

during the gas cooling process is negligible, probably due to the fast cooling rate and the short residence time. At 800 and 900 °C, the CO_2 concentration increased by 122 and 213 ppmv, showing a decomposition fraction of 48.8% and 85.2%, respectively. However, XRD analysis of the collected solid samples showed that $K_2CO_3{\cdot}1.5H_2O$ is the only solid product collected from the K_2CO_3 vaporization experiments. The results imply that the KOH aerosols collected by the metal filter probably reacted with CO_2 and moisture during the process of collecting, storage, or delivery for XRD analysis, forming $K_2CO_3{\cdot}1.5H_2O$.

The KCl vaporization experiments show that all samples were collected in the filter at temperatures above 1100 °C, implying a complete vaporization of KCl at 1100 °C. At 800 and 900 C, 4.6% and 2.5% of the product solid samples were collected in the cyclone. The equilibrium calculations on KCl showed that at temperatures above 740 °C, potassium appeared mainly as gaseous KCl. Above 800 °C, some KOH appeared but gaseous KCl remained the dominant K-species. Solid samples collected from KCl vaporization experiments were analyzed with XRD and showed that all collected products were KCl, with no potassium carbonate or potassium hydrate detected.

The equilibrium calculation results showed that the melting point of K_2SO_4 was 1070 °C, and KOH starts to form at 900 °C. At 900−1070 °C, solid, gaseous K_2SO_4 and gaseous KOH coexisted, while at 1070−1220 °C, liquid, gaseous K_2SO_4, and gaseous KOH coexisted, with gaseous K_2SO_4 being the dominant species. At temperatures 1200−1800 °C, gaseous KOH became the major K-species. The mass distribution of the solid samples collected from K_2SO_4 vaporization experiments is illustrated in Figure 1C. It shows that more than 99% of the solid samples were collected from the filter above 1100 °C. However, the filter fraction is obviously lower at 800 and 900 °C, as 91% and 95% respectively, indicating a lower degree of K_2SO_4 vaporization. The XRD analysis of the solid product samples shows that only K_2SO_4 was present, although a decomposition of K_2SO_4 forming KOH and SO_3/SO_2 was predicted by the equilibrium calculations. This is probably because K_2SO_4 was reformed rapidly during the cooling down process. This can also explain the fact that no SO_2 was detected in the flue gas during the K_2SO_4 vaporization experiments.

3.2. K_2CO_3 Capture by Kaolin. *Equilibrium Calculation.* The equilibrium calculation results of K_2CO_3 capture by kaolin at 50−1000 ppmv of K (25−500 ppmv of K_2CO_3) in flue gas showed that the K-capture behavior of K_2CO_3 was the same as that of KOH.[58] Detailed results can be found in appendix II of the Supporting Information. This is because at high temperatures K_2CO_3 decomposed, forming KOH and CO_2, and then the formed KOH reacted with kaolin.

Impact of Potassium Concentration. The experimental results of K_2CO_3 capture by kaolin at different K-concentrations at 1100 °C are compared with the equilibrium calculation results in Figure 2. The experimental C_K and X_K generally followed the equilibrium predictions. The C_K increased from 0.019 to 0.216 g K/(g additive) when the K_2CO_3 concentration increased from 25

Table 3. Results of Equilibrium Calculations of KCl-Capture by Kaolin

input conditions	temp/°C	K-species appearing	% Al-con.	% Si-con.	% K-con.	K-capture/(g K/g additive)
50 ppmv KCl, K/(Al + Si) = 0.048	800	100% $KAlSi_3O_8$	9	24	100	0.023
	900	100% $KAlSi_3O_8$	9	24	100	0.023
	1100	99% $KAlSi_3O_8$ + 1% KCl	9	24	99	0.023
	1300	97% $KAlSi_3O_8$ + 3% KCl	8	23	97	0.022
	1450	92% $KAlSi_3O_8$ + 7% KCl + 1% KOH	8	22	92	0.022
250 ppmv KCl, K/(Al + Si) = 0.240	800	21% $KAlSi_3O_8$ + 79% $KAlSi_2O_6$	50	98	100	0.131
	900	23% $KAlSi_3O_8$ + 77% $KAlSi_2O_6$ + 1% KCl	50	98	99	0.130
	1100	28% $KAlSi_3O_8$ + 70% $KAlSi_2O_6$ + 3% KCl	49	99	97	0.128
	1300	33% $KAlSi_3O_8$ + 60% $KAlSi_2O_6$ + 7% KCl	46	97	93	0.121
	1450	45% $KAlSi_3O_8$ + 41% $KAlSi_2O_6$ + 13% KCl	43	97	87	0.113
500 ppmv KCl, K/(Al + Si) = 0.481	800	33% $KAlSi_2O_6$ + 43% $KAlSiO_4$ + 24% KCl	75	100	76	0.198
	900	54% $KAlSi_2O_6$ + 1% $KAlSiO_4$ + 45% KCl	54	100	55	0.143
	1100	54% $KAlSi_2O_6$ + 46% KCl	54	100	54	0.142
	1300	54% $KAlSi_2O_6$ + 45% KCl	54	100	54	0.142
	1450	54% $KAlSi_2O_6$ + 45% KCl + 1% KOH	54	100	54	0.142
750 ppmv KCl, K/(Al + Si) = 0.721	800	10% $KAlSi_2O_6$ + 56% $KAlSiO_4$ + 35% KCl	98	100	65	0.256
	900	22% $KAlSi_2O_6$ + 32% $KAlSiO_4$ + 47% KCl	80	100	53	0.209
	1100	38% $KAlSi_2O_6$ + 62% KCl	56	100	38	0.147
	1300	37% $KAlSi_2O_6$ + 62% KCl	56	100	37	0.147
	1450	37% $KAlSi_2O_6$ + 61% KCl + 1% KOH	56	100	37	0.147
1000 ppmv KCl, K/(Al + Si) = 0.961	800	4% $KAlSi_2O_6$ + 47% $KAlSiO_4$ + 49% KCl	100	100	50	0.263
	900	6% $KAlSi_2O_6$ + 42% $KAlSiO_4$ + 52% KCl	95	100	48	0.251
	1100	27% $KAlSi_2O_6$ + 73% KCl	54	100	27	0.142
	1300	27% $KAlSi_2O_6$ + 72% KCl + 1% KOH	54	100	27	0.142
	1450	27% $KAlSi_2O_6$ + 71% KCl + 1% KOH	54	100	27	0.142

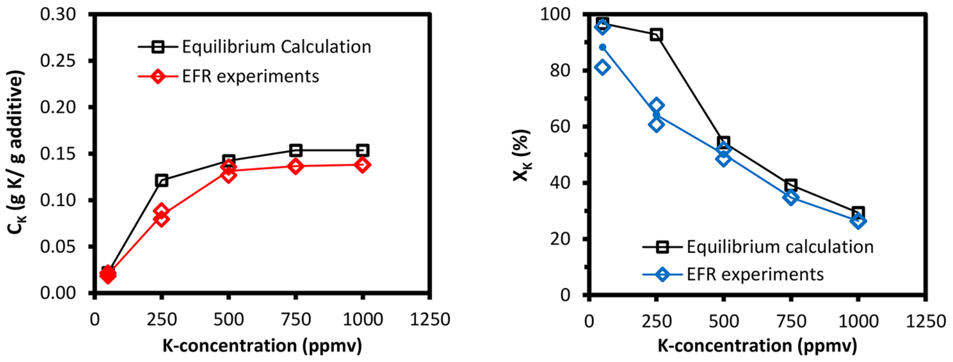

(A) K-capture level (C_K) (B) K-conversion (X_K)

Figure 4. K-capture level (C_K) and K-conversion (X_K) of KCl capture by kaolin at 50−1000 ppmv KCl, the corresponding molar K/(Al + Si) ratio varied from 0.048 to 0.961, reaction temperature was 1300 °C. Gas residence time at 1300 °C was 1.0 s, and others were 1.2 s. Equilibrium calculation results are included for comparison.

to 250 ppmv (molar ratio of K/(Al + Si) in reactants changed from 0.048 to 0.481), with X_K staying almost constant, at around 82.0%. When the concentration of K_2CO_3 increased further to 375 ppmv (K/(Al + Si) = 0.721) and 500 ppmv (K/(Al + Si) = 0.961), C_K did not increase compared to that at 250 ppmv K_2CO_3. At the same time, X_K decreased from 80.6% to 40.8%, indicating that more K_2CO_3 stayed unreacted with kaolin. This is probably because, as indicated by the equilibrium calculation, a complete conversion of kaolin to K-aluminosilicate has taken place, at 250 ppmv K_2CO_3. Thereby, the increased K_2CO_3 was not captured by kaolin forming K-aluminosilicates at 375 and 500 ppmv K_2CO_3.

Impact of Reaction Temperature. The influence of reaction temperature on the K_2CO_3-capture reaction by kaolin was investigated experimentally at 800−1450 °C. The K_2CO_3 concentration was kept constant at 250 ppmv (500 ppmv K in flue gas), with a gas residence time of 1.2 s. The experimental C_K and X_K are compared with the equilibrium calculation results in Figure 3. It is seen that C_K increased from 0.159 to 0.231 g K/(g additive) by 31.1%, when the reaction temperature increased from 800 to 1300 °C. Simultaneously, X_K increased from 59.3% to 86.1%. Whereas, when the reaction temperature increased further to 1450 °C, the C_K and X_K decreased slightly to 0.204 g of K/(g of additive) and 66.1%, respectively. This is likely due to the

DOI: 10.1021/acs.energyfuels.7b04055
Energy Fuels 2018, 32, 3566−3578

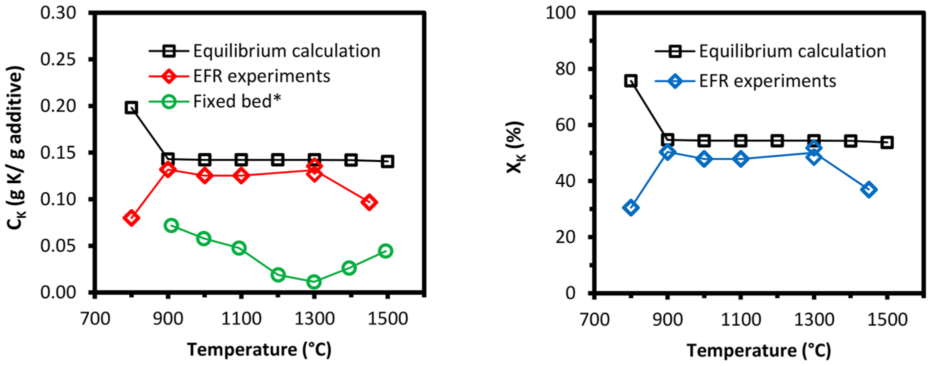

(A) C_K at 500 ppmv KCl (B) X_K at 500 ppmv KCl

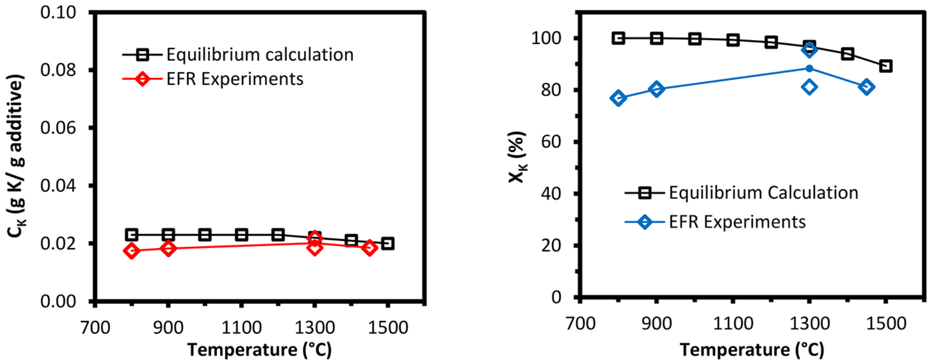

(C) C_K at 50 ppmv KCl (D) X_K at 50 ppmv KCl

Figure 5. C_K (K-capture level) and X_K (K-conversion) of KCl capture by kaolin at different temperatures (800−1450 °C). KCl-concentration was 500 ppmv in (A) and (B), and it was 50 ppmv in (C) and (D). The gas residence time at 1300 °C was 1.0 s, others were 1.2 s. (∗) Fixed bed data (1100 °C, 1000 ppmv KCl, residence time was 1 h) is calculated from the literature.[50]

change of reaction products. Equilibrium calculation suggests a decreased formation of kaliophilite ($KAlSiO_4$) and an increased formation of leucite ($KAlSi_2O_6$) at 1450 °C. However, leucite was not detected by XRD in the 1450 °C sample, probably because some amorphous K-species with K:Al:Si = 1:1:2 was formed. Considering the results on KOH-capture by kaolin in our previous study,[58] 900−1300 °C is a preferable temperature window for KOH and K_2CO_3 capture by kaolin.

3.3. KCl Capture by Kaolin.

Equilibrium Calculation. The results of equilibrium calculations of KCl capture by kaolin at different temperatures and KCl-concentrations were summarized in Table 3. Detailed results of the equilibrium calculation are available in Appendix III of the Supporting Information. The type of the K-aluminosilicate products formed varied with the molar K/(Al + Si) ratio in the reactants. As shown in Table 3, with a molar ratio of K/(Al + Si) = 0.048 (50 ppmv KCl), the main K-aluminosilicate product was sanidine ($KAlSi_3O_8$) with a molar K:Al:Si ratio of 1:1:3. As the molar K/(Al + Si) ratio in reactants increased to 0.240 (250 ppmv KCl), leucite ($KAlSi_2O_6$) with a molar K:Al:Si ratio of 1:1:2, became the dominant K-aluminosilicate with some sanidine ($KAlSi_3O_8$) coexisting. When the molar ratio of K/(Al + Si) in reactants increased to 0.481 or higher (≥500 ppmv KCl), kaliophilite ($KAlSiO_4$) with a molar K:Al:Si ratio of 1:1:1 was predicted at the lower temperature range (800−900 °C), while at high temperatures (1100−1450 °C), leucite ($KAlSi_2O_6$) remained the dominant K-aluminosilicate.

Impact of Potassium Concentration. The impact of KCl concentration on the KCl-capture reaction by kaolin was investigated by EFR experiments using 50−1000 ppmv KCl and a reactor temperature of 1300 °C. The experimental C_K and X_K are compared with the equilibrium calculation results in Figure 4. The trend of the experimental C_K and X_K generally followed the equilibrium calculation data at 1300 °C. The C_K increased significantly from 0.020 g K/(g additive) to 0.131 g K/(g additive), when the KCl-concentration increased from 50 to 500 ppmv (K/(Al + Si) increased from 0.048 to 0.481 correspondingly). However, when the KCl-concentration increased further to 750 ppmv and 1000 ppmv (with a K/(Al + Si) molar ratio of 0.721 and 0.961, respectively), C_K did not increase. On the other hand, X_K decreased significantly from 90.1% to about 25.3% when the KCl-concentration increased from 50 ppmv to 1000 ppmv. This is probably because all the free Si has been consumed forming K-aluminosilicate at 500 ppmv KCl, with no Si available for further KCl capture. According to the equilibrium calculation, the main product of the KCl-kaolin reaction is leucite ($KAlSi_2O_6$), and the K-capture level is limited by the availability of Si. The formation of leucite was confirmed by the XRD analysis results, see Figure 6.

Impact of Reaction Temperature. To investigate the influence of reaction temperature on the KCl-capture reaction, experiments were conducted at temperatures from 800 to 1450 °C. In all experiments, the KCl concentration in flue gas was 500 ppmv, corresponding to a molar K/(Al + Si) ratio of 0.481 in reactants. The gas residence time was 1.2 s. The experimental results are compared to the equilibrium calculation results in Figure 5.

As shown in parts a and b of Figure 5, at 500 ppmv KCl, the K-capture level (C_K) was close to the equilibrium prediction and stayed steady at about 0.142 g of K/(g of additive) at temperatures from 900 to 1300 °C. The K-conversion (X_K) was also steady at about 55.0%. The C_K and X_K of KCl were lower

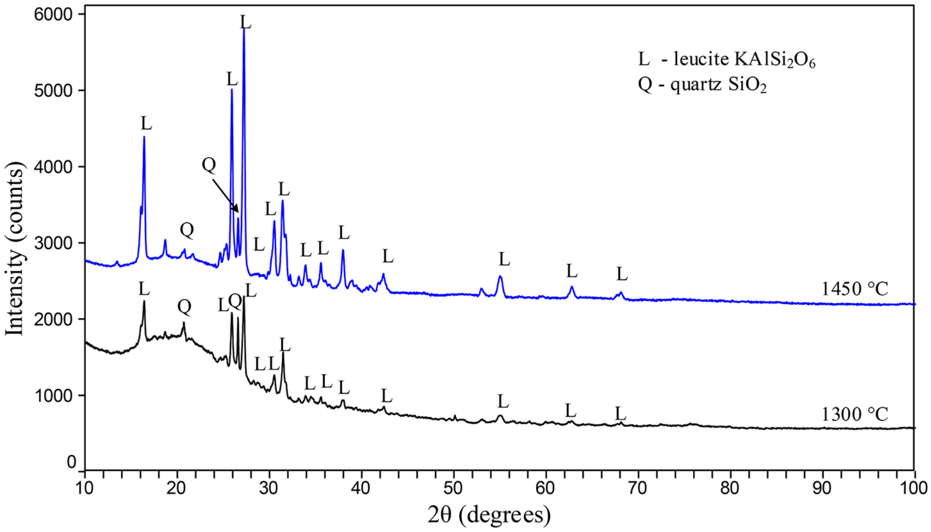

Figure 6. XRD spectra of water-washed KCl-reacted kaolin samples at 1300 and 1450 °C, KCl concentration in flue gas was 500 ppmv, molar K/(Al + Si) ratio in reactants was 0.481, gas residence time was 1.0 and 1.2 s at 1300 and 1450 °C, respectively.

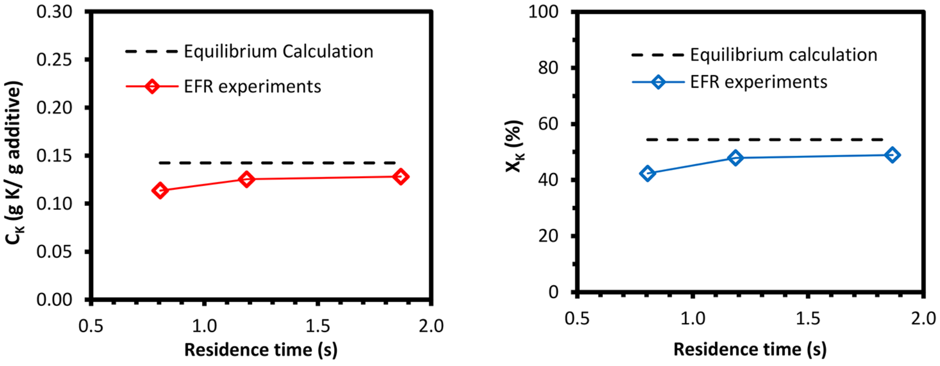

(A) K-capture level C_K at 1100 °C

(B) K-conversion X_K at 1100 °C

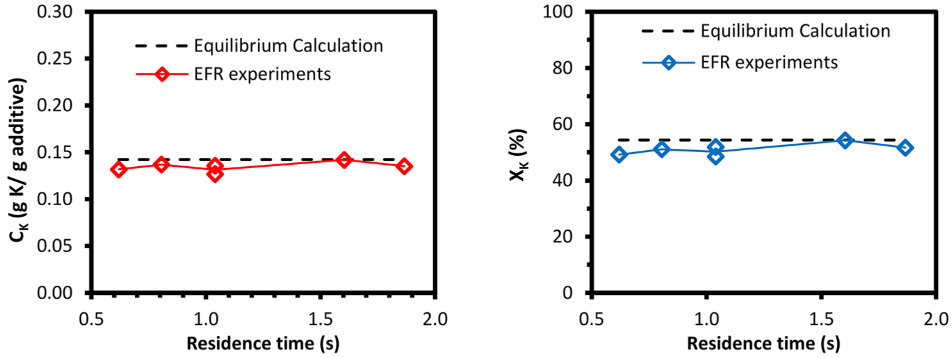

(C) K-capture level (C_K) at 1300 °C

(D) K-conversion (X_K) at 1300 °C

Figure 7. K-capture level (C_K) and K-conversion (X_K) of KCl capture by kaolin at different residence time. KCl concentration in flue gas was 500 ppmv, (molar K/(Al + Si) ratio in reactants was 0.481). Reaction temperatures were 1100 and 1300 °C.

than that of KOH capture by kaolin (C_K of KOH was 0.193–0.241 g of K/(g of additive), and X_K was 72.1–90.0%). This could be explained that kaliophilite ($KAlSiO_4$) was detected by XRD in the KOH-reacted kaolin, while leucite ($KAlSi_2O_6$) was detected in the KCl-reacted kaolin (Figure 6). The formation of leucite consumed more Si than kaliophilite.

At 800 and 1450 °C, C_K was obviously lower than that at 900–1300 °C. At 800 °C, the reaction is probably kinetically controlled and do not reach the equilibrium state. Additionally, the incomplete vaporization of KCl at 800 °C, may also contribute to the low KCl conversion. At 1450 °C, the decrease of C_K may be due to an increased transformation of kaolin into mullite and amorphous silica,[39] which are less reactive toward KCl.[50] XRD analysis of calcinated kaolin samples in the EFR showed that the mullite formation became significant only above 1450 °C.

Table 4. Equilibrium Calculation Results of K_2SO_4 Capture by Kaolin

input conditions	temp/°C	K-species appearing	% Al-con.	% Si-con.	% K-con.	K-capture/ (g K/g additive)
25 ppmv K_2SO_4, K/(Al + Si) = 0.048	800	100% $KAlSi_3O_8$	10	28	100	0.027
	900	100% $KAlSi_3O_8$	10	28	100	0.027
	1100	100% $KAlSi_3O_8$	10	28	100	0.027
	1300	100% $KAlSi_3O_8$	10	28	100	0.027
	1450	99% $KAlSi_3O_8$ + 1% KOH	10	28	99	0.026
125 ppmv K_2SO_4, K/(Al + Si) = 0.240	800	92% $KAlSi_2O_6$ + 8% $KAlSi_3O_8$	51	98	100	0.134
	900	92% $KAlSi_2O_6$ + 8% $KAlSi_3O_8$	51	98	100	0.134
	1100	93% $KAlSi_2O_6$ + 7% $KAlSi_3O_8$	51	97	100	0.134
	1300	93% $KAlSi_2O_6$ + 7% $KAlSi_3O_8$	51	96	100	0.134
	1450	94% $KAlSi_2O_6$ + 5% $KAlSi_3O_8$	51	96	100	0.133
250 ppmv K_2SO_4, K/(Al + Si) = 0.481	800	53% $KAlSi_2O_6$ + 47% K_2SO_4	54	100	53	0.142
	900	53% $KAlSi_2O_6$ + 47% K_2SO_4	54	100	53	0.142
	1100	7% $KAlSi_2O_6$ + 90% % $KAlSiO_4$ + 1% KOH	100	99	98	0.262
	1300	13% $KAlSi_2O_6$ + 80% % $KAlSiO_4$ + 6% KOH	95	100	93	0.250
	1450	31% $KAlSi_2O_6$ + 44% % $KAlSiO_4$ + 24% KOH	76	100	75	0.201
375 ppmv K_2SO_4, K/(Al + Si) = 0.721	800	35% $KAlSi_2O_6$ + 65% K_2SO_4	54	99	35	0.141
	900	35% $KAlSi_2O_6$ + 65% K_2SO_4	54	100	35	0.142
	1100	5% $KAlSi_2O_6$ + 61% % $KAlSiO_4$ + 33% K_2SO_4 + 2% KOH	100	100	65	0.263
	1300	5% $KAlSi_2O_6$ + 61% % $KAlSiO_4$ + 5% K_2SO_4 + 29% KOH	100	100	65	0.263
	1450	5% $KAlSi_2O_6$ + 61% % $KAlSiO_4$ + 34% KOH	100	100	65	0.263
500 ppmv K_2SO_4, K/(Al + Si) = 0.961	800	26% $KAlSi_2O_6$ + 74% K_2SO_4	54	100	26	0.141
	900	26% $KAlSi_2O_6$ + 74% K_2SO_4	54	100	26	0.142
	1100	4% $KAlSi_2O_6$ + 45% % $KAlSiO_4$ + 50% K_2SO_4 + 1% KOH	100	100	49	0.263
	1300	4% $KAlSi_2O_6$ + 45% % $KAlSiO_4$ + 14% K_2SO_4 + 36% KOH	100	100	49	0.263
	1450	4% $KAlSi_2O_6$ + 45% % $KAlSiO_4$ + 1% K_2SO_4 + 49% KOH	100	100	49	0.263

As shown in Figure 5A, C_K was also compared with the results from a study using a fixed bed reactor where cylindrical kaolin pellets of diameter of 1.5 mm was utilized for KCl capture.[50] The C_K values obtained in the fixed bed reactor are obviously lower than that in the EFR experiments, although the reaction time in the fixed bed reactor (about 1 h) was much longer than that in the EFR (about 1 s). One possible reason is that in the fixed bed reactor it was actually mullite that reacted with KCl due to a long residence time of up to 1 h. Another possible reason is that kaolin was in the shape of pellets of 1.5 mm, where the reaction was strong controlled by internal diffusion. Another difference is that the results from fixed bed reactor have an opposite temperature-dependence trend comparing to that of the EFR. This is presumably because the controlling mechanisms in the two reactors are different. In the fixed bed experiments, the reaction was controlled by diffusion as mentioned above. Thus, C_K decreased from 900 to 1300 °C, due to the increased sintering degree of kaolin pellets. However, C_K increased again when temperature was further increased to 1400 and 1500 °C, due to the enhanced inner diffusion caused by melting of kaolin pellets.[50] However, in the EFR, the reaction was mainly equilibrium controlled at 900−1300 °C. In summary, the favorable temperature window for KCl-capture by kaolin is 900−1300 °C.

Figure 5 C and D shows that at 50 ppmv KCl, the experimental X_K and C_K were almost constant, and they generally followed the equilibrium predictions. The C_K was about 0.021 g of K/(g of additive) with about 80.2% KCl captured by kaolin forming water-insoluble K-aluminosilicate.

The XRD spectra of water-washed KCl-reacted kaolin samples at 1300 and 1450 °C are compared in Figure 6. The results show that leucite ($KAlSi_2O_6$) was formed by the KCl−kaolin reaction at 1300 and 1450 °C. At 1450 °C, peaks of leucite are much stronger than that at 1300 °C. However, the ICP-OES analysis results showed than more leucite was formed at 1300 °C than experiments at 1450 °C. This indicates that a large amount of amorphous K-aluminosilicate was present in the 1300 °C product, and the leucite formed at 1450 °C was much more crystalline.

Impact of Gas Residence Time. The impact of residence time on the KCl-capture reaction was studied at 1100 and 1300 °C. The KCl concentration in the flue gas was kept constant at 500 ppmv, with K/(Al + Si) = 0.481. The C_K and X_K results are shown in Figure 7.

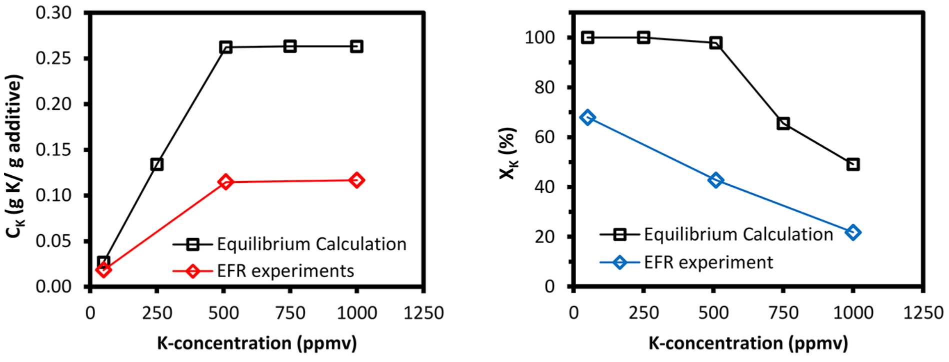

(A) K-capture level (C_K) (B) K-conversion (X_K)

Figure 8. C_K (K-capture level) and X_K (K-conversion) of K_2SO_4 capture by kaolin at 25−500 ppmv K_2SO_4 (50−1000 ppmv K) in flue gas (molar ratio of K/(Al + Si) in reactants varied from 0.048 to 0.961). Reaction temperature was 1100 °C. Gas residence time was 1.2 s. Equilibrium calculation results were included for comparison.

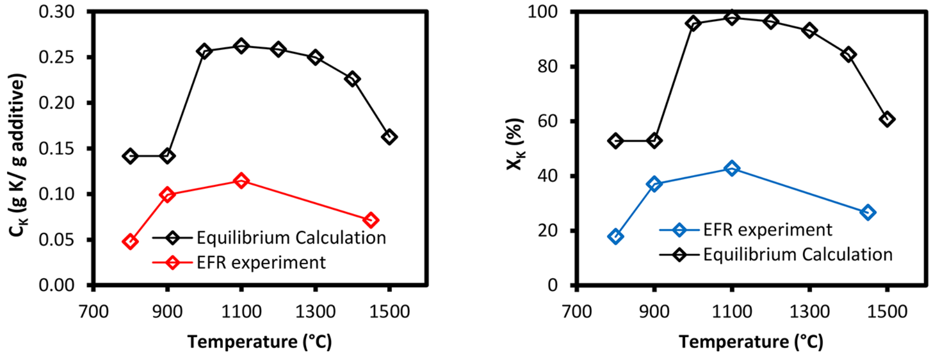

(A) K-capture level (C_K) (B) K-conversion (X_K)

Figure 9. K-capture level (C_K) and K-conversion (X_K) of K_2SO_4 capture by kaolin at 800−1450 °C. K_2SO_4 concentration was 250 ppmv (500 ppmv K). Residence time was 1.2 s. Equilibrium calculation results are included for comparison.

The results in Figure 7 A and B show that at 1100 °C when the gas residence time increased from 0.8 to 1.2 s, the C_K increased from 0.114 g of K/(g of additive) to 0.128 g of K/(g of additive) by 12.3%. The X_K (K-conversion) increased from 42.4% to 49.0%. This indicates that at 1100 °C, the K-capture at residence time below 1.2 s is to some degree limited by kinetics or diffusion.

The results at 1300 °C show that the value of C_K and X_K did not change when the residence time increased from 0.6 to 1.9 s and the number was close to the equilibrium prediction, implying that the KCl-capture reaction was at equilibrium. The results imply that at 1300 °C, with kaolin particles of D_{50} = 5.47 μm, it took very short time (≤0.6 s) for the KCl-capture reaction to reach equilibrium.

3.4. K_2SO_4 Capture by Kaolin.

Equilibrium Calculation. The equilibrium calculation results of K_2SO_4 capture by kaolin at 25−500 ppmv K_2SO_4 (K-concentration was 50 ppmv to 1000 ppmv) are summarized in Table 4. Detailed results of the equilibrium calculation are available in Appendix IV of the Supporting Information. The type and amount of K-aluminosilicate formed changed with the K_2SO_4 concentration in flue gas (molar ratio of K/(Al + Si) in reactants). At 25 ppmv K_2SO_4 (molar ratio of K/(Al + Si) = 0.048), sanidine ($KAlSi_3O_8$) is predicted to be the main K-aluminosilicate product, with K:Al:Si = 1:1:3. At 125 ppmv K_2SO_4 (molar ratio of K/(Al + Si) = 0.240), leucite ($KAlSi_2O_6$) became the main K-aluminosilicate product, with sanidine ($KAlSi_3O_8$) coexisting. At 250, 375, and 500 ppmv K_2SO_4, (molar ratio of K/(Al + Si) ≥ 0.481), kaliophilite ($KAlSiO_4$) turned to be the main K-aluminosilicate product.

Impact of Potassium Concentration. The experimental K-capture level (C_K) and K-conversion (X_K) at 25−500 ppmv K_2SO_4 (50−1000 ppmv K) were compared with the equilibrium calculation results in Figure 8. Generally, the experimental C_K and X_K were obviously lower than the equilibrium data, although they followed a similar trend. The experimental C_K increased from 0.018 to 0.115 g of K/(g of additive), when the K_2SO_4-concentration in flue gas increased from 25 to 250 ppmv. At the same time, the experimental X_K decreased from 68.0% to 42.7% correspondingly. As K_2SO_4-concentration increased further to 500 ppmv (K/(Al + Si) = 0.961), the C_K did not increase, while X_K decreased significantly to 21.7%.

Impact of Reaction Temperature. The experimental C_K and X_K of K_2SO_4-capture by kaolin at different reaction temperatures from 800 to 1450 °C are compared with the equilibrium predictions in Figure 9. The results show that the experimental data did not follow the equilibrium predicted trend, and the experimental C_K and X_K were obviously lower than the equilibrium values. The experimental C_K and X_K increased significantly when the reaction temperature increased from 800 to 1100 °C. However, when the reaction temperature increased further to 1450 °C, the experimental C_K and X_K decreased slightly. This is because at temperatures below 1100 °C, the reaction was kinetically controlled, and the incomplete vaporization of K_2SO_4 at low temperatures also inhibited the

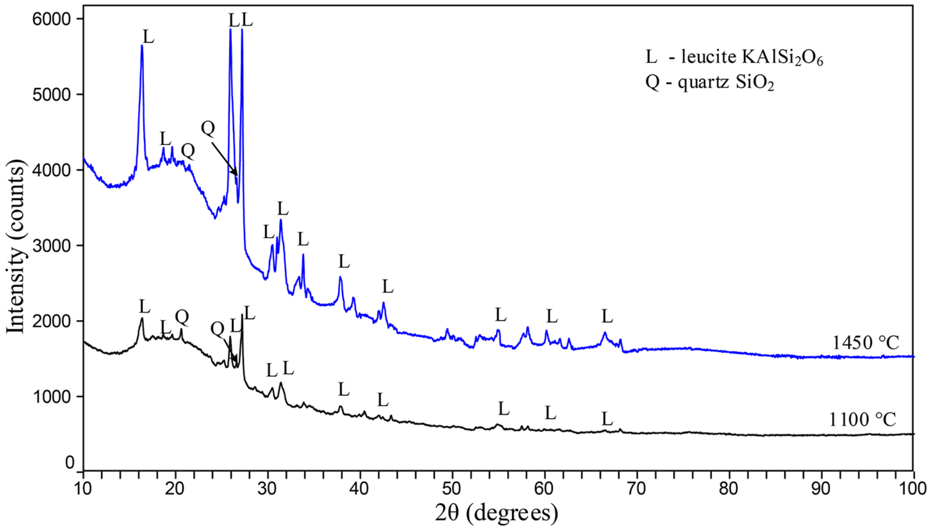

Figure 10. XRD spectra of water-washed K_2SO_4-reacted kaolin at 1100 and 1450 °C. K_2SO_4 concentration was 250 ppmv (500 ppmv K) in flue gas. Molar K/(Al + Si) ratio in reactants was 0.481. Gas residence time was 1.2 s.

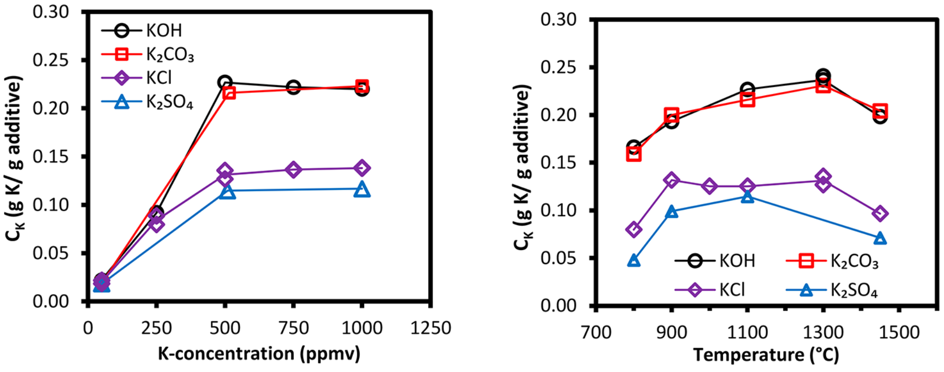

(A) C_K at different K-concentrations

(B) C_K at different temperatures

Figure 11. Comparison of KOH, K_2CO_3, KCl, and K_2SO_4 capture by kaolin at different K-concentrations and temperatures. In part A, KOH, K_2CO_3, and K_2SO_4 experiments were at 1100 °C, and KCl experiments were at 1300 °C. In part B, the K-concentration was 500 ppmv for all experiments.

conversion of K_2SO_4. At 1450 °C, the transformation of kaolin into mullite became significant, and the formed mullite is less reactive toward K_2SO_4.[50,61] In summary, K_2SO_4 may be capture by kaolin most effectively at 900−1300 °C.

It is remarkable that the experimental C_K and X_K of K_2SO_4 are so much lower than the equilibrium predictions. But interestingly they were reasonably similar to the levels found for KCl, although the equilibrium predicted C_K and X_K for K_2SO_4 is considerably higher than that of KCl.

Kaliophilite ($KAlSiO_4$) was predicted as the main K-aluminosilicate product at 1100 °C and 500 ppmv K (250 ppmv K_2SO_4) for K_2SO_4-capture reaction by kaolin. However, the XRD analysis results show that leucite ($KAlSi_2O_6$) was detected instead of kaliophilite ($KAlSiO_4$), see Figure 10. Thereby the equilibrium product of K_2SO_4 capture by kaolin was wrongly predicted and the reaction product of K_2SO_4 capture by kaolin was the same as KCl.

3.5. Comparison of Different K-Species.

The experimental results of using different K-species, including KOH, K_2CO_3, KCl and K_2SO_4, to react with kaolin at different K-concentration and different temperatures are compared in Figure 11. In Figure 11A, the experiments of KOH, K_2CO_3, and K_2SO_4 were all conducted at 1100 °C, while the KCl experiments were conducted at 1300 °C. However, the EFR experimental results (shown in Figure 5A) indicate that KCl-capture by kaolin behaved similarly at 1100 and 1300 °C, so the results are still comparable.

The results show that KCl and K_2SO_4 were captured in a similar way, while KOH and K_2CO_3 behaved similarly. This is probably because the reaction between K_2CO_3 and kaolin took place according to reaction R3, R4, and R5. K_2CO_3 first decomposed into KOH and CO_2, and then the formed KOH reacted with kaolin forming K-aluminosilicate. The decomposition of K_2CO_3 has been observed in the K_2CO_3 vaporization and transformation experiments, which has been discussed in section 3.1.

$$K_2CO_3 + H_2O \rightarrow 2KOH + CO_2\ (g) \quad \text{(R3)}$$

$$Al_2O_3{\cdot}2SiO_2 + 2KOH \rightarrow 2KAlSiO_4\ (\text{kaliophilite}) + 2H_2O \quad \text{(R4)}$$

$$Al_2O_3{\cdot}2SiO_2 + 2SiO_2 + 2KOH \rightarrow 2KAlSi_2O_6\ (\text{leucite}) + 2H_2O \quad \text{(R5)}$$

Another important result is that at 500 ppmv K in flue gas and above, KCl and K_2SO_4 are captured by kaolin less effectively compared to KOH or K_2CO_3. Although the equilibrium calculation predicted a similar K-capture level for K_2SO_4 and K_2CO_3 capture by kaolin at temperatures above 1100 °C. One reason is that at 500 ppmv K and above, kaliophilite ($KAlSiO_4$) was formed as product from KOH and K_2CO_3 capture reaction, while leucite ($KAlSi_2O_6$) existed as the main K-aluminosilicate product from KCl and K_2SO_4 capture experiments, which has been confirmed by the XRD analysis. More Si was consumed in the KCl and K_2SO_4 capture reaction due to the formation of leucite ($KAlSi_2O_6$). Another reason is that the presence of HCl and SO_2 in KCl and K_2SO_4 capture reactions inhibited the K-capture reaction by kaolin, similar phenomena was observed in a previous sodium capture study.[51] The results indicate that more Al−Si based additive shall be used in boilers if Cl-rich fuels are fired and all K shall be converted to K-aluminosilicate. Additionally, an Al−Si additive with a relatively higher content of Si (like Si-rich coal fly ash) seems more suitable for K-capture when burning Cl-rich biomass fuels.

The results also show that kaolin captured KCl slightly more effectively than K_2SO_4. This may be good news for the situation of cofiring straw and coal where KCl and K_2SO_4 both exist, since Al and Si from the cofired coal can destroy the corrosive KCl more effectively, and the less corrosive K_2SO_4 is captured at a lower level.

4. CONCLUSIONS

A thorough understanding of the K-capture reaction by kaolin under suspension-firing conditions is wanted to mitigate alkali-related problems in biomass combustion boilers. The reaction of KOH, K_2CO_3, KCl, and K_2SO_4 capture by kaolin was studied by entrained flow reactor experiments and equilibrium calculations. The influence of molar ratio of K/(Al + Si) in reactants, K-concentration in flue gas, reaction temperature, K-species type, and residence time on the K-capture reaction was investigated.

The experimental results of using different K-concentrations show that for KCl at 1300 °C, and for KOH, K_2CO_3, and K_2SO_4 at 1100 °C, the K-capture level (C_K) increased when the K-concentration increased from 50 to 500 ppmv (molar ratio K/(Al + Si) increased from 0.048 to 0.481). But it did not increase, when the K-concentration increased further to 750 and 1000 ppmv (molar ratio of K/(Al + Si) in reactants was 0.721 and 0.961), probably because all active compound in kaolin had already been converted forming K-aluminosilicates.

For KCl, KOH and K_2CO_3, C_K and X_K generally followed the equilibrium predictions at temperatures above 1100 °C, when applying a kaolin particle size of $D_{50} = 5.47\ \mu m$ and a residence time of 1.2 s. However, at lower temperatures (800 and 900 °C), the reactions were probably kinetically controlled, and the measured K-capture level was lower than the equilibrium predictions. For K_2SO_4, the measured C_K was significantly lower than the equilibrium predictions even at temperatures above 1100 °C. This is most likely because kaliophilite ($KAlSiO_4$) was predicted by the equilibrium calculations, but XRD analysis revealed that leucite ($KAlSi_2O_6$) was formed from the reaction. The KCl-capture experiments conducted with different residence times show that, at 1100 °C, the K-capture level increased slightly with residence time, indicating a kinetically limited reaction at this temperature. However, at 1300 °C, C_K reached the equilibrium level at a residence time as short as 0.6 s.

Experiments using different K-species show that, K_2CO_3 behaved the same as KOH in terms of being captured by kaolin at suspension fired conditions. KCl and K_2SO_4 behaved similarly, but they were captured less effectively than KOH and K_2CO_3. The study indicates that the main product of the KCl and K_2SO_4 reactions with kaolin when excess potassium is available are $KAlSi_2O_6$ (leucite) while $KAlSiO_4$ (kaliophilite) is mainly formed when KOH and K_2CO_3 reacted with kaolin with excess potassium available. The maximum obtainable K-capture level (C_K) for KCl and K_2SO_4 was approximately 0.12 g K/g kaolin while for KOH and K_2CO_3 a maximum capture level of approximately 0.24 g of K/g kaolin could be obtained. The results imply that more kaolin shall be used in boilers if Cl-rich fuels are fired and all K shall be converted to K-aluminosilicate. In addition, an Al−Si additive with a relatively higher content of Si (like Si-rich coal fly ash) may be more effective for K-capture when burning Cl-rich biomass fuels.

■ ASSOCIATED CONTENT

Supporting Information

The Supporting Information is available free of charge on the ACS Publications website at DOI: 10.1021/acs.energy-fuels.7b04055.

> Appendix I, detailed experimental conditions of the EFR experiments; appendix II, complete results of the equilibrium calculations of K_2CO_3 capture by kaolin; appendix III, complete results of the equilibrium calculations of KCl capture by kaolin; appendix IV, complete results of the equilibrium calculations of K_2SO_4 capture by kaolin. (PDF)

■ AUTHOR INFORMATION

Corresponding Author

*(G.W.) E-mail: guow@kt.dtu.dk.

ORCID

Guoliang Wang: 0000-0002-9663-5160

Hao Wu: 0000-0003-0462-2491

Peter Glarborg: 0000-0002-6856-852X

Notes

The authors declare no competing financial interest.

■ ACKNOWLEDGMENTS

This work is part of the project “Flexible use of biomass on PF fired power plants” funded by Energinet.dk through the ForskEL programme, Ørsted Bioenergy & Thermal Power A/S, and DTU.

■ REFERENCES

(1) The Danish Government. Our Future Energy: Denmark, 2011.

(2) Wu, H.; Glarborg, P.; Frandsen, F. J.; Dam-Johansen, K.; Jensen, P. A. *Energy Fuels* **2011**, *25*, 2862−2873.

(3) Frandsen, F. J. *Fuel* **2005**, *84*, 1277−1294.

(4) Sander, B. *Biomass Bioenergy* **1997**, *12*, 177−183.

(5) Gao, X.; Yani, S.; Wu, H. *Energy Fuels* **2015**, *29*, 5171−5175.

(6) Hansen, S. B.; Jensen, P. A.; Frandsen, F. J.; Wu, H.; Bashir, M. S.; Wadenbäck, J.; Sander, B.; Glarborg, P. *Energy Fuels* **2014**, *28*, 3539−3555.

(7) Bashir, M. S.; Jensen, P. A.; Frandsen, F. J.; Wedel, S.; Dam-Johansen, K.; Wadenbäck, J.; Pedersen, S. T. *Energy Fuels* **2012**, *26*, 2317−2330.

(8) Laxminarayan, Y.; Jensen, P. A.; Wu, H.; Frandsen, F. J.; Sander, B.; Glarborg, P. *Energy Fuels* **2017**, *31*, 8733−8741.

(9) Baxter, L. L. *Biomass Bioenergy* **1993**, *4*, 85−102.

(10) Bashir, M. S.; Jensen, P. A.; Frandsen, F. J.; Wedel, S.; Dam-Johansen, K.; Wadenbäck, J. *Energy Fuels* **2012**, *26*, 5241.

(11) Okoro, S. C.; Montgomery, M.; Frandsen, F. J.; Pantleon, K. *Energy Fuels* **2014**, *28*, 6447−6458.

(12) Sandberg, J.; Karlsson, C.; Fdhila, R. B. *Appl. Energy* **2011**, *88*, 99−110.

(13) Kling, Å.; Andersson, C.; Myringer, Å.; Eskilsson, D.; Järås, S. G. *Appl. Catal., B* **2007**, *69*, 240−251.

(14) Zheng, Y.; Jensen, A. D.; Johnsson, J. E.; Thøgersen, J. R. *Appl. Catal., B* **2008**, *83*, 186−194.

(15) Zheng, Y.; Jensen, A. D.; Johnsson, J. E. *Ind. Eng. Chem. Res.* **2004**, *43*, 941−947.

(16) Jensen, P. A.; Frandsen, F. J.; Hansen, J.; Dam-Johansen, K.; Henriksen, N.; Hörlyck, S. *Energy Fuels* **2004**, *18*, 378−384.

(17) Wu, H.; Bashir, M. S.; Jensen, P. A.; Sander, B.; Glarborg, P. *Fuel* **2013**, *113*, 632−643.

(18) Baxter, L. L.; Miles, T. R.; Miles, T. R., Jr.; Jenkins, B. M.; Milne, T.; Dayton, D.; Bryers, R. W.; Oden, L. L. *Fuel Process. Technol.* **1998**, *54*, 47−78.

(19) Sippula, O.; Lind, T.; Jokiniemi, J. *Fuel* **2008**, *87*, 2425−2436.

(20) Wiinikka, H.; Gebart, R.; Boman, C.; Boström, D.; Nordin, A.; Öhman, M. *Combust. Flame* **2006**, *147*, 278−293.

(21) Blomberg, T. *Mater. Corros.* **2006**, *57*, 170−175.

(22) Wang, G.; Shen, L.; Sheng, C. *Energy Fuels* **2012**, *26*, 102−111.

(23) Niu, Y.; Tan, H.; Hui, S. e. *Prog. Energy Combust. Sci.* **2016**, *52*, 1−61.

(24) Glarborg, P.; Marshall, P. *Combust. Flame* **2005**, *141*, 22−39.

(25) Lindberg, D.; Backman, R.; Chartrand, P. *J. Chem. Thermodyn.* **2007**, *39*, 1001−1021.

(26) Nielsen, H. P.; Frandsen, F. J.; Dam-Johansen, K.; Baxter, L. L. *Prog. Energy Combust. Sci.* **2000**, *26*, 283−298.

(27) Frandsen, F. J. *Ash Formation, Deposition and Corrosion When Utilizing Straw for Heat and Power Production*. Doctoral Thesis; Technical University of Denmark: 2011.

(28) Bashir, M. S.; Jensen, P. A.; Frandsen, F.; Wedel, S.; Dam-Johansen, K.; Wadenbäck, J.; Pedersen, S. T. *Fuel Process. Technol.* **2012**, *97*, 93−106.

(29) Skrifvars, B.-J.; Laurén, T.; Hupa, M.; Korbee, R.; Ljung, P. *Fuel* **2004**, *83*, 1371−1379.

(30) Damoe, A. J.; Wu, H.; Frandsen, F. J.; Glarborg, P.; Sander, B. *Energy Fuels* **2014**, *28*, 3217−3223.

(31) Wang, L.; Skjevrak, G.; Hustad, J. E.; Skreiberg, Ø. *Energy Fuels* **2014**, *28*, 208−218.

(32) Punjak, W. A.; Uberoi, M.; Shadman, F. *AIChE J.* **1989**, *35*, 1186−1194.

(33) Xu, L.; Liu, J.; Kang, Y.; Miao, Y.; Ren, W.; Wang, T. *Energy Fuels* **2014**, *28*, 5640−5648.

(34) Liao, Y.; Wu, S.; Chen, T.; Cao, Y.; Ma, X. *Energy Procedia* **2015**, *75*, 124−129.

(35) Ahmaruzzaman, M. *Prog. Energy Combust. Sci.* **2010**, *36*, 327−363.

(36) Punjak, W. A.; Shadman, F. *Energy Fuels* **1988**, *2*, 702−708.

(37) Wang, M. R.; Jia, D. C.; He, P. G.; Zhou, Y. *Mater. Lett.* **2010**, *64*, 2551−2554.

(38) Insley, H.; Ewell, R. H. *J. Res. Natl. Bur. Stand* **1935**, *14*, 615−27.

(39) Tran, K.-Q.; Iisa, K.; Steenari, B.-M.; Lindqvist, O. *Fuel* **2005**, *84*, 169−175.

(40) Tran, K.-Q.; Iisa, K.; Hagström, M.; Steenari, B.-M.; Lindqvist, O.; Pettersson, J. B. C. *Fuel* **2004**, *83*, 807−812.

(41) Tran, Q. K.; Steenari, B.-M.; Iisa, K.; Lindqvist, O. *Energy Fuels* **2004**, *18*, 1870−1876.

(42) Chen, Y.; Wang, G.; Sheng, C. *Energy Fuels* **2014**, *28*, 136−145.

(43) Yao, Z. T.; Ji, X. S.; Sarker, P. K.; Tang, J. H.; Ge, L. Q.; Xia, M. S.; Xi, Y. Q. *Earth-Sci. Rev.* **2015**, *141*, 105−121.

(44) Vassilev, S. V.; Vassileva, C. G. *Fuel* **2007**, *86*, 1490−1512.

(45) Shaheen, S. M.; Hooda, P. S.; Tsadilas, C. D. *J. Environ. Manage.* **2014**, *145*, 249−267.

(46) Blissett, R. S.; Rowson, N. A. *Fuel* **2012**, *97*, 1−23.

(47) Davidsson, K. O.; Steenari, B. M.; Eskilsson, D. *Energy Fuels* **2007**, *21*, 1959−1966.

(48) Bashir, M. S. *Characterization and Quantification of Deposit Build-up and Removal in Straw Suspension-Fired Boilers*; Technical University of Denmark: 2012.

(49) Uberoi, M.; Punjak, W. A.; Shadman, F. *Prog. Energy Combust. Sci.* **1990**, *16*, 205−211.

(50) Zheng, Y.; Jensen, P. A.; Jensen, A. D. *Fuel* **2008**, *87*, 3304−3312.

(51) Mwabe, P. O.; Wendt, J. O. L. Mechanisms governing trace sodium capture by kaolinite in a downflow combustor, In *26th Symposium on Combustion*, Napoli, Italy, 1996.

(52) Punjak, W. A. *High temperature interactions of alkali vapors with solids during coal combusiton and gasification*. Ph.D. Thesis; The University of Arizona: 1988.

(53) Shadman, F.; Punjak, W. A. *Thermochim. Acta* **1988**, *131*, 141−152.

(54) Damoe, A. J.; Jensen, P. A.; Frandsen, F. J.; Wu, H.; Glarborg, P. *Energy Fuels* **2017**, *31*, 555−570.

(55) Wang, L.; Skreiberg, Ø.; Becidan, M. *Appl. Therm. Eng.* **2014**, *70*, 1262−1269.

(56) Steenari, B. M.; Lindqvist, O. *Biomass Bioenergy* **1998**, *14*, 67−76.

(57) Mwabe, P. O. *Mechanisms governing alkali metal capture by kaolinite in a downflow combustor*. Ph.D. Thesis; The University of Arizona: 1993.

(58) Wang, G.; Jensen, P. A.; Wu, H.; Frandsen, F. J.; Sander, B.; Glarborg, P. *Energy Fuels* **2018**, *32*, 1851.

(59) Bale, C. W.; Chartrand, P.; Degterov, S. A.; Eriksson, G.; Hack, K.; Ben Mahfoud, R.; Melançon, J.; Pelton, A. D.; Petersen, S. *CALPHAD: Comput. Coupling Phase Diagrams Thermochem.* **2002**, *26*, 189−228.

(60) Bale, C. W.; Bélisle, E.; Chartrand, P.; Decterov, S. A.; Eriksson, G.; Hack, K.; Jung, I. H.; Kang, Y. B.; Melançon, J.; Pelton, A. D.; Robelin, C.; Petersen, S. *CALPHAD: Comput. Coupling Phase Diagrams Thermochem.* **2009**, *33*, 295−311.

(61) Gale, T. K.; Wendt, J. O. L. *Aerosol Sci. Technol.* **2003**, *37*, 865−876.

July 2019

ForskEL project no. 12150/EUDP 64018-003

Final report: Flexible use of biomass on PF Fired power plants

Appendix F. Journal paper: Wang G., Jensen P.A., Wu H., Laxminarayan, Y., Frandsen F.J., Sander B., Glarborg P. KOH capture by Coal Fly Ash. Fuel 2019, 242, 828 – 836.

1. **Department of Chemical and Biochemical Engineering**
Technical University of Denmark
Søltofts Plads, Building 229, DK-2800, Kgs. Lyngby, Denmark
2. **Ørsted Bioenergy & Thermal power,**
Kraftværksvej 53, DK-7000, Fredericia, Denmark

CHEC no. R1902

Fuel 242 (2019) 828–836

Contents lists available at ScienceDirect

Fuel

journal homepage: www.elsevier.com/locate/fuel

Full Length Article

KOH capture by coal fly ash

Guoliang Wang[a,*], Peter Arendt Jensen[a], Hao Wu[a], Flemming Jappe Frandsen[a], Yashasvi Laxminarayan[a], Bo Sander[b], Peter Glarborg[a]

[a] *Department of Chemical and Biochemical Engineering, Technical University of Denmark, Søltofts Plads, Building 229, DK-2800 Kgs. Lyngby, Denmark*
[b] *Ørsted Bioenergy & Thermal Power A/S, Kraftværksvej 53, 7000 Fredericia, Denmark*

ARTICLE INFO

Keywords:
Coal fly ash
Potassium capture
Biomass combustion
Additive
KOH

ABSTRACT

The KOH-capture reaction by coal fly ash at suspension-fired conditions was studied through entrained flow reactor (EFR) experiments and chemical equilibrium calculations. The influence of KOH-concentration (50–1000 ppmv), reaction temperature (800–1450 °C), and coal fly ash particle size (D_{50} = 6.03–33.70 μm) on the reaction was investigated. The results revealed that, at 50 ppmv KOH (molar ratio of K/(Al + Si) = 0.048 of feed), the measured K-capture level (C_K) of coal fly ash was comparable to the equilibrium prediction, while at 250 ppmv KOH and above, the measured data were lower than chemical equilibrium. Similar to the KOH-kaolin reaction reported in our previous study, leucite ($KAlSi_2O_6$) and kaliophilite ($KAlSiO_4$) were formed from the KOH-coal fly ash reaction. However, coal fly ash captured KOH less effectively compared to kaolin at 250 ppmv KOH and above. Studies at different temperatures showed that, at 800 °C, the KOH-coal fly ash reaction was probably kinetically controlled. At 900–1300 °C it was diffusion limited, while at 1450 °C, it was equilibrium limited to some extent. At 500 ppmv KOH (molar ratio of K/(Al + Si) = 0.481), and a gas residence time of 1.2 s, 0.063 g K/(g additive) and 0.087 g K/(g additive) was captured by coal fly ash (D_{50} = 10.20 μm) at 900 and 1450 °C, respectively. Experiments with coal fly ash of different particle sizes showed that a higher K-capture level were obtained using finer particle sizes, indicating some internal diffusion control of the process.

1. Introduction

Existing coal suspension-fired boilers have been converted to biomass combustion to increase the share of renewable power and district heat production in Denmark [1,2]. Compared to traditional biomass grate-fired power plants, biomass suspension-fired power plants have higher efficiency, and they can compensate for the fluctuations of the wind power production [3]. However, the alkali elements (mainly K) in biomass fuels to a high degree evaporates during combustion in PF (pulverized fuel) boilers [4–7], and are present in the gas phase as KOH, KCl or K_2SO_4 [8–10]. When the flue gas is cooling down, these K-compounds condense and may form sticky deposit on super-heater and reheater tubes, resulting in accelerated deposit formation as well as corrosion. Additionally, K-salt aerosols formed from nucleation and condensation of gaseous K-species can deteriorate the performance of de-NO_x SCR catalyst through physical deposition and chemical poisoning [11–14].

One option to deal with these alkali-induced problems is to inject additives that can react with volatile alkali species to form less problematic compounds with higher melting points. Various additives have been investigated, and they can largely be categorized into four groups: Al-Si based [3,15–18], S-based [19–21], P-based [22] and Ca-based [23], according to the major elements that are present in the additives [3,24]. Among the different additives, coal fly ash was the only one that has been commercially utilized in full-scale suspension-fired boilers due to its low cost and high effectiveness [1,2,25].

Coal fly ash is a solid residue from combustion of coal. Approximately 500 million tons of coal fly ash are produced worldwide each year [26]. Coal fly ash could be an environmental concern if not handled properly [26]. The mineralogical composition of coal fly ash is quite complex, depending on the parental coal and the combustion technology. The dominant mineral phases include quartz, mullite, illite and siderite [27]. The effectiveness of coal fly ash in capturing volatile K-species from biomass has been observed in co-combustion of coal and biomass [28–30].

The K-capture reaction by coal fly ash was studied by Wu and coworkers in a full-scale biomass suspension-fired boiler [1,2]. The impact of injection of coal fly ash in different amounts on the deposition behavior, deposit composition and the formation of aerosols was investigated. With the addition of coal fly ash, the amount of aerosols

---

* Corresponding author.
E-mail address: guow@kt.dtu.dk (G. Wang).

https://doi.org/10.1016/j.fuel.2018.12.088
Received 2 May 2018; Received in revised form 15 December 2018; Accepted 18 December 2018

formed was greatly suppressed, with its composition changed from K-S-Cl rich to Ca-P-Si rich [2]. The composition of the ash deposit is also significantly influenced. The amount of K_2SO_4 in inner layer deposit collected from high-temperature flue gas (1300 °C) was greatly reduced. KCl, KOH, and K_2CO_3 completely disappeared, when adding coal fly ash. The large outer deposit also transferred from K-Ca-Si rich to Si-Al rich, resulting in an easier and more frequent removal of the deposits. In the deposits formed at low-temperature flue gas (800 °C), KCl disappeared, and the content of KOH and K_2CO_3 was significantly decreased. The corrosion risk was considerably decreased consequently. However, because of the complexity of the full-scale system, no quantitative data such as the potassium capture amount of per unit of coal fly ash could be obtained.

Quantitative and detailed study on K-capture reaction by coal fly ash at high-temperature conditions is still rare. To the authors' knowledge, the only two quantitative studies on K-capture by coal fly ash were both conducted in fixed bed reactors, where coal fly ash pellets with a diameter of 1.5 mm or piles of coal ash were utilized [15,31]. However, the residence time of coal fly ash in these fixed bed reactors was in an order of hours, significantly larger than that of biomass suspension-fired boilers, where coal fly ash particles only stay a few seconds in the flue gas [1,2].

The objective of this work is to study quantitatively the K-capture behavior of coal fly ash at well-controlled conditions in suspension, and to understand the influence of reaction conditions. This paper focuses on the KOH capture by coal fly ash. Results on K_2CO_3, KCl and K_2SO_4 capture by coal fly ash will be published in another paper.

2. Experimental

2.1. Materials

A coal fly ash from the unit 2 of Asnæsværket Power Plant (ASV2), Denmark was utilized in this work. The ASV2 coal fly ash was sieved to 0–32 µm and 32–45 µm, named as ASV2CFA0-32 and ASV2CFA32-45, respectively. Additionally, the ASV2CFA0-32 was ground in a ball mill to get a finer coal ash sample, named as ASV2CFAGR. The three ash samples were all analyzed with a Malvern 3000 particle size analyzer. The median diameter (D_{50}) of ASV2CFA0-32, ASV2CFA32-45 and ASV2CFAGR was 10.20 µm, 33.70 µm and 6.03 µm, respectively. The D_{50} of ASV2CFAGR is comparable with that of kaolin (5.47 µm) and mullite (5.90 µm) utilized in our previous studies [32,33]. A sieving analysis showed that ASV2CFA0-32 contributed 63.0 wt% of the ASV2 coal fly ash, while ASV2CFA32-45 made up 14.4 wt%. The three coal fly ashes size fractions were also subjected to ICP-OES analysis, with the results summarized in Table 1. The three ash size fractions had similar composition and were all rich in Al and Si. The molar ratio of (K + Na)/(Al + Si) of the three ash fractions was around 0.02, indicating that there was a large surplus of Al and Si in the ashes which could participate the K-capture reaction. The coal fly ashes was also analyzed with XRD (X-ray Diffraction), and the results showed that mullite ($3Al_2O_3 \cdot 2SiO_2$) and quartz (SiO_2) were the main crystalline phases, with no crystalline alkali or alkali earth species detected. This indicated that the small amounts of Na, K, Ca and Mg detected by ICP-OES were present in amorphous species.

Table 1
Characteristics of the coal fly ashes.

Name	ASV2CFAGR	ASV2CFA0-32	ASV2CFA32-45
particle size (µm)	0–32	0–32	32–45
D_{50} (µm)	D_{50} = 6.03	D_{50} = 10.20	D_{50} = 33.70
BET surface area (m^2/g)	9.07	8.04	3.41
O (wt% dry base)	46.60	46.60	45.06
S (wt% dry base)	0.26	0.26	0.21
P (wt% dry base)	0.64	0.64	0.57
Si (wt% dry base)	22.0	22.0	21.0
Al (wt% dry base)	14.0	14.0	13.0
Fe (wt% dry base)	2.9	2.9	3.0
Ca (wt% dry base)	4.50	4.50	5.2
Mg (wt% dry base)	0.97	0.97	0.88
Na (wt% dry base)	0.27	0.27	0.2
K (wt% dry base)	0.87	0.87	0.67
Ti (wt% dry base)	0.88	0.88	0.74

2.2. Setup

The DTU Entrained Flow Reactor (EFR) (Fig. 1) utilized in this study, can simulate the conditions in suspension-fired boilers. It consists of a gas supply system, a liquid/slurry sample feeding system, a gas preheater, a vertical reactor tube, a bottom chamber and a particle and flue gas sampling system. The vertical reactor tube is 2 m long and the inner diameter is 79 mm. It can be heated up to 1450 °C by 7 electrical heating elements.

Instead of feeding solid KOH powder and coal fly ash directly into the reactor [19], solid KOH and coal fly ashes were mixed with deionized water, to make a homogeneous slurry. The slurry was subsequently fed into the reactor through water-cooled feeding probe, with a feeding rate varying from 3.2 to 6.2 g/min. The slurry was subsequently atomized by a 30 Nl/min primary air. The atomized slurry droplets were mixed with preheated secondary air (40–87 Nl/min) and subsequently vaporized. KOH evaporated and reacted with coal fly ash in the reactor tube. Solid particles and aerosols were collected by a cyclone (with a cut-off diameter of 2.3 µm) and a metal filter (with a pore size of 0.8 µm), respectively. The cyclone and filter were heated to 200 °C to avoid condensation of water vapor. Detailed information on the EFR reactor and the slurry feeding system can be found elsewhere [32,33].

2.3. Experimental matrix

The conditions of the EFR experiments of KOH capture by coal fly ashes are summarized in Table 2. The influence of the KOH-concentration, the molar ratio of K/(Al + Si) in reactants, the reaction temperature and the coal fly ash particle size on the KOH-capture reaction were investigated.

In the experimental series (A) of Table 2, the concentration of coal fly ash in the feeding slurry was kept constant while the feed amount of KOH was varied, to investigate the effect of KOH concentration in flue gas (50–1000 ppmv) and the molar ratio of K/(Al + Si) in reactants (0.048–0.961). In series (B), the temperature in reactor was changed from 800 to 1450 °C. Two different KOH concentrations in the flue gas were studied: 50 ppmv and 500 ppmv. In series (C), the influence of coal fly ash particle size on the K-capture reaction was studied, using ASV2CFAGR (D_{50} = 6.03 µm), ASV2CFA0-32 (D_{50} = 10.20 µm) and ASV2CFA32-45 (D_{50} = 33.70 µm). The results were also compared to data from our previous study on KOH capture by kaolin and mullite [32,33]. The gas residence time in the reactor was kept at 1.2 s in all the experiments.

2.4. Analytical methods

The collected solid samples were subjected to ICP-OES (Inductively Coupled Plasma Atomic Emission Spectroscopy) to quantify the amount of potassium captured by coal fly ash. The concentrations of major elements were determined according to the Danish Standard DS/EN 15290 (Solid Biofuels- Determination of Major Elements). The concentration of water-soluble K and Cl was analyzed according to the standard DS/EN ISO 16995 (Solid Biofuels- Determination of water-soluble Chloride, Sodium and Potassium).

Two parameters were defined to quantify the K-capture degree by coal fly ash: the K-conversion (X_K), and the K-capture level (C_K). X_K is the percentage (%) of input K-compound (KOH) chemically captured by additives (coal fly ash) forming water-insoluble K-aluminosilicate. C_K is

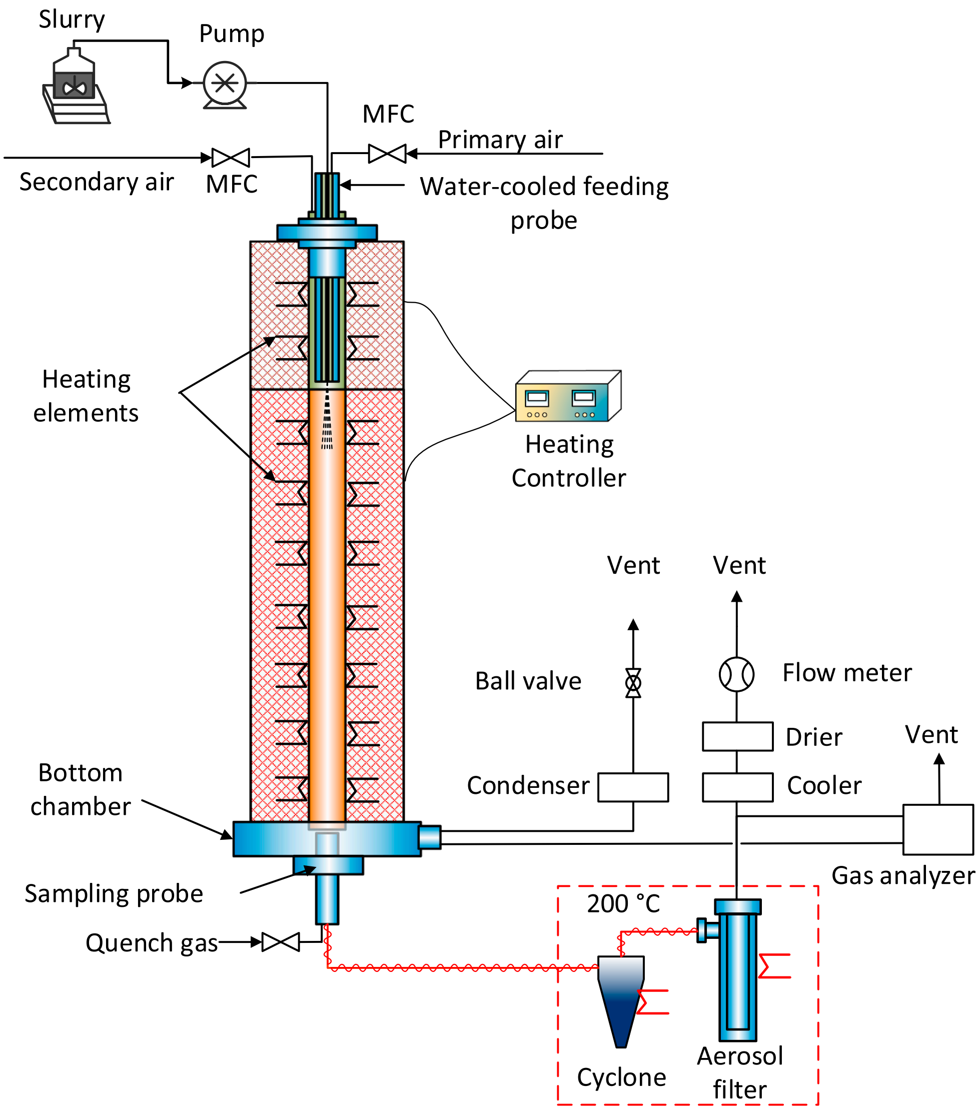

Fig. 1. Schematic of the Entrained Flow Reactor (EFR).

the mass of potassium captured by 1 g of additive (coal fly ash) (g K/g additive). Details of the calculation method can be found in our previous work [32,33].

Additionally, solid products were also analyzed with XRD (X-ray diffraction analysis) to determine the mineralogical composition. Samples collected from the EFR experiments were washed with deionized water at room temperature for 24 h to remove the water-soluble compounds (like unreacted K-salts) and then filtered and dried. The XRD spectra were obtained with a Huber diffractometer, and the main crystalline phases were identified with JADE 6.0 using database of PDF2-2004.

Table 2
Conditions of the experiments in the Entrained Flow Reactor (EFR).

Experimental series	K-species	additives	D_{50} of additives/µm	Temp./°C	Gas residence time/s	K in gas /ppmv	K/(Al + Si)
(A) KOH-capture by CFA (impact of **K-concentration**)	KOH	ASV2CFA0-32	10.20	1300	1.2	50	0.048
						250	0.240
						500	0.481
						750	0.721
						1000	0.961
(B) KOH-capture by CFA (impact of **temperature**)	KOH	ASV2CFA0-32	10.20	800	1.2	50, 500	0.481
				900			
				1100			
				1300			
				1450			
(C) KOH-capture by CFA (impact of **CFA particle size**)	KOH	ASV2CFAGR0-32	6.03	1300	1.2	500	0.481
		ASV2CFA0-32	10.20				
	KOH	AMVCFA0-32	33.70				

Table 3
Equilibrium calculation results of KOH capture by coal fly ash (ASV2CFA0-32).

Input conditions	Temp. /°C	K-species appearing	Al-con. /%	Si-con. /%	C_K/%	C_K/(g K/(g additive))
50 ppmv KOH, K/(Al + Si) = 0.048	800	100% $KAlSi_3O_8$	12	24	100	0.023
	900	100% $KAlSi_3O_8$	12	24	100	0.023
	1100	100% $KAlSi_3O_8$	12	24	100	0.023
	1300	100% $KAlSi_3O_8$	12	24	100	0.023
	1450	98% $KAlSi_3O_8$ + 1% KOH + 1% KCl	12	24	98	0.023
250 ppmv KOH, K/(Al + Si) = 0.240	800	100% $KAlSi_2O_6$	60	81	100	0.117
	900	100% $KAlSi_2O_6$	60	80	100	0.116
	1100	98% $KAlSi_2O_6$ + 1% KOH	60	80	98	0.115
	1300	93% $KAlSi_2O_6$ + 6% KOH	56	75	93	0.108
	1450	93% $KAlSi_2O_6$ + 6% KOH	56	75	93	0.109
500 ppmv KOH, K/(Al + Si) = 0.481	800	72% $KAlSiO_4$ + 10% $KAlSi_2O_6$	100	75	83	0.193
	900	71% $KAlSiO_4$ + 12% $KAlSi_2O_6$ + 2% KOH	100	77	83	0.193
	1100	55% $KAlSiO_4$ + 28% $KAlSi_2O_6$ + 15% KOH	100	89	83	0.193
	1300	55% $KAlSiO_4$ + 28% $KAlSi_2O_6$ + 16% KOH	100	90	83	0.193
	1450	57% $KAlSi_2O_6$ + 42% KOH	69	92	57	0.133
750 ppmv KOH, K/(Al + Si) = 0.721	800	55% $KAlSiO_4$ + 41% K_2SiO_3 + 2% KOH	100	67	55	0.193
	900	55% $KAlSiO_4$ + 36% K_2SiO_3 + 2% $K_2Si_2O_5$ + 4% KOH	100	67	55	0.193
	1100	55% $KAlSiO_4$ + 18% $K_2Si_2O_5$ + 24% KOH	100	67	55	0.193
	1300	36% $KAlSiO_4$ + 19% $KAlSi_2O_6$ + 44% KOH	100	90	55	0.193
	1450	29% $KAlSiO_4$ + 23% $KAlSi_2O_6$ + 47% KOH	94	91	52	0.181
1000 ppmv KOH, K/(Al + Si) = 0.961	800	32% $KAlSiO_4$ + 9% $KAlO_2$ + 52% K_2SiO_3 + 4% KOH	78	52	32	0.151
	900	41% $KAlSiO_4$ + 1% $KAlO_2$ + 36% K_2SiO_3 + 21% KOH	99	66	41	0.191
	1100	41% $KAlSiO_4$ + 15% $K_2Si_2O_5$ + 41% KOH	100	67	41	0.193
	1300	27% $KAlSiO_4$ + 14% $KAlSi_2O_6$ + 58% KOH	100	90	41	0.193
	1450	27% $KAlSiO_4$ + 14% $KAlSi_2O_6$ + 58% KOH + 1% K	100	90	41	0.193

2.5. Equilibrium calculation

Chemical equilibrium calculations have been widely utilized to investigate the speciation of alkali as well as the interaction between alkali and coal ash minerals during combustion [28–30]. In the present study, global equilibrium calculations were carried out using the equilibrium module of FactSage 7.0. Experimental results and equilibrium calculation data were compared to better understand the results.

The chemical equilibrium calculations were performed at atmospheric pressure in the temperature range of 500–1800 °C. Four databases including FactPS, FToxid, FTsalt and FTpulp were employed. Gas, liquid and solid compound species were selected for the equilibrium calculations. Detailed information about the databases [34] and calculation settings are included in the Supplementary material. The calculation results of key points are summarized in Table 3.

3. Results and discussion

3.1. Representativeness of solid product samples

Although the solid samples obtained from the sampling system (sampling tube, cyclone, and filter) were carefully collected, the mass balance for each experiment only closed within about 58–75%. The difference was due to the deposition on the inner wall of the vertical reactor tube and other places. The calculation of K-capture level (C_K) and K-conversion (X_K) was based on the assumption that the collected samples are representative. The representativeness of the product samples was examined by comparing the molar ratio of K/(Al + Si) in products with that of the fed reactants. The result basing on ICP-OES analysis is shown in Fig. 2. It shows that the molar ratio of K/(Al + Si) in the collected solid samples is close to that of fed reactants, suggesting that the solid samples are representative.

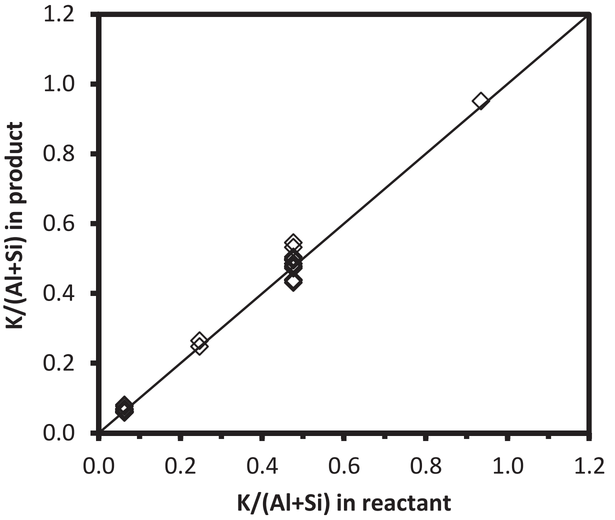

Fig. 2. Comparison of K/(Al + Si) in collected solid products and reactants fed into the EFR.

3.2. KOH capture by coal fly ash

3.2.1. Equilibrium calculations

The equilibrium calculation results of KOH capture by ASV2CFA0-32 at different temperatures (800–1450 °C) and KOH concentrations (50–1000 ppmv) are summarized in Table 3. Results that are more detailed can be found in the Supplementary material.

The calculations indicate that the type of the K-aluminosilicates formed from the KOH-capture reaction changes with the K-concentration or the molar ratio of K/(Al + Si) in reactants. At 50 ppmv KOH (molar K/(Al + Si) in reactant was 0.048), sanidine ($KAlSi_3O_8$) with K:Al:Si = 1:1:3 was predicted as the main K-aluminosilicate through the whole temperature range 800–1450 °C. When the KOH concentration increased to 250 ppmv, leucite ($KAlSi_2O_6$) with a molar ratio of K:Al:Si = 1:1:2 became the dominant K-aluminosilicate. At 500, 750 and 1000 ppmv KOH, kaliophilite ($KAlSiO_4$) with a molar ratio of K:Al:Si = 1:1:1 was the main K-aluminosilicate product.

3.2.2. Impact of KOH concentration

The measured K-capture level (C_K) and K-conversion (X_K) of KOH

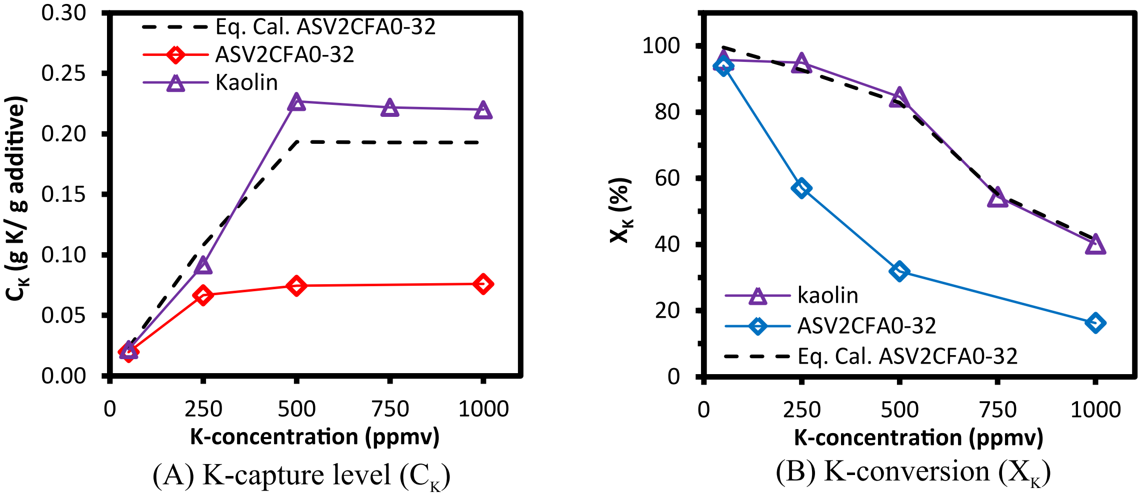

(A) K-capture level (C_K)	(B) K-conversion (X_K)

Fig. 3. K-capture level (C_K) and K-conversion (X_K) of KOH-capture by ASV2CFA0-32 and kaolin (D_{50} = 5.47 μm) [33] at KOH concentrations from 50 to 1000 ppmv. Molar ratio of K/(Al + Si) in the reactants varied from 0.048 to 0.961. Reaction temperature for ASV2CFA0-32 was 1300 °C and reaction temperature of kaolin was 1100 °C; gas residence time was 1.2 s. Equilibrium calculation results for KOH capture by ASV2CFA0-32 are included for comparison.

capture by ASV2CFA0-32 at different KOH concentrations (50–1000 ppmv) and 1300 °C are compared with equilibrium calculations in Fig. 3. For 50 ppmv KOH, the measured C_K (0.022 g K/(g additive)) and X_K (95%) of ASV2CFA0-32 are close to the equilibrium values. However, the experimental C_K and X_K become remarkably lower than the equilibrium data at 250 ppmv KOH and above. As the KOH-concentration in the flue gas increases from 50 ppmv to 500 ppmv, although the K-capture level (C_K) increased considerably from 0.022 g K/(g additive) to 0.074 g K/(g additive), K-conversion (X_K) decreased sharply from 95% to 32%. With a further increase in KOH to 750 and 1000 ppmv, no obvious increase of C_K was observed, and the K-conversion (X_K) dropped to 16% at 1000 ppmv, showing that most KOH remained unreacted in this case. The difference between equilibrium data and experimental data implied that only part of the coal fly ash participated in the K-capture reaction.

Also, the measured C_K and X_K of KOH reaction with kaolin from our previous study [33] are included for comparison in Fig. 3. The experiments of KOH capture by kaolin were conducted at 1100 °C, while the experiments with ASV2CFA0-32 were conducted at 1300 °C. Although the reaction temperature was different, the results are still comparable, because the K-capture behavior of kaolin at 1100 °C and 1300 °C is similar according to our previous study [33]. The results show that the measured C_K and X_K of ASV2CFA0-32 were considerably lower than that of kaolin. There may be several reasons for the lower efficiency of the coal fly ash compared to kaolin. One possible reason is that the main mineral phase of coal fly ash, mullite, is less reactive towards potassium than kaolin and metakaolin. Another possible reason is that the BET surface area of ASV2CFA0-32 (8.04 m^2/g) is smaller than that of kaolin (12.70 m^2/g), and the median diameter of ASV2CFA0-32 (10.20 μm) is larger than that of kaolin (5.47 μm). Consequently, there were fewer active sites for KOH-capture in ASV2CFA0-32 [33]. In addition, diffusion limitations for KOH inside the coal fly ash particles may have also played a role, resulting in an incomplete consumption of mullite in the coal fly ash case. The incomplete consumption of mullite is supported by the XRD results shown in Fig. 4, in which peaks corresponding to mullite were detected in the KOH-reacted coal fly ash.

The XRD spectra of water-washed KOH-reacted ASV2CFA0-32 at 50 ppmv, 250 ppmv and 500 ppmv KOH are compared in Fig. 4. At 50 ppmv KOH, only mullite and quartz originated from the raw coal fly ash were detected. No crystalline K-aluminosilicate was detected, although sanidine ($KAlSi_3O_8$) was predicted by the equilibrium calculations. This is probably because either the content of K-aluminosilicate in the products was too low to be detected, or amorphous K-aluminosilicates were formed which cannot be detected by XRD. In the 250 ppmv sample, leucite ($KAlSi_2O_6$) was detected as the main K-aluminosilicate product. In the 500 ppmv sample, kaliophilite ($KAlSiO_4$) was present as the dominant K-aluminosilicate. The type of K-aluminosilicates detected by XRD, generally agrees with the equilibrium results as shown in Table 3. Notably, mullite was detected in all the three KOH-reacted coal fly ash samples, showing that part of the mullite remained unreacted in those samples. This is different from what was observed in the study of KOH capture by kaolin, where a full conversion of kaolin to K-aluminosilicate was observed and no mullite was detected in the product samples at 500 ppmv KOH and above with a reaction temperature of 1100 °C [33].

3.2.3. *Impact of reaction temperature*

The measured K-capture level (C_K) and K-conversion (X_K) of KOH capture by ASV2CFA0-32 at different reaction temperatures (800–1450 °C) are compared with the equilibrium calculation results in Fig. 5. KOH concentrations of 50 ppmv and 500 ppmv in the flue gas were studied. The C_K and X_K of KOH capture by kaolin at the same conditions [33] are included as well for comparison. As shown in Fig. 5(A) and (B), at 500 ppmv KOH, the measured C_K and X_K of KOH capture by ASV2CFA0-32 were both significantly lower than equilibrium data. At 800 °C, the K-capture level (C_K) was only 0.025 g K/(g additive), with 11% of KOH captured as K-aluminosilicate. When the temperature increased to 900 °C, C_K increased significantly to 0.063 g K/(g additive), with 27% of KOH converted to K-aluminosilicate. At temperatures of 900–1100 °C, the C_K stayed constant. However, when the reaction temperature increased further to 1300 °C and 1450 °C, C_K increased by 38% reaching 0.087 g K/(g additive), with 37% of fed KOH chemically bonded by coal fly ash as K-aluminosilicate at 1450 °C.

At 50 ppmv KOH, the measured C_K and X_K of ASV2CFA0-32 were close to the equilibrium predictions; see Fig. 5(C) and (D). The C_K and X_K were both constant and independent of the reaction temperature in the temperature range of 900–1300 °C. The C_K was around 0.019 g K/(g additive), with about 94% KOH converted to K-aluminosilicate.

Comparison of results of KOH-ASV2CFA0-32 and KOH-kaolin in Fig. 5 shows that, at 500 ppmv KOH, the C_K and X_K of ASV2CFA0-32 were considerably lower than that of kaolin, showing that coal fly ash (ASV2CFA0-32) captures KOH less effectively in this case. Additionally, the trend of the C_K and X_K of kaolin and ASV2CFA0-32 at 500 ppmv was obviously different. For kaolin, C_K and X_K firstly increased and then

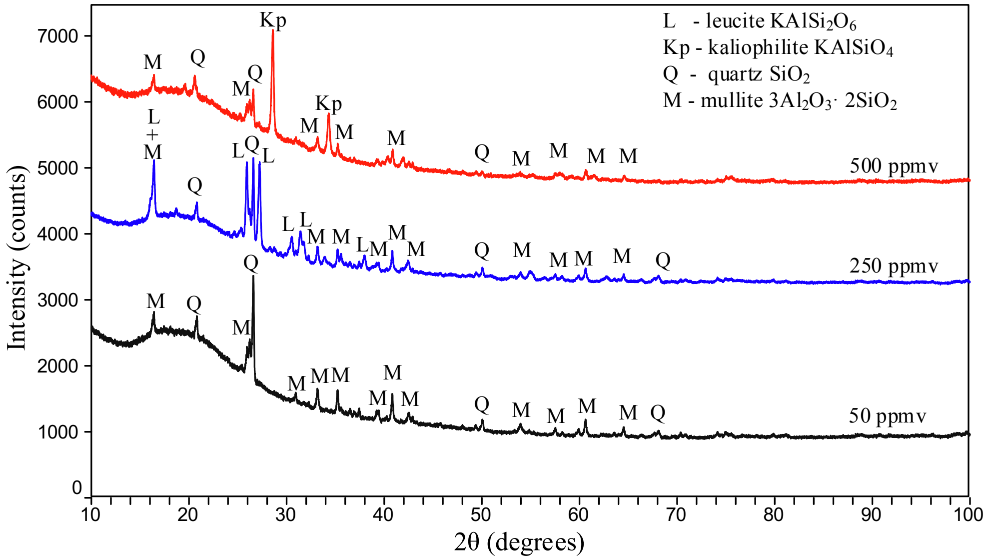

Fig. 4. XRD spectra of water-washed KOH-reacted ASV2CFA0-32 at 50 ppmv, 250 ppmv and 500 ppmv KOH. The reaction temperature was 1300 °C; the molar ratio of K/(Al + Si) in the reactants was 0.048, 0.240 and 0.481; the gas residence time was 1.2 s.

decreased when the reaction temperature was changed from 800 °C to 1450 °C, reaching a peak at 1300 °C. The C_K and X_K of ASV2CFA0-32 increased sharply when the temperature increased from 800 °C to 900 °C, and it stayed constant at 900–1100 °C. When the reaction temperature increased further to 1300 °C and 1450 °C, they increased again, probably because the melting of the coal fly ash particles accelerated the internal diffusion of KOH. However, at 50 ppmv KOH, the C_K and X_K of ASV2CFA0-32 were comparable to that of kaolin. The trend at different temperatures of the two additives (kaolin and ASV2CFA) was also the same.

The XRD spectra of water-washed 500 ppmv KOH-reacted coal fly ash at different temperatures (800–1450 °C) are compared in Fig. 6. Additionally, experiments feeding only coal fly ash (ASV2CFA0-32) without KOH were carried out at 1100 °C, 1300 °C and 1450 °C. The

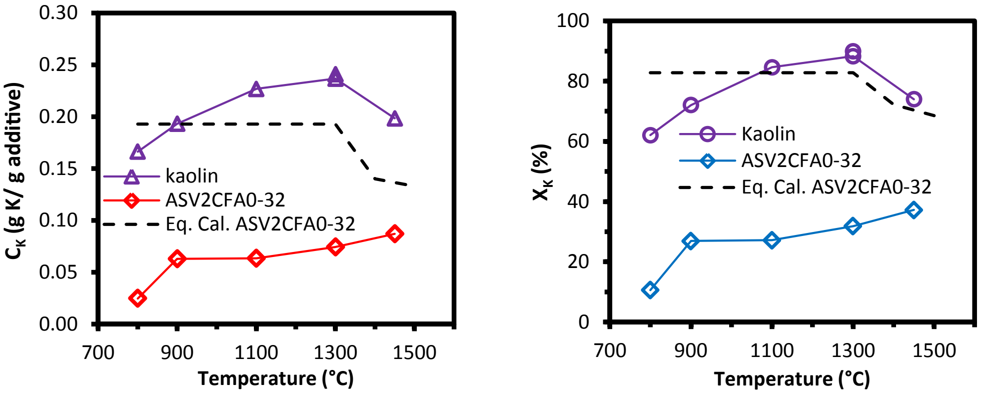

(A) C_K at 500 ppmv KOH (B) X_K at 500 ppmv KOH

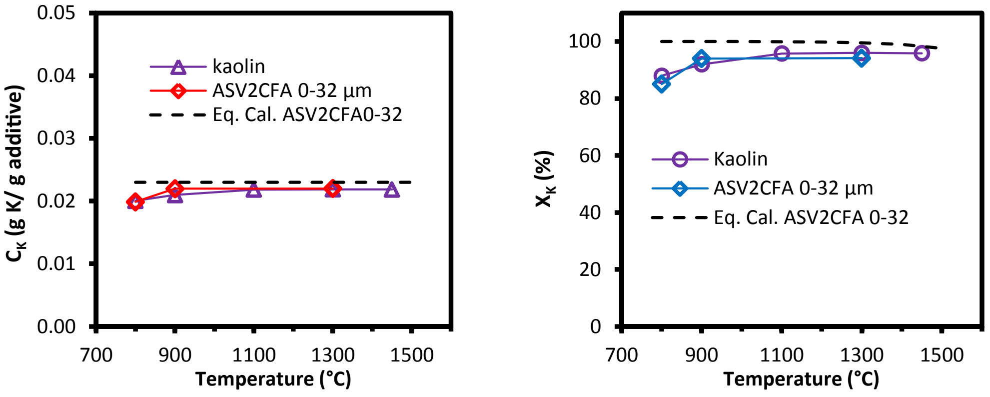

(C) C_K at 50 ppmv KOH (D) X_K at 50 ppmv KOH

Fig. 5. Comparison of K-capture level (C_K) and K-conversion (X_K) of KOH capture by ASV2CFA0-32 and kaolin (D_{50} = 5.47 μm) [33] at temperatures 800–1450 °C. The KOH concentration was 500 ppmv (molar ratio of K/(Al + Si) = 0.481) in (A) and (B), and 50 ppmv (molar ratio of K/(Al + Si) = 0.048) in (C) and (D). The gas residence time was 1.2 s, and equilibrium results of KOH capture by ASV2CFA0-32 are included for comparison.

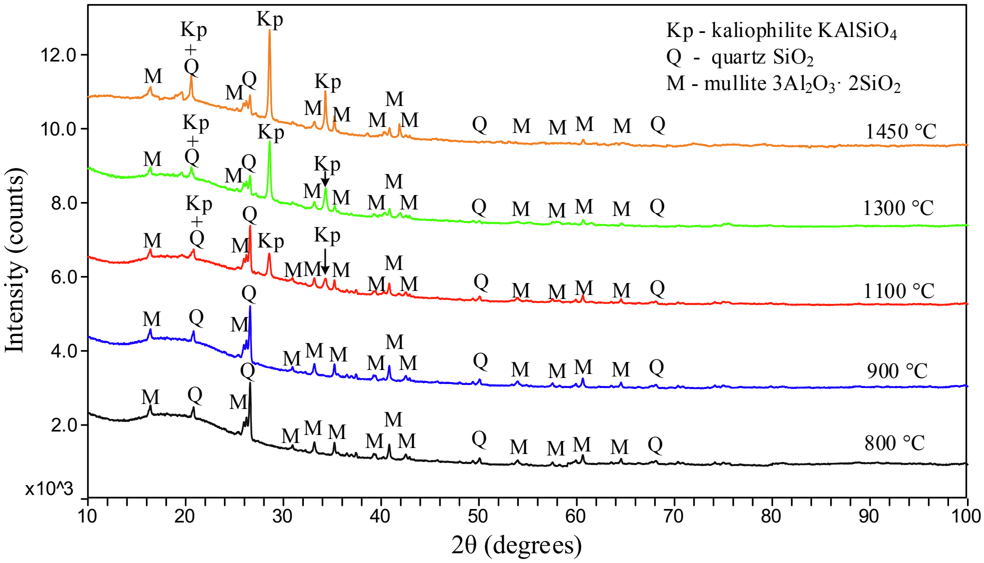

Fig. 6. XRD spectra of water washed KOH-reacted ASV2CFA0-32 samples at different temperatures (800–1450 °C). The KOH-concentration was 500 ppmv, with molar ratio of K/(Al + Si) in reactants of 0.481. The gas residence time was 1.2 s.

XRD spectra of the residues were the same as that of the raw ASV2CFA0-32, with only mullite and quartz being detected. This reveals that, without KOH addition, no large change of the mineralogical composition of the coal fly ash took place.

The results in Fig. 6 show that, with KOH addition, at 800 °C and 900 °C, the spectra were almost the same as that of the parental coal fly ash, with only mullite and quartz detected although chemically captured K was detected by the ICP analysis (Fig. 5). This shows that the formed K-aluminosilicate remained in amorphous phase, or that the concentration of crystalline phase was too low to be detected. In the 1100 °C sample, crystalline kaliophilite ($KAlSiO_4$) was detected. When the reaction temperature increased further to 1300 °C and 1450 °C, the peaks of kaliophilite ($KAlSiO_4$) became stronger, indicating that more crystalline kaliophilite ($KAlSiO_4$) was formed. Notably, mullite and quartz were detected in all the product samples, showing an incomplete conversion of the coal fly ash (ASV2CFA). This supports the results that the measured K-capture level (C_K) and K-conversion (X_K) were considerably lower than those predicted by equilibrium calculations. In our previous study on KOH capture by kaolin [33], full conversion of kaolin into K-aluminosilicate was observed. The difference between kaolin and ASV2CFA0-32 indicates that, the controlling mechanisms of KOH-capture reaction by coal fly ash and kaolin in the EFR are different. In the KOH-kaolin system, the reaction was equilibrium limited, while the KOH-coal fly ash reaction was probably diffusion or kinetically controlled.

3.2.4. Impact of coal fly ash particle size

The K-capture level (C_K) and K-conversion (X_K) of KOH by ASV2 coal fly ash of different particle sizes are compared in Fig. 7. At 800 °C, the C_K and X_K of ASV2 coal fly ash of different particle sizes are almost independent of different particle size, probably due to a kinetically controlled reaction at this temperature. When the reaction temperature increased to 900 °C and above, the C_K of the finer coal fly ash (ASV2CFAGR) was significantly higher than that of normal coal fly ash (ASV2CFA0-32). The C_K and X_K of coarse coal fly ash (ASV2CFA32-45) were lower than that of ASV2CFA0-32. This indicates that at 900–1300 °C, the reaction was diffusion-influenced.

3.2.5. KOH capture by kaolin, mullite and coal fly ash

The measured K-capture level (C_K) and K-conversion (X_K) of KOH-coal fly ash (ASV2CFA0-32 and ASV2CFAGR) obtained at different temperatures are compared with the experimental results of KOH-kaolin and mullite from our previous study [33] in Fig. 8. The mullite sample was generated by heating kaolin at 1100 °C for 24 h [33]. The median diameter D_{50} of ASV2CFAGR (D_{50} = 6.02 μm) was comparable to that of the kaolin (D_{50} = 5.47 μm) and mullite powder (D_{50} = 5.90 μm), while the D_{50} of ASV2CFA0-32 was somewhat larger (10.2 μm). The BET surface area of kaolin (12.7 m^2/g) was higher than those of mullite (5.30 m^2/g) and ASV2CFAGR (9.07 m^2/g). The main mineral phase of the mullite powder and the ASV2 coal fly ash (ASV2CFAGR, ASV2CFA0-32) was mullite, whereas it was kaolinite for kaolin powder.

The results show that at 800 °C, the C_K of ASV2CFA0-32, ASV2CFAGR and mullite was at the same level, about 0.020 g K/(g additive), while the value for kaolin was much higher at 0.167 g K/(g additive). One possible reason is that the BET surface areas of coal fly ash and mullite were smaller than that of kaolin, resulting in a smaller amount of reactive spots and a slower internal diffusion of KOH. Another possible reason is that the kinetics of the KOH-capture reaction by mullite and kaolinite are different and it is probably slower for mullite than that of kaolinite or metakaolin. Considering that the BET surface area and median diameter D_{50} of ASV2CFAGR were comparable to those of kaolin but that the C_K of kaolin was still considerably higher than that of ASV2CFAGR, the difference of the kinetics of KOH-capture by kaolinite and mullite might be the main reason for the observed difference of C_K at 800 °C.

In the temperature range 900–1300 °C, the C_K of coal fly ashes, mullite and kaolin all increased with increasing temperature, but the C_K of coal fly ash and mullite was both considerably lower than that of kaolin. When the temperature increased further to 1450 °C, the C_K of mullite increased significantly, and it became comparable to that of kaolin. However, there is a less pronounced increase in C_K for the two ASV2 coal fly ashes. At 1450 °C, the relatively lower C_K of the two ASV2 coal fly ashes may be partly due to the equilibrium limit as shown in Fig. 9, and partly due to internal diffusion limitations. In summary, the KOH-capture reaction by kaolin, mullite and coal fly ash at 800 °C were all kinetically controlled. At 900–1300 °C, KOH capture by mullite and coal fly ash were more diffusion-influenced. At 1450 °C, KOH capture by kaolin, and mullite was limited by equilibrium, while it is diffusion influence for coal fly ash (ASV2CFA0-32 and ASV2CFAGR).

4. Conclusions

The KOH-capture reaction by coal fly ash was studied by entrained

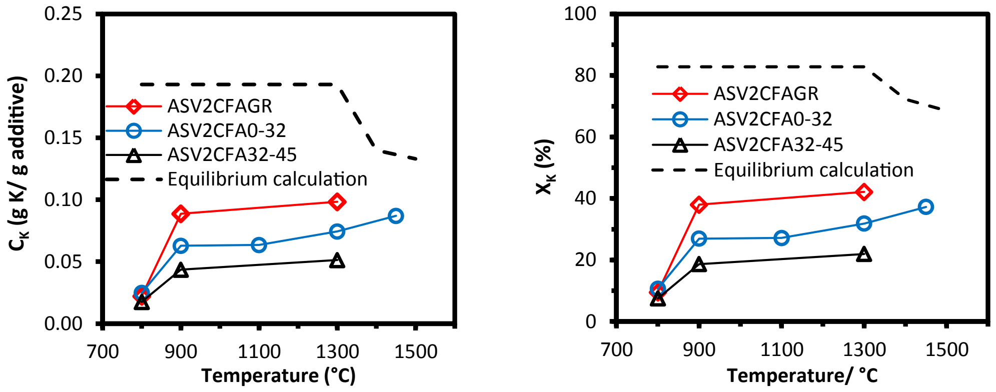

(A) K-capture level (C_K)

(B) K-conversion (X_K)

Fig. 7. Comparison of K-capture level (C_K) and K-conversion (X_K) of KOH capture by ASV2 coal fly ash of different particle sizes: ASV2CFAGR (D_{50} = 6.03 µm), ASV2CFA0-32 (D_{50} = 10.20 µm), and ASV2CFA32-45 (D_{50} = 33.70 µm). The reaction temperature was 1300 °C; the gas residence time was 1.2 s; the KOH concentration in the flue gas was 500 ppmv, with a molar K/(Al + Si) ratio of 0.481. Equilibrium calculation results are included for comparison.

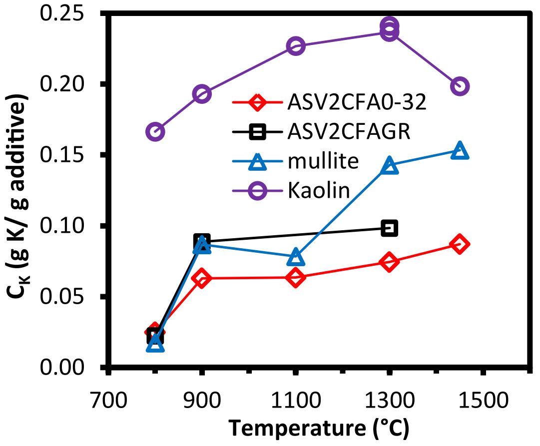

Fig. 8. Comparison of K-capture level (C_K) and K-conversion (X_K) of ASV2 coal fly ashes of different particle size (ASV2CFA0-32 and ASV2CFAGR), kaolin and mullite [33]. The KOH concentration was 500 ppmv in all experiments, with molar K/(Al + Si) ratio of 0.481. Gas residence time was 1.2 s.

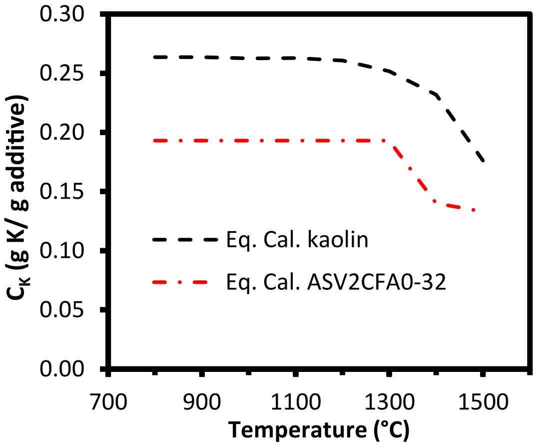

Fig. 9. Comparison of equilibrium calculated K-capture level (C_K) of KOH capture by kaolin [33] and ASV2CFA0-32. The KOH concentration was 500 ppmv in the flue gas, with a molar K/(Al + Si) ratio of 0.481.

flow reactor experiments and equilibrium calculations. The impacts of KOH-concentration, molar ratio of K/(Al + Si) in reactants, reaction temperature and particle size of coal fly ash were investigated. The results of KOH-capture experiments using coal fly ash were also compared with that of kaolin and mullite from our previous studies [33].

The experimental results at different KOH concentrations (different molar ratio of K/(Al + Si) in feed) with a reaction temperature of 1300 °C, and a gas residence time of 1.2 s showed that, the K-capture level (C_K) of coal fly ash increased with the KOH concentration at 50–500 ppmv KOH (K/(Al + Si) = 0.048–0.481), but no further increase of K-capture level (C_K) was observed at a K-concentration of 750–1000 ppmv. At 50 ppmv KOH, the measured K-capture level (C_K) of coal fly ash was comparable to the equilibrium calculation data and the experimental C_K of kaolin from our previous study [33]. However, at 250 ppmv KOH and above (molar K/(Al + Si) ≥ 0.240), the measured C_K was lower than the equilibrium data. The main alkali product species formed were leucite ($KAlSi_2O_6$) at 250 ppmv, and kaliophilite ($KAlSiO_4$) at 500 ppmv. Although the types of formed K-aluminosilicates (predicted by equilibrium calculations) agreed with those of the KOH-kaolin reaction, coal fly ash captured KOH less effectively at 250 ppmv KOH and above (molar K/(Al + Si) ≥ 0.240).

At 500 ppmv KOH (K/(Al + Si) = 0.481), when the temperature changed from 800 to 1450 °C, C_K of the coal fly ash generally increased from 0.025 g K/(g additive) to 0.087 g K/(g additive). The K-capture level (C_K) of coal fly ash was lower than that of kaolin throughout the whole temperature range studied. At 800 °C, with a median particle size of 10.20 µm, the KOH-capture reaction by coal fly ash was probably kinetically controlled. At 900–1300 °C, the K-capture level increased with the decreased particle size and was probably transport or kinetically limited. At 1450 °C the reaction was limited by equilibrium as well. The gradual increase of C_K at 900–1450 °C may be caused by the increased internal or external transport of KOH.

At 50 ppmv KOH (K/(Al + Si) = 0.048), representative for the gaseous potassium level in wood suspension-fired plants, C_K of coal fly ash (around 0.02 g K/(g additive)) was comparable to the equilibrium data. Results of the reaction between KOH and coal fly ash of different particle sizes at 900–1300 °C showed that, decreasing the coal fly ash particle size from D_{50} = 10.20 µm to D_{50} = 6.03 µm could increase the K-capture level (C_K) from 0.05 to 0.08 g K/(g additive).

Acknowledgment

This work is part of the project ‘Flexible use of Biomass on PF fired power plants’ funded by Energinet.dk through the ForskEL programme, Ørsted Bioenergy & Thermal Power A/S and DTU.

Funding

This work was supported by Energinet.dk [ForskEL-project number. 2014-1-12150], Ørsted Bioenergy & Thermal Power A/S and DTU.

Appendix A. Supplementary data

Detailed results of the equilibrium calculation of KOH capture by coal fly ash are included in the supplementary material. Supplementary data to this article can be found online at https://doi.org/10.1016/j.fuel.2018.12.088.

References

[1] Wu H, Bashir MS, Jensen PA, Sander B, Glarborg P. Impact of coal fly ash addition on ash transformation and deposition in a full-scale wood suspension-firing boiler. Fuel 2013;113:632–43.

[2] Damoe AJ, Wu H, Frandsen FJ, Glarborg P, Sander B. Impact of coal fly ash addition on combustion aerosols (PM 2.5) from full-scale suspension-firing of pulverized wood. Energy Fuels 2014;28:3217–23.

[3] Wu H, Glarborg P, Frandsen FJ, Dam-Johansen K, Jensen PA. Dust-firing of straw and additives: ash chemistry and deposition behavior. Energy Fuels 2011;25:2862–73.

[4] Christensen KA, Stenholm M, Livbjerg H. The formation of submicron aerosol particles, HCl and SO_2 in straw-fired boilers. J. Aerosol Sci 1998;29:421–44.

[5] Dayton DC, French RJ, Milne TA. Direct observation of alkali vapor release during biomass combustion and gasification. 1. Application of molecular beam/mass spectrometry to switchgrass combustion. Energy Fuels 1995;9:855–65.

[6] Vassilev SV, Baxter D, Andersen LK, Vassileva CG. An overview of the composition and application of biomass ash. Fuel 2013;105:19–39.

[7] Gao X, Yani S, Wu H. Emission of inorganic PM_{10} during the combustion of spent biomass from mallee leaf steam distillation. Energy Fuels 2015;29:5171–5.

[8] Johansen JM, Aho M, Paakkinen K, Taipale R, Egsgaard H, Jakobsen JG, et al. Release of K, Cl, and S during combustion and co-combustion with wood of high-chlorine biomass in bench and pilot scale fuel beds. Proc. Combust. Inst. 2013;34:2363–72.

[9] Yin C, Rosendahl LA, Kær SK. Grate-firing of biomass for heat and power production. Prog. Energy Combust. Sci. 2008;34:725–54.

[10] Damoe AJ, Jensen PA, Frandsen FJ, Wu H, Glarborg P. Fly Ash formation during suspension firing of biomass: effects of residence time and fuel type. Energy Fuels 2017;31:555–70.

[11] Zheng Y, Jensen AD, Johnsson JE. Deactivation of V_2O_5-WO_3-TiO_2 SCR catalyst at a biomass-fired combined heat and power plant. Appl Catal, B 2005;60:253–64.

[12] Zheng Y, Jensen AD, Johnsson JE. Laboratory investigation of selective catalytic reduction catalysts: deactivation by potassium compounds and catalyst regeneration. Ind. Eng. Chem. Res. 2004;43:941–7.

[13] Castellino F, Rasmussen SB, Jensen AD, Johnsson JE, Fehrmann R. Deactivation of vanadia-based commercial SCR catalysts by polyphosphoric acids. Appl Catal, B 2008;83:110–22.

[14] Castellino F, Jensen AD, Johnsson JE, Fehrmann R. Influence of reaction products of K-getter fuel additives on commercial vanadia-based SCR catalysts Part I. Potassium phosphate. Appl Catal, B 2009;86:196–205.

[15] Zheng Y, Jensen PA, Jensen AD. A kinetic study of gaseous potassium capture by coal minerals in a high temperature fixed-bed reactor. Fuel 2008;87:3304–12.

[16] Wang L, Becidan M, Skreiberg Ø. Sintering behavior of agricultural residues ashes and effects of additives. Energy Fuels 2012;26:5917–29.

[17] Uberoi M, Punjak WA, Shadman F. The kinetics and mechanism of alkali removal from flue gases by solid sorbents. Prog. Energy Combust. Sci. 1990;16:205–11.

[18] Tran K-Q, Iisa K, Steenari B-M, Lindqvist O. A kinetic study of gaseous alkali capture by kaolin in the fixed bed reactor equipped with an alkali detector. Fuel 2005;84:169–75.

[19] Iisa K, Lu Y, Salmenoja K. Sulfation of potassium chloride at combustion conditions. Energy Fuels 1999;13:1184–90.

[20] Zeuthen JH, Jensen PA, Jensen JP, Livbjerg H. Aerosol formation during the combustion of straw with addition of sorbents. Energy Fuels 2007;21:699–709.

[21] Davidsson KO, Steenari BM, Eskilsson D. Kaolin addition during biomass combustion in a 35 MW circulating fluidized-bed boiler. Energy Fuels 2007;21:1959–66.

[22] De Fusco L, Boucquey A, Blondeau J, Jeanmart H, Contino F. Fouling propensity of high-phosphorus solid fuels: predictive criteria and ash deposits characterization of sunflower hulls with P/Ca-additives in a drop tube furnace. Fuel 2016;170:16–26.

[23] Wu H, Castro M, Jensen PA, Frandsen FJ, Glarborg P, Dam-Johansen K, et al. Release and transformation of inorganic elements in combustion of a high-phosphorus fuel. Energy Fuels 2011;25:2874–86.

[24] Wang L, Hustad JE, Skreiberg Ø, Skjevrak G, Grønli M. A critical review on additives to reduce ash related operation problems in biomass combustion applications. Energy Procedia 2012;20:20–9.

[25] Bashir MS. Characterization and quantification of deposit build-up and removal in straw suspension-fired boilers. Copenhagen: Department of Chemical and Biochemical Engineering, Technical University of Denmark; 2012.

[26] Ahmaruzzaman M. A review on the utilization of fly ash. Prog. Energy Combust. Sci. 2010;36:327–63.

[27] Blissett RS, Rowson NA. A review of the multi-component utilization of coal fly ash. Fuel 2012;97:1–23.

[28] Zheng Y, Jensen PA, Jensen AD, Sander B, Junker H. Ash transformation during co-firing coal and straw. Fuel 2007;86:1008–20.

[29] Wei X, Lopez C, von Puttkamer T, Schnell U, Unterberger S, Hein KRG. Assessment of chlorine – alkali – mineral interactions during co-combustion of coal and straw. Energy Fuels 2002;16:1095–108.

[30] Dayton DC, Belle-Oudry D, Nordin A. Effect of coal minerals on chlorine and alkali metals released during biomass/coal cofiring. Energy Fuels 1999;13:1203–11.

[31] Liu Y, Duan X, Cao X, Che D, Liu K. Experimental study on adsorption of potassium vapor in flue gas by coal ash. Powder Technol. 2017;318:170–6.

[32] Wang G, Jensen PA, Wu H, Frandsen FJ, Sander B, Glarborg P. Potassium capture by Kaolin, Part 2: K_2CO_3, KCl and K_2SO_4. Energy Fuels 2018;32:3566–78.

[33] Wang G, Jensen PA, Wu H, Frandsen FJ, Sander B, Glarborg P. Potassium capture by Kaolin, Part 1: KOH. Energy Fuels 2018;32:1851–62.

[34] Bale CW, Bélisle E, Chartrand P, Decterov SA, Eriksson G, Hack K, et al. FactSage thermochemical software and databases — recent developments. Calphad 2009;33:295–311.

July 2019

ForskEL project no. 12150/EUDP 64018-003

Final report: Flexible use of biomass on PF Fired power plants

Appendix G. Journal paper: Wang G., Jensen P.A., Wu H., Laxminarayan, Y., Frandsen F.J., Sander B., Glarborg P. Potassium Capture by Coal Fly Ash: K_2CO_3, KCl and K_2SO_4. Accepted for publication in: Fuel Processing Technology 2019.

1. **Department of Chemical and Biochemical Engineering**
Technical University of Denmark
Søltofts Plads, Building 229, DK-2800, Kgs. Lyngby, Denmark
2. **Ørsted Bioenergy & Thermal power,**
Kraftværksvej 53, DK-7000, Fredericia, Denmark

CHEC no. R1902

Potassium Capture by Coal Fly Ash: K_2CO_3, KCl and K_2SO_4

Guoliang Wang [a*], *Peter Arendt Jensen* [a], *Hao Wu* [a], *Flemming Jappe Frandsen* [a], *Yashasvi Laxminarayan* [a], *Bo Sander* [b], *Peter Glarborg* [a]

[a] Department of Chemical and Biochemical Engineering, Technical University of Denmark,
Søltofts Plads, Building 229, DK-2800 Kgs. Lyngby, Denmark

[b] Ørsted Bioenergy & Thermal Power A/S, Kraftværksvej 53, 7000 Fredericia, Denmark

[*]**Corresponding Author E-mail:** guow@kt.dtu.dk

Permanent address:

Department of Chemical and Biochemical Engineering, Technical University of Denmark, Søltofts Plads, Building 229, DK-2800 Kgs. Lyngby, Denmark

Manuscript submitted to ***Fuel Processing Technology***

Abstract:

The potassium capture behavior of two coal fly ashes at well-controlled suspension-fired conditions was investigated through entrained flow reactor (EFR) experiments and chemical equilibrium calculations. The impact of local reaction conditions, i.e., the type of K-salts (K_2CO_3, KCl or K_2SO_4), K-concentration in flue gas (molar K/(Al+Si) ratio in reactants), reaction temperature, and coal ash type on the reaction was studied. The results show that the K-capture level of coal fly ash at a K-concentration of 500 ppmv (K/(Si+Al) = 0.481) was considerably lower than the equilibrium data as well as the measured K-capture level of kaolin. However, at 50 ppmv K (with a molar K/(Si+Al) ration of 0.048), no obvious difference between kaolin and coal fly ash was observed in this work. Comparison of results for different K-species showed that coal fly ash captured KOH and K_2CO_3 more effectively than KCl and K_2SO_4. Additionally, a coal fly ash with higher content of Si and a lower melting point captured KCl more effectively than the reference coal fly ash.

Keywords: Coal fly ash, potassium capture, biomass combustion, additive, K_2CO_3, KCl

1 Introduction

Biomass suspension-combustion has a higher electrical efficiency and higher load-flexibility compared to traditional grate-fired boilers, but the ash-related problems, including deposition, corrosion and SCR catalyst deactivation, may be more severe [1] than that in grate-fired boilers [2-10], due to a higher concentration of fly ash in the flue gas [6]. Potassium originating from biomass is the primary cause for the ash-related problems. Potassium may be present as KOH, KCl, K_2SO_4 in the flue gas or other forms depending on the fuel composition, ash transformation chemistry, combustion conditions, etc. [3]. In the combustion of woody biomass which contains relatively lower chlorine and sulfur, potassium exists in the flue gas in the boiler chamber mainly as gaseous KOH [11, 12]. When firing straw or other chlorine-rich biomass, chlorine facilitates the release of potassium, and KCl becomes the main K-species in the high temperature flue gas [8, 13]. Apart from accelerating deposit formation and SCR catalyst deactivation, severe corrosion is also attributed to KCl [14-18]. When firing bio-fuels containing sulfur, another K-compound, K_2SO_4, can be formed [9]. The binary system of KCl and K_2SO_4 may melt at temperatures as low as 690 °C [19], forming a sticky surface on super-heaters and boiler surfaces, which results in accelerated fouling and slagging.

Various technologies have been developed to overcome these ash-related problems in biomass-fired boilers, including the use of additives [20-28], co-firing [29], leaching [30-33], and application of anti-corrosion coating or materials [34, 35]. Kaolin and coal fly ash are effective additives which can chemically capture K-species forming K-aluminosilicates with higher melting points.

Coal fly ash is the only additive that has been commercially utilized in full-scale biomass suspension-fired boilers for K-capture [12, 36]. In a full-scale boiler measuring campaign conducted by Wu and co-workers [36], the influence of the addition of coal fly ash on the transformation of potassium, the deposition behavior, the deposit composition and the formation of sub-micrometer aerosols was systematically investigated [12, 36]. The formation of aerosols was significantly suppressed, and the composition of the aerosols changed from K-S-Cl rich to Ca-P-Si rich [12] with the addition of coal fly ash. The large outer deposit changed from K-Ca-Si rich to Si-Al rich, resulting in an easier and more frequent removal of the deposits [36]. However, due to the complexity of full-scale boiler combustion and the inevitable variation of conditions (bulk chemistry of fuel, load of boiler, etc.), it is almost impossible to conduct well-controlled quantitative studies on the K-capture reaction of coal fly ash in full-scale boilers.

Some lab-scale experiments have been carried out to understand the K-capture reaction systematically [37, 38]. Zheng et al. [37] studied the KCl capture behavior of coal fly ash pellets in a lab-scale fixed bed reactor, where two types of coal ash were utilized: bituminous coal ash and lignite coal ash. The influences of parent coal type, the reaction temperature, and the K-concentration on the reaction were investigated. The results were also compared with that of kaolin [39], showing that bituminous coal ash with a high content of Al and Si behaved similarly to kaolin and captured KCl effectively. However, the lignite coal ash pellets, which were rich in Ca and Mg, only captured negligible amounts of potassium [37].

In another fixed bed reactor study, Liu et al.[38] investigated the KCl capture reaction by bituminous coal fly ash (70-100 μm) which were paved in a stainless steel wires holder [38]. The impact of reaction temperature, KCl-concentration and the reaction atmosphere was investigated. The results indicated that 900 °C was the optimal K-capture temperature for the investigated coal fly ash. In addition, a reducing atmosphere and the presence of water vapor promoted the K-capture capability of the coal fly ash [38].

Through these fixed bed studies, important data on K-capture by coal fly ash were obtained. However, the reaction conditions in the fixed bed reactors are obviously different from those in full-scale suspension-fired boilers [37]. In the fixed bed reactors, coal ash was usually in the form of pellets, flakes, piles or paved in holders [37, 40, 41], causing the reaction with gaseous K-species to be limited by internal diffusion. In suspension-fired boilers, coal ash particles are well-dispersed in the flue gas, having a size smaller than 100 μm, and the controlling mechanism can be quite different. The K-capture reaction under suspension-fired conditions can be limited by thermal equilibrium, mass transfer, or chemical kinetics. Additionally, local reaction temperature, gas atmosphere, additive particle size, additive composition and reaction time also impact upon the K-capture reaction by coal fly ash [37, 42, 43]. However, knowledge on the K-capture reaction of coal ash is limited, and quantitative experimental results on K-capture by coal fly ash at suspension-fired conditions are still not available. Understanding the reaction as well as its relation to local parameters is desirable to achieve an optimal performance of added coal fly ash and model development.

The objective of this work is to investigate quantitatively the reaction between coal fly ash and K-species at suspension-fired conditions. The impacts of coal ash type, ash particle size, K-species type, K-concentration, and reaction temperature on the K-capture reaction were investigated. This paper is the second one of a series of two papers studying the potassium capture reaction with coal fly ash. The first paper focused on the KOH capture reaction by coal fly ash [44], and the present paper addresses the reaction of coal fly ash with KCl, K_2CO_3 and K_2SO_4.

2 Experimental

2.1 Materials

Two types of coal fly ashes were utilized in this study. One was from unit 2 of Asnæsværket Power Plant Denmark, and it was named as ASV2CFA. The other ash sample was from Amager Power Plant and it was named as AMVCFA. Both coal fly ashes were sieved to 0-32 μm, and the sieved samples were named as ASV2CFA0-32 and AMVCFA0-32, respectively. The characteristics of the ash samples are listed in Table 1. Both coal fly ashes have a high content of Al and Si. The molar ratio (K+Na)/(Al+Si) of ASV2CFA0-32 and AMVCFA0-32 was 0.02, and 0.07, respectively. Both values are relatively low, indicating that there was a large fraction of Al and Si available for the K-capture reaction.

Table 1. Characteristics of the coal fly ashes.

Name	**ASV2CFA0-32**	**AMVCFA0-32**
particle size (µm)	0-32	0-32
D_{50} (µm)	10.20	8.42
O (wt. % dry base)	46.60	49.92
S (wt. % dry base)	0.26	0.23
P (wt. % dry base)	0.64	0.30
Si (wt. % dry base)	22.00	25.00
Al (wt. % dry base)	14.00	11.00
Fe (wt. % dry base)	2.90	4.30
Ca (wt. % dry base)	4.50	4.10
Mg (wt. % dry base)	0.97	1.40
Na (wt. % dry base)	0.27	0.92
K (wt. % dry base)	0.87	2.10
Ti (wt. % dry base)	0.88	0.53
BET surface area (m^2/g)	8.04	3.18
deformation temperature (°C)	1280	1200
hemisphere temperature (°C)	1390	1290
flow temperature (°C)	1440	1380

One difference between the two coal fly ashes was the alkali metal content. The concentration of (K+Na) in AMVCFA0-32 was about 3.0 wt. %, while it was as low as 1.1 % in ASV2CFA0-32. Alkali elements generally stay in the form of alkali-aluminosilicates in coal ash. A higher content of alkali elements in coal ash may thus reduce the availability of Al and Si for alkali-capture. Another difference was that, the Si/Al molar ratio of ASV2CFA0-32 was around 1.5, while the ratio for AMVCFA0-32 was

2.2. Usually, Si is present in the form of mullite, quartz or other amorphous species in coal ash. A relatively higher Si or lower Al content usually implies a lower content of mullite, which is considered as a crucial mineral phase in coal ash for K-capture reaction forming K-aluminosilicate [36, 37, 42].

Among the alkaline earth metal elements, the content of Ca in AMVCFA0-32 was slightly lower than that of ASV2CFA0-32, while Mg was slightly higher. Ca is primarily present in coal ash as lime, anhydrite or calcite [45, 46], and it can also exist together with Mg as CaMg-silicate [47, 48]. Therefore, Ca and Mg may also affect the availability of Al and Si, but to a lower extent. In summary, the relatively lower content of Al and higher content of K and Na would be expected to weaken the K-capture ability of AMVCFA0-32.

In addition to Al and Si, S may also constitute a protective element in coal fly ash, since it can react with KCl or KOH forming less corrosive potassium sulfate [36]. However, the concentration of S in the two selected ashes was very low, around 0.25 %, and may not play a key role in the K-capture reaction in this study.

XRD results show that quartz (SiO_2) and mullite ($3Al_2O_3 \cdot 2SiO_2$) exist in both two coal fly ashes as the main mineral phases. However, no crystalline species containing alkali or alkaline earth metal elements were detected, implying either that the small amount of Na, K, Ca and Mg detected by ICP-OES stay in the form of amorphous species, or that the concentrations were too low to be detected.

Additionally, the melting points (deformation temperature, hemisphere temperature and flow temperature) of the two coal fly ashes were also analyzed according to ISO540:2008 (Hard coal and coke - Determination of ash fusibility) in an oxidizing atmosphere. The results are listed in Table 1, and it revealed that and the melting points of AMVCFA0-32 are lower than that of ASV2CFA0-32.

2.2 Experimental methods

The DTU Entrained Flow Reactor (EFR) was employed in the experimental work. Detailed information about the reactor is available elsewhere [27, 39]. The experimental conditions are summarized in Table 2. In series A of Table 2, to study the influence of KCl concentration, the concentration of coal fly ash in flue gas was kept constant, while the KCl concentration in flue gas was varied from 50 ppmv to 750 ppmv. In series (B) and (C), the KCl-concentration was kept constant, while the reaction temperature was changed from 800 to 1450 °C, to investigate the influence of reaction temperature. ASV2CFA0-32 and AMVCFA0-32 were utilized in series B and C to compare the KCl capture behavior of the two ashes. The K_2CO_3 and K_2SO_4 capturing behavior by coal fly ash at different temperatures was investigated in series (D) and (E).

126 Table 2. Experimental conditions of K-capture experiments using coal fly ashes in the EFR.

Experimental series	**K-species**	**Additives**	**Temp./°C**	**Gas residence time/s**	**K in gas /ppmv**	**K/(Al+Si)**
(A) KCl-capture by ASV2CFA0-32 (impact of **K-concentration**)	KCl	ASV2CFA0-32	1300	1.2	50*	0.048
					250	0.240
					500*	0.481
					750	0.961
(B) KCl-capture by ASV2CFA0-32 (impact of t**emperature**)	KCl	ASV2CFA0-32	800	1.2	50, 500	0.048, 0.481
			900			
			1100			
			1300			
			1450			
(C) KCl-capture by AMVCFA0-32 (impact of **temperature**)	KCl	AMVCFA0-32	800	1.2	500	0.481
			900			
			1100			
			1300			
			1450			
(D) K_2CO_3-capture by ASV2CFA0-32 (impact of **temperature**)	K_2CO_3	ASV2CFA0-32	800	1.2	500	0.481
			900			
			1300			
(E) K_2SO_4-capture by ASV2CFA0-32 (impact of **temperature**)	K_2SO_4	ASV2CFA0-32	800	1.2	500	0.481
			900			
			1300*			

127 *Experiments were repeated.

Table 3. Equilibrium calculation results of KCl capture by ASV2CFA0-32.

Input conditions	Temp. /°C	K-species appearing	Al-conversion /%	Si-conversion /%	K-conversion (X_K) /%	K-capture (C_K) /(g K/g additive)
50 ppmv KCl, K/(Al+Si) =0.048	800	100 % $KAlSi_3O_8$	12	24	100	0.023
	900	100 % $KAlSi3O_8$	12	24	100	0.023
	1100	99 % $KAlSi_3O_8$ + 1 % KCl	12	24	99	0.023
	1300	97 % $KAlSi_3O_8$ + 3 % KCl	12	23	97	0.023
	1450	92 % $KAlSi_3O_8$ + 7 % KCl + 1 % KOH	11	22	92	0.021
250 ppmv KCl, K/(Al+Si) =0.240	800	95 % $KAlSi_2O_6$ + 5 % KCl	57	77	95	0.111
	900	94 % $KAlSi_2O_6$ + 6 % KCl	57	76	94	0.110
	1100	89 % $KAlSi_2O_6$ + 11 % KCl	54	72	89	0.104
	1300	84 % $KAlSi_2O_6$ + 16 % KCl	50	68	84	0.098
	1450	81 % $KAlSi_2O_6$ + 18 % KCl + 1 % KOH	49	66	81	0.095
500 ppmv KCl, K/(Al+Si) =0.481	800	6 % $KAlSiO_4$ + 51 % $KAlSi_2O_6$ + 40 % KCl	69	88	57	0.134
	900	55 % $KAlSi_2O_6$ + 45 % KCl	66	88	55	0.128
	1100	47 % $KAlSi_2O_6$ + 53 % KCl	57	76	47	0.110
	1300	46 % $KAlSi_2O_6$ + 53 % KCl + 1 % KOH	56	75	46	0.109
	1450	45 % $KAlSi_2O_6$ + 54 % KCl + 1 % KOH	54	72	45	0.104
750 ppmv KCl, K/(Al+Si) =0.721	800	33 % $KAlSiO_4$ + 19 % $KAlSi_2O_6$ + 46 % KCl	95	72	52	0.184
	900	3 % $KAlSiO_4$ + 35 % $KAlSi_2O_6$ + 63 % KCl	68	73	37	0.131
	1100	33 % $KAlSi_2O_6$ + 67 % KCl	59	65	33	0.114
	1300	31 % $KAlSi_2O_6$ + 68 % KCl + 1 % KOH	56	62	31	0.109
	1450	31 % $KAlSi_2O_6$ + 67 % KCl + 2 % KOH	56	62	31	0.109
1000 ppmv KCl, K/(Al+Si) =0.961	800	29 % $KAlSiO_4$ + 19 % $KAlSi_2O_6$ + 57 % KCl	100	87	41	0.193
	900	16 % $KAlSiO_4$ + 19 % $KAlSi_2O_6$ + 65 % KCl	84	87	35	0.162
	1100	25 % $KAlSi_2O_6$ + 75 % KCl	60	81	25	0.116
	1300	25 % $KAlSi_2O_6$ + 75 % KCl + 1 % KOH	56	75	23	0.109
	1450	23 % $KAlSi_2O_6$ + 75 % KCl + 2 % KOH	56	75	23	0.109

Table 4. Summary of the equilibrium calculation results of K_2CO_3 capture by ASV2CFA0-32.

Input conditions	Temp. /°C	K-species appearing	Al-conversion /%	Si-conversion /%	K-conversion (X_K) /%	K-capture (C_K) /(g K/g additive)
250 ppmv K_2CO_3, K/(Al+Si) = 0.481	800	73 % $KAlSiO_4$ + 10 % $KAlSi_2O_6$	100	76	83	0.194
	900	71 % $KAlSiO_4$ + 12 % KAlSi2O$_6$ + 2 % KOH	100	77	83	0.194
	1100	55 % $KAlSiO_4$ + 28 % $KAlSi_2O_6$ + 15 % KOH	100	90	83	0.194
	1300	55 % $KAlSiO_4$ + 28 % $KAlSi_2O_6$ + 17 % KOH	100	90	83	0.194
	1450	57 % $KAlSi_2O_6$ + 42 % KOH	69	92	57	0.133

Table 5. Summary of the equilibrium calculation results of K_2SO_4 capture by ASV2CFA0-32.

Input conditions	Temp. /°C	K-species appearing	Al-conversion /%	Si-conversion /%	K-conversion (X_K) /%	K-capture (C_K) /(g K/g additive)
250 ppmv K_2SO_4, K/(Al+Si) = 0.481	800	60 % $KAlSi_2O_6$ + 40 % K_2SO_4	73	98	60	0.141
	900	59 % $KAlSi_2O_6$ + 28 % K_2SO_4	72	96	59	0.139
	1100	54 % $KAlSiO_4$ + 28 % $KAlSi_2O_6$ + 4 % KOH	99	89	82	0.191
	1300	54 % $KAlSiO_4$ + 28 % $KAlSi_2O_6$ + 16 % KOH	100	90	83	0.193
	1450	57 % $KAlSi_2O_6$ + 42 % KOH	69	92	57	0.133

The solid products collected from the EFR experiments were analyzed with ICP-OES (Inductively Coupled Plasma Atomic Emission Spectroscopy) to obtain the elemental composition. For the ICP-OES analysis, solid samples were totally digested in acid solution or dissolved in water to determine the total content or the water-soluble content of different elements, including major elements and water soluble elements. The major elements (Al, Ca, Fe, Mg, P, S, K, Si, Na and Ti) were determined according to the Danish Standard of DS/EN 15290 (Solid Biofuels - Determination of Major Elements). The concentration of water-soluble elements (K and Cl) was analyzed following the standard of DS/EN ISO 16995 (Solid Biofuels- Determination of water soluble Chloride, Sodium and Potassium). Additionally, XRD (X-ray Diffraction) analysis was employed to get the mineralogical composition of solid products. The XRD spectra were obtained with a Huber diffractometer, and the main crystalline phases were identified with the JADE 6.0 software package (MDI Livermore, CA) and the diffraction database of PDF2-2004.

To quantify the K-capture reaction by coal fly ash, two parameters have been defined: K-conversion (X_K) and K-capture level (C_K). X_K is the percentage (%) of fed K-species chemically captured by solid additive (coal fly ash) forming water-insoluble K-aluminosilicates. C_K is the mass of potassium captured by 1 g of additive (coal fly ash) (g K/g additive). Both two parameters can be calculated based on ICP-OES results, and the detailed calculation method is available in the supplementary material.

2.3 Equilibrium calculations

Equilibrium data were obtained by preforming global chemical equilibrium calculations using FactSage 7.0. The equilibrium calculation results were compared with experimental results to obtain a better understand of the experimental data. But one should note that equilibrium calculation data are obtained assuming a fully mixing of all reactants with an enough long time, which could be not reached in real experiments, and the difference of equilibrium calculation and experimental results can be partly contributed to this.

3 Results and discussion

3.1 KCl capture by coal fly ash

3.1.1 Equilibrium calculations

Equilibrium calculation results of KCl capture by ASV2CFA0-32 at 50-1000 ppmv KCl and 800-1450 °C were summarized in Table 3. Detailed results of the equilibrium calculations are provided in Appendix A of the supplementary material. The results show that the type of K-aluminosilicate formed from the K-capture reaction varied with the changing KCl-concentration and the corresponding molar ratio of K/(Al+Si) in reactants. At 50 ppmv KCl (K/(Al+Si) = 0.048), sanidine ($KAlSi_3O_8$) was the main K-aluminosilicate. When the KCl concentration increased to 250 ppmv and 500 ppmv (K/(Al+Si) = 0.240 and 0.481), leucite ($KAlSi_2O_6$) was predicted to be the dominant K-aluminosilicate at 1100-1450 °C. At 800-900 °C, kaliophilite ($KAlSiO_4$) and leucite ($KAlSi_2O_6$) co-existed in the solid products. The equilibrium K-capture level (C_K) increased when the KCl concentration changed from 50 ppmv to 500 ppmv. However, when the KCl concentration was increased further to 750 and 1000 ppmv, no further increase of equilibrium C_K was observed.

3.1.2 Impact of KCl concentration

To investigate the KCl-capture behavior of coal fly ash at different KCl concentrations, experiments were conducted at 50 ppmv to 750 ppmv KCl, where the molar ratio of K/(Al+Si) in reactants changed from 0.048 to 0.721, correspondingly. The experimental results and equilibrium calculation data are compared in Figure 1. Results for KCl-capture by kaolin from our previous study [39] were also included for comparison.

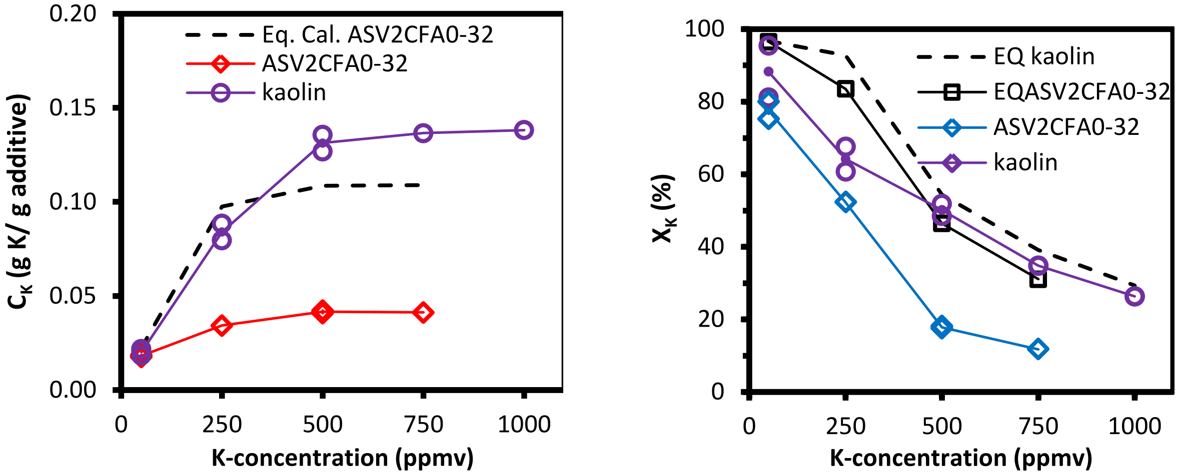

(A) K-capture level (C_K)

(B) K-conversion (X_K)

Figure 1. K-capture level (C_K) and K-conversion (X_K) of KCl capture by ASV2CFA0-32 at 50-750 ppmv KCl (molar ratio of K/(Al+Si) changed from 0.048 to 0.721). Reaction temperature was 1300 °C; the gas residence time was 1.2 s. Experimental data of KCl capture by kaolin from our previous study [39] and equilibrium calculation data of KCl capture by ASV2CFA0-32 were included for comparison.

It is seen from Figure 1, that the measured K-capture level (C_K) of ASV2CFA0-32 increased from 0.019 g K/(g additive) to 0.041 g K/(g additive), when the KCl concentration increased from

50 ppmv to 500 ppmv. Measured K-conversion (X_K) of ASV2CFA0-32 decreased from 80.0 % to 17.5 % correspondingly. However, when the KCl-concentration increased further to 750 ppmv and 1000 ppmv, C_K did not increase, with X_K decreased further to 11.7 %. Comparing to the equilibrium calculation results, the measured C_K and X_K was considerably lower. This implied that the KCl-ASV2CFA0-32 reaction was far from reaching chemical equilibrium probably due to internal diffusion limitations of KCl.

Comparing the C_K and X_K of ASV2CFA0-32 with kaolin [39] in Figure 1, at 250 ppmv KCl and above, the experimental C_K and X_K of ASV2CFA0-32 were remarkably lower than that of kaolin [39]. The lower BET surface area (8.04 m^2/g) and the relatively bigger particle size (D_{50} = 10.20 μm) of ASV2CFA0-32 compared with kaolin (BET surface area = 12.70 m^2/g, D_{50} = 5.47 μm) was one possible reason; another possible reason being the lower reactivity of mullite in coal fly ash towards potassium, compared to kaolinite [37]. At 50 ppmv KCl (K/(Al+Si) in reactants was 0.048), the measured C_K and X_K of ASV2CFA0-32 were comparable to those of kaolin [39]. The results indicated that at low K-concentrations (50 ppmv) or low K/(Al+Si) molar ratio (0.048), which is representative for the gaseous potassium level in practical wood suspension-fired plants [36, 49-51], the K-capture capacity of kaolin and coal fly ash is similar. This is probably because at lower K/(Al+Si), the mullite in the surface layer of coal fly ash particles is probably sufficient for capturing the low amount of potassium, therefore the reaction is less influenced by the internal diffusion of KCl.

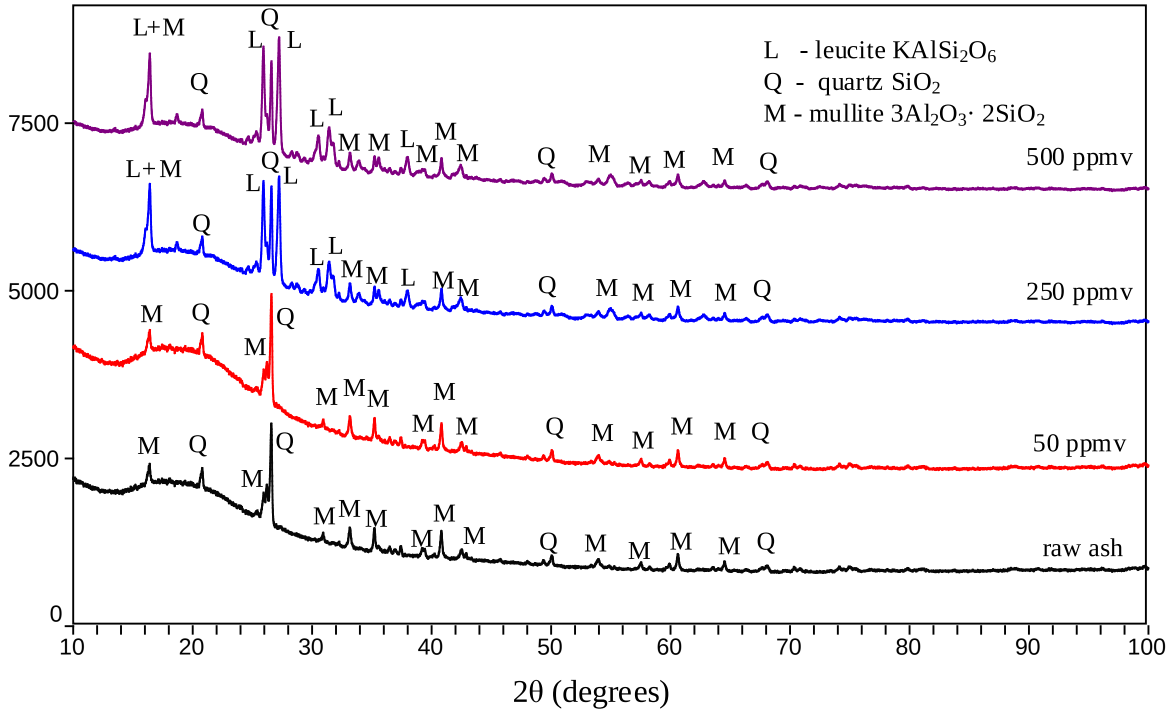

Figure 2. XRD spectra of water-washed KCl-reacted ASV2CFA0-32 at 50 ppmv, 250 ppmv and 500 ppmv KCl. The reaction temperature was 1300 °C. The molar ratio of K/(Al+Si) in the reactants changed from 0.048 to 0.481. The gas residence time was 1.2 s. XRD spectrum of coal fly ash without K feeding was also included for comparison.

The XRD results of water-washed KCl-reacted ASV2CFA0-32 are shown in Figure 2. It shows that the XRD spectrum of 50 ppmv KCl-reacted ash is almost identical as that of coal ash without K feeding, and no crystalline K-aluminosilicate was detected, although sanidine (KAlSi$_3$O$_8$) was predicted by the equilibrium calculations (Table 3) and some water-insoluble potassium was detected by ICP-OES analysis. This is probably because K-aluminosilicate products existed in amorphous phase or its content was too low to be detected. Leucite (KAlSi$_2$O$_6$) was detected both in the 250 ppmv and 500 ppmv KCl-reacted ash samples. This agrees with the equilibrium prediction shown in Table 3. Additionally, the types of K-aluminosilicate detected also agreed with what was observed in KCl-kaolin reaction in our previous study [39]. Notably, in addition to K-aluminosilicate, mullite ($3Al_2O_3 \cdot 2SiO_2$) and quartz (SiO_2) were also detected in all the KCl-reacted ash samples, indicating that some mullite and quartz originating from the parental coal fly ash remained unreacted. This is presumably the reason why the measured K-capture level (C_K) of ASV2CFA0-32 was remarkably lower than the equilibrium prediction.

3.1.3 Impact of reaction temperature

The K-capture level (C_K) and K-conversion (X_K) of KCl capture by ASV2CFA0-32 and AMVCFA0-32 at different temperatures are shown in Figure 3 and Figure 4, respectively. For ASV2CFA0-32, experiments were conducted at both 50 ppmv and 500 ppmv KCl. For AMVCFA0-32, experiments were only conducted with a KCl concentration of 500 ppmv.

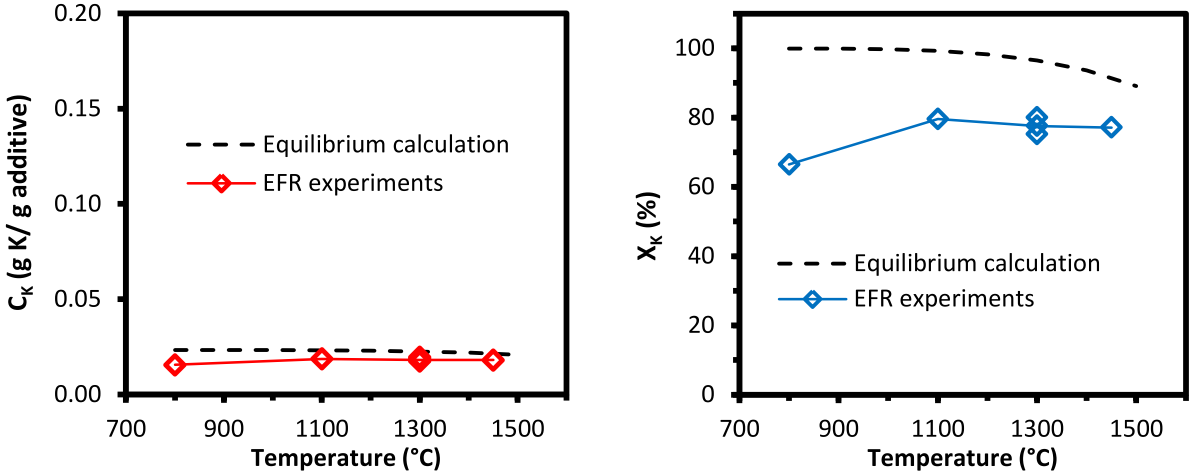

(A) K-capture level (C_K) at 50 ppmv KCl (B) K-conversion (X_K) at 50 ppmv KCl

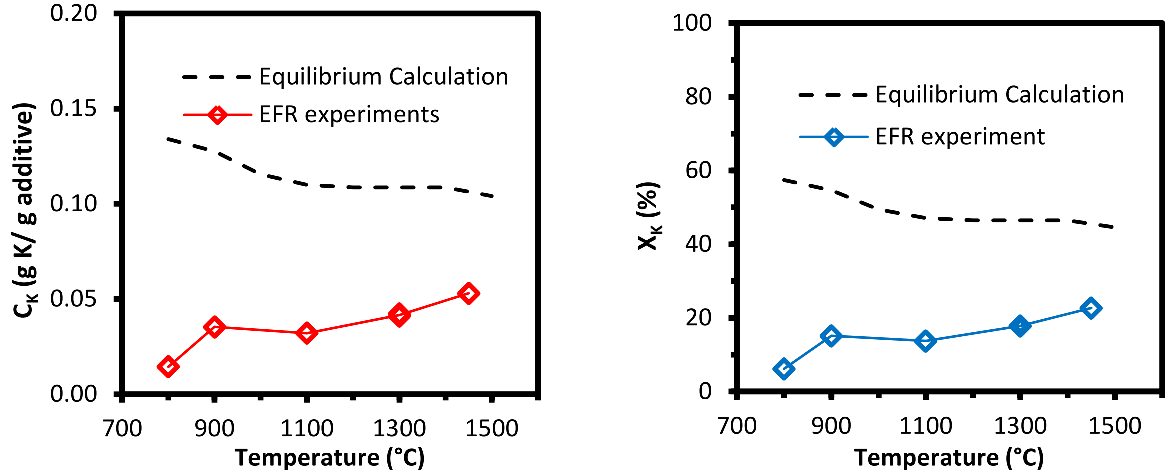

(C) K-capture level (C_K) at 500 ppmv KCl (D) K-conversion (X_K) at 500 ppmv KCl

Figure 3. K-capture level (C_K) and K-conversion (X_K) of KCl-capture by ASV2CFA0-32 at 800-1450 °C. KCl-concentration was 50 ppmv (molar ratio of K/(Al+Si) = 0.048) in (A) and (B), and 500 ppmv (molar ratio of K/(Al+Si) = 0.481) in (C) and (D). The gas residence time was 1.2 s. Equilibrium calculation results are included for comparison.

As shown in Figure 3(A) and (B), at 50 ppmv KCl (K/(Al+Si) = 0.048), the measured C_K and X_K of ASV2CFA0-32 were close to the equilibrium calculation data and no obvious change of C_K

was observed within the studied temperature range (800-1450 °C). C_K was around 0.018 g K/(g additive), with about 80 % of the potassium fed captured by coal fly ash.

Figure 3(C) and (D) show that, at 800 °C and 500 ppmv KCl (K/(Al+Si) = 0.481), the experimental C_K is fairly low (0.015 g K/(g additive)). However, when the reaction temperature increased to 900 °C, the experimental C_K increased significantly to 0.035 g K/(g additive). In the temperature range 900-1100 °C, no significant change of C_K and X_K was observed. We believe that this is because, at 800 °C, the KCl-coal fly ash reaction was probably kinetically controlled, and it was less kinetically influenced at 900-1100 °C. As the reaction temperature increased further to 1300 and 1450 °C, C_K increased gradually to 0.053 g K/(g additive). However, the experimental C_K and X_K were both obviously lower than the equilibrium predictions. Noticing the vaporization degree of KCl (500 ppmv) at different temperatures from 800 to 1450 °C in the EFR was similar (95.4-99.7%) [39]. The increase of C_K at 900-1450 °C, especially at 1300 °C and 1450 °C, is probably due to the melting of coal ash particles (deformation temperature of ASV2CFA0-32 was 1280 °C), which enhanced the KCl diffusion inside the particle (D_{50} = 10.20 μm). A similar phenomenon was observed in the KCl capture experiments using AMVCFA0-32, as discussed below.

Another interesting result in Figure 3 is that, at 800 °C, C_K at 500 ppmv KCl (0.015 g K/(g additive)) is comparable to that at 50 ppmv KCl (0.014 g K/(g additive)). It shows that, at 800 °C, increasing the KCl-concentration from 50 to 500 ppmv did not elevate the amount of potassium captured by coal fly ash under the studied condition. This is probably because the reaction at 800 °C was kinetically controlled and the KCl concentration did not to a large degree influence the reaction.

The experimental C_K and X_K for KCl-capture by AMVCFA0-32 are shown in Figure 4 (A) and (B). The trend of C_K and X_K of AMVCFA0-32 at different temperatures was similar to that of ASV2CFA0-32. At 800 °C, C_K was as low as 0.015 g K/(g additive), and it increased to around 0.030 g K/(g additive) at 900 and 1100 °C. When the temperature increased further to 1300 and 1450 °C, C_K increased considerably to 0.069 g K/(g additive).

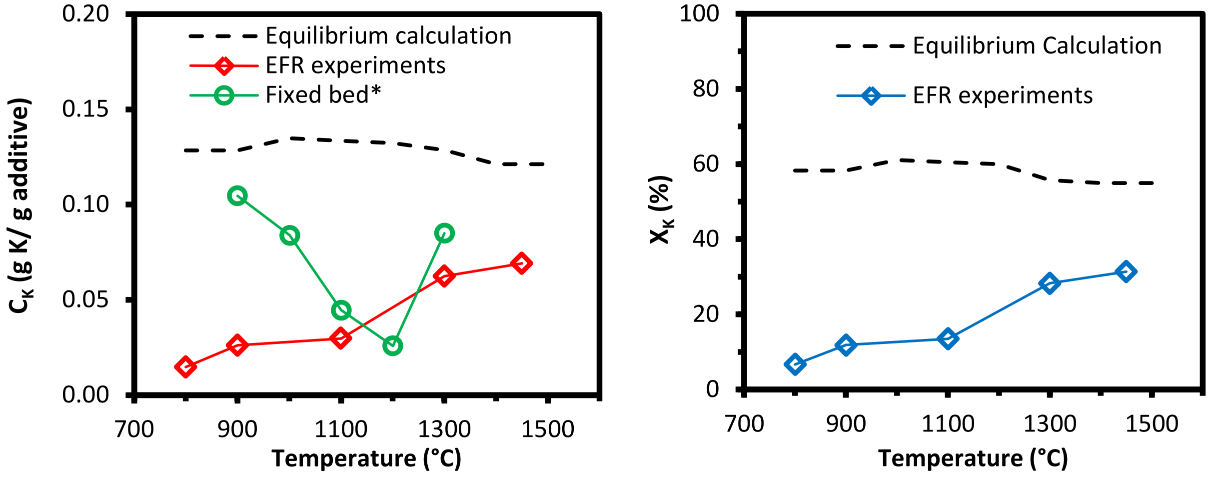

(A) K-capture level of AMVCFA0-32 (B) K-conversion of AMVCFA0-32

Figure 4. K-capture level (C_K) and K-conversion (X_K) of KCl capture by AMVCFA0-32 at different temperatures (800-1450 °C). KCl concentration was 500 ppmv with molar ratio of K/(Al+Si) = 0.481 in reactants. The gas residence time was 1.2 s. Equilibrium calculation results and fixed bed reactor data* (bituminous coal ash pellets with diameter of 1.5 mm, 1100 °C, 1000 ppmv KCl, residence time was 1 hour) calculated from literature [37] are included for comparison.

The experimental C_K for KCl capture by bituminous coal fly ash pellets (diameter of 1.5 mm in a fixed bed reactor) from literature [37] is included in Figure 4 (A) for comparison. The KCl concentration in the fixed bed reactor was 1000 ppmv, and the residence time was 1 hour, i.e., much longer than that in the EFR (1.2 s) of this study. It is seen that C_K in the fixed bed reactor from literature was considerably higher than that in the EFR at 800-1100 °C. This is because the longer residence time in the fixed bed reactor favored the reaction and more Al and Si from coal fly ash participated in the KCl capture reaction. However, at 1300 °C, the C_K in fixed bed and EFR became comparable despite the difference in residence time and KCl concentration. Possibly, this is because the melting of the ash particles at high temperature (1300 °C and 1450 °C) made the reaction in the EFR less diffusion-influenced.

3.1.4 Impact of coal fly ash type

The experimental C_K of the two coal ashes (ASV2CFA0-32 and AMVCFA0-32) as well as that of kaolin from our previous study [39] are compared in Figure 5. The equilibrium calculation data of KCl capture by the two coal fly ashes were also included. Below 1100 °C, C_K and X_K of ASV2CFA0-32 and AMVCFA0-32 were similar, whereas at 1300 °C and 1450 °C, AMVCFA0-32 captured KCl more effectively than ASV2CFA0-32, despite its higher content of K and Na. One possible explanation is that the melting point of AMVCFA0-32 is lower than that of ASV2CFA0-32 as shown in Table 1. The melting of the ash particles presumably facilitates internal diffusion of KCl. Similar phenomena, that the K-capture amount by coal fly ash increased at 1200 °C and above, was observed by Zheng in a fixed bed study of KCl capture by coal fly ash pellets [37]. Another possible reason is that the Si concentration in AMVCFA0-32 is higher than that in ASV2CFA0-32. The higher Si content facilitated the formation of leucite ($KAlSi_2O_6$) (K:Al:Si = 1:1:2) in the KCl-coal fly ash reaction. A higher C_K of AMVCFA0-32 was observed both in the equilibrium calculations and the EFR experiments at 1300 °C and 1450 °C.

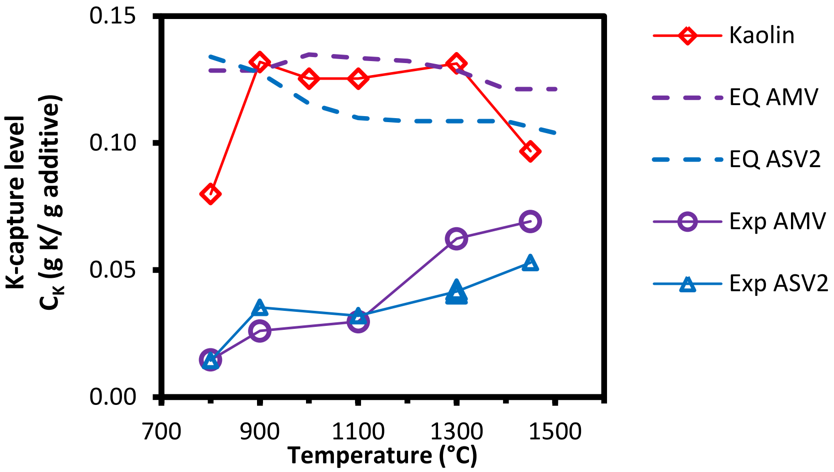

Figure 5. Comparison of C_K of KCl capture by ASV2CFA0-32, AMVCFA0-32 and kaolin [39] at different temperature. KCl-concentration was 500 ppmv with molar ratio of K/(Al+Si) = 0.481, gas residence time was 1.2 s. Equilibrium calculation data of KCl capture by ASV2CA0-32 and AMVCFA0-32 were included for comparison.

3.2 K_2CO_3 capture by coal fly ash

3.2.1 Equilibrium calculation

Equilibrium calculations of K_2CO_3 capture by ASV2CFA0-32 were conducted with a K_2CO_3 concentration of 250 ppmv (K-concentration in flue gas was 500 ppmv), and reaction temperatures changing from 500 °C to 1800 °C. The equilibrium calculation results are summarized in Table 4, and detailed data can be found in Appendix B of the supplementary material.

The equilibrium calculation results generally agreed with the prediction for KOH-capture by ASV2CFA0-32 in our previous study [44]. At 250 ppmv K_2CO_3 (K/(Al+Si) = 0.481) and 800-1300 °C, kaliophilite ($KAlSiO_4$) was predicted to be the dominant K-aluminosilicate in products, together with some (leucite) $KAlSi_2O_6$. At 1450 °C, leucite ($KAlSi_2O_6$) was present as the dominant K-aluminosilicate product. The equilibrium C_K and X_K was constant at 800-1300 °C, and a decreased C_K was predicted at 1450 °C.

3.2.2 Impact of reaction temperature

The measured C_K and X_K of K_2CO_3 capture by ASV2CFA0-32 are compared to the equilibrium calculations in Figure 6, under the conditions of 800-1300 °C, 250 ppmv K_2CO_3 and a gas residence time of 1.2 s. The experimental C_K and X_K of K_2CO_3 capture by kaolin (D_{50} = 5.47 μm) from our previous study [39] were included for comparison. We believe that at the applied temperatures (800°C and above) K_2CO_3 decomposes to KOH that reacts with the coal fly ash.

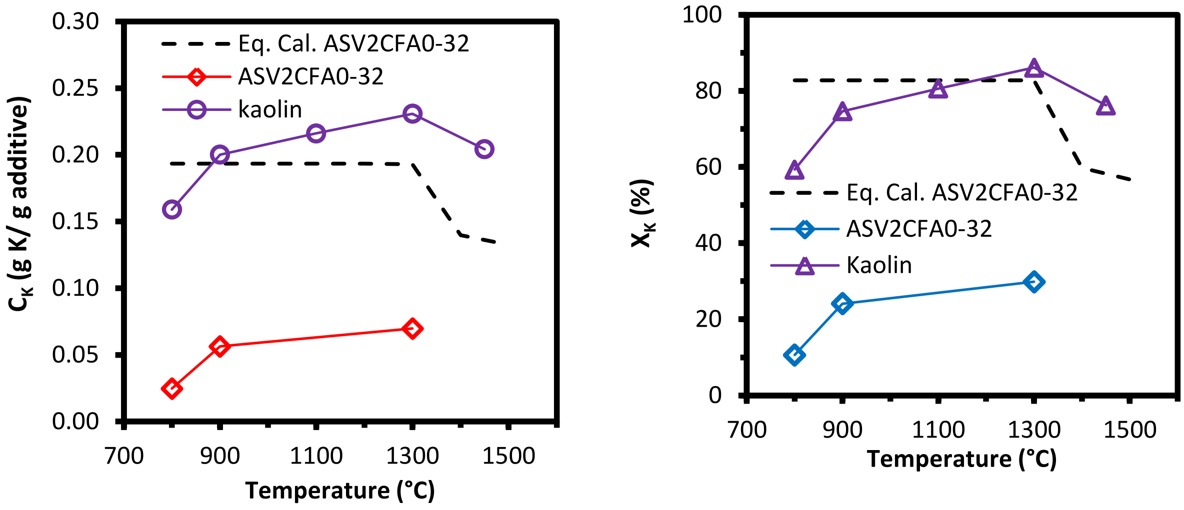

(A) K-capture level C_K (B) K-conversion X_K

Figure 6. K-capture level (C_K) and K-conversion (X_K) of K_2CO_3 capture by ASV2CFA0-32 at 800-1300 °C. K_2CO_3 concentration was 250 ppmv (molar ratio of K/(Al+Si) = 0.481). The gas residence time was 1.2 s. Equilibrium calculation results of K_2CO_3 capture by ASV2CFA0-32, and experimental results of K_2CO_3-capture by kaolin from our previous study [39] are included for comparison.

According to our previous work, the vaporization degree of K_2CO_3 at 800-1450 °C in the EFR was similar (97.3-99.7 %). However, experimental C_K (0.025 g K/(g additive)) at 800 °C was much lower than that at 900 °C (0.056 g K/(g additive)). The significant difference is probably because the reaction was kinetically controlled at 800 °C. When the reaction temperature increased to 1300 °C, C_K increased slightly to 0.070 g K/(g additive). The experimental X_K had the same trend as that of C_K, and it was below 30 % throughout the whole temperature range studied.

The results also show that the experimental C_K and X_K of ASV2CFA0-32 were significantly lower than that of kaolin [39] and the data predicted by equilibrium calculations. The lower BET surface area of coal fly ash (8.04 m^2/g) than that of kaolin (12.70 m^2/g), and the bigger particle size of ASV2CFA0-32 (D_{50} = 12.70 μm) than that of kaolin (D_{50} = 5.47 μm) may cause some of the difference. Another possible reason is that the main mineral phase in ASV2CFA0-32, mullite, was less active towards K_2CO_3. Additionally, the relatively lower Al content of ASV2CFA0-32 may have contributed to the lower C_K as well.

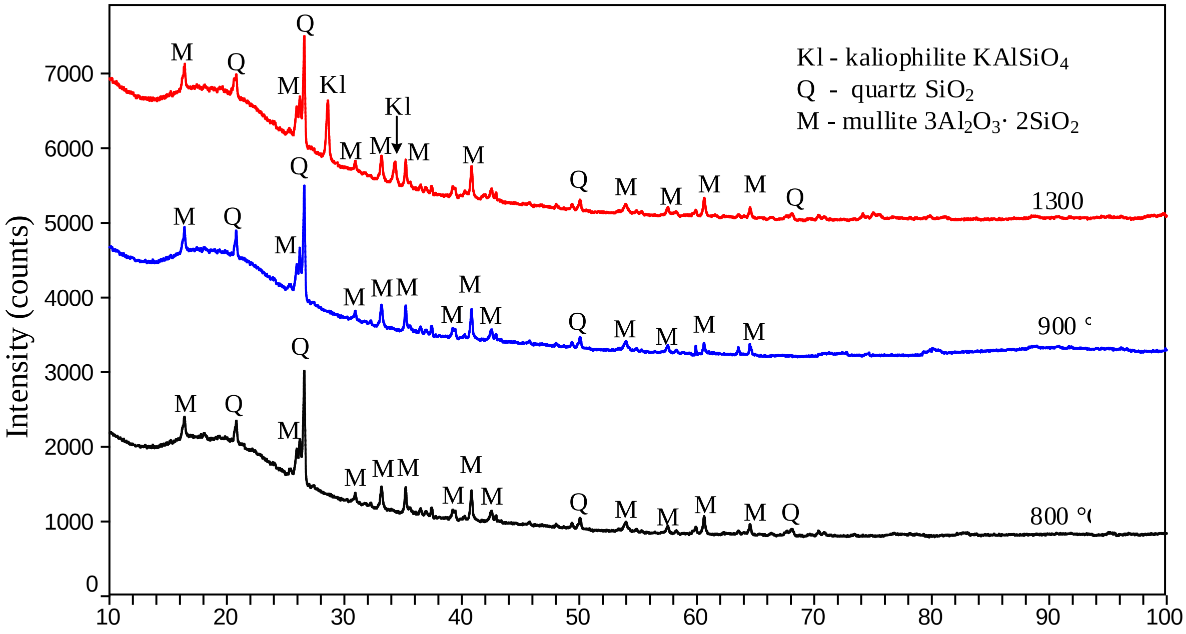

Figure 7. XRD spectra of water-washed K_2CO_3-reacted ASV2CFA0-32. K_2CO_3 concentration in flue gas was 250 ppmv; molar ratio of K/(Al+Si) in reactants was 0.481. Gas residence time was 1.2 s.

The XRD spectra of water-washed K_2CO_3-reacted ASV2CFA0-32 at different temperatures were compared in Figure 7. In the 1300 °C sample, kaliophilite ($KAlSiO_4$) was detected together with mullite and quartz. However, in the 800 °C and 900 °C samples, no crystalline K-aluminosilicate was detected although the ICP-OES analysis showed that the experimental C_K at

900 °C was similar as that of 1300 °C. This is probably because, at 900 °C, only amorphous K-aluminosilicate was formed, and it cannot be detected by XRD.

3.3 K_2SO_4 capture by coal fly ash

3.3.1 Equilibrium calculation

Equilibrium calculations of K_2SO_4 capture by ASV2CFA0-32 were conducted at 250 ppmv K_2SO_4 and a temperature range from 500 °C to 1800 °C. The equilibrium calculation results are summarized in Table 5. Detailed results are provided in Appendix C of the supplementary material.

The equilibrium calculations show that at 800 °C, 900 °C and 1450 °C, leucite ($KAlSi_2O_6$) was predicted to be the dominant K-aluminosilicate product. At 1100 °C and 1300 °C, kaliophilite ($KAlSiO_4$) was predicted to be present as the main K-aluminosilicate in the product. The calculated C_K firstly increased and then decreased with the increasing temperature in the studied temperature range.

3.3.2 Impact of temperature

The experimental C_K and X_K of K_2SO_4 capture by ASV2CFA0-32 are compared with equilibrium calculations as well as the experimental C_K and X_K of K_2SO_4 capture by kaolin [39] in Figure 8. At 800 °C, C_K of ASV2CFA0-32 was 0.013 g K/(g additive), with only 5.7 % K_2SO_4 converted into K-aluminosilicate. The low conversion was partly because of an incomplete vaporization of K_2SO_4, and partly because of that the reaction was slow at 800 °C. At 900 °C and 1300 °C, C_K increased to 0.025 g K/(g additive) and 0.037 g K/(g additive) respectively. However, similar to what was observed for KCl and K_2CO_3 capture by ASV2CFA0-32, the measured C_K and X_K of K_2SO_4 were remarkably lower than the equilibrium data. This is because the fly ash only partly reacted, with some mullite remaining unreacted in products. This was supported by the XRD results discussed below.

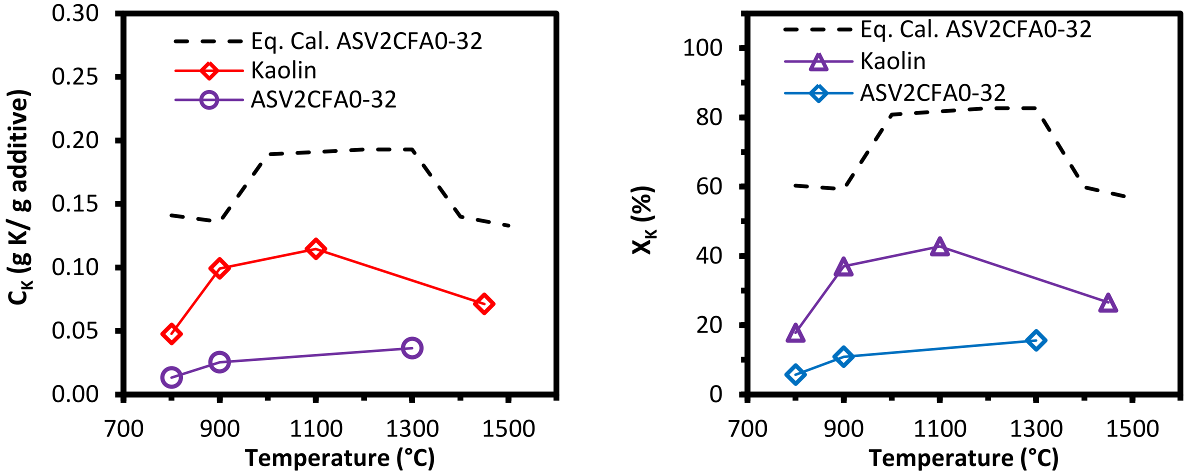

(A) K-capture level (C_K) (B) K-conversion (X_K)

Figure 8. K-capture level (C_K) and K-conversion (X_K) of K_2SO_4 capture by ASV2CFA0-32 at temperatures 800-1300 °C. K_2SO_4 concentration in flue gas was 250 ppmv (K-concentration in flue gas is 500 ppmv), and molar ratio of K/(Al+Si) in reactants was 0.481. The gas residence time was 1.2 s. Equilibrium calculation results of K_2SO_4 capture by ASV2CFA0-32, and experimental C_K of K_2SO_4 capture by kaolin [39] are included for comparison.

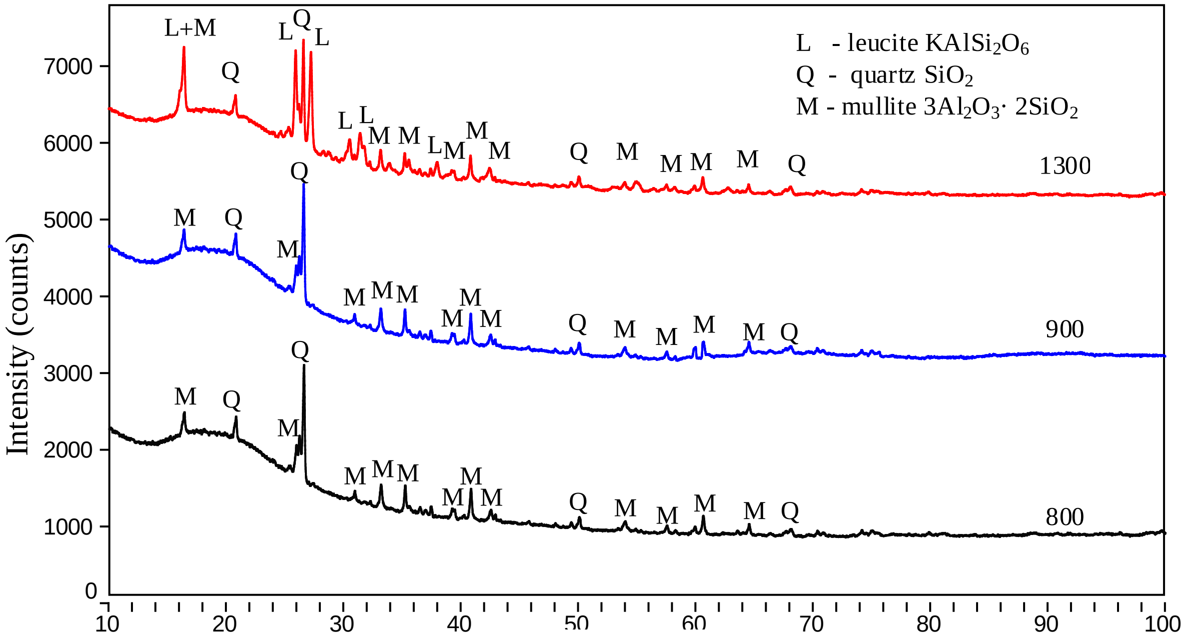

Figure 9. XRD spectra of water-washed K_2SO_4-reacted ASV2CFA0-32 at different temperatures (800, 900 and 1300 °C). K_2SO_4 concentration was 250 ppmv; molar K/(Al+Si) ratio in reactants was 0.481. The gas residence time was 1.2 s.

The XRD spectra of water-washed K_2SO_4-reacted ASV2 coal fly ash are compared in Figure 9. At 800 °C and 900 °C, only mullite and quartz were detected in the products, with no indication of crystalline K-aluminosilicates. In the 1300 °C sample, leucite ($KAlSi_2O_6$) was the only K-aluminosilicate detected, although kaliophilite ($KAlSiO_4$) and leucite ($KAlSi_2O_6$) were predicted to co-exist by the equilibrium calculation. Similar results were observed in the K_2SO_4-kaolin reaction using in our previous study [39].

3.4 Comparison of different K-species

Reaction between ASV2CFA0-32 and different K-species (KOH, K_2CO_3, KCl and K_2SO_4) is compared in Figure 10. The results of KOH-ASV2CFA0-32 reaction are from our previous study [44]. It shows that the K-capture level (C_K) for KOH and K_2CO_3 by ASV2CFA0-32 were very similar (0.05-0.07 g K/(g additive)). We attribute this to a rapid conversion of K_2CO_3 to KOH in the reactor followed by reaction of KOH with ASV2CFA0-32. A similar behavior was observed in our previous study where KOH and K_2CO_3 capture by kaolin was investigated [39]. The trend of C_K of K_2SO_4 capture by ASV2CFA0-32 at different temperatures generally agreed with that of KCl (C_K = 0.02-0.04 g K/(g additive)). Similar results were also seen in our previous study of KCl and K_2SO_4 capture by kaolin [39]. ASV2CFA0-32 captured KOH and K_2CO_3 more effectively than KCl and K_2SO_4 in the studied temperature range and K-concentration.

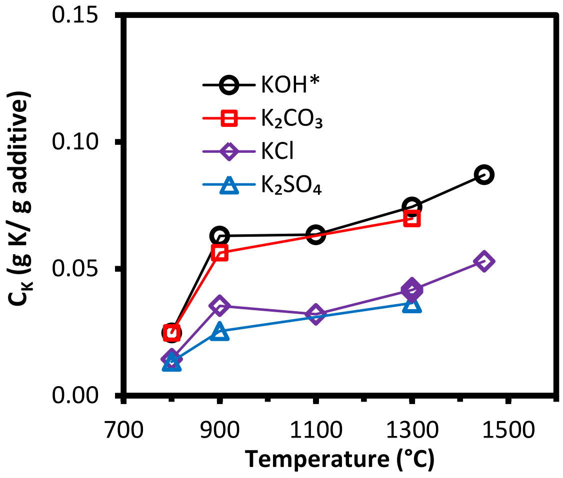

Figure 10. Comparison of C_K of K-capture by ASV2CFA0-32 using different K-species (KOH, K_2CO_3, KCl and K_2SO_4). The K-concentration was 500 ppmv; molar K/(Al+Si) ratio in reactants was 0.481. The gas residence time was 1.2 s. *Data of KOH capture by ASV2CFA0-32 was from our previous study [44].

The results imply that in the case of capturing KCl or K_2SO_4, more additives may be needed to achieve a satisfactory K-capture. The reason for this is that at high temperatures the main product of the reaction with KCl or K_2SO_4, is leucite ($KAlSi_2O_6$) while the main product of reactions with KOH and K_2CO_3 is kaliophilite ($KAlSiO_4$). In addition, coal fly ash with a relatively higher content of Si seems more suitable than coal fly ash with a similar Al and Si contents for K-capture when burning Cl-rich biomass fuels.

4 Conclusions

The K-capture behavior of two coal fly ashes were studied by conducting experiments in an entrained flow reactor and doing chemical equilibrium calculations. The influence of the type of K-species, the K-concentration in flue gas (molar ratio of K/(Al+Si) in reactants), reaction temperature, as well as the type of coal fly ashes on the K-capture reaction was systematically investigated.

For KCl at 1300 °C, the K-capture level (C_K) of coal fly ashes increased from 0.02 g K/(g additive) to 0.04 g K/(g additive) when the KCl concentration increased from 50 ppmv to 500 ppmv (molar ratio of K/(Al+Si) in reactants increased from 0.048 to 0.481). However, C_K did not increase when the KCl concentration increased further to 750 ppmv (molar ratio of K/(Al+Si) = 0.721).

At 800 °C, the K-capture reaction was kinetically limited and a relatively low K-capture level (C_K) was observed for all studied K-species (KOH, KCl, K_2CO_3 and K_2SO_4). At 900 °C and up to 1450 °C, C_K generally increased with increasing reaction temperature for all the applied K-species. Possibly the melting of coal fly ash at high temperature (1300 and 1450 °C) enhanced the internal diffusion of K-species, and resulted a higher C_K values. KOH and K_2CO_3 had similar C_K levels of 0.05-0.07 g K/(g additive), and KCl and K_2SO_4 obtained C_K levels of 0.02-0.04 g K/(g additive) in the temperature range from 900 to 1450°C (with a K-concentration of 500 ppmv, molar K/(Al+Si) ratio in reactants of 0.481, and a residence time of 1.2 s). At high temperature (1300 °C) crystalline kaliophilite ($KAlSiO_4$) was detected in K_2CO_3-reacted coal fly ash, but leucite ($KAlSi_2O_6$) were detected in KCl and K_2SO_4-reacted coal fly ashes. In addition, mullite was detected in reacted coal fly ashes by XRD, showing that coal fly ash remained only partially reacted in the product samples.

The C_K and X_K levels of the two coal fly ashes were compared with that of kaolin from our previous studies [27, 39]. C_K of the two coal fly ashes was obviously lower than that of kaolin at 500 ppmv K (K/(Al+Si) = 0.481). However, at 50 ppmv K (K/(Al+Si) = 0.048), which is comparable to the conditions in full-scale wood suspension-fired boilers, C_K of kaolin and coal fly ash was similar. The AMVCFA0-32 coal ash with a lower melting point and high Si content captured more KCl than ASV2CFA0-32, probably because the internal diffusion of KCl inside the AMV coal ash particles was enhanced by the melting of the coal ash particles, and the high Si content facilitated the formation of leucite ($KAlSi_2O_6$).

Based on the results obtained from this study, some guidelines on using additives in full-scale PF-boilers are summarized below.

- The composition of coal fly ash can affect the K-capture behavior. Bituminous coal ash with high Al and Si contents are preferred as K-capture additive.
- Coal fly ash captures potassium from woody biomass more effectively than from straw (Cl-rich). Dosage of coal ash should be increased when firing herbaceous biomass containing Cl or S, like, straw.

- High-temperature can enhance the K-capture reaction by coal fly ash. Premixing fuel with coal fly ash and feed the mixture into boilers is preferred, since fully mixing and high temperatures can both be obtained.

5 Acknowledgements

This work is part of the project ‘Flexible use of Biomass on PF fired power plants’ funded by Energinet.dk through the ForskEL programme, Ørsted Bioenergy & Thermal Power A/S and DTU.

Supplementary material. Appendix A of the supplementary material: Detailed results of the equilibrium calculations of KCl capture by ASV2CFA0-32; Appendix B of the supplementary material: Detailed results of the equilibrium calculations of K_2CO_3 capture by ASV2CFA0-32; Appendix C of the supplementary material: Detailed results of the equilibrium calculations of K_2SO_4 capture by ASV2CFA0-32; Appendix D of the supplementary material: Detailed results of the equilibrium calculations of KCl capture by AMVCFA0-32.

6 References

[1] Wu H, Glarborg P, Frandsen F J, Dam-Johansen K, Jensen P A. Dust-Firing of Straw and Additives: Ash Chemistry and Deposition Behavior. Energy Fuels 2011; 25: 2862-2873.

[2] Vassilev S V, Baxter D, Andersen L K, Vassileva C G. An overview of the composition and application of biomass ash. Fuel 2013; 105: 19-39.

[3] Johansen J M, Aho M, Paakkinen K, Taipale R, Egsgaard H, Jakobsen J G, Frandsen F J, Glarborg P. Release of K, Cl, and S during combustion and co-combustion with wood of high-chlorine biomass in bench and pilot scale fuel beds. Proc. Combust. Inst. 2013; 34: 2363-2372.

[4] Vassilev S V, Baxter D, Andersen L K, Vassileva C G, Morgan T J. An overview of the organic and inorganic phase composition of biomass. Fuel 2012; 94: 1-33.

[5] Vassilev S V, Baxter D, Andersen L K, Vassileva C G. An overview of the chemical composition of biomass. Fuel 2010; 89: 913-933.

[6] Frandsen F J, Ash Formation, Deposition and Corrosion When Utilizing Straw for Heat and Power Production, in: Department of Chemical and Biochemical Engineering, Technical University of Denmark, Denmark, 2011.

[7] Laxminarayan Y, Jensen P A, Wu H, Frandsen F J, Sander B, Glarborg P. Deposit Shedding in Biomass-Fired Boilers: Shear Adhesion Strength Measurements. Energy Fuels 2017; 31: 8733-8741.

[8] Damoe A J, Jensen P A, Frandsen F J, Wu H, Glarborg P. Fly Ash Formation during Suspension Firing of Biomass: Effects of Residence Time and Fuel Type. Energy Fuels 2017; 31: 555-570.

[9] Li L, Yu C, Huang F, Bai J, Fang M, Luo Z. Study on the Deposits Derived from a Biomass Circulating Fluidized-Bed Boiler. Energy Fuels 2012; 26: 6008-6014.

[10] Anicic B, Lin W, Dam-Johansen K, Wu H. Agglomeration mechanism in biomass fluidized bed combustion – Reaction between potassium carbonate and silica sand. Fuel Process. Technol. 2018; 173: 182-190.

[11] Niu Y, Tan H, Hui S e. Ash-related issues during biomass combustion: Alkali-induced slagging, silicate melt-induced slagging (ash fusion), agglomeration, corrosion, ash utilization, and related countermeasures. Prog. Energy Combust. Sci. 2016; 52: 1-61.

[12] Damoe A J, Wu H, Frandsen F J, Glarborg P, Sander B. Impact of Coal Fly Ash Addition on Combustion Aerosols (PM 2.5) from Full-Scale Suspension-Firing of Pulverized Wood. Energy Fuels 2014; 28: 3217-3223.

[13] Wang G, Shen L, Sheng C. Characterization of Biomass Ashes from Power Plants Firing Agricultural Residues. Energy Fuels 2012; 26: 102-111.

[14] Nielsen H P, Frandsen F J, Dam-Johansen K, Baxter L L. The implications of chlorine-associated corrosion on the operation of biomass-fired boilers. Prog. Energy Combust. Sci. 2000; 26: 283-298.

[15] Nielsen H. Deposition of potassium salts on heat transfer surfaces in straw-fired boilers: a pilot-scale study. Fuel 2000; 79: 131-139.

[16] Hansen L A, Nielsen H P, Frandsen F J, Dam-Johansen K, Hørlyck S, Karlsson A. Influence of deposit formation on corrosion at a straw-fired boiler. Fuel Process. Technol. 2000; 64: 189-209.

[17] Zheng Y, Jensen A D, Johnsson J E. Deactivation of V_2O_5-WO_3-TiO_2 SCR catalyst at a biomass-fired combined heat and power plant. Appl. Catal., B: Environ. 2005; 60: 253-264.

[18] Zheng Y, Jensen A D, Johnsson J E, Thøgersen J R. Deactivation of V_2O_5-WO_3-TiO_2 SCR catalyst at biomass fired power plants: Elucidation of mechanisms by lab- and pilot-scale experiments. Appl. Catal., B: Environ. 2008; 83: 186-194.

[19] Lindberg D, Backman R, Chartrand P. Thermodynamic evaluation and optimization of the ($NaCl+Na_2SO_4+Na_2CO_3+KCl+K_2SO_4+K_2CO_3$) system. The Journal of Chemical Thermodynamics 2007; 39: 1001-1021.

[20] Aho M, Vainikka P, Taipale R, Yrjas P. Effective new chemicals to prevent corrosion due to chlorine in power plant superheaters. Fuel 2008; 87: 647-654.

[21] Davidsson K O, Åmand L E, Steenari B M, Elled A L, Eskilsson D, Leckner B. Countermeasures against alkali-related problems during combustion of biomass in a circulating fluidized bed boiler. Chem. Eng. Sci. 2008; 63: 5314-5329.

[22] Wang L, Skjevrak G, Hustad J E, Grønli M, Skreiberg Ø. Effects of additives on barley straw and husk ashes sintering characteristics. Energy Procedia 2012; 20: 30-39.

[23] Wang L, Hustad J E, Skreiberg Ø, Skjevrak G, Grønli M. A Critical Review on Additives to Reduce Ash Related Operation Problems in Biomass Combustion Applications. Energy Procedia 2012; 20: 20-29.

[24] Xu L, Liu J, Kang Y, Miao Y, Ren W, Wang T. Safely Burning High Alkali Coal with Kaolin Additive in a Pulverized Fuel Boiler. Energy Fuels 2014; 28: 5640-5648.

[25] Steenari B M, Lindqvist O. High-temperature reactions of straw ash and the anti-sintering additives kaolin and dolomite. Biomass Bioenergy 1998; 14: 67-76.

[26] De Fusco L, Boucquey A, Blondeau J, Jeanmart H, Contino F. Fouling propensity of high-phosphorus solid fuels: Predictive criteria and ash deposits characterisation of sunflower hulls with P/Ca-additives in a drop tube furnace. Fuel 2016; 170: 16-26.

[27] Wang G, Jensen P A, Wu H, Frandsen F J, Sander B, Glarborg P. Potassium Capture by Kaolin, Part 1: KOH. Energy Fuels 2018; 32: 1851-1862.

[28] Fuller A, Omidiji Y, Viefhaus T, Maier J, Scheffknecht G. The impact of an additive on fly ash formation/transformation from wood dust combustion in a lab-scale pulverized fuel reactor. Renewable Energy 2019; 136: 732-745.

[29] Zheng Y, Jensen P A, Jensen A D, Sander B, Junker H. Ash transformation during co-firing coal and straw. Fuel 2007; 86: 1008-1020.

[30] Dayton D C, Jenkins B M, Turn S Q, Bakker R R, Williams R B, Belle-Oudry D, Hill L M. Release of Inorganic Constituents from Leached Biomass during Thermal Conversion. Energy Fuels 1999; 13: 860-870.

[31] Jenkins B M, Bakker R R, Wei J B. On the properties of washed straw. Biomass Bioenergy 1996; 10: 177-200.

[32] Turn S, Kinoshita C, Ishimura D, Jenkins B, Zhou J. Leaching of Alkalis in Biomass Using Banagrass as a Prototype Herbaceous Species, National Renewable Energy Laboratory, California, 2003.

[33] Davidsson K O, Korsgren J G, Pettersson J B C, Jäglid U. The effects of fuel washing techniques on alkali release from biomass. Fuel 2002; 81: 137-142.

[34] Oksa M, Auerkari P, Salonen J, Varis T. Nickel-based HVOF coatings promoting high temperature corrosion resistance of biomass-fired power plant boilers. Fuel Process. Technol. 2014; 125: 236-245.

[35] Uusitalo M A, Vuoristo P M J, Mäntylä T A. High temperature corrosion of coatings and boiler steels below chlorine-containing salt deposits. Corros. Sci. 2004; 46: 1311-1331.

[36] Wu H, Bashir M S, Jensen P A, Sander B, Glarborg P. Impact of coal fly ash addition on ash transformation and deposition in a full-scale wood suspension-firing boiler. Fuel 2013; 113: 632-643.

[37] Zheng Y, Jensen P A, Jensen A D. A kinetic study of gaseous potassium capture by coal minerals in a high temperature fixed-bed reactor. Fuel 2008; 87: 3304-3312.

[38] Liu Y, Duan X, Cao X, Che D, Liu K. Experimental study on adsorption of potassium vapor in flue gas by coal ash. Powder Technol. 2017; 318: 170-176.

[39] Wang G, Jensen P A, Wu H, Frandsen F J, Sander B, Glarborg P. Potassium Capture by Kaolin, Part 2: K_2CO_3, KCl and K_2SO_4. Energy Fuels 2018; 32: 3566-3578.

[40] Punjak W A, Uberoi M, Shadman F. High-temperature adsorption of alkali vapors on solid sorbents. AlChE J. 1989; 35: 1186-1194.

[41] Punjak W A, Shadman F. Aluminosilicate sorbents for control of alkali vapors during coal combustion and gasification. Energy Fuels 1988; 2: 702-708.

[42] Tran K-Q, Iisa K, Steenari B-M, Lindqvist O. A kinetic study of gaseous alkali capture by kaolin in the fixed bed reactor equipped with an alkali detector. Fuel 2005; 84: 169-175.

[43] Aho M, Ferrer E. Importance of coal ash composition in protecting the boiler against chlorine deposition during combustion of chlorine-rich biomass. Fuel 2005; 84: 201-212.

[44] Wang G, Jensen P A, Wu H, Frandsen F J, Laxminarayan Y, Sander B, Glarborg P. KOH capture by coal fly ash. Fuel 2019; 242: 828-836.

[45] Izquierdo M, Querol X. Leaching behaviour of elements from coal combustion fly ash: An overview. International Journal of Coal Geology 2012; 94: 54-66.

[46] Kim A G, Kazonich G, Dahlberg M. Relative Solubility of Cations in Class F Fly Ash. Environmental Science & Technology 2003; 37: 4507-4511.

[47] Blissett R S, Rowson N A. A review of the multi-component utilisation of coal fly ash. Fuel 2012; 97: 1-23.

[48] Vassilev S V, Vassileva C G. A new approach for the classification of coal fly ashes based on their origin, composition, properties, and behaviour. Fuel 2007; 86: 1490-1512.

[49] Bashir M S, Jensen P A, Frandsen F J, Wedel S, Dam-johansen K, Wadenbäck J. Suspension-Firing of Biomass. Part 2: Boiler Measurements of Ash Deposit Shedding. Energy Fuels 2012.

[50] Bashir M S, Jensen P A, Frandsen F J, Wedel S, Dam-johansen K, Wadenbäck J, Pedersen S T. Suspension-Firing of Biomass . Part 1 : Full-Scale Measurements of Ash Deposit Build-up. Energy Fuels 2012; 26: 2317-2330.

[51] Wu H, Bashir M S, Jensen P A. Full-scale ash deposition measurements at Avedøre Power Plant unit 2 during suspension-firing of wood with and without coal ash addition, Technical University of Denmark, Denmark, 2012.

Potassium Capture by Coal Fly Ash: K_2CO_3, KCl and K_2SO_4: Supplementary Material

Guoliang Wang [a*], *Peter Arendt Jensen* [a], *Hao Wu* [a], *Flemming Jappe Frandsen* [a], *Yashasvi Laxminarayan* [a], *Bo Sander* [b], *Peter Glarborg* [a]

[a] Department of Chemical and Biochemical Engineering, Technical University of Denmark,
Søltofts Plads, Building 229, DK-2800 Kgs. Lyngby, Denmark

[b] Ørsted Bioenergy & Thermal Power A/S, Kraftværksvej 53, 7000 Fredericia, Denmark

Keywords: Coal fly ash, potassium capture, biomass combustion, additive, K_2CO_3, KCl, K_2SO_4

[*]Corresponding Author E-mail: guow@kt.dtu.dk

Appendix I: Quantification of potassium capture reaction

Two parameters have been defined in this study to quantify the potassium capture reaction between K-salts and coal fly ash: K-conversion (X_K) and K-capture level (C_K). K-conversion (X_K) is the fraction (%) of fed K-salts chemically captured by solid additive (coal fly ash) forming water-insoluble K-aluminosilicates. K-capture level (C_K) is the mass of potassium captured by 1 g of additive (coal fly ash) (g K/g additive).

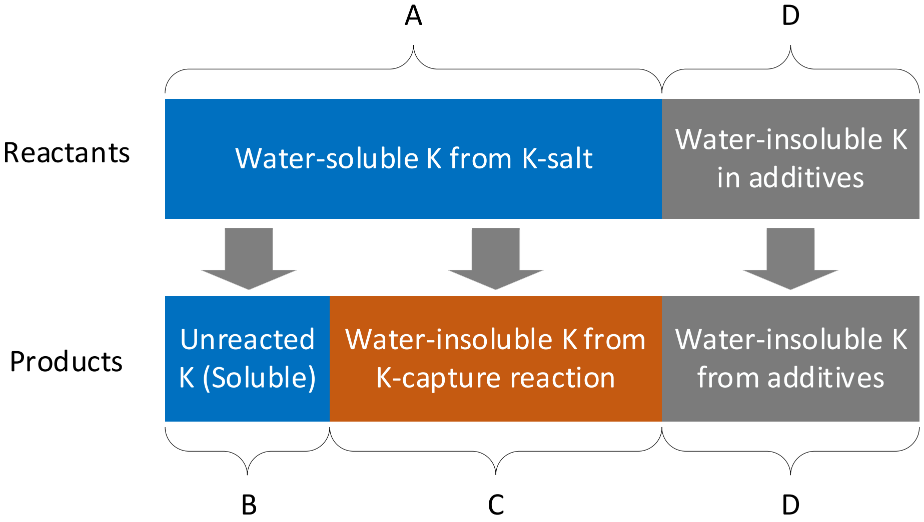

Figure 1. Potassium transformation during the reaction between K-salts and solid additives (coal fly ash).

As shown in Figure 1, in the reactants, potassium is composed of water-soluble potassium from K-salts (A), and water-insoluble potassium (D) from additive. During the K-capture reaction, a fraction of water-soluble potassium reacted with coal fly ash forming water-insoluble K-aluminosilicate (C). The rest water-soluble K-salt did not react and remained water-soluble (B).

Based on this transformation, K-conversion (X_K), and K-capture level (C_K) can are fined as equation (1) and (2).

$$X_K = \frac{C}{A} \times 100\ \% \qquad (1)$$

$$C_K = \frac{n_{KOH} M_K X_K}{m_{ad.}} \qquad (2)$$

In equation (1), C is the molar amount of water-insoluble potassium formed through the K-capture reaction, and A is the molar amount of K-salt fed into the reactor, as shown in Figure 1. In equation (2), n_{Ksalt} (mol) is the molar amount of K-salt fed into the reactor, M_K is the molar mass of potassium (39 g/mol) and $m_{ad.}$ is the mass of solid additives fed into the reactor (g). The K-conversion (X_K) can be calculated according to Equation (3).

$$X_K = \frac{C}{A} = \frac{A-B}{A} = \frac{\frac{A}{A+D} - \frac{B}{A+D}}{\frac{A}{A+D}} = \frac{Y_F - Y_P}{Y_F} \times 100\% \qquad (3)$$

Where Y_F and Y_P are the molar ratio of water-soluble K to total K in the reactants and collected solid products, respectively. Y_F can be calculated based on the constituents of slurry and potassium content in utilized additives, while Y_P can be calculated based on the ICP-OES result of collected solid samples. Consequently, C_K can be calculated based on X_K according to Equation (2).

Appendix II: Equilibrium calculation

In order to understand the mechanisms of the K-capture reaction by coal fly ash, equilibrium calculations of KCl, K_2CO_3 and K_2SO_4 capture by coal fly ash were conducted using the equilibrium module of FactSage 7.0. Four databases, including FactPS, FToxid, FTsalt and FTpulp were employed in the calculations. Gas, liquid and solid compounds were included in the product phase. Detailed description of the databases can be found in literatures [1, 2]. The input elements for all calculations are listed in Table 1. The calculation results of KCl capture by ASV2CFA0-32 were shown in Figure 2(A-E). The results on K_2CO_3 and K_2SO_4 capture by ASV2CFA0-32 were shown in Figure 3 and Figure 4, respectively.

Table 1. Input conditions for equilibrium calculation of KCl, K_2CO_3 and K_2SO_4 capture by ASV2CFA0-32 and AMVCFA0-32.

Additive	K-salts	Conditions	Input elements (mol)													
			Al	Si	Fe	Ca	Mg	Na	K	Cl	S	P	O	N	H	C
ASV2CFA 0-32	KCl	50 ppmv K, K/(Al+Si) = 0.048	8.28	12.37	0.86	1.88	0.67	0.20	1.00	1.09	0.14	0.34	9927.86	31564.90	3011.24	39.09
		250 ppmv K, K/(Al+Si) = 0.240	1.66	2.47	0.17	0.38	0.13	0.04	1.00	1.02	0.03	0.07	1921.74	6095.19	589.80	7.76
		500 ppmv K, K/(Al+Si) = 0.481	0.83	1.24	0.09	0.19	0.07	0.02	1.00	1.01	0.01	0.03	965.02	3050.86	300.96	3.88
		750 ppmv K, K/(Al+Si) = 0.721	0.55	0.82	0.06	0.13	0.04	0.01	1.00	1.01	0.01	0.02	644.68	2031.73	204.13	2.59
		1000 ppmv K, K/(Al+Si) = 0.961	0.41	0.62	0.04	0.09	0.03	0.01	1.00	1.00	0.01	0.02	489.06	1576.69	135.78	1.95
	K_2CO_3	500 ppmv K, K/(Al+Si) = 0.481	0.83	1.23	0.09	0.19	0.07	0.02	1.00	0.01	0.01	0.03	914.34	2825.33	316.54	4.71
	K_2SO_4	500 ppmv K, K/(Al+Si) = 0.481	0.83	1.23	0.09	0.19	0.07	0.02	1.00	0.01	0.51	0.03	903.48	2827.02	294.91	4.21
AMVCFA 0-32	KCl	500 ppmv K, K/(Al+Si) = 0.481	0.63	1.39	0.14	0.18	0.10	0.07	1.00	0.01	0.01	0.02	904.40	2826.38	299.59	3.83

A. Detailed equilibrium calculation results of KCl capture by ASV2CFA0-32.

The equilibrium calculation results of KCl capture by ASV2CFA0-32 are shown in Figure 2 (A-E). The primary Y-axis (left Y-axis) is the fraction of different K-compounds or the conversion fraction (%) of K, Al or Si forming K-aluminosilicates. The secondary Y-axis (right Y-axis) is the K-capture level (C_K, g K/g additive). The KCl concentration in flue gas was 50, 250, 500, 750 and 1000 ppmv. Corresponding molar ratio of K/(Al+Si) in reactants was varied from 0.048 to 0.961. The reaction temperature was changed from 500 °C to 1800 °C.

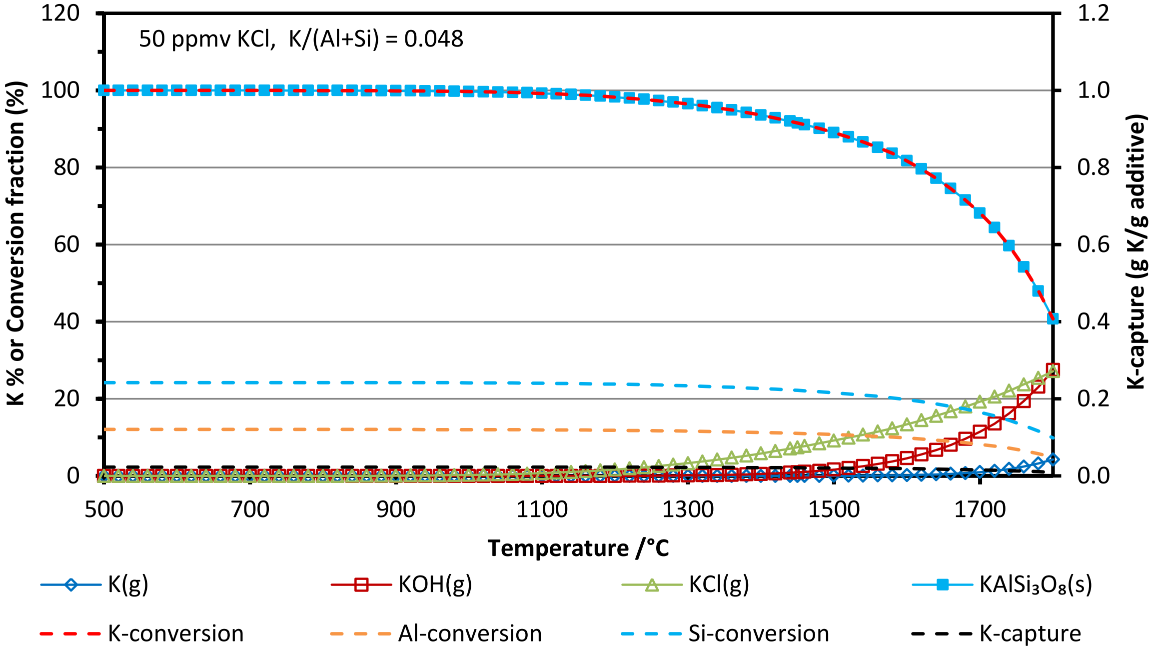

(A) 50 ppmv KCl, K/(Al+Si) = 0.048

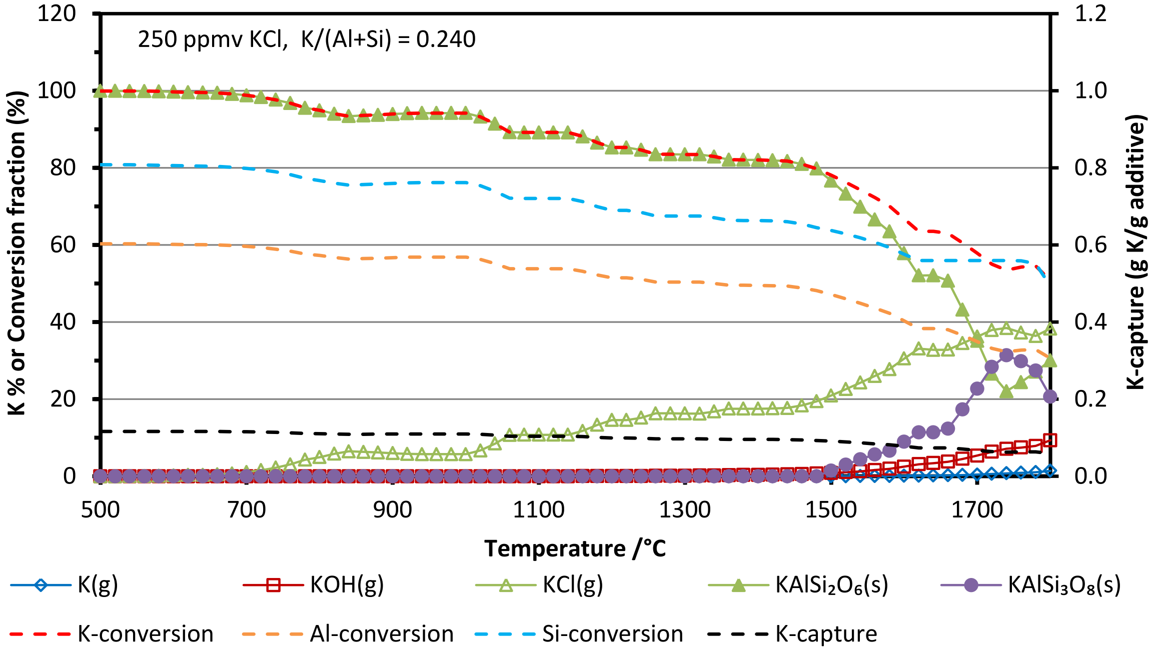

(B) 250 ppmv KCl, K/(Al+Si) = 0.240

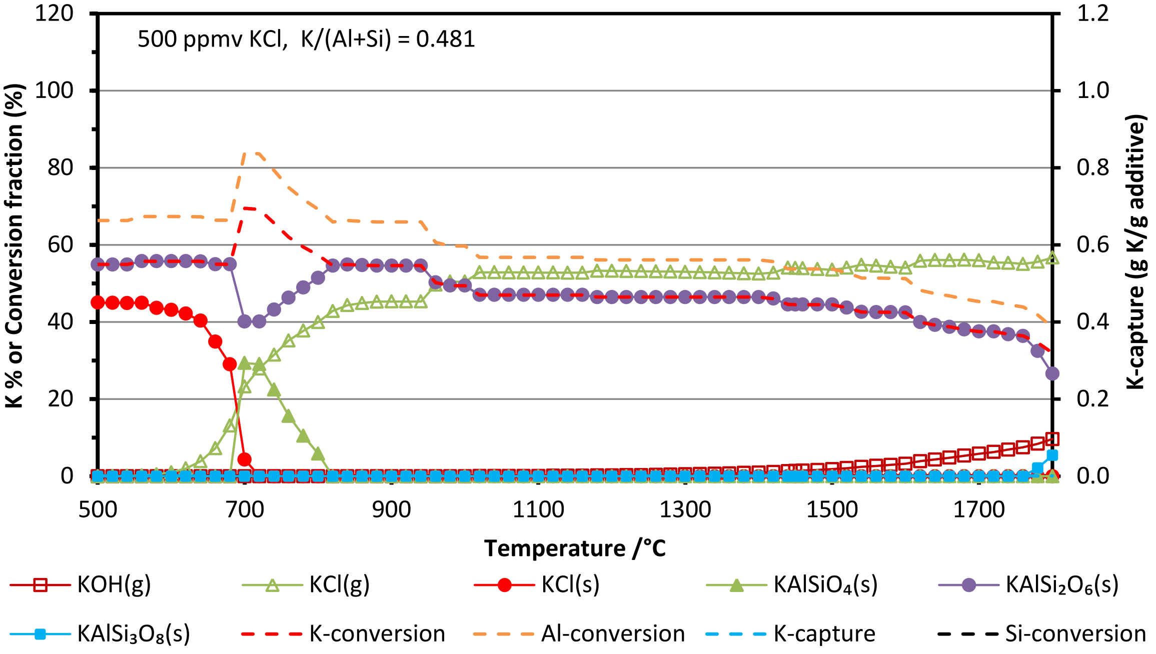

(C) 500 ppmv KCl, K/(Al+Si) = 0.481

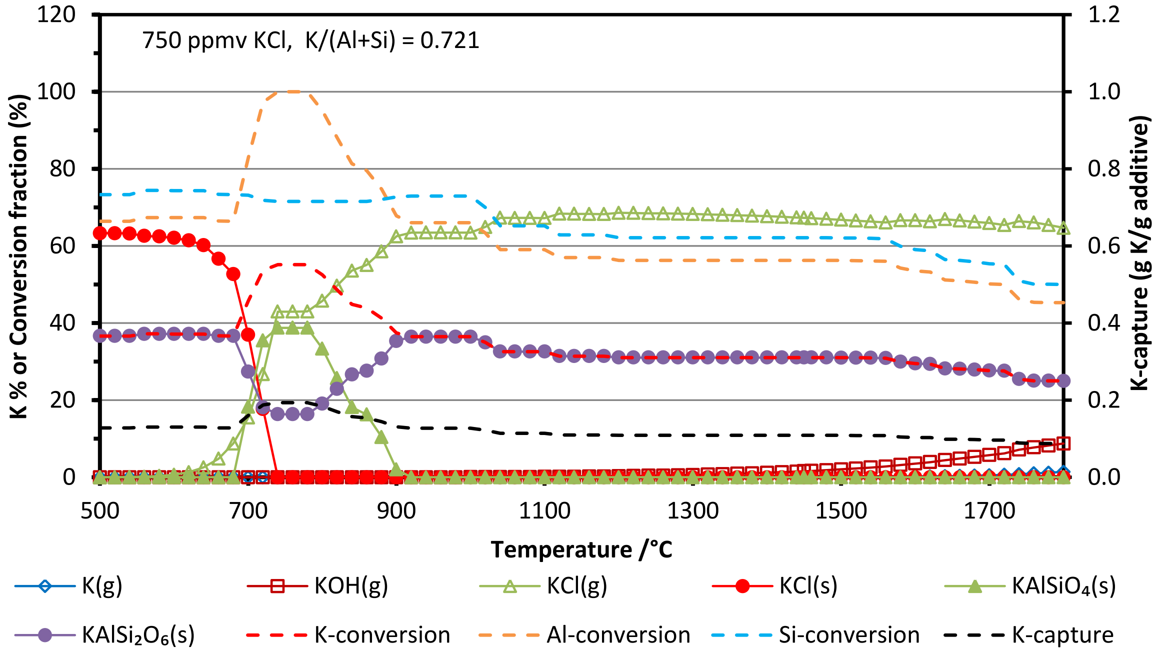

(D) 750 ppmv KCl, K/(Al+Si) = 0.721

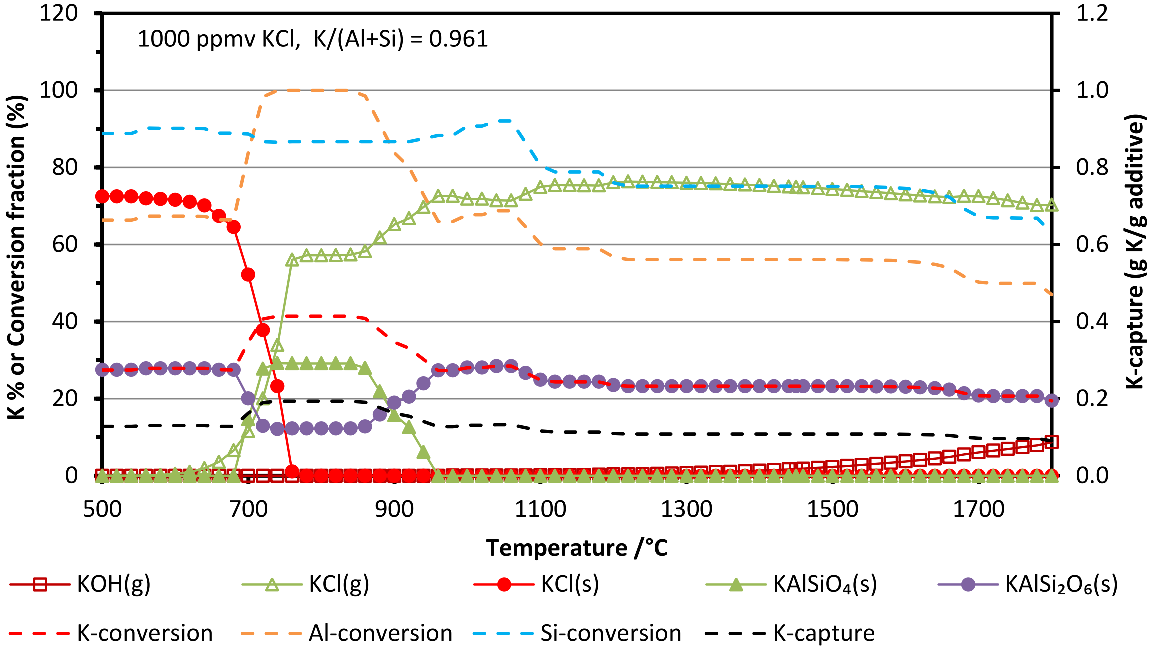

(E) 1000 ppmv KCl, K/(Al+Si) = 0.961

Figure 2. Detailed equilibrium calculation results of KCl capture by ASV2CFA0-32.

B. Detailed equilibrium calculation results of K_2CO_3 capture by ASV2CFA0-32.

The equilibrium calculations of K_2CO_3 capture by ASV2 coal fly ash 0-32 µm (ASV2CFA0-32) were performed with a K_2CO_3 concentration of 250 ppmv in the flue gas (K-concentration was 500 ppmv). The reaction temperature varied from 500 °C to 1800 °C. The detailed results of the equilibrium calculations were shown in Figure 3.

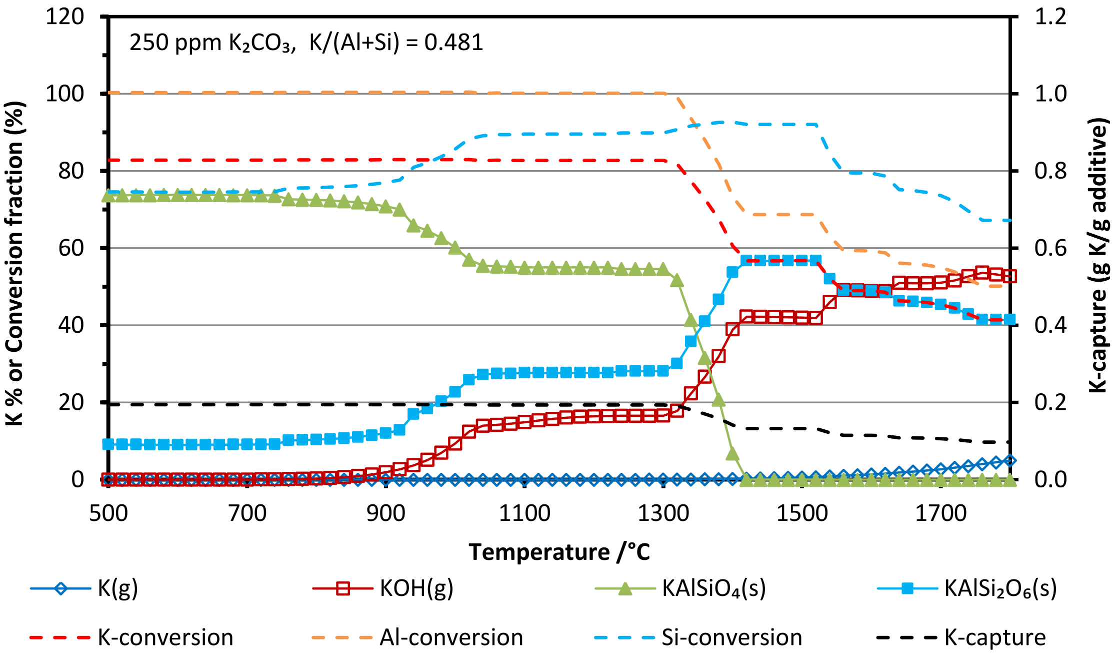

Figure 3. Equilibrium calculation results of K_2CO_3 capture by ASV2CFA0-32. K_2CO_3 concentration in flue gas was 250 ppmv.

C. Detailed equilibrium calculation results of K_2SO_4 capture by ASV2CFA0-32.

The equilibrium calculations of K_2SO_4 capture by ASV2CFA0-32 was conducted with a K_2SO_4 concentration of 250 ppmv in the flue gas (K-concentration was 500 ppmv). The reaction temperature varied from 500 °C to 1800 °C. The detailed results of the equilibrium calculations were shown in Figure 4.

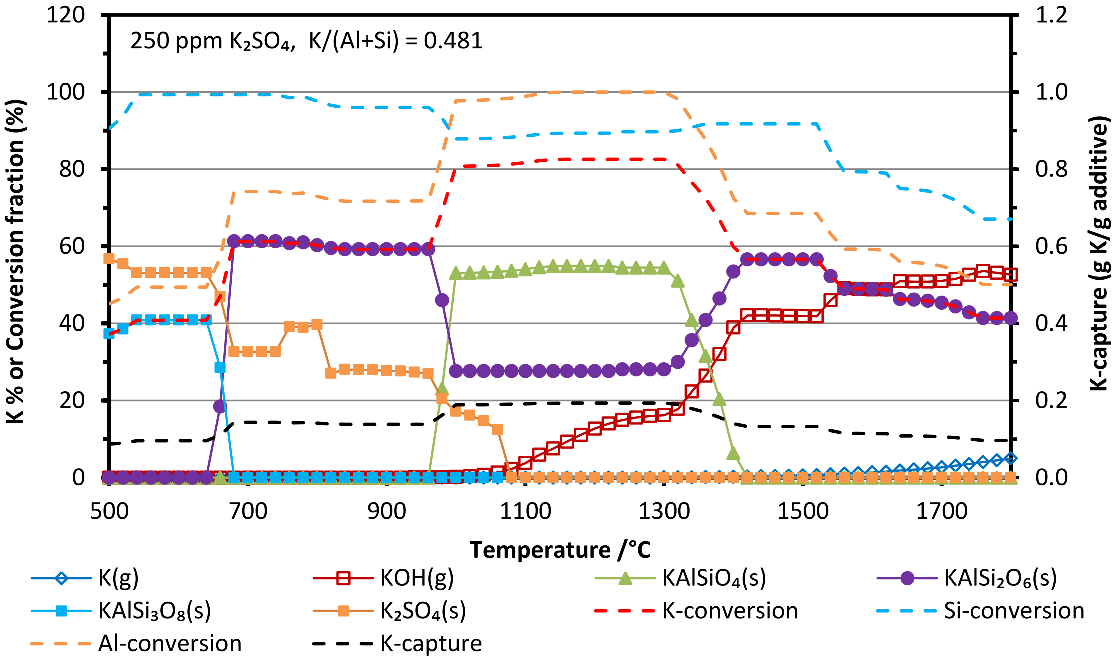

Figure 4. Detailed equilibrium calculation results of K_2SO_4 capture by ASV2CFA0-32. K_2SO_4 concentration in flue gas was 250 ppmv.

D. Detailed equilibrium calculation results of KCl capture by AMVCFA0-32.

The equilibrium calculations of KCl capture by AMV coal fly ash 0-32 μm (AMVCFA0-32) were performed with a KCl concentration of 500 ppmv in the flue gas. The reaction temperature varied from 500 °C to 1800 °C. The detailed results of the equilibrium calculations were shown in Figure 5.

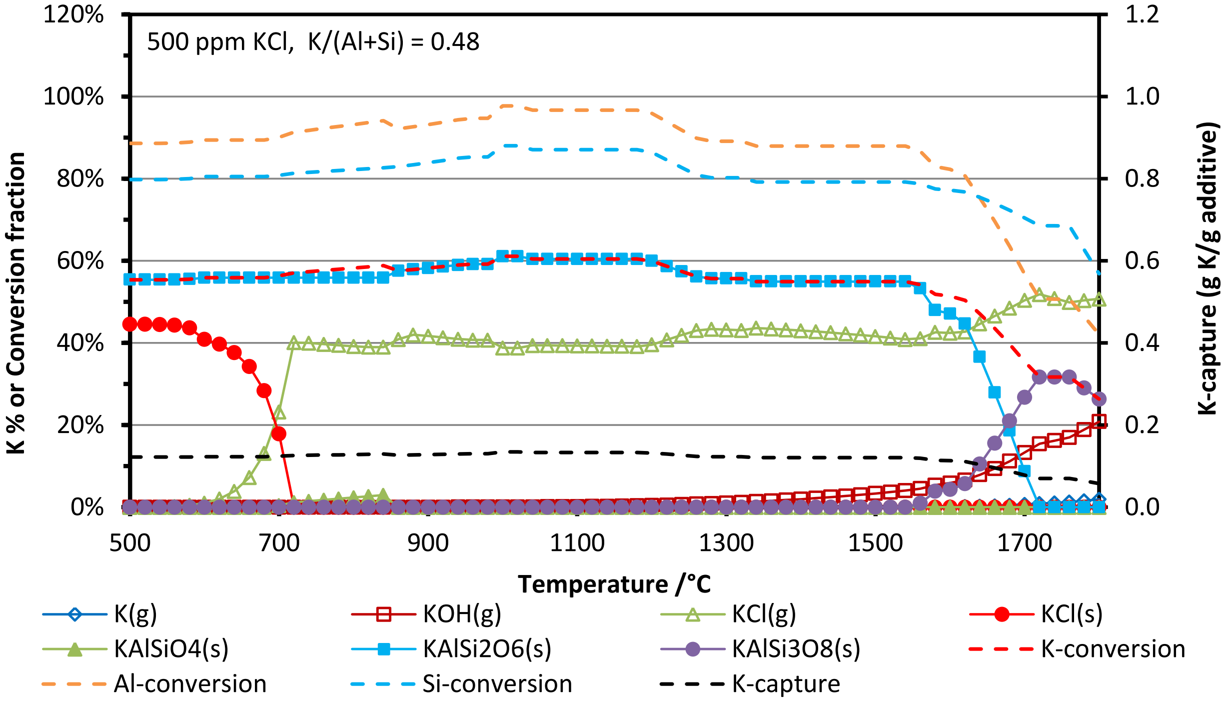

Figure 5. Detailed equilibrium calculation results of KCl capture by AMVCFA0-32. KCl concentration in flue gas was 500 ppmv.

[1] Bale CW, Bélisle E, Chartrand P, Decterov SA, Eriksson G, Hack K, et al. FactSage thermochemical software and databases — recent developments. Calphad. 2009;33:295-311.

[2] Bale CW, Chartrand P, Degterov SA, Eriksson G, Hack K, Ben Mahfoud R, et al. FactSage thermochemical software and databases. Calphad. 2002;26:189-228.

July 2019

ForskEL project no. 12150/EUDP 64018-003

Final report: Flexible use of biomass on PF Fired power plants

Appendix H. Journal paper: Schwarzer, L., Sárossy, Z., Jensen, P.A., Glarborg, P., Holm, J.K., Dam-Johansen, K.: Kinetic parameters for biomass at self-ignition conditions: Low-temperature oxidation and pyrolysis. Submitted to Energy & Fuels 2019.

1. **Department of Chemical and Biochemical Engineering**
Technical University of Denmark
Søltofts Plads, Building 229, DK-2800, Kgs. Lyngby, Denmark
2. **Ørsted Bioenergy & Thermal power,**
Kraftværksvej 53, DK-7000, Fredericia, Denmark

CHEC no. R1902

Kinetic parameters for biomass at self-ignition conditions: low-temperature oxidation and pyrolysis

Lars Schwarzer,*,† Zsuzsa Sárossy,† Peter Arendt Jensen,*,† Peter Glarborg,†
Jens Kai Holm,‡ and Kim Dam-Johansen†

†*Department of Chemical and Biochemical Engineering, Technical University of Denmark, Søltofts Plads 229, 2800 Kgs. Lyngby, Denmark*
‡*Ørsted A/S, Nesa Allé 1, 2820 Gentofte, Denmark*

E-mail: laschw@kt.dtu.dk; paj@kt.dtu.dk

Abstract

Pulverized biomass may self-heat and spontaneously ignite when stored or processed at intermediate or even low temperatures. In this work, reaction kinetic parameters for biomass oxidation and pyrolysis were determined for the temperature range 423–523 K. Thermogravimetric analysis was used to determine mass loss kinetics in a stepwise-isothermal heating program. Two wood species (pine, beech), two agricultural residues (wheat straw, sunflower husks) and two commercial wood pellet samples were investigated. Atmospheres with 0 %, 20 % and 80 % oxygen were used in the experiments. A pyrolysis model of four parallel reactions for extractives, hemicellulose, celluose and lignin fit the experimental data for 0 % O_2 well. Oxidation kinetics could be modelled by additional reactions in parallel to the pyrolysis mechanism. Two mechanisms were tested: (1) considering oxidation of a lumped

’volatilizable’ component plus oxidation of char; and (2) separate oxidation reactions for volatilizable extractives, hemicellulose, celluose and lignin, plus char. The more complex mechanism did not give a clear advantage over the simpler mechanism. It was further found that pyrolysis and oxidation reactions for the components could be modelled with the same activation energy, regardless of which biomass they appear in. For the lumped component oxidation model, an apparent activation energy of 130 kJ/mol was found. The observed reaction order in oxygen was in range 0.4–0.5. The models also compared favorably to additional experimental data between 373–773 K for a heating rate of 5 K/ min. The kinetic models presented here are intended mainly to describe low-temperature reactions, such as self-heating of biomass and the onset of smoldering combustion.

1 Introduction

Biomass can replace coal as a fuel for heat and power generation in pulverized fuel fired boilers. One recent example is the conversion of Danish combined heat and power (CHP) plants originally built as pulverized-coal fired boilers. This technological switch requires to store and process solid biomass materials, mainly in form of pellets, in large quantities. In CHP-facilities, fires have occured in storages and power plant mills that were likely caused by spontaneous ignition. Excessive self-heating, leading to thermal decomposition and ignition, is a known problem for storages.[1,2] To the authors’ knowledge, the role of self-ignition of biomass in mill fires, i.e. at elevated temperatures above 423 K, has not been explicitly researched. However, based on older studies of coal mills, settled dust beds may build up and self-ignite in these devices.[3–5] Predicting such events requires accurate reaction kinetic data for low temperatures. Unfortunately, such data are scarce for typical fuels such as wood pellets and agricultural residues.

Additionally, there does not appear to be a consensus on the appropriate kinetic model for low temperature oxidative conversion. Different researchers have proposed single-reaction models,[1,6–10] models with two or more parallel reactions,[11–17] models with two or more sequential reactions,[18–20] and models involving combinations of serial and parallel reactions.[21–26] Where several reactions are used, these have been used to distinguish between pyrolysis and oxidation, between different biomass components, or different stages of pyrolysis and/or oxidation reaction pathways. A short overview will be given below in the light of determining kinetic parameters at temperatures relevant to self-heating in power plant mills.

If only a single reaction is used to model low temperature oxidation, the reported kinetic parameters vary widely. Activation energies for wood pellets from isothermal calorimetry at low temperatures (300–350 K) have been measured as 50–80 kJ/mol.[1,7] From oven heating tests, 89 kJ/mol are reported for mahogany wood at 375–450 K.[11] Data compiled from oven tests of different wood species at 370–570 K result in activation energies of 110–125 kJ/mol.[6]

From self-ignition oven tests according to EN 15188, activation energies of 139 kJ/mol and 207 kJ/mol are reported for sunflower husk pellets and softwood chips, respectively.[10] Kinetic parameters from tests on larger samples may also be influenced by heat and mass transfer limitations. Thermogravimetric analysis (TGA) is considered a method to avoid such transport limitations. Single-reaction models have been fit to TGA data, and activation energies for oxidation of forestry and agricultural residues are given in the range of 61–68 kJ/mol (at 293–1073 K)[9] and 75–116 kJ/mol (at 500–630 K).[8]

Thermogravimetric analysis has also been used to determine reaction kinetic parameters for biomass oxidation and pyrolysis in more complex models.[12–20,22–26] The most widespread method is to conduct experiments at several constant heating rates from ambient conditions to temperatures exceeding 873 K or higher. The experimental data are in turn used to fit the parameters of a reaction model consisting of two or more seuqential or parallel reactions, so that this best matches the conversion rate dX/dt as a function of temperature. Mass loss at low temperatures (<470–525 K) is frequently very low, however, and not well resolved in the reported experimental data. In the few cases in which mass loss is reported at these temperatures, it is attributed to evaporation of moisture.[25,26] In both of those cited works, the evaporation peak is also clearly offset from oxidation and/or pyrolysis of the organic fraction when plotting conversion rate over temperature. Significant thermal or oxidative degradation below 470 K is not described in any of the cited TGA-studies.[12–20,22–26] Comparison with the experiments at low temperatures (370–570 K) and long holding times (minutes to years),[1,6,7,11] where significant conversion of the organic fraction is observed, suggests that the heating rates used in typical TGA-studies are too high to resolve the slow reactions at low temperatures. While experimental procedures slightly vary among researchers,[12–20,22–26] the lower bound for heating rates is usually 5–10 K/ min (Anca-Couce et al.[14] also investigated 2.5 K/ min), with an upper bound of typically 20–40 K/ min. Such heating rates are interesting to describe propagation of smoldering combustion, which is associated with heating rates in order of 10–1000 K/ min.[21] In contrast, this work focuses on the initiation and onset of smoldering. Based on practical experience with ignition in mill fires, it is suspected that this incipient smoldering occurs on much larger timescales and at lower temperatures. Isothermal[27–30] and stepwise isothermal thermogravimetric analysis[31,32] have been used to investigate torrefaction reactions (a mild pyrolysis, ≈473–573 K), while only few comparable works are available for oxidative atmosphere (e.g.,[33]).

The aim of this work is to extend kinetic models of devolatilization and oxidation to lower temperatures and heating rates. We present a model to describe mass loss kinetics for six different biomasses, distinguishing between pyrolysis and heterogeneous oxidation as parallel processes. Thermogravimetric analysis with stepwise isothermal programs in the range of 423–523 K is used to find the values of the kinetic parameters for each of the biomasses investigated. The oxygen concentration is varied in the experiments (0 %, 20 % and 80 % oxygen) to separate purely thermal decomposition (pyrolysis) from oxidative reactions, and to determine the influence of oxygen on the reaction rates. The kinetic models found for low temperatures under isothermal conditions are then compared to thermogravimetric experiments at intermediate heating rates (5 K/ min) and temperature ranges 373–773 K to ensure that they are consistent with the data available in the literature for those conditions.

2 Experimental

Six different biomasses were investigated: beech wood, pine wood and wheat straw as raw materials, as well as two types of wood pellets obtained from a local CHP-plant, and a sample of sunflower husk pellets as commercial pelletized fuels. Additionally, experiments were carried out with cellulose (*Sigma-Aldrich* C6288), xylan (from cornstalk; *abcr Chemie* AB143294) and lignin (alkali; *Sigma-Aldrich* 471003). Rapeseed oil was used as a model substance for extractives, as it contains a mix of saturated and unsaturated fatty acids (mainly C18:1 and C18:2). Unsaturated fatty acids may play a role in the autooxidation of biomass.[2] In order to model extractives bound in a matrix, experiments were carried out with mixtures of oil and SiO_2 as well as oil and cellulose, both 50 %/50 % by weight.

The two woods were provided in pulverized form (beech: 0–250 µm, pine: 50–200 µm). The other biomass samples were milled and a size fraction <125 µm was used in the experiments. Cellulose, lignin and xylan were used as provided by the manufacturer. Information on the chemical properties of the six biomass materials used is found in Table 1. Results from proximate and ultimate analysis fall within the range of values typically found in the literature, although pine and wood pellets appear to have low char and high volatile contents. Of the inorganic elements present in the samples, especially potassium and sodium are known to have a catalytic effect on thermal conversion.[30,34–37] Other metals observed to have catalytic effects are magnesium[30] and, to a lesser extent, calcium.[34]

2.1 Biopolymer analysis

Klason lignin and carbohydrate composition of the six samples were determined by sulfuric acid hydrolysis. 1.5 mL of 72 % H_2SO_4 were added to 0.16 g sample, which was prehydrolyzed for 60 minutes at 303 K. After dilution of the hydrolyzate with Milli-Q purified water (42 mL), the liquid samples were autoclaved at 393 K for further 60 minutes. Filtered liquids were analyzed on an HPLC (high-pressure/high-performance liquid chromatography) column, while the solid residue was heated to 823 K to determine the lignin ash content. Results are summarized in Table 1. For the two wood pellet samples, analyses from an external lab were available. The results agreed with the ones presented here within ±0.01 kg/kg, with the exception of glucose (0.401 kg/kg and 0.395 kg/kg for wood pellets I1 and I2, repsectively), which showed slightly larger deviations.

Acid methanolysis and GC-MS (gas chromatography – mass spectrometry) was applied to three of the biomass samples in order to separate and quantify their hemicellulose-bound glucose content. The method is described elsewhere in more detail.[38] The analysis was done in duplicate and results were repeatable within 10 % of the reported values. Data is included in Table 1, based on the total dry matter.

Extractives were measured following a procedure based on an NREL report, *Determination of Extractives in Biomass* (NREL/TP-510-42619). Lipids were extracted with ethanol (96 v/v%) in a Soxhlet extractor for 6 hours to measure the amount of total extractives. The extracts were then chemically modified with 1.25 M HCl in methanol to produce fatty acid methyl esters, so that the fatty acids become detectable for the GC-MS instrument. An Agilent 7890B gas chromatograph interfaced to an Agilent 5977B Mass Selective Detector was used in this part of the study. Samples of 1 µL were injected in split mode (1:20). The source and rod temperatures were 503 K and 423 K, respectively. The products were separated using two HP-5ms ultra inert columns (15 m, 0.25 mm, 0.25 µm coating). Separation of products was achieved using a temperature program from 343–523 K at 10 K/ min. Results are included in Table 1, where the relative abundance of the C 16:0–C 22:0 fatty acids are given for each biomass. The fatty acid values given are proportions, and do not allow an absolute quantification.

Table 1: Proximate, elemental and compositional analysis of the biomasses used used in this study. Difference to one in the sum of the compositional analysis is balance error.

	Beech	Pine	Sunflower	Wheat	W. pellets I1	W. pellets I2
Proximate analysis, dry base [kg/kg]						
Volatiles	0.771	0.856	0.756	0.774	0.845	0.839
Char	0.202	0.141	0.193	0.184	0.149	0.155
Ash	0.027	0.003	0.052	0.042	0.006	0.006
Moisture (average)	0.059	0.049	0.085	0.061	0.060	0.057
Elemental analysis, dry base [kg/kg]						
C	0.512	0.528	0.521	0.480	0.507	0.511
H	0.057	0.061	0.059	0.057	0.061	0.061
O	0.429	0.410	0.503	0.457	0.430	0.427
N	0.002	0.001	0.015	0.004	0.002	0.001
Inorganic elements (selection), dry base [mg/kg]						
Ca	4600	900	2600	2300	2000	1400
K	4600	360	8000	7500	1200	640
Mg	830	130	1400	690	420	320
Na	280	71	10	260	33	94
Compositional analysis, dry base [kg/kg]						
Arabinose	0.005	0.015	0.022	0.032	0.010	0.014
Galactose	0.007	0.025	0.009	0.011	0.013	0.026
Mannose	0.015	0.117	0.006	0.005	0.046	0.106
Rhamnose	0.004	0.002	0.008	0.002	0.003	0.002
Xylose	0.168	0.055	0.174	0.271	0.134	0.074
Galacturonic acid	0.025	0.013	0.048	0.008	0.024	0.013
Glucuronic acid	0.001	0.001	0.006	0.004	0.001	–
Sum non-glucose sugars	0.225	0.228	0.273	0.333	0.231	0.235
Glucose (total)	0.337	0.440	0.270	0.424	0.423	0.431
Non-cellulose glucose	0.016	0.037	0.009	n.a.	n.a.	n.a
Klason lignin	0.346	0.278	0.316	0.208	0.273	0.316
Extractives	0.015	0.093	0.089	0.039	0.066	0.072
Sum (composition)	0.923	1.039	0.948	1.004	0.993	1.054
Lignin ash	0.009	0.002	0.006	0.014	0.006	0.004
Fatty acids analysis, relative abundance [arbitrary units]						
C 16:0	0.255	0.045	0.101	0.332	0.200	0.158
C 18:0	0.058	n.a	0.084	0.052	0.038	0.046
C 18:1	0.190	0.207	0.199	0.123	0.188	0.184
C 18:2	0.082	0.020	0.231	0.045	0.186	0.025
C 18:3	n.a.	n.a.	0.046	n.a.	0.038	n.a.
C 20:0	0.039	n.a.	0.018	0.020	0.024	n.a.
C 22:0	0.108	0.024	n.a.	0.036	0.034	n.a.

2.2 Thermogravimetric analysis

Thermogravimetric measurements were carried out on a Netzsch STA 449-F1 Jupiter. The instrument was checked by repeating a round-robin study on cellulose pyrolysis,[39] as well as repeating pyrolysis experiments on beech[40] and pine[14,40] at a heating rate of 5 K/ min. Agreement between our data and the kinetic models presented in the literature[14,39,40] was good. It was also found that kinetics derived from TGA with 5 K/ min heating rates does not predict low-temperature mass loss well (see supporting information).

The focus of this work is on low temperature kinetics. Therefore, a temperature program for the TGA experiments was designed to investigate the region 423–523 K. The program consisted of a series of six isothermal stages: 423 K, 443 K, 463 K, 483 K, 503 K and 523 K. Each isothermal condition was held for one hour, with heating rates of 10 K/ min in between stages and up to the first isothermal holding point (compare the top part of Fig. 1). Temperatures measured at the sample crucible generally followed the preset temperature programs well. A mild excess in temperature was seen at the beginning of each isothermal interval, which was attributed to a controller overshoot. The measured temperature history was used in the analysis of the data.

The gas flow rate through the oven was 150 mL/ min, and experiments were run under 0 %, 20 % and 80 % oxygen (balance: nitrogen). Experiments were duplicated in range 423–503 K. To compare kinetic parameters determined in this work to data available in the literature, additional experiments were carried out at a constant heating rate of 5 K/ min from ambient to 773 K, both under inert atmosphere and with 10 % and 20 % oxygen each. These experiments were also duplicated.

Samples were placed in alumina cups of 7 mm diameter and 4 mm height, which were filled to less than a third of their height. For the 5 K/ min temperature-ramp experiments, the sample mass was kept below 5 mg to avoid mass- and heat transfer limitations. For the isothermal experiments, slightly higher sample masses of <10 mg were allowed in order to better resolve the low mass loss at low temperatures.

The biomass samples were used as-is, i.e. without prior drying. Evaporation of moisture was clearly visible in the recorded data as a pronounced loss of mass (between 4–8 % depending on the individual sample, with typical values around 5 % of the total) within the first 10 minutes of the experiment. As evaporation of moisture and decomposition of the organic matter were easily distinguished, no dedicated drying period was included in the heating programs. The measured moisture content was used to rescale the data to dry values.

Data were automatically recorded in 0.05-minute intervals for isothermal experiments, and in 0.01-minute intervals at constant heating rate. The sampling rates follow the default settings of the instrument. Recorded mass loss data were corrected for buyoancy effects by subtracting a correction carried out on an empty crucible for each experimental program. A simple routine for pre-processing the data was developed and applied to all datasets. Mass loss data were rescaled to dry-base for further treatment, and m_0 refers to the initial dry mass in the following. To determine the conversion X,

$$X(t) = \frac{m_0 - m(t)}{m_0 - m_\mathrm{f}} \tag{1}$$

the final mass m_f was set to the sum of char and ash (from proximate analysis) for pyrolysis experiments, and only ash for experiments under oxidative atmosphere. Ash and char contents are found in Table 1. Owing to noise on the measured signal, the conversion rates dX/dt were determined from smoothed data. Data were initially smoothed by calculating the moving average of $X(t)$ with a filter width of 120 records. From these data, the conversion rate was calculated as the temporal gradient by central differences. The conversion rate was then filtered again by applying the same moving average filter.

Repeatability of the experiments was generally good. In order to compare duplicate runs, the root-mean-square (RMS) difference was used.

$$\delta_\varphi = \sqrt{\frac{\sum \left(\varphi_1(t) - \varphi_2(t)\right)^2}{N}}; \qquad \varphi = \{m/m_0, dX/dt, T\} \tag{2}$$

In this equation, N is the total number of datapoints measured at time t, and φ is a placeholder for the compared quantities: remaining mass scaled by initial mass, conversion rate and temperature. This difference can also be scaled to the range of φ-values by

$$\delta_{\mathrm{S},\varphi} = \frac{\delta_\varphi}{\varphi_{\max} - \varphi_{\min}} \tag{3}$$

Root-mean-square differences, data range, and scaled differences were determined individually for each biomass sample in each temperature program. In the following, only the maximum differences and scaled differences across all measurements are given. The temperature-time programs agreed within a difference of $\delta_T = 0.35\,\mathrm{K}$ for all experiments. The relative mass remaining m/m_0 was repeatable within 0.0094 (6.5 % of the measured range) for the isothermal experiments and 0.015 (1.8 % of the measured range) for the constant heating rate experiments. For the conversion rates, the corresponding maximum RMS-differences were $7.5 \times 10^{-6}\,\mathrm{s}^{-1}$ (scaled 13.3 %) for the isothermal experiments and $3.0 \times 10^{-5}\,\mathrm{s}^{-1}$ (scaled 3.4 %) for experiments at constant heating rate of 5 K/ min. Scaled RMS-differences of m/m_0 and dX/dt in the isothermal experiments are generally higher owing to the low overall conversion or mass loss at the low temperatures (<503 K) for which those experiments were repeated.

Experimental data from thermogravimetric analysis are summarized in Figures 1 and 2. The data from isothermal experiments clearly reveals differences among the different biomasses in the temperature range 423–523 K. Sunflower husk pellets show the highest mass loss through most of the temperature range tested. The two wood pellets are among the least reactive in the entire temperature range of the isothermal experiments. Pine initially loses mass at rates similar to sunflower, but is less reactive at higher temperatures (≥483 K). The opposite is observed for wheat and beech, for which mass loss accelerates above this temperature. Measured mass loss in oxidative atmosphere differs from that in inert atmosphere from approximately the third isothermal stage (463 K) onward. It was considered

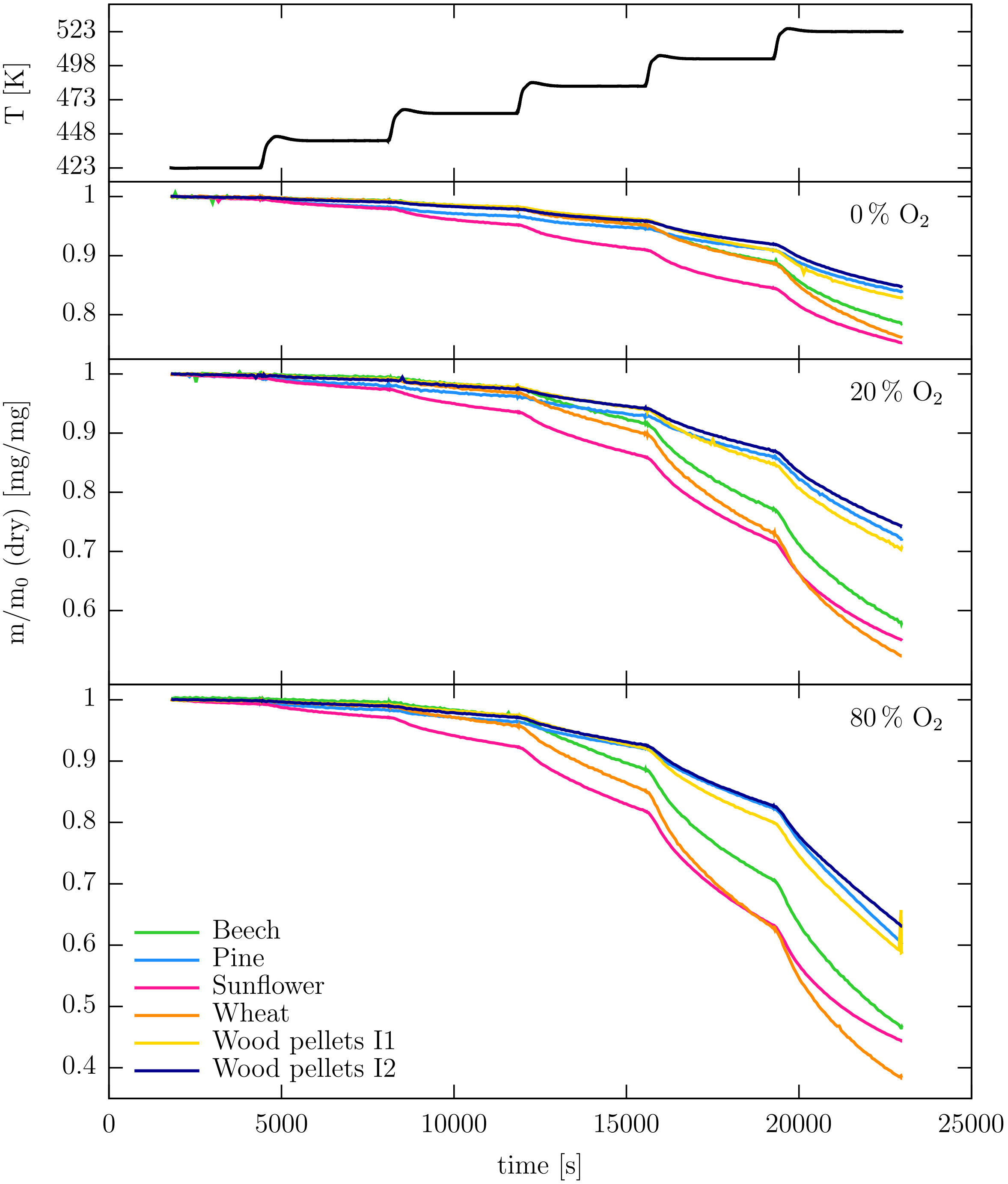

Figure 1: Experimental data from isothermal experiments reveals differences both between biomasses and between heating in oxidative and inert atmosphere in range 423–523 K. From top to bottom: measured (actual) heating profile, measured mass loss (scaled) in 0 % oxygen, 20 % oxygen and 80 % oxygen atmosphere

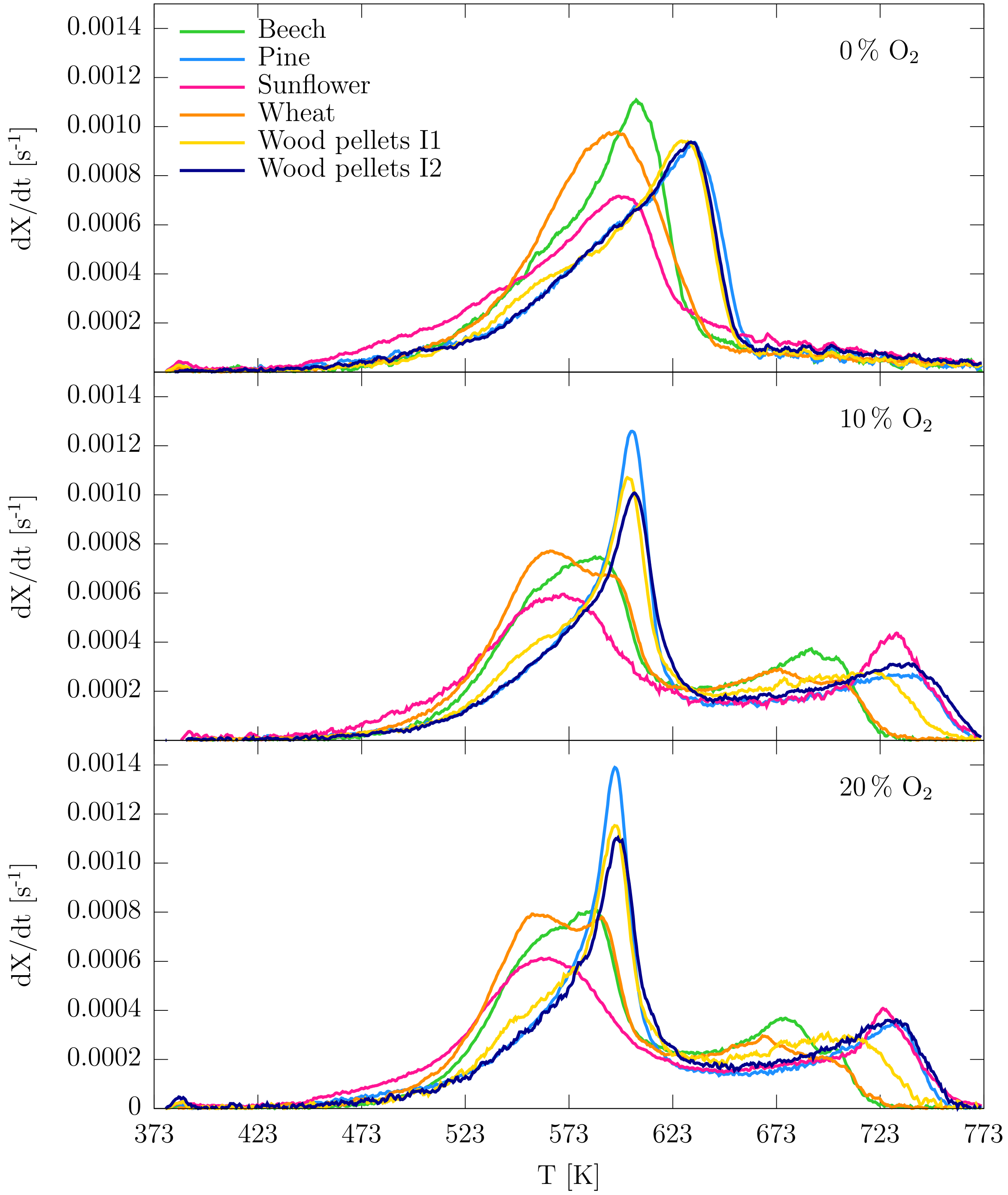

Figure 2: Experimental data from 5 K/ min experiments does not allow to distinguish between fuel (except sunflower) in range 423–523 K. Differences in conversion rate as a function of temperature are most apparent between 523–623 K. From top to bottom: in 0 % oxygen, 10 % oxygen and 20 % oxygen atmosphere

whether air entrapped in the sample beds may lead to few, early oxidation reactions, even when the experiments are run with nitrogen atmosphere. However, interstitial air could only supply <0.2 % of the oxygen necessary for conversion of the sample, and the entrapped oxygen is additionally expected to diffuse out rapidly. Purge flow rates of 150 mL/ min are moreover sufficient to replace the gas volume enclosed in the oven in the first few minutes of the experiment.

For the experiments at constant heating rate, the conversion rate is shown as a function of temperature to allow better comparison with the data available in literature.[8,12–17,22,24–26,44] With the exception of sunflower, these data does not allow to distinguish between different biomasses and different atmospheres below 473 K. The dominating feature in this data presentation is the peak in conversion rate, typically attributed to reactions of cellulose. Presence of oxygen is seen to accelerate mass loss in all cases, in agreement with published data. However, the effect of oxygen concentration is small, when comparing the experiments under 10 % and 20 % oxygen atmosphere. The location of the peak decomposition rate is shifted by 5–10 K, and the rates themselves are slightly higher. With oxygen present, two characteristic peaks can be seen. The secondary peaks in range ≥673 K can likely be attributed to char oxidation.

Dimensionless Biot (Bi), Pyrolysis (Py) and Damköhler (Da) numbers were evaluated to determine the influence of heat transfer limitations (during transient heating) and mass transfer limitations (for oxidation experiments). Heat transfer has negligble influence on the observed mass loss, when internal heat transfer is faster than external heat transfer ($\mathrm{Bi} \ll 1$), and when both are faster than reaction rates ($\mathrm{Py} \gg 1$).[41,42] Mass transfer limitations are considered for oxygen only, and kinetic control can be assumed when diffusion rates are faster than reaction rates ($\mathrm{Da} \ll 1$). Addiditonally, the dimensionless Frank-Kamenetskii-parameter[43] was calculated to determine whether thermal runaway (heat release exceeds internal heat dissipation) could occur in the samples with oxygen present. Details of these calculations can be found in the supporting information. Based on the evaluation of the dimensionless parameters, conditions for the stepwise isothermal experiments were free from heat- and mass transfer limitations. Transport limitations may play a minor role for the experiments at constant heating rate: The Biot number becomes independent of particle or sample size for near-stagnant flows.[42] Bi evaluated to 0.1–0.2 for single particles and Bi < 0.4 for the full sample (i.e., the bed of particles). The Pyrolysis number criterion can be used to estimate a critical maximum particle size.[42] Using this approach, kinetic control is predicted up to 700 K (pyrolysis) and 625 K (oxidation) based on modelled rates for the largest particles used (250 µm). Oxygen diffusion limitations were estimated to be wholly negligible below 570 K. By conservative estimate, self-ignition of the samples cannot occur below 530 K under the experimental conditions used, and no self-heating was observed in the experiments. Other possible influences, such as particle specific surface area, particle porosity and bed structure were not quantified. The former two would influence availability of active sites to oxygen attack, while the latter determine diffusion through the sample as well as the bed thermal conductivity. While kinetic control was assumed in interpreting the experiments, the results are strictly valid only for the size range and morphology of the particles used.

3 Modelling

Reactions are described by a differential equation for the conversion X,

$$\frac{dX}{dt} = k(T) \cdot f_1(X) \cdot f_2(p_{\mathrm{O_2}}) \tag{4}$$

k is the rate constant modelled by an Arrhenius-expression,

$$k = k_0 \cdot \exp\left(-\frac{E_{\mathrm{a}}}{R \cdot T}\right) \tag{5}$$

and f_1 and f_2 are functions of conversion and oxygen partial pressure, respectively. Most common models for f_1 are first- or n-order reactions:

$$f_1(X) = (1 - X)^{n_1} \tag{6}$$

Oxygen-dependent reactions can be modelled by introducing a reaction order in oxygen partial pressure,

$$f_2(p_{O_2}) = \left(\frac{p_{\mathrm{O_2}}}{p_{\mathrm{ref}}}\right)^{n_2} \tag{7}$$

where a reference pressure p_{ref} is introduced to non-dimensionalize the oxygen partial pressure.

Initial attempts at fitting a single first order reaction to the pyrolysis experiment and combining it with a first order reaction for oxidation yielded poor fits. The quality of the model fit could be improved slightly when an n-order reaction was considered. However, fitting only selected temperature ranges of the experimental mass loss curve yielded different sets of kinetic parameters, indicating that a process consisting of several steps was taking place.

Several researchers have linked these steps in the reaction to parallel and independent reactions of the components hemicellulose, cellulose and lignin.[13–18,25,45] In this work, extractives are considered as a separate fourth component. Pyrolysis and oxidation of these four components are modelled as parallel reactions, similar to literature.[12,14,23,25,26] For consistency, char is included as an additional fifth component. Char is defined as the remainder of a complete biomass devolatilization in this model. Char oxidation dominates at higher temperatures, when the volatilizable fractions of hemicellulose, cellulose, lignin and extractives have been removed. Although this process is physically in sequence to pyrolysis and primary oxidation, several authors have demonstrated that, mathematically, it may also be modelled as an additional parallel reaction.[13–17] Following this approach, it is not necessary to track the formation of char. Instead, the biomass components are split into volatilizable and non-volatilizable fractions, i.e. char is considered present already in the unreacted biomass from a modelling point of view. Considering the non-volatilizable fractions as a lumped species, the following mechanism of nine parallel reactions is applied:

$$\mathrm{XTR} \rightarrow \mathrm{Volatiles} \tag{R1}$$

$$\mathrm{HC} \rightarrow \mathrm{Volatiles} \tag{R2}$$

$$\mathrm{LIG} \rightarrow \mathrm{Volatiles} \tag{R3}$$

$$\mathrm{CELL} \rightarrow \mathrm{Volatiles} \tag{R4}$$

$$\mathrm{XTR} + \mathrm{O_2} \rightarrow \mathrm{Gas} \tag{R5}$$

$$\mathrm{HC} + \mathrm{O_2} \rightarrow \mathrm{Gas} \tag{R6}$$

$$\mathrm{LIG} + \mathrm{O_2} \rightarrow \mathrm{Gas} \tag{R7}$$

$$\mathrm{CELL} + \mathrm{O_2} \rightarrow \mathrm{Gas} \tag{R8}$$

$$\mathrm{CHAR} + \mathrm{O_2} \rightarrow \mathrm{Gas} \tag{R9}$$

Reactions R1–4 represent pyrolysis of the volatilizable fractions of extractives (XTR), hemicellulose (HC), lignin (LIG) and cellulose (CELL) components. Reactions R5–8 are the corresponding oxidation reactions. The final reaction R9 describes the oxidation of char, regardless of the component or reaction pathway it originates from. The conversion X_i of each of the five species (volatilizable extractives, hemicellulose, lignin and cellulose, plus char) is then described by:

$$\frac{dX_\mathrm{i}}{dt} = k_{\mathrm{pyr,i}} \cdot (1 - X_\mathrm{i}(t))^{n_{\mathrm{pyr,i}}} + k_{\mathrm{ox,i}} \cdot (1 - X_\mathrm{i}(t))^{n_{\mathrm{ox,i}}} \cdot \left(\frac{p_{\mathrm{O_2}}}{p_{\mathrm{ref}}}\right)^{n_{\mathrm{O_2,i}}} \tag{8}$$

where n is the apparent reaction order and the rate constant k is expressed by an Arrhenius law.

$n_{\mathrm{O_2}}$ is the reaction order with respect to partial pressure of oxygen $p_{\mathrm{O_2}}$. The reference pressure p_{ref} is used to non-dimensionallize this quantity. Here, p_{ref} is simply 1 Pa. For char, i.e. the non-volatilizable organic fraction, $k_{\mathrm{pyr}} = 0$. Since only the reacting fractions of the components are considered (i.e. $m_{i,f} = 0$), the remaining mass fraction of each component i is given by

$$w_{\mathrm{i}}(t) = \frac{m_{\mathrm{i}}(t)}{m_{\mathrm{i,0}}} = 1 - X_{\mathrm{i}}(t) \tag{9}$$

If $w_{i,0}$ is the original mass fraction of species i, then the total mass fraction is given by:

$$w(t) = \frac{m(t)}{m_0} = \sum_i w_{\mathrm{i,0}} \cdot w_{\mathrm{i}}(t) \tag{10}$$

The amount of ash is constant. The model requires five parameters for the original mass fractions $w_{\mathrm{i,0}}$, as well as four reaction kinetic triplets $\{E_{\mathrm{a}}, k_0, n_{\mathrm{pyr}}\}$ for the pyrolysis reactions and five sets $\{E_{\mathrm{a}}, k_0, n_{\mathrm{ox}}, n_{\mathrm{O_2}}\}$ for the oxidation reactions, i.e. a total of 37 parameters per fuel.

In order to reduce the model complexity, the following assumptions are made:

1. The fractions of extractives, hemicellulose, cellulose and lignin can be estimated from the composition analysis (Table 1).

2. The total char yield can be determined from the ultimate analysis. The individual char yield of the components extractives, hemicellulose, cellulose and lignin, i.e. the split into volatilizable and non-volatilizable fractions, can be estimated from the behavior of the pure components.

3. Similar sets of activation energies $E_{\mathrm{a,pyr,i}}$ and $E_{\mathrm{a,ox,i}}$ can be found for each component i, regardless of which biomass they appear in. The activation energies can be estimated from the behavior of the pure components.

4. Similar sets of apparent reaction orders in the solid conversion ($n_{\mathrm{pyr,i}}$ and $n_{\mathrm{ox,i}}$) can be found for each component i, regardless of which biomass they appear in.

By combining the first two assumptions, the original mass fractions $w_{\mathrm{i,0}}$ can be found. The third assumption fixes all activation energies, so they need not be included in the parameter fitting routine. The different biomass conversion models are then defined by 23 parameters: 8 belonging to the four pyrolysis reactions, i.e. $\{k_{0,\mathrm{pyr}}, n_{\mathrm{pyr}}\}_{\mathrm{i}}$ and 15 for the additional oxidation reactions $\{k_{0,\mathrm{ox}}, n_{\mathrm{ox}}, n_{\mathrm{O_2}}\}_{\mathrm{i}}$. Adding the fourth assumption further reduces the biomass-specific parameters to four parameters $k_{0,\mathrm{pyr,i}}$ for pyrolysis and five sets $\{k_{0,\mathrm{ox}}, n_{\mathrm{O_2}}\}_{\mathrm{i}}$ for oxidation. It was further evaluated whether a hybrid model of a component-specific pyrolysis model and a lumped species for oxidation can describe the measured data. Assumptions 1–4 are then kept for the pyrolysis mechanism, but replaced with the following for oxidation:

5. Oxidation reactions for the four components extractives, hemicellulose, cellulose and lignin can be modelled with the same set of four kinetic parameters $\{E_{\mathrm{a}}, k_0, n_{\mathrm{ox}}, n_{\mathrm{O_2}}\}$, which are then specific to each biomass.

6. The oxidation reactions have the same activation energy for all biomasses considered (leaving 3 free parameters per biomass for oxidation).

The model based on assumptions (5) and (6) is referred to as *Model I* in the following, the one without those assumptions as *Model II.* In model I, activation energies from pure component studies were only used in the pyrolysis reactions. However, even if the oxidation reactions are unified in this way, the different volatilizable species need to be tracked individually, as their pyrolysis reactions are different.

The original mass fractions $w_{\mathrm{i,0}}$ for volatilizable extractives, hemicellulose, lignin and cellulose, as well as char can be calculated from the composition shown in Table 1. Some estimations are made to account for the balance error in determining the composition, as well as the split between volatilizable and char-forming fraction of each component: Extractives (ethanol-soluble) and lignin (Klason) are taken as measured. Cellulose was determined by subtracting the hemicellulose-glucose from the total glucose. For beech, pine and sunflower, the hemicellulose-glucose was measured by acid hydrolysis. The two wood pellet samples appeared to have a carbohydrate composition somewhere in between beech (hardwood) and pine (softwood). The hemicellulose-glucose was therefore approximated with 0.02 kg/kg for both samples (beech: 0.037 kg/kg, pine: 0.016 kg/kg – compare Table 1). All measured glucose in wheat was assumed to be cellulose. All other organic substance, i.e. the remaining monosaccharides, the uronic acids and the hemicellulose-glucose, was lumped into the hemicellulose component. The sum of these four components is then normalized to one. Char yields from commerical cellulose, lignin and xylan samples were measured, rounded, and then used to distribute the char among the biomass components (see supporting information). For modelling, 10 % of the char was associated with cellulose, 30 % with hemicellulose and 60 % with lignin. It was assumed that extractives are completely volatilizable. The model composition of the six biomasses, based on the above, is summarized in Table 2.

From isothermal experiments following the same procedure as for the native biomasses, pyrolysis activation energies of 60 kJ/mol for extractives, 120 kJ/mol for xylan/hemicellulose, 125 kJ/mol for lignin and 185 kJ/mol for cellulose were obtained. Data from these measurements can be found in the supporting information.

The thermogravimetric data measured in inert atmosphere was then used to determine kinetic parameters of the four pyrolysis reactions. This was carried out in two steps. In the first step, fitting was done by simulating a large series of conversion curves for the isothermal

Table 2: Composition $w_{i,0}$ used in the reaction kinetics model. Data calculated from composition analysis (compare Table 1). See text for discussion.

	Beech wood	Pine wood	Sunflower	Wheat straw	Wood pellets I1	Wood pellets I2
XTR	0.019	0.090	0.085	0.038	0.070	0.070
HC	0.183	0.207	0.217	0.261	0.204	0.192
LIG	0.249	0.185	0.197	0.091	0.189	0.205
CELL	0.320	0.375	0.256	0.384	0.383	0.372
CHAR	0.202	0.141	0.193	0.184	0.149	0.155
Ash	0.027	0.003	0.052	0.042	0.006	0.006

experiments and finding kinetic parameter sets so that the root-mean-square deviations of relative mass remaining and mass loss rate are minimized. The RMS-deviation is defined as

$$\delta_{\varphi} = \sqrt{\frac{\sum \left(\varphi_{\mathrm{exp}}(t) - \varphi_{\mathrm{sim}}(t)\right)^2}{N}}; \qquad \varphi = \{m/m_0, dm/dt\} \tag{11}$$

Due to numerical compensation effects, several combinations of $\{k_{0,\mathrm{pyr,i}}, n_{\mathrm{pyr,i}}\}$ can model the data from isothermal experiments within a similar error range. Therefore, those parameter sets which best fit the isothermal data were then checked against the data from the 5 K/ min experiments. The twenty combinations minimizing mass loss error (δ_{m/m_0}) and those minimizing error on the mass loss rate ($\delta_{dm/dt}$) were compared to the constant heating rate data in this second step. That parameter set from the reduced number of combinations which minimizes the deviation in predicting the conversion rate (i.e., $\varphi = dX/dt$ in the above equation) within 373–773 K was then selected for each biomass. The procedure was repeated iteratively to determine uniform $n_{\mathrm{pyr,i}}$ for the components, regardless of which biomass they appear in (modelling assumption 4).

The same procedure was then applied to the isothermal experiments carried out in oxidative atmosphere. The pyrolysis reactions were modelled by the kinetic parameters obtained previously. For the simpler oxidation model (model I), the fitting procedure was run iteratively to determine a common activation energy for all biomasses. The remaining kinetic parameters (k_0, n_{ox} and $n_{\mathrm{O_2}}$) for each biomass were then found by again simulating curves with a large number of parameter combinations, and selecting those with minimal error. For the more complex scheme (model II), activation energies for oxidation of the volatilizable fractions were determined as 75 kJ/mol for extractives, 150 kJ/mol for xylan/hemicellulose, 120 kJ/mol for lignin and 225 kJ/mol for cellulose. These estimates are based on the behavior of the commercial samples when subjected to the same heating program (see supporting information). In both model I and II (i.e. single- and component oxidation model), the models for 20 % and 80 % oxygen were optimized simultaneously in order to determine the reaction order in oxygen. Again, the parameter sets that best fit the isothermal data are compared to the non-isothermal experiments, and that set which best represents the conversion rate between 373–773 K was chosen.

Char oxidation was assumed to be negligible in the temperature range below 523 K. A simple kinetic calculation was carried out to check this assumption. Char in this case refers to that fraction of the material which cannot undergo further devolatilization. We assume this to be identical with the char as determined in the ultimate analysis. Branca and Di Blasi[16,18] suggest a single oxidation reaction with $E_\mathrm{a} = 185\,\mathrm{kJ/mol}$ for a completely devolatilized biomass residue. This value was also used here. Pre-exponential factor and reaction order in the solid conversion were then adapted to the experimental data to match the char peaks apparent in Figure 2. The shift in char peaks from the experiments at 10 % and 20 % oxygen apparent in the data can be represented with a reaction order between 0 and 1. Here, the reaction order in oxygen for char was fixed at 0.5, which falls within the lower end of the range of values reported in the literature.[14,25,46] It should be emphasized that optimizing the kinetics for char oxidation is not in focus of this work.

4 Results and Discussion

The kinetic parameters fitted to the six biomasses are found in Tables 3, 4 and 5 for the pyrolysis model, oxidation model I and oxidation model II, respectively. The same pyrolysis- and char oxidation kinetics are used with oxidation models I and II. Modelled mass losses compared well to the isothermal experiments for pyrolysis and both oxidation models. Figure 3 shows the comparison for model I. Results for oxidation model II are very similar and can be found in the supporting information. Differences between the two oxidation models were more apparent when compared to the experiments with a constant 5 K/ min heating rate (Figure 4). Results from this work show that some (but not all) parameters of the kinetic models can be obtained from pure component studies. The models are evaluated

Table 3: Kinetic data for the pyrolysis models. Differences between biomasses are modelled by different pre-exponential factors $k_{0,\mathrm{pyr}}$. Apparent activation energies and reaction orders of the components are uniform for all biomasses, with the exception of cellulose n_{pyr}: Beech: 0.9, Pine: 1.1, Sunflower: 1.7, Wheat: 2.0, Wood pellets I1: 1.1, Wood pellets I2: 1.1

	Extractives	Hemicellulose	Lignin	Cellulose
$E_{\mathrm{a,pyr}}$ [kJ/mol]	60	150	125	185
n_{pyr} [–]	2.5	3	4	(0.9–2.0)
$k_{0,\mathrm{pyr}}$ [s^{-1}]				
Beech	1.6×10^{3}	5.6×10^{11}	2.8×10^{8}	4.30×10^{13}
Pine	8.0×10^{2}	1.4×10^{11}	1.0×10^{8}	8.02×10^{12}
Sunflower	1.2×10^{3}	7.4×10^{11}	4.0×10^{7}	7.94×10^{13}
Wheat	1.0×10^{3}	3.2×10^{11}	4.0×10^{8}	7.47×10^{13}
Wood pellets I1	4.0×10^{2}	2.6×10^{11}	1.2×10^{8}	1.36×10^{13}
Wood pellets I2	6.0×10^{2}	1.4×10^{11}	1.2×10^{8}	1.06×10^{13}

Table 4: Oxidation model I: kinetics for oxidation of a lumped volatilizable component and char. The same char kinetics are used in oxidation model II.

	Extr./Hemicell./Lig./Cell			Char		
E_{a} [kJ/mol]	130			185		
	k_0 [s^{-1}]	n_{ox} [–]	$n_{\mathrm{O_2}}$ [–]	k_0 [s^{-1}]	n_{ox} [–]	$n_{\mathrm{O_2}}$ [–]
Beech	2.00×10^{7}	2.2	0.45	5.7×10^{9}	1.0	0.5
Pine	1.04×10^{7}	1.25	0.40	5.0×10^{8}	0.55	0.5
Sunflower	1.62×10^{7}	2.5	0.50	5.0×10^{8}	0.65	0.5
Wheat	1.49×10^{7}	1.6	0.50	5.7×10^{9}	1.0	0.5
Wood pellets I1	7.52×10^{6}	2.2	0.45	1.1×10^{9}	0.8	0.5
Wood pellets I2	5.60×10^{6}	2.5	0.45	4.2×10^{8}	0.5	0.5

Table 5: Model II: kinetic data for the component-dependent oxidation model. Differences between biomasses are modelled by different pre-exponential factors $k_{0,\mathrm{ox}}$ and reaction orders in oxygen n_{O_2}. Apparent activation energies and reaction orders of the components are uniform for all biomasses, with the exception of cellulose n_{ox}: Beech: 2.2, Pine: 0.6, Sunflower: 3.7, Wheat: 1.8, Wood pellets I1: 0.9, Wood pellets I2: 1.0. Char kinetic data is the same as in Table 4

	Extractives	Hemicellulose	Lignin	Cellulose	Char
$E_{\mathrm{a,ox}}$ [kJ/mol]	(75)	200	120	225	185
n_{ox} [–]	(1)	1.6	2.5	(0.6–3.7)	(0.5–1.0)
$k_{0,\mathrm{ox}}$ [s^{-1}]					
Beech	0	2.45×10^{15}	1.55×10^{6}	2.5×10^{13}	5.7×10^{9}
Pine	0	5.0×10^{14}	1.0×10^{5}	5.5×10^{12}	5.0×10^{8}
Sunflower	0	6.5×10^{14}	3.9×10^{5}	2.5×10^{13}	5.0×10^{8}
Wheat	0	1.0×10^{15}	6.7×10^{5}	4.0×10^{13}	5.7×10^{9}
Wood pellets I1	0	4.0×10^{14}	1.0×10^{5}	6.5×10^{12}	1.1×10^{9}
Wood pellets I2	0	8.5×10^{14}	1.0×10^{5}	4.5×10^{12}	4.2×10^{8}
n_{O_2} [–]					
Beech	–	0.4	0.5	1.1	0.5
Pine	–	0.4	0.6	1.1	0.5
Sunflower	–	0.5	0.7	1.1	0.5
Wheat	–	0.5	0.7	1.1	0.5
Wood pellets I1	–	0.5	0.6	1.1	0.5
Wood pellets I2	–	0.3	0.7	1.1	0.5

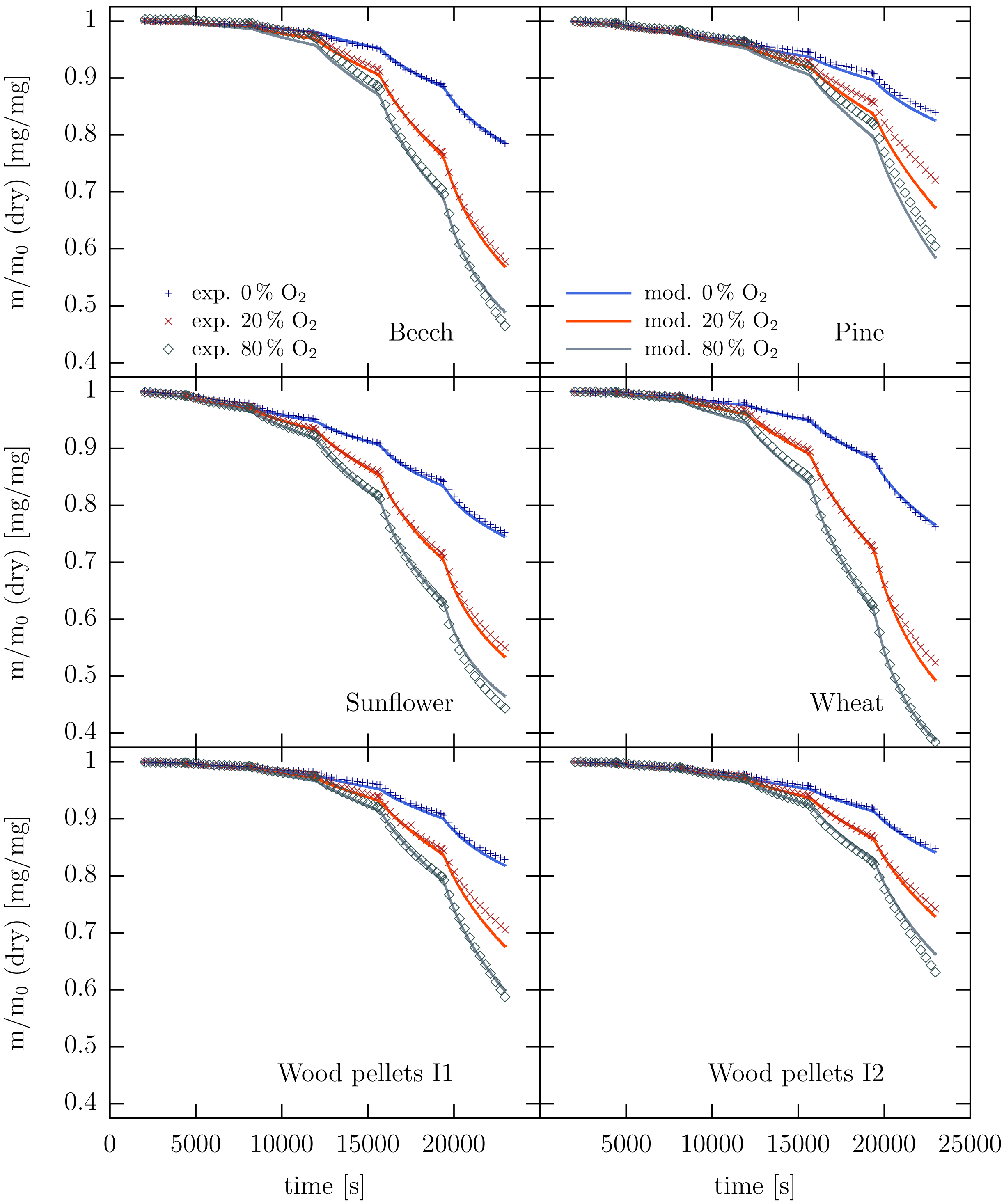

Figure 3: Oxidation model I: comparison of isothermal experiments and models for six biomasses, assuming that the oxidation of hemicellulose, cellulose, lignin and extractives can be modelled by the same set of kinetic data. Kinetic parameters are listed in Tables 3 and 4.

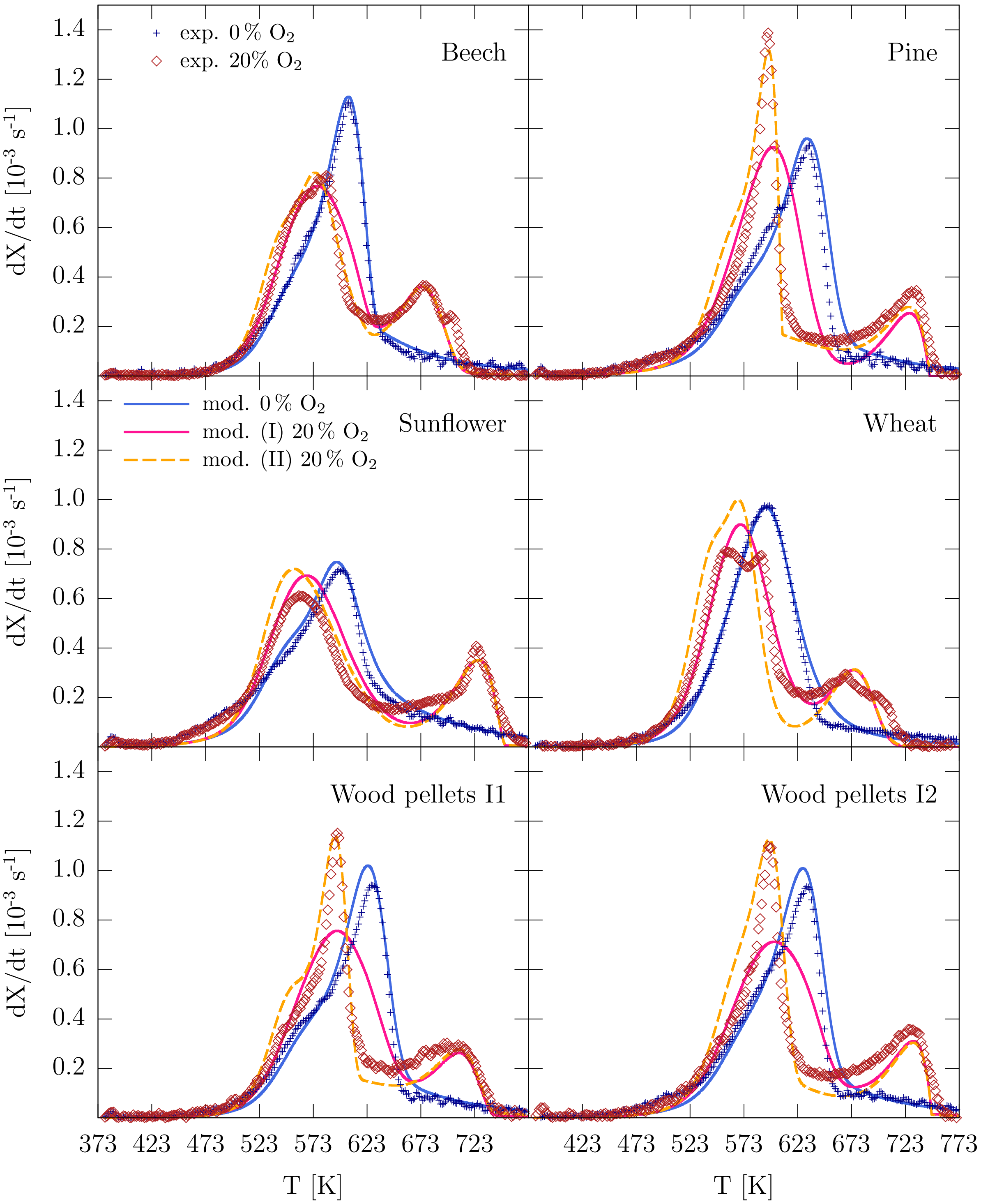

Figure 4: Oxidation model I and II: comparison of experiments at constant heating rate and models for six biomasses, assuming uniform (model I) and separate oxidation kinetics (model II) of hemicellulose, cellulose, lignin and extractives. Symbols represent experimental data, lines are modelled data. Kinetic parameters are listed in Tables 3, 4 and 5.

for numerical, rather than physical or chemical accuracy – i.e., the model representations of extractives, hemicellulose, lignin and cellulose cannot fully capture the complex behavior of these components as they are found in the biomasses. Additionally, structural influences and component interactions are neccessarily convoluted in the kinetic parameters in the proposed scheme of independent and parallel reactions.

Results from modelling pyrolysis and oxidation kinetics are discussed separately below.

4.1 Pyrolysis kinetics

The kinetic parameters found could explain the experimental data both for the isothermal experiments and those at 5 K/ min. Table 6 lists the scaled root-mean-square deviations between model and experiment. Scaled deviations between model and measurement are similar in magnitude to the scaled deviations among repeated experiments (compare section 2.2). The values found for the activation energies are moreover in good agreement with those found in the literature (e.g., as reviewed in[35,47]).

An initial loss of mass (423–443 K) could be associated with high amounts of extractives in pine and sunflower (both 9 %), although this effect was absent in both wood pellet samples (each 7 % extractives), compare Figures 1, 3 and Table 1. The model predicts that extrac-

Table 6: Scaled root-mean-square deviations ($\delta_{\mathrm{S},\varphi}$) between modelled and measured data in inert atmosphere. "Isothermal" refers to the stepwise isothermal experiments, "ramp" to those at constant heating rate 5 K/ min.

	$\delta_{\mathrm{S}}(m/m_0)$		$\delta_{\mathrm{S}}(dX/dt)$	
Experiment	isothermal [%]	ramp [%]	isothermal [%]	ramp [%]
Beech	0.84	3.60	10.23	2.22
Pine	4.44	6.51	10.33	7.16
Sunflower	1.83	5.13	12.05	6.07
Wheat straw	2.40	4.39	9.64	3.62
Wood pellets I1	5.13	4.95	12.10	5.31
Wood pellets I2	4.75	5.68	15.61	6.38

tives are pyrolyzed to a large degree (70–90 %) in the isothermal experiments. However, extractives make up only a small part of the biomasses. In the full temperature range of the isothermal experiments, 423–523 K, pyrolysis of the six biomasses is dominated primarily by the decomposition of hemicellulose (25–65 % conversion) and, secondly, of lignin (15–25 %). An exception is sunflower husk pellets, where the model predicts a slightly lower mass loss of lignin compared to cellulose (6 % and 10 %, respectively). Modelled mass losses of the cellulose component are otherwise low in this temperature range (1–11 %). Additionally, pure cellulose did not show any significant pyrolytic conversion below 503 K (see supporting information). In the experiments at 5 K/ min heating rate, a near-complete devolatilization of all biomass samples is observed. This is also captured in the model, as conversion rates approach zero at 773 K in Figure 4.

The activation energy found in the xylan experiments, 125 kJ/mol, does not represent the hemicellulose components of all biomasses in the 5 K/ min constant-heating-rate experiments very well. An increased value of 150 kJ/mol provides a better agreement between model and measurement. This can be justified by the inhomogeneous nature of hemicellulose (compare Table 1), which varies among plant species.[37,48,49] Thermal behavior of hemicelluloses may differ substantially, depending on their composition.[37,50–52] Xylan is thermally less stable than most other hemicelluloses.[51] A higher activation energy for the heterogeneous hemicelluloses of the six biomasses is therefore plausible.

Owing to its low conversion in the isothermal experiments, the free parameters of the cellulose component in the pyrolysis model ($k_{0,\mathrm{pyr,CELL}}$ and $n_{\mathrm{pyr,CELL}}$) could not be reliably established from the isothermal experiments. Kinetic parameters were therefore adapted to match the peak seen in the conversion rate/temperature plots (Figures 1 and 4). Inorganic elements present in the biomass are known to catalyze pyrolysis of the cellulose component.[36,53] For several biomasses, it has been shown that the temperature of peak conversion rate is decreased with increasing potassium content.[36,54,55] The data for the biomasses investigated here agree with these reported trends, and this can be used to calculate the pre-exponential factors $k_{0,\mathrm{pyr,CELL}}$ of cellulose pyrolysis from the potassium content. For an activation energy of 185 kJ/mol, the pre-exponential factors can be linearly correlated with the potassium mass fraction w_{K} by

$$k_{0,\mathrm{pyr,CELL}} = (9.34 \times 10^{15} \cdot w_{\mathrm{K}} + 2.37 \times 10^{12} \pm 2.29 \times 10^{12}) \cdot \mathrm{s}^{-1} \tag{12}$$

to reproduce the temperatures of peak decomposition rate. Details can be found in the supporting information. The apparent reaction order in the solid was then set to match the value of the peak decomposition rate. Catalytic effects of inorganic elements have also been used to model hemicellulose pyrolysis.[56] In our experiments, catalytic effects seemed to be smaller than compositional effects for hemicellulose pyrolysis. The inorganic content could therefore only be used to predict cellulose kinetic parameters, but not those of the other components.

The different biomasses can be compared in an Arrhenius plot, Figure 5. The sum of the modelled rate constants k_{i} is plotted over $1/T$, i.e.

$$k_{\mathrm{tot}}(T) = \sum_{\mathrm{i}} k_{0,\mathrm{i}} \cdot \exp\left(-\frac{E_{\mathrm{a,i}}}{R \cdot T}\right); \qquad i = \{\mathrm{XTR}, \mathrm{HC}, \mathrm{LIG}, \mathrm{CELL}\} \tag{13}$$

In the above expression, k_{tot} does not take the degree of conversion into account, since this depends on the time-temperature history of the samples. The slope of a curve on an Arrhenius plot is proportional to $-E_{\mathrm{a}}/R$, i.e., the thermal behavior of the biomasses can be compared in this way. The plot shows a high-temperature and a low-temperature regime for all six biomasses, with a transition region at ca. 450–550 K. At temperatures below the transition region, the slope of the curves approach that of the extractive component (60 kJ/mol). For temperatures above the transition region, the slope of the curve roughly corresponds to that given by the hemicellulose component (150 kJ/mol), and would asymptotically approach that of the cellulose component if extrapolated further (above ≈1000 K). In practical experiments, the hemicellulose is depleted already at lower temperatures, so the measured rates

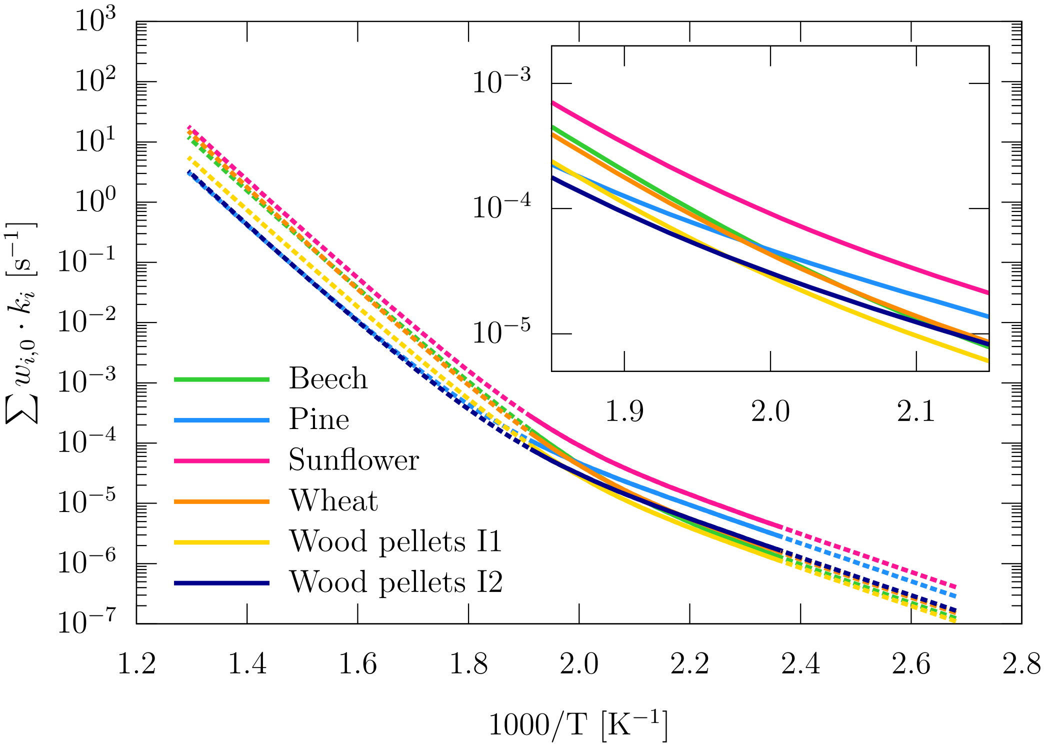

Figure 5: Arrhenius plot of the pyrolysis models. Solid lines represent the interval 423–523 K of the stepwise isothermal experiments. The dashed lines extend to 373 K and 773 K, respectively, covering the range of the constant heating rate experiments. The inset magnifies the region 465–540 K.

become dominated by cellulose kinetics around 600 K (see e.g.[18,35,40,57]). By comparison wih Figure 2, the transition region (450–550 K) is not well resolved in experiments with constant heating rate of 5 K/ min or above, which make up the majority of TG-data reported in the literature. This may explain why models fitted to such data do not explain kinetics at these temperatures (and below) very well. The plot also illustrates the relative reactivity of the six biomasses. Sunflower has the highest reaction rate over the entire temperature range, while the reactivity of wheat increases most over the range evaluated. This compares well to experimental data (Figures 1 and 2). Pine appears more reactive at low temperatures and less reactive at high temperatures. This can be explained by its high amount of extractives (low temperature behavior, <500 K) on one hand, and by the low reactivity of its hemicellulose and cellulose components (see $k_{0,\mathrm{pyr}}$ in Table 3) on the other (high temperature behavior, >550 K). In comparison, wheat has a high content of cellulose and a low content of lignin, resulting in a steeper gradient (high activation energy of cellulose component) at the high temperature end of the graph than those seen for other biomasses. The model behavior in the transition zone is explained by both the composition and the reactivity of the individual components. The analysis also shows that no single property of the biomass determines its pyrolysis behavior over the entire temperature range. Rather, rates appear to change from being extractives-dominated, to a hemicellulose-controlled range, and finally to a combined cellulose-hemicellulose controlled regime.

4.2 Oxidation kinetics

Both oxidation models I and II are in agreement with data from the stepwise isothermal experiments at 20 % and 80 % oxygen concentration. In model I, an apparent activation energy of 130 kJ/mol describes the oxidation of the volatile fractions of extractives, hemicellulose, lignin and cellulose in the temperature range of 423–523 K. The corresponding reaction orders in oxygen are between 0.4 and 0.5 (model I, Table 4). Similar rates are found in this region as the sum of hemicellulose, lignin and cellulose kinetics (model II, Table 5).

Both oxidation models give a quality of fit similar to the pyrolysis models, where the quality of fit is measured by the scaled root-mean-square deviations between model and experiment (see supporting information). From the standpoint of numerical accuracy, there is no reason to prefer one model over the other in describing the TGA-experiments. The reason why model II, despite its larger number of parameters, does not give a significantly better fit may be due to the constraints placed on some of these parameters – most notably, setting the activation energies to constant values derived from pure component measurements.

The most apparent difference between models I and II is how the overlap between hemicellulose and cellulose oxidation is described at temperatures within 520–670 K, Figure 4. Model I predicts a flatter conversion rate profile, with lower peak rates (pine, wood pellets) and a more smooth drop in coversion rates. The higher maximum conversion rates of pine and both wood pellets ($0.0014\,\mathrm{s}^{-1}$, $0.0012\,\mathrm{s}^{-1}$) can be modelled by initially low cellulose oxidation rates, that rapidly accelerate at higher temperatures (>550 K). However, the lower reactivity of cellulose at temperatures below ≈550 K is compensated by a higher hemicellulose reactivity to model the mass loss observed in the stepwise isothermal experiment (model II). This leads to an over-estimation of conversion rates between 520–570 K (Figure 4, especially pronounced for both wood pellet samples and pine). The onset behavior (≈450–520 K) of sunflower in the 5 K/ min experiments is only approximated by the pyrolysis model and both oxidation models. This could possibly be traced to the parameters of the hemicellulose model.

Differences in modelling the individual components also appear in the stepwise isothermal experiments, although nearly the same total mass loss is predicted by both models for each biomass. The general trend is that model I predicts higher conversion of the cellulose component and a lower hemicellulose conversion up to 523 K, compared to model II. In model I, conversion of hemicellulose is within 45–70 % for the six biomasses, lignin within 30–55 % and cellulose 25–55 %. In comparison, model II predicts 55–90 % conversion for hemicellullose, 20–65 % for lignin and 5–25 % for cellulose. In general, the conversion of the components is qualitatively proportional to the total conversion for the six biomasses, i.e., biomasses with a high degree of conversion of hemicellulose also have high degrees of conversion of lignin and cellulose. More details can be seen in the supporting information. Predicted conversion of extractives does not differ much between the two oxidation models and is in the range of 70–90 % for the six biomasses. The values given refer to conversion as the combined effect of pyrolysis and oxidation.

The apparent activation energy for oxidation found in model I (130 kJ/mol) falls in the middle of the range of values reported in the literature (90–210 kJ/mol)[6,10,11] . It should be noted that these literature values were derived without separating oxidation and pyrolysis reactions. Activation energies found for model II are also comparable to those reported in the literature: 70–294 kJ/mol for hemicellulose, 54–289 kJ/mol for lignin and 70–295 kJ/mol for cellulose.[13,14,17,23–25,45] A direct comparison is difficult owing to the different reaction models chosen by different authors. As for the pyrolysis model, the apparent activation energy for hemicellulose (200 kJ/mol) was set higher than that of the xylan experiments (150 kJ/mol). Apparent reaction orders in oxygen of the cellulose component are slightly > 1, which is somewhat unexpected, and probably a result of the numeric fitting routine. For model II, no contribution of extractives oxidation was found. This will be discussed further below.

The oxidation models can be compared using the same type of Arrhenius plot as for the pyrolysis experiments, as shown in Figure 6. Both models are evaluated as combined rates of oxidation and pyrolysis reactions. Similar to the pyrolysis model, a transition region around 450–550 K can be seen. In the low temperature range of the plot (<450 K), the overall apparent rate is mainly dependent on the pyrolysis of extractives ($E_\mathrm{a} = 60$ kJ/mol). The contribution of the oxidation reaction is more pronounced from 500 K and upwards (compare Figure 5), which is also where predictions of the two oxidation models begin to diverge. Model II generally predicts higher rates k_tot, while the order of biomasses with respect to reactivity is similar in both models over a broad temperature range (with sunflower, wheat and beech the most, and wood pellets I2 and pine the least reactive above 525 K). In comparison

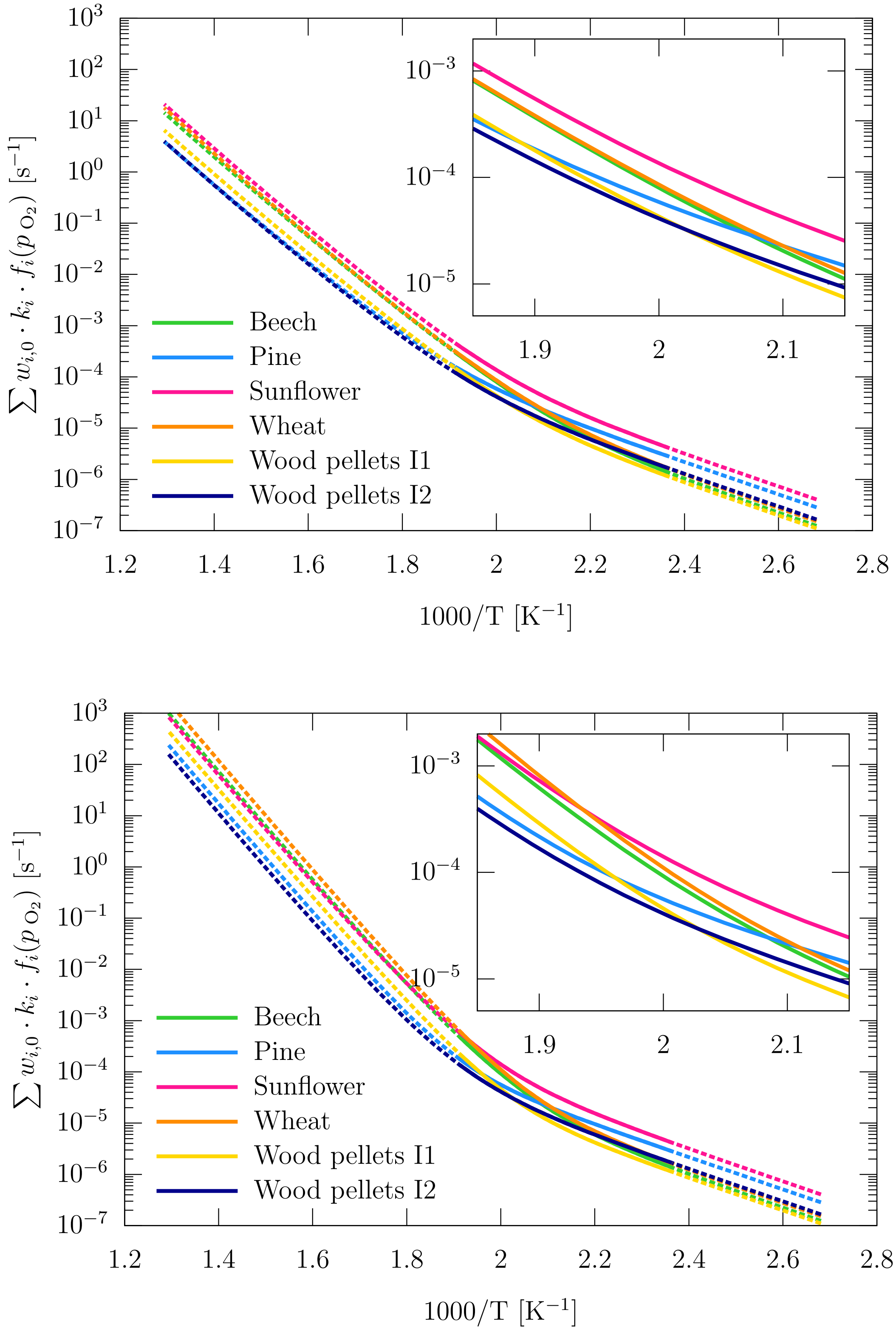

Figure 6: Arrhenius plot of the oxidation models for model I (top) and II (bottom), evaluated at $p_{\mathrm{O}_2} = 20\,\mathrm{kPa}$. Solid lines represent the interval 423–523 K of the stepwise isothermal experiments. The dashed lines extend to 373 K and 773 K, respectively, covering the range of the constant heating rate experiments. The insets magnify the region 465–540 K.

with measured data (Figures 1 and 2), conversion rates of beech and wheat exceed those of sunflower at higher temperature (>503 K in Figure 1). This is also reflected in the pre-exponential factors in both oxidation models (Tables 4 and 5), but not seen in the Arrhenius plot for model I, and visible only for temperatures above 550 K in model II. For model II, the rates k_{tot} are strongly influenced by the pre-exponential factor for oxidation of cellulose (Table 5) above 525 K, so that beech is modelled most reactive at higher temperatures (>625 K). For model I, the pyrolysis kinetics of cellulose determine the order of biomasses on the Arrhenius plot. The contribution of the global oxidation reaction to the modelled rate is weak, owing to its lower activation energy ($E_{\text{ox}} = 130\,\text{kJ/mol}$, compared to $E_{\text{pyr,CELL}} = 185\,\text{kJ/mol}$ and $E_{\text{pyr,HC}} = 150\,\text{kJ/mol}$).

Conversion-free rates k_{tot} can also be calculated from published reaction mechanisms for pine.[13,14,17] The model presented in[14] gives k_{tot}-rates very similar to model I. The model presented in[13] for pine is also in fair agreement with our model II from temperatures of 500 K and above, and gives rates k_{tot} that are slightly higher below this temperature. Evaluating a third model[17] gave significantly higher rates than the ones found here.

The absence of extractives oxidation in model II was unexpected, as spontaneous oxidation of extractives can occur at very low temperatures (303–323 K)[1,2] and with low activation energies (as low as 55–60 kJ/mol).[1,7] Reactions at very low temperatures (<400 K) and with low activation energies are difficult to detect in the experimental program used, however. As briefly discussed above, the rate k_{tot} becomes increasingly dominated by higher activation energy reactions (especially of hemicellulose) with higher temperatures, and reactions with $E_a < 60\,\text{kJ/mol}$ are drowned out. At the low temperature stage of the isothermal experiments (423 K), the lowest measurable reaction rates were in order of $10^{-6}\,\text{s}^{-1}$, and this is also represented in the model (compare Figures 5 and 6). At this point, mass loss due to pyrolysis and oxidation could not be distinguished (Figure 3). Oxidation of extractives would therefore require significantly higher rates than those of their pyrolysis to be visible in the experiments. Moreover, extractives could also have been partially evaporated rather than pyrolyzed or oxidized in the experiments. Boiling points of C8:0–C18:0 fatty acids are in a range of 510–630 K, with corresponding enthalpies of evaporation 50–122 kJ/mol.

Similar to the pyrolysis kinetics, no clear correlation between composition (Table 1) and reactivity (Figure 6) was found. One trend that can be seen is that biomasses rich in potassium (sunflower, wheat; and to a lesser extent, beech) are more reactive at temperatures above ≈500 K than those with low amounts of alkali and alkaline earth metals (pine, both wood pellet samples). This tendency agrees with the trend observed for pyrolysis. Qualitatively, the same observation as for pyrolysis can be made: total reaction rates are dominated by (pyrolysis) extractive kinetics at low temperatures (<450 K) and become increasingly controlled by hemicellulose and cellulose at higher temperatures (model II) or the combination of oxidation of the lumped volatilizable species and pyrolysis of hemicellulose and cellulose (model I). The role of lignin is difficult to distinguish, and its reactions appear to take place in the background. Consequentially, the kinetic parameters determined for the lignin component in model II (Table 5) are very similar to the global parameters determined in model I (Table 4) for the lumped volatilizable component.

5 Conclusions

Owing to its high reactivity at low temperatures, biomass may self-heat and spontaneously ignite when kept or processed in hot environments (>423 K) such as power plant mills. Thermogravimetric analysis of stepwise isothermal experiments at 423–523 K was carried out for six biomasses: two wood species (beech, pine), two commercial wood pellet samples, and two agricultural residues (wheat straw and pelletized sunflower husks). These data were modelled by a reaction scheme considering oxidation and pyrolysis separately, and by modelling biomass as the sum of volatilizable hemicellulose, cellulose, lignin and extractives, as well as a non-volatilizable, combustible fraction (char), and ash as inert component. The pyrolysis model (Table 3) of four volatilizable components was in good agreement with measured data in nitrogen atmosphere. The mechanisms also compared favorably to further experiments carried out between 373–773 K at a constant heating rate of 5 K/ min.

For the oxidation process, two different approaches were considered. In the first model (model I, Table 4), the volatilizable components were treated as a lumped species, i.e. modelled by the same oxidation kinetic parameters. In an alternative model (model II, Table 5), the oxidation of volatilizable hemicellulose, cellulose, lignin and extractives were treated separately. Both models compared well with experimental data for stepwise isothermal experiments at 423–523 K in 20 % and 80 % oxygen atmosphere. Oxidation (globally, i.e. for the lumped volatilizable component) had an apparent reaction order in oxygen of 0.4–0.5. The oxidation models could with fair accuracy also be applied to experiments at 373–773 K with a constant heating rate of 5 K/ min under 10 % and 20 % oxygen atmosphere. Differences between the two oxidation models were mainly found in the predicted degree of conversion of hemicellulose and cellulose. For the global mass loss in the temperature range of 423–523 K, the simpler oxidation model is considered as sufficiently accurate, and considering oxidation of the components separately does not offer an advantage.

Some simplifications to the oxidation and pyrolysis models were possible. It was found that activation energies for the biomass components could be set to the same value, regardless of which biomass they appear in. In this work, activation energies were fixed to values derived from experiments on commercial cellulose, lignin and xylan samples. This is to be understood as a numerically, rather than physically correct description of the mass loss kinetics. Values found for activation energies were consistent with those published in the literature. The models developed here mainly differ from previous work in the description of the low temperature range (423–523 K). This could especially be seen in a change from a low-temperature regime <450 K, which appeared dominated by extractive kinetics, to a higher temperature regime >500 K, which is controlled mainly by reactions of hemicellulose and, to a lesser extent, by cellulose (Figures 5 and 6). Biomass rich in extractives (sunflower, pine) correspondingly appeared most reactive at the lower end of the investigated temperature range, whereas biomass with large potassium content (possibly catalyzing cellulose conversion) showed larger mass loss rates (wheat, sunflower) at the upper end of the temperature range.

The kinetic models presented here can be used in simulations of low temperature conversion processes, especially self-heating, self-ignition and smoldering combustion of pulverized biomass. While some trends could be observed, there does not appear to be a strong coupling between any single component and the observed reactivity of the different biomasses. Further research combining composition information and kinetic parameters may be able to shed more light on the relation between the two.

Supporting Information

The supplementary material contains a comparison of two models from the literature with measured data from this work, showing that models fitted to classical TGA-experiments do not represent low temperature mass loss very well. It further contains: an assessment of kinetic control in the TG-experimnets; data from cellulose, lignin, xylan and rapeseed oil experiments; as well as additional information on the modelled conversion of components for the biomasses used.

Acknowledegements

The authors thank Ørsted A/S and Energinet for financial support of this work. Tareq Abdulrahman is thanked for assisting in the TGA measurements. Marvin Masche is acknowledged for providing the wood pellet samples and additional analysis data.

Symbols and abbreviations

symbol	quantity	base units
Bi	Biot number	–
E_a	apparent activation energy	$\mathrm{J\,mol^{-1}}$
k	reaction rate	$\mathrm{s^{-1}}$
k_0	pre-exponential factor	$\mathrm{s^{-1}}$
m	mass	kg
N	number of data points	–
n	apparent reaction order	–
p	pressure	Pa
R	universal gas constant	$\mathrm{J\,mol^{-1}K^{-1}}$
T	temperature	K
t	time	s
w	mass fraction	$\mathrm{kg\,kg^{-1}}$
X	conversion	–
δ_φ	deviation of φ	units of φ
$\delta_{\mathrm{S},\varphi}$	scaled deviation of φ	–

indices	
0	initial
exp	experiment
f	final
ox	oxidation
pyr	pyrolysis
ref	reference
sim	simulation

vol	volatilizable
CELL	cellulose
HC	hemicellulose
LIG	lignin
XTR	extractives

abbreviations

RMS	root-mean-square
TGA	thermo-gravimetric analysis

References

(1) Guo, W.; Trischuk, K.; Bi, X.; Lim, C. J.; Sokhansanj, S. Measurements of wood pellets self-heating kinetic parameters using isothermal calorimetry. *Biomass and Bioenergy* **2014**, *63*, 1–9.

(2) Rahman, M. A.; Hopke, P. K. Mechanistic Pathway of Carbon Monoxide Off-Gassing from Wood Pellets. *Energy and Fuels* **2016**, *30*, 5809–5815.

(3) Birkby, C.; Brown, J.; Street, P. J. The early detection of mill fires by monitoring for carbon monoxide. *Combustion* **1973**, *45*, 38–42.

(4) Ren, T. X.; Edwards, J. S.; Clarke, D. Adiabatic oxidation study on the propensity of pulverised coals to spontaneous combustion. *Fuel* **1999**, *78*, 1611–1620.

(5) Savolainen, K. Co-firing of biomass in coal-fired utility boilers. *Applied Energy* **2003**, *74*, 369–381.

(6) Stamm, A. J. Thermal Degradation of Wood and Cellulose. *Industrial and Engineering Chemistry* **1956**, *48*.

(7) Wadsö, L. Measuring chemical heat production rates of biofuels by isothermal calorimetry for hazardous evaluation modelling. *Fire and Materials* **2007**, *31*, 241–255.

(8) Munir, S.; Daood, S. S.; Nimmo, W.; Cunliffe, A. M.; Gibbs, B. M. Thermal analysis and devolatilization kinetics of cotton stalk, sugar cane bagasse and shea meal under nitrogen and air atmospheres. *Bioresource Technology* **2009**, *100*, 1413–1418.

(9) García-Torrent, J.; Fernandez Anez, N.; Medic Pejic, L.; Montenegro Mateos, L. Assessment of self-ignition risks of solid biofuels by thermal analysis. *Fuel* **2015**, *143*, 484–491.

(10) Jones, J. M.; Saddawi, A.; Dooley, B.; Mitchell, E. J. S.; Werner, J.; Waldron, D. J.; Weatherstone, S.; Williams, A. Low temperature ignition of biomass. *Fuel Processing Technology* **2015**, *134*, 372–377.

(11) Topf, P. Die thermische Zersetzung von Holz bei Temperaturen bis 180 C – Zweite Mitteilung: Versuche zur Frage der Selbstentzündung, des Gewichtsverlustes, des Brennwertes und der Elementaranalysen. *Holz als Roh- und Werkstoff* **1971**, *29*, 295–300.

(12) Cordero, T.; Rodriguez-Maroto, J. M.; Garcia, F.; Rodriguez, J. J. Thermal decomposition of wood in oxidizing atmosphere. A kinetic study from non-isothermal TG experiments. *Thermochimica Acta* **1991**,

(13) Amutio, M.; Lopez, G.; Aguado, R.; Artetxe, M.; Bilbao, J.; Olazar, M. Kinetic study of lignocellulosic biomass oxidative pyrolysis. *Fuel* **2012**, *95*, 305–311.

(14) Anca-Couce, A.; Zobel, N.; Berger, A.; Behrendt, F. Smouldering of pine wood: Kinetics and reaction heats. *Combustion and Flame* **2012**, *159*, 1708–1719.

(15) Broström, M.; Nordin, A.; Pommer, L.; Branca, C.; Di Blasi, C. Influence of torrefaction on the devolatilization and oxidation kinetics of wood. *Journal of Analytical and Applied Pyrolysis* **2012**, *96*, 100–109.

(16) Branca, C.; Di Blasi, C. A unified mechanism of the combustion reactions of lignocellulosic fuels. *Thermochimica Acta* **2013**, *565*, 58–64.

(17) Niu, H.; Liu, N. Thermal decomposition of pine branch: Unified kinetic model on pyrolytic reactions in pyrolysis and combustion. *Fuel* **2015**, *160*, 339–345.

(18) Branca, C.; Di Blasi, C. Global interinsic kinetics of wood oxidation. *Fuel* **2004**, *83*, 81–87.

(19) Safi, M. J.; Mishra, I. M.; Prasad, B. Global degradation kinetics of pine needles in air. *Thermochimica Acta* **2004**, *412*, 155–162.

(20) Shen, D. K.; Gu, S.; Luo, K. H.; Bridgwater, A. V.; Fang, M. X. Kinetic study on thermal decomposition of woods in oxidative environment. *Fuel* **2009**, *88*, 1024–1030.

(21) Ohlemiller, T. J. Modeling of smoldering combustion propagation. *Progress in Energy and Combustion Science* **1985**, *11*, 277–310.

(22) Senneca, O.; Chirone, R.; Salatino, P. A Thermogravimetric Study of Nonfossil Solid Fuels. 2. Oxidative Pyrolysis and Char Combustion. *Energy & Fuels* **2002**, *16*, 661–668.

(23) Font, R.; Conesa, J. A.; Moltó, J.; Muñoz, M. Kinetics of pyrolysis and combustion of pine needles and cones. *Journal of Analytical and Applied Pyrolysis* **2009**, *85*, 276–286.

(24) Abreu Naranjo, R.; Conesa, J.; Foppa Pedretti, E.; Romero Romero, O. Kinetic analysis: Simultaneous modelling of pyrolysis and combustion processes of dichrostachys cinerea. *Biomass and Bioenergy* **2012**, *36*, 170–175.

(25) Huang, X.; Rein, G. Thermochemical conversion of biomass in smouldering combustion across scales: The roles of heterogeneous kinetics, oxygen and transport phenomena. *Bioresource Technology* **2016**, *207*, 409–421.

(26) Benkorichi, S.; Fateh, T.; Richard, F.; Consalvi, J.-L.; Nadjai, A. Investigation of thermal degradation of pine needles using multi-step reaction mechanisms. *Fire Safety Journal* **2017**, *91*, 811–819.

(27) Prins, M. J.; Ptasinski, K. J.; Janssen, F. J. J. G. Torrefaction of wood: Part 1. Weight loss kinetics. *Journal of Analytical and Applied Pyrolysis* **2006**, *77*, 28–34.

(28) Chen, W.-H.; Kuo, P.-C. Torrefaction and co-torrefaction characterization of hemicellulose, cellulose and lignin as well as torrefaction of some basic constituents in biomass. *Energy* **2011**, *36*, 803–811.

(29) Ren, S.; Lei, H.; Wang, L.; Bu, Q.; Chen, S.; Wu, J. Thermal behaviour and kinetic study for woody biomass torrefaction and torrefied biomass pyrolysis by TGA. *Biosystems Engineering* **2013**, *116*, 420–426.

(30) Khazraie Shoulaifar, T.; DeMartini, N.; Karlström, O.; Hupa, M. Impact of organically bonded potassium on torrefaction: Part 1. Experimental. *Fuel* **2016**, *165*, 544–552.

(31) Alves, S. S.; Figueiredo, J. L. Pyrolysis kinetics of lignocellulosic materials by multistage isothermal thermogravimetry. *Journal of Analytical and Applied Pyrolysis* **1988**, *13*, 123–134.

(32) Becidan, M.; Várhegyi, G.; Hustad, J. E.; Skreiberg, Ø. Thermal Decomposition of Biomass Wastes. A Kinetic Study. *Industrial & Engineering Chemistry Research* **2007**, *46*, 2428–2437.

(33) Várhegyi, G.; Sebestyén, Z.; Czégény, Z.; Lezsovits, F.; Könczöl, S. Combustion Kinetics of Biomass Materials in the Kinetic Regime. *Energy & Fuels* **2011**, *26*, 1323–1335.

(34) Nik-Azar, M.; Hajaligol, M. R.; Sohrabi, M.; Dabir, B. Mineral matter effects in rapid pyrolysis of beech wood. *Fuel Processing Technology* **1997**, *51*, 7–17.

(35) Di Blasi, C. Modeling chemical and physical processes of wood and biomass pyrolysis. *Progress in Energy and Combustion Science* **2008**, *34*, 47–90.

(36) Saddawi, A.; Jones, J. M.; Williams, A. Influence of alkali metals on the kinetics of the thermal decomposition of biomass. *Fuel Processing Technology* **2012**, *104*, 189–197.

(37) Wang, S.; Dai, G.; Yang, H.; Luo, Z. Lignocellulosic biomass pyrolysis mechanism: A state-of-the-art review. *Progress in Energy and Combustion Science* **2017**, *62*, 33–86.

(38) Sárossy, Z.; Plackett, D.; Egsgaard, H. Carbohydrate analysis of hemicelluloses by gas chromatography–mass spectrometry of acetylated methyl glycosides. *Analytical and Bioanalytical Chemistry* **2012**, *403*, 1923–1930.

(39) Grønli, M.; Antal, M. J.; Várhegyi, G. A Round-Robin Study of Cellulose Pyrolysis Kinetics by Thermogravimetry. *Industrial & Engineering Chemistry Research* **1999**, *38*, 2238–2244.

(40) Grønli, M. G.; Várhegyi, G.; Blasi, C. D. Thermogravimetric Analysis and Devolatilization Kinetics of Wood. *Industrial and Engineering Chemistry Research* **2002**, *41*, 4201–4208.

(41) Pyle, D. L.; Zaror, C. A. Heat transfer and kinetics in the low temperature pyrolysis of solids. *Chemical Engineering Science* **1984**, *39*, 147–158.

(42) Hayhurst, A. N. The kinetics of the pyrolysis or devolatilisation of sewage sludge and other solid fuels. *Combustion and Flame* **2013**, *160*, 138–144.

(43) Frank-Kamenetskii, D. A. *Diffusion and Heat Transfer in Chemical Kinetics*, 2nd ed.; Plenum Press, 1969; English translation by J. P. Appleton.

(44) Rogers, F. E.; Ohlemiller, T. J. Cellulosic Insulation Material I. Overall Degradation Kinetics and Reaction Heats. *Combustion Science and Technology* **1980**, *24*, 129–137.

(45) Conesa, J. A.; Domene, A. Biomasses pyrolysis and combustion kinetics through n-th order parallel reactions. *Thermochimica Acta* **2011**, *523*, 176–181.

(46) Di Blasi, C. Combustion and gasification rates of lignocellulosic chars. *Progress in Energy and Combustion Science* **2009**, *35*, 121–140.

(47) Anca-Couce, A. Reaction mechanisms and multi-scale modelling of lignocellulosic biomass pyrolysis. *Progress in Energy and Combustion Science* **2016**, *53*, 41–79.

(48) Ebringerová, A.; Hromádková, Z.; Heinze, T. *Polysaccharides I*; Springer-Verlag, 2005; pp 1–67.

(49) Chen, H. *Biotechnology of Lignocellulose*; Springer Netherlands, 2014.

(50) Beall, F. C. Differential calometric analysis of wood and wood components. *Wood Science and Technology* **1971**, *5*, 159–175.

(51) Werner, K.; Pommer, L.; Broström, M. Thermal decomposition of hemicelluloses. *Journal of Analytical and Applied Pyrolysis* **2014**, *110*, 130–137.

(52) Dussan, K.; Dooley, S.; Monaghan, R. Integrating compositional features in model compounds for a kinetic mechanism of hemicellulose pyrolysis. *Chemical Engineering Journal* **2017**, *328*, 943–961.

(53) Antal, M. J.; Varhegyi, G. Cellulose Pyrolysis Kinetics: The Current State of Knowledge. *Industrial & Engineering Chemistry Research* **1995**, *34*, 703–717.

(54) Jensen, A.; Dam-Johansen, K.; Wójtowicz, M. A.; Serio, M. A. TG-FTIR Study of the Influence of Potassium Chloride on Wheat Straw Pyrolysis. *Energy & Fuels* **1998**, *12*, 929–938.

(55) Eom, I.-Y.; Kim, J.-Y.; Kim, T.-S.; Lee, S.-M.; Choi, D.; Choi, I.-G.; Choi, J.-W. Effect of essential inorganic metals on primary thermal degradation of lignocellulosic biomass. *Bioresource Technology* **2012**, *104*, 687–694.

(56) Khazraie Shoulaifar, T.; DeMartini, N.; Karlström, O.; Hemming, J.; Hupa, M. Impact of organically bonded alkali metals on torrefaction: Part 2. Modeling. *Fuel* **2016**, *168*, 107–115.

(57) Orfão, J. J. M.; Antunes, F. J. A.; Figueiredo, J. L. Pyrolysis kinetics of lignocellulosic materials—three independent reactions model. *Fuel* **1999**, *78*, 349–358.

Kinetic parameters for biomass at self-ignition conditions: low-temperature oxidation and pyrolysis

Lars Schwarzer,*,† Zsuzsa Sárossy,† Peter Arendt Jensen,*,† Peter Glarborg,†
Jens Kai Holm,‡ and Kim Dam-Johansen†

†*Department of Chemical and Biochemical Engineering, Technical University of Denmark, Søltofts Plads 229, 2800 Kgs. Lyngby, Denmark*
‡*Ørsted A/S, Nesa Allé 1, 2820 Gentofte, Denmark*

E-mail: laschw@kt.dtu.dk; paj@kt.dtu.dk

Supporting Information

Reproduction of published experiments

Some published experiments were reproduced to ensure the validity of the thermogravimetric measurements. Grønli et al.[1] published a round-robin study on pyrolysis of cellulose. The experiment at 5 K/ min was reproduced and compared to the model published in.[1] The measured peak decomposition rate temperature in this experiment was on the higher end (605 K) of the range reported in the original study (600 K ± 5 K), Figure 1. Instead of Avicel cellulose, cellulose from Sigma-Aldrich was used. Total gas flow rate was 150 mL/ min of nitrogen.

Two experiments for pyrolysis of pine published by Grønli et al.[2] and Anca-Couce et al.[3]

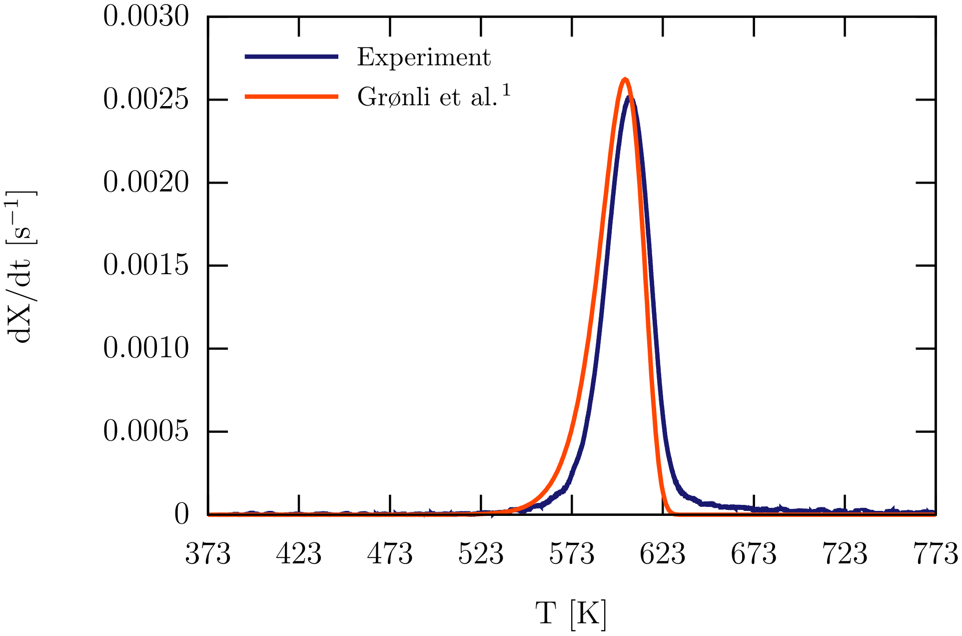

Figure 1: Reproduction of a round-robin study on cellulose pyrolysis kinetics. Model data:,[1] experimental data: cellulose, 5 K/ min heating rate, 150 mL/ min nitrogen

were also reproduced. Results are summarized in Figure 2. Of the models presented by Grønli et al.,[2] the biomass named "pine A" showed a better agreement with the measured data in this work. The model consists of four components, extractives, hemicellulose, cellulose and lignin.[2] Anca-Couce et al.[3] consider only hemicellulose, cellulose and lignin as components. The experimental in this work was measured at a constant heating rate of 5 K/ min and a nitrogen flow rate of 150 mL/ min. The measured data shows slightly higher conversion rates than either model below 523 K. Between 550–650 K, experimental data of this work falls between the two models.[2,3]

A comparison between the kinetic models[2,3] and experiments carried out at 423–523 K is shown in Figure 3. The experiment consisted of six isothermal holding stages (423 K, 443 K, 463 K, 483 K, 503 K and 523 K) held for one hour each, with rapid heating of 10 K/ min between stages and to reach the first iosthermal stage. Gas flow rates were 150 mL/ min of nitrogen. Experiments reported by Grønli et al.[2] were originally carried out at 383–773 K, 5 K/ min heating rate and 150 mL/ min nitrogen flow. Anca-Couce et al.[3] report data for

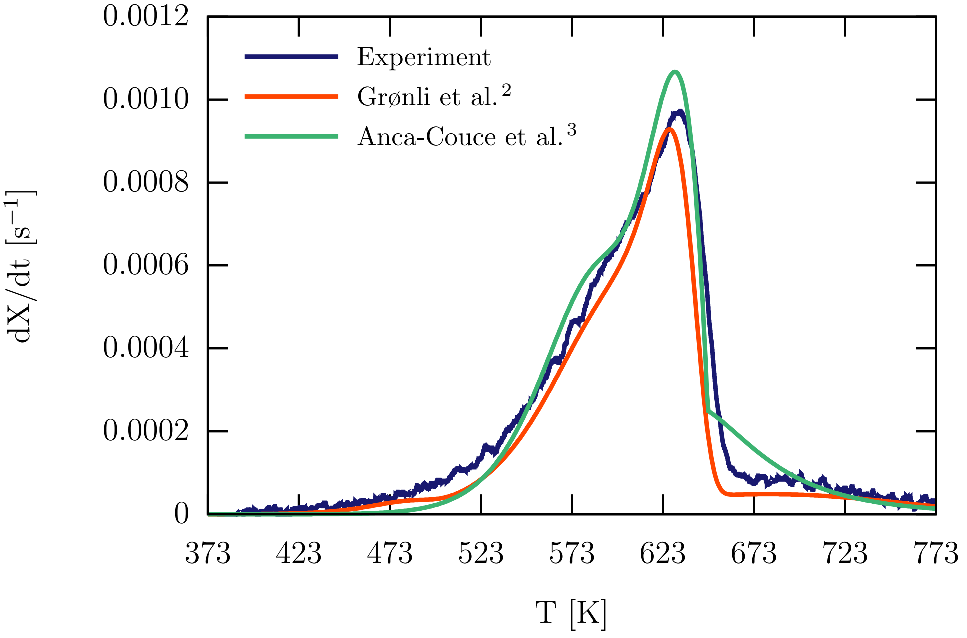

Figure 2: Reproduction of published TGA experiments on pine pyrolysis kinetics. Model data from[2] refers to species "pine A", model data from[3] is the model with three components hemicellulose, cellulose and lignin. Experimental data: pine, 5 K/ min heating rate, 150 mL/ min nitrogen

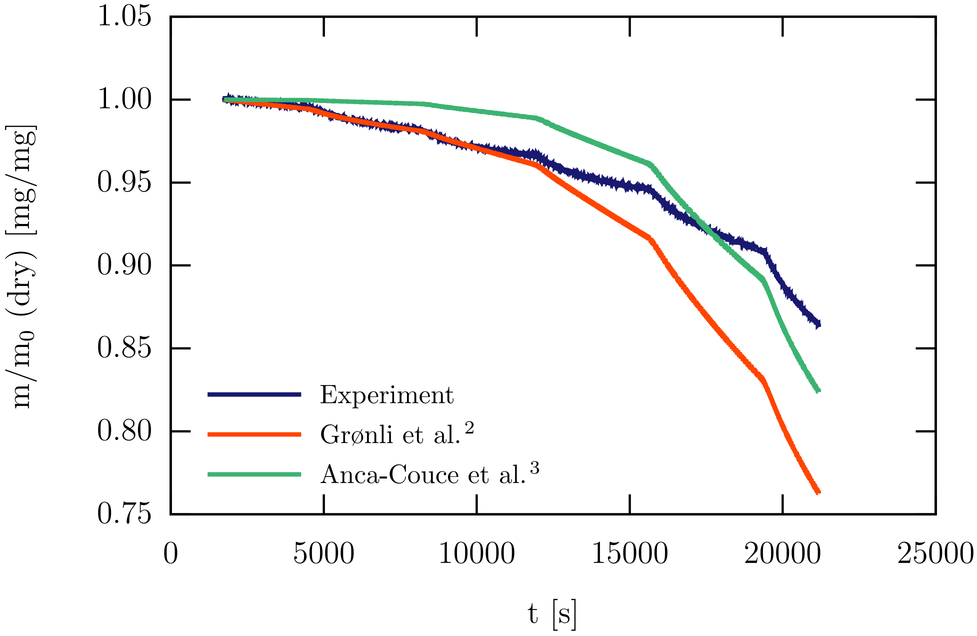

Figure 3: Extrapolation of published pine pyrolysis kinetics. Model data from[2] refers to species "pine A", model data from[3] is the model with three components hemicellulose, cellulose, lignin. Experimental data: pine, 150 mL/ min nitrogen, six isothermal stages at 423 K, 443 K, 463 K, 483 K, 503 K and 523 K held for one hour each.

473–723 K and heating rates 2.5–10 K/ min, so that the models presented in[2,3] are strictly only valid under those conditions. The comparison shows that the models do not extrapolate very well to low temperatures and low heating rates or isothermal conditions. The model of Grønli et al.[2] predicts mass loss well during the first three isothermal stages 423–463 K, but overpredicts mass loss for higher temperatures. The model by Anca-Couce et al.[3] predicts lower mass loss rates than measured between 423–463 K, and higher rates than measured for 483–523 K.

Kinetic control

Experiments under transient heating conditions can become limited by heat transfer, if heat transfer to and within the particle are not significantly faster than reaction rates.[4] Heat transfer limitations in the pyrolysis experiments were checked against criteria presented by Hayhurst.[5] Following that work, experiments with transient heating need to satisfy:

$$\mathrm{Bi} = 0.6\,\frac{\mathrm{Nu}}{2}\,\frac{\lambda_\mathrm{g}}{\lambda_\mathrm{s}} < 0.1 \tag{1}$$

where Bi is the Biot number, Nu the Nusselt number and λ_g and λ_s the thermal conductivities of gas and solid, respectively. Approximating Nu = 2 for spherical particles in near stagnant flow,[5] as well as biomass solid thermal conductivities $\lambda_\mathrm{s} = 0.12$–$0.18\,\mathrm{W/(m\,K)}$[6] and thermal conductivity of air or nitrogen 0.04 W/(m K) at 523 K,[6] Bi = 0.13–0.2. This value is slightly higher than that used in the literature,[5] yet still smaller than unity (equal timescales of external and internal heat transfer). As discussed in,[5] the above expression does not depend on particle size, if gas velocities are low enough that size influences on Nu are negligible.

The Biot number was also estimated for the entire sample, i.e. the crucible with the particle bed. The crucible is approximated as a spherical object in near-stagnant flow, so that Nu = 2. Thermal conductivity of the crucible material (alumina) is one order of magnitude higher than that of wood ($\lambda \approx 2\,\mathrm{W/(m\,K)}$), so that it does not limit heat transfer through the bed. Thermal conductivity of the particle bed depends on the thermal conductivities of solid particles and interstitial gas, as well as the porosity ϕ of the bed. Assuming loosely packed beds, $\phi = 0.5$–0.8, and an effective thermal conductivity[7] of

$$\lambda_{\text{eff}} = \phi\,\lambda_{\text{g}} + (1-\phi)\,\lambda_{\text{s}} \tag{2}$$

Biot-numbers for the *sample* evaluate to 0.2–0.4. Temperature in the sample bed is therfore mainly, but not exclusively controlled by external heat transfer. Approximate kinetic control was nevertheless assumed, as $\text{Bi} < 0.1$ is difficult to achieve in practice.[5]

As internal heat transfer is faster than external heat transfer, the external Pyrolysis number Py, i.e. the rate of external heat transfer to reaction rate,[4] was evaluated. To assume kinetic control, in addidition to $\text{Bi} \ll 1$, the timescale of reactions must be much larger than that of heat transfer, $\text{Py} = \tau_{\text{kin}}/\tau_{\text{heat}} \gg 1$, where τ_{kin} is the kinetic timescale and τ_{ht} the heat transfer timescale. The criterion gives a maximum value for the particle radius r:[5]

$$\frac{2\,\rho\,c_{\text{p}} r^2}{3\,\text{Nu}\,\lambda_{\text{g}}} < 0.1 \cdot \tau_{\text{kin}} \tag{3}$$

where ρ is the density of the solid and c_{p} its specific heat capacity. The kinetic timescale is estimated as $\tau_{\text{kin}} = 1/k$, where k are the modelled reaction rates. Reaction rates are below $1 \times 10^{-3}\,\text{s}^{-1}$ for temperatures below 523 K. Assuming $\rho = 600\,\text{kg/m}^3$,[6] and $c_{\text{p}} = 2000\,\text{J/(kg K)}$,[7] this allows for particle sizes up to 6 mm diameter. The above expression was also used to calculate the critical rate for 250 µm particles (the largest particle size used) results in $k = 0.6\,\text{s}^{-1}$. Such rates were only predicted above 700 K for pyrolysis and above 625 K for the oxidation models. The same calculation was carried out for the entire bed of particles, i.e. for lower densities (bulk density instead of solid density). Again assuming $\text{Nu} = 2$ and using the bed depth ($1/3 \cdot 4\,\text{mm}$) instead of the particle radius, critical reaction rates would be reached at temperatures of 555 K (20 % oxygen, $\phi = 0.5$), 570 K (20 % oxygen,

$\phi = 0.8$), 590 K (pyrolysis, $\phi = 0.5$) and 620 K (pyrolysis, $\phi = 0.8$). Critical temperatures are lower for the oxidation experiments as total reaction rates are higher when oxygen is present.

In the oxidation experiments, lack of oxygen can inhibit kinetic control in addition to possible heat transfer limitations. For the loosely packed sample in the crucible, diffusion through the bed is the main mode of mass transfer. The ratio of oxygen consumption to oxygen diffusion can be expressed by a Damköhler number Da. In this work, it was estimated by:

$$\mathrm{Da} = \frac{k(T) \cdot f(p_{\mathrm{O}_2})\, C_{\mathrm{O}_2,\mathrm{stoich}}\, L^2}{D\, C_{\mathrm{O}_2,\mathrm{amb}}} \tag{4}$$

where $k(T) \cdot f(p_{\mathrm{O}_2})$ is the reaction rate including oxygen partial-pressure dependency, $C_{\mathrm{O}_2,\mathrm{stoich}}$ the concentration of oxygen required for complete conversion (i.e., molar amount of oxygen per unit volume occupied by the sample), $C_{\mathrm{O}_2,\mathrm{amb}}$ the concentration of oxygen in the surroundings and D the diffusion coefficient. L is a characteristic length, in this case, the sample depth, 1.3 mm (one third of the crucible height). Kinetic control is given for $\mathrm{Da} \ll 1$. The kinetic expression was evaluated for wheat, using the rate of oxidation model I. The diffusion coefficient was estimated by

$$D = 1.5 \times 10^{-5} \left(\frac{T}{T_{\mathrm{ref}}} \right)^{1.75}; \qquad T_{\mathrm{ref}} = 300\,\mathrm{K} \tag{5}$$

Stoichiometric oxygen demand can be calculated from the elemental composition. Ambient oxygen concentrations were calculated assuming a pressure of 101 325 Pa, 20 % oxygen, and by assuming sample and surroundings in thermal equilibrium. Based on these values, diffusion is much faster than consumption of oxygen ($\mathrm{Da} < 0.1$) for $T < 570\,\mathrm{K}$.

Thermal runaway of samples can occur when heat is (locally) released faster than it can be dissipated by internal heat transfer. Such possible self-ignition of the sample was evaluating the dimensionless Frank-Kamenetskii parameter[8] δ:

$$\delta = \frac{h_{\mathrm{R}}\,\rho}{\lambda_{\mathrm{eff}}}\,\frac{E_{\mathrm{a}}}{R\,T^2}\,L^2 \cdot k(T) \cdot f(p_{\mathrm{O_2}}) \tag{6}$$

where the mass-specific enthalpy of reaction h_{R} was set equal to the lower heating value of wheat (18.2 MJ/kg), the bulk density of the sample was $\rho = 97\,\mathrm{kg/m^3}$, the effective thermal conductivity of the sample $\lambda_{\mathrm{eff}} = 0.07\,\mathrm{W/(m\,K)}$. The sample depth was used as characteristic length L. According to the theory of thermal explosions, samples are stable, i.e., do not self-ignite, when $\delta < \delta_{\mathrm{crit}}$. The critical values δ_{crit} depend only on geometry, and are given as 0.88 for infinite slabs, 2.00 for infinite cylinders and 3.23 for spheres.[8] In the worst-case assumption, the sample was treated as an infinite layer. Evaluating δ as a function of temperature T gave a critical temperature of 530 K. Assuming the sample can be represented by a sphere resulted in $T_{\mathrm{crit}} = 555\,\mathrm{K}$. Repeating this calculation for 80 % oxygen, i.e. higher reaction rates, gave critical temperatures of 520 K and 540 K, respectively. Heat release kinetics are likely overestimated in the above calculation, as the smoldering conversion typical of the temperature range investigated leads to highly incomplete conversion[9] (and thus lower heat release). Additionally, thermal runaway should be fairly easy to observe if it occured at low heating rates or during the isothermal stages – however, no excessive (uncompensated) self-heating was measured in any of the experiments.

In conclusion, which transport limitation is most critical with respect to assuming kinetic control depends on the type of experiment. The largest concern in experiments with constant heating rate was the Biot-number. For the stepwise isothermal experiment, this can be neglected, as the transient phases are short compared to the isothermal holding periods. As discussed by Hayhurst,[5] the Biot-number depends largely on material properties, and values $1 < \mathrm{Bi} < 0.1$ are difficult to avoid for biomass. Possible self-ignition of the sample could be a concern in experiments with oxygen present. By conservative estimate, samples may come close to thermal runaway during the TG-experiments. Thermal runaway was however not observed experimentally. Diffusion limitations were found to be negligible in the temperature range of interest. All estimations of critical parameters were carried out by neglecting the influence of conversion on reaction rates. Measured conversion rates were much lower ($< 0.0015\,\mathrm{s}^{-1}$) than the reaction rates (compare the Arrhenius plots) used in the above calculations, so that the critical parameters include a considerable safety margin. The stepwise isothermal experiments are expected to be free from transport limitations, even if the above strict criteria are applied.

Kinetic data for cellulose, lignin, xylan and rapeseed oil

Kinetic parameters for the model components extractives, hemicellulose, lignin and cellulose were determined by thermogravimetric analysis and using the same time-temperature programs as for the six biomass samples. Rapeseed oil was used as a model compound for extractives. To simulate extractives bound in a matrix (i.e. as opposed to a bulk liquid), the oil was mixed in a ratio of 1:1 by weight with SiO_2 as an inert substrate. The consistency of the mixture was that of a thin paste. Alternative mixtures of rapessed oil and cellulose, and of linseed oil and either SiO_2 or cellulose were also investigated, but gave qualitatively similar results. As a model compound for hemicellulose, xylan (from cornstalk; abcr Chemie AB143294) was used. Lignin and cellulose were also acquired from a commercial supplier (alkali lignin: Sigma-Aldrich 471003, and cellulose powder: Sigma-Aldrich C6288).

Char yields of the model components were measured by heating in inert atmosphere at 5 K/ min to 773 K, holding that temperature for 30 minutes, followed by a burnoff under 10 % oxygen and 10 K/ min heating rate to 973 K. Results of the heating in inert atmosphere are summarized in Figure 4 for xylan, lignin and cellulose. Extractives were assumed to be completely volatilizable, either by pyrolytic decomposition or by evaporation. The residues at 773 K were approximately 9 % for cellulose, 25 % for xylan and 65 % for lignin. On burnout, cellulose and xylan left no residue, while the lignin sample left around 5 % ash residue. Char ratios of the three components were therefore 9:25:60 (cellulose:xylan:lignin),

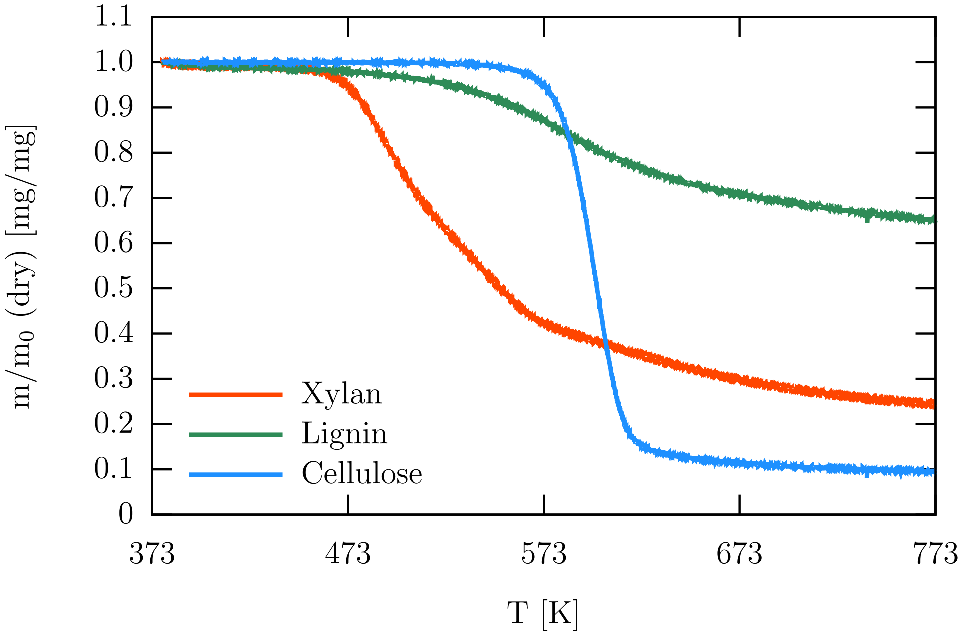

Figure 4: Experiments at 5 K/ min heating rate under 0 % oxygen to determine the volatilizable fractions of hemicellulose, cellulose and lignin. Xylan was used as a hemicellulose model component.

which was rounded to 10:30:60 in the model.

Activation energies of extractives, hemicellulose, lignin and cellulose were determined by the same stepwise isothermal heating program used for the six biomasses: holding for one hour each at 423 K, 443 K, 463 K, 483 K, 503 K and 523 K, with rapid heating (10 K/ min) to reach the first isothermal period and in between isothermal stages. Experiments were carried out under 0 %, 20 % and 80 % oxygen. Kinetic parameters were then obtained by the same model as for the six biomasses, i.e. total conversion rate is the sum of pyrolysis and oxidation rate

$$\frac{dX_i}{dt} = k_{\text{pyr, i}} \cdot (1 - X_i(t))^{n_{\text{pyr, i}}} + k_{\text{ox, i}} \cdot (1 - X_i(t))^{n_{\text{ox i}}} \cdot \left(\frac{p_{O_2}}{p_{\text{ref}}}\right)^{n_{O_2,i}} \tag{7}$$

for each component i. Reactions were assumed to be n-order and reaction rates k were modelled by an Arrhenius-expression as outlined above. Kinetic parameters were found by a least-square fit of the reaction model to the measured data. This was carried out in two steps: the parameters of the pyrolysis reaction $\{E_a, k_0, n_{\text{pyr}}\}$ were determined first from experimental data under 0 % oxygen. These parameters were then kept fixed, while those of the oxidation reaction $\{E_a, k_0, n_{\text{ox}}, n_{O_2}\}$ were fitted. The numeric results are summarized in Table 1, and modelled and experimental data are compared in Figures 5 through 8. The value of the kinetic parameters depended to some degree on the final mass $m_{\text{f, i}}$ that was assumed in their fitting. For xylan, lignin and cellulose, the remaining mass fraction for pyrolysis up to 500 °C (Figure 4) was used. For the rapeseed-oil-SiO_2 mixture, it was assumed that all oil is reacted or evaporated and only the inert substrate remains.

Over the temperature range 423–523 K, xylan showed the highest mass loss. However, lignin and the rapeseed-oil-SiO_2 mixture have high 'baselines' of inert material (65 % and 50 %, respectively), so that the relative loss of reactive material is also considerable in the temperature range investigated. Cellulose showed very little mass loss during the lower temperature stages of the experiment, but reactions were found to rapidly accelerate beyond 503 K.

The overall beahvior of lignin interestingly resembled that of native biomasses from a qualitative point of view. Similar to the native biomasses, its behavior is only approximated by the combination of two n-order reactions for pyrolysis and oxidation. Rapeseed oil, xylan

Table 1: Kinetic parameters for volatilizable fractions of extractives, hemicellulose, lignin and cellulose. Rapeseed oil mixed (50 % by weight) with SiO_2 as inert substrate was used as a model compound for extractives in a matrix. Xylan was used as a model compound for hemicellulose.

		Rapeseed oil+SiO_2	Xylan	Lignin	Cellulose
m_f/m_0	[kg/kg]	0.5	0.25	0.65	0.09
$E_{\text{a, pyr}}$	[kJ/mol]	58.9	118	126	184
$k_{\text{0, pyr}}$	[s^{-1}]	2.02×10^1	2.85×10^9	5.63×10^8	1.56×10^{13}
n_{pyr}	[–]	1	6.98	7.51	1
$E_{\text{a, ox}}$	[kJ/mol]	72.8	150	117	226
$k_{\text{0, ox}}$	[s^{-1}]	8.85×10^2	3.64×10^{-5}	2.41×10^4	1.31×10^{15}
n_{ox}	[–]	14.3	1	1.42	1
n_{O_2}	[–]	0.40	1	0.76	0.67

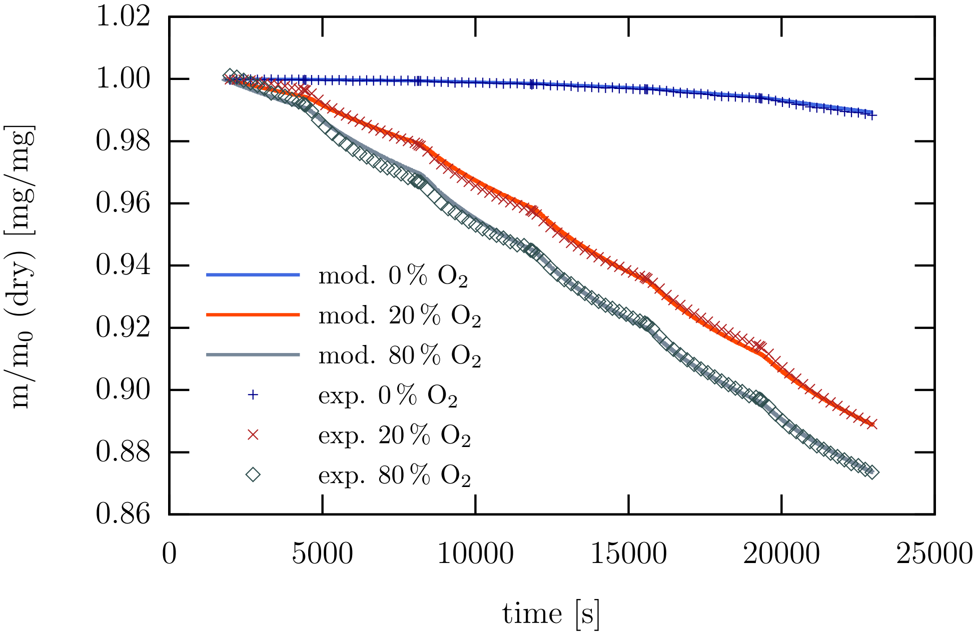

Figure 5: Modelled and measured mass loss of rapeseed oil on SiO_2 powder, mixed 1:1 by weight. Six isothermal stages at 423 K, 443 K, 463 K, 483 K, 503 K and 523 K held for one hour each, different oxygen concentrations.

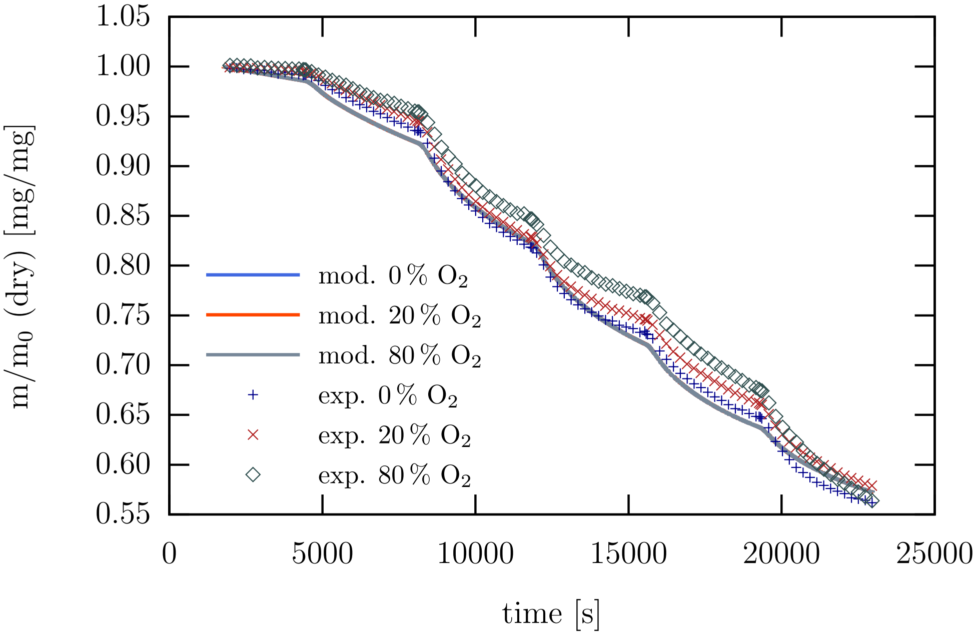

Figure 6: Modelled and measured mass loss of xylan. Six isothermal stages at 423 K, 443 K, 463 K, 483 K, 503 K and 523 K held for one hour each, different oxygen concentrations.

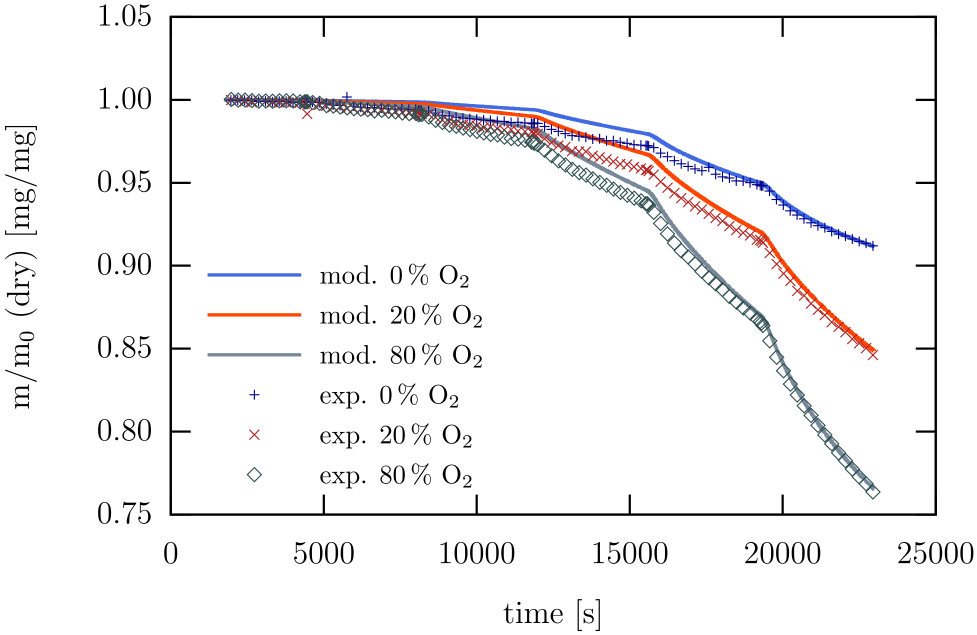

Figure 7: Modelled and measured mass loss of lignin. Six isothermal stages at 423 K, 443 K, 463 K, 483 K, 503 K and 523 K held for one hour each, different oxygen concentrations.

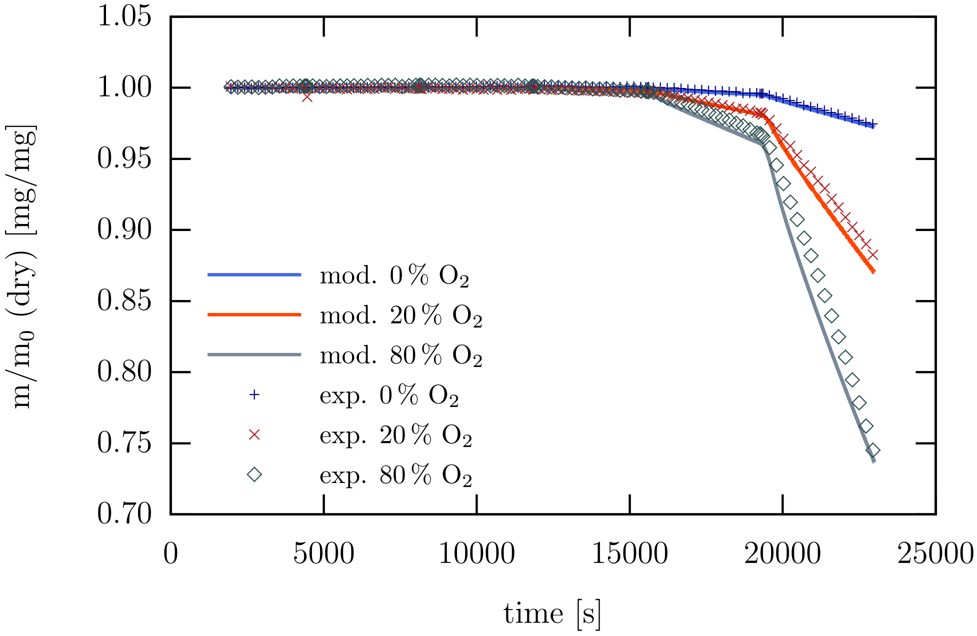

Figure 8: Modelled and measured mass loss of cellulose. Six isothermal stages at 423 K, 443 K, 463 K, 483 K, 503 K and 523 K held for one hour each, different oxygen concentrations.

and cellulose on the other hand showed very specific trends. The decomposition of xylan did not appear to be affected by the concentration or presence of oxygen. The modelled oxidation reaction has very low rates, so that the three model curves for 0 %, 20 % and 80 % oxygen collapse onto the pyrolysis curve. Two explanations are possible: either oxidation of xylan is very slow compared to its pyrolysis, or the experiment was not kinetically controlled. Several researchers working in temperature ranges from ambient temperature to 800 K or higher consider 5 mg sufficiently small to avoid diffusion limitations,[2,10–15] while some allow up to 10 mg.[16–19] Sample masses were 6.8 mg, 6.5 mg and 7.1 mg in the experiments show in Figure 6, while final temperatures and heating rates were lower in our experiments (implying lower reaction rates) than those reported in the literature.[2,10–19]

It was also noted that the xylan powder was very hygroscopic and would immediately absorb humidity from the surrounding air when preparing the samples, forming sticky agglomerates in the process. This may have led to additional transport limitations. Ultimately, the reasons for the observed behavior of xylan could not be resolved. The activation energy reported for xylan in Table 1 was initially used to model the hemicellulose component of the biomass, but replaced with higher values for reasons described in the results section of this work.

Pyrolysis reactions of both the rapeseed oil mixture and cellulose could be equally well represented by a first or zero-order reaction in the temperature range 423–523 K. The reaction order did not appear to affect the respective values determined for the activation energies.

Comparing the kinetic parameters for the pure coponents in Table 1 with those for the components as they appear in the biomasses (see main text) shows rather large differences in the pre-exponential factors k_0 and reaction orders n. This behavior is expected, owing to physical and chemical changes introduced during separation procedures, neglecting interactions among components and absence of catalytic effects of inorganic matter when studying the isolated components.[20]

Comparison of oxidation models I and II

Oxidation models I and II showed only minor differences in the temperature region of interest, 423–523 K. A comparison of model I and measured data can be seen in the main body of the text. The corresponding plots for model II are found in Figure 9. Differences between the models become apparent at temperatures above ca. 520–550 K for a heating rate of 5 K/ min.

Table 2 lists the scaled root-mean-square deviations of both oxidation models compared to measured data. Both models represent measured data with similar accuracy.

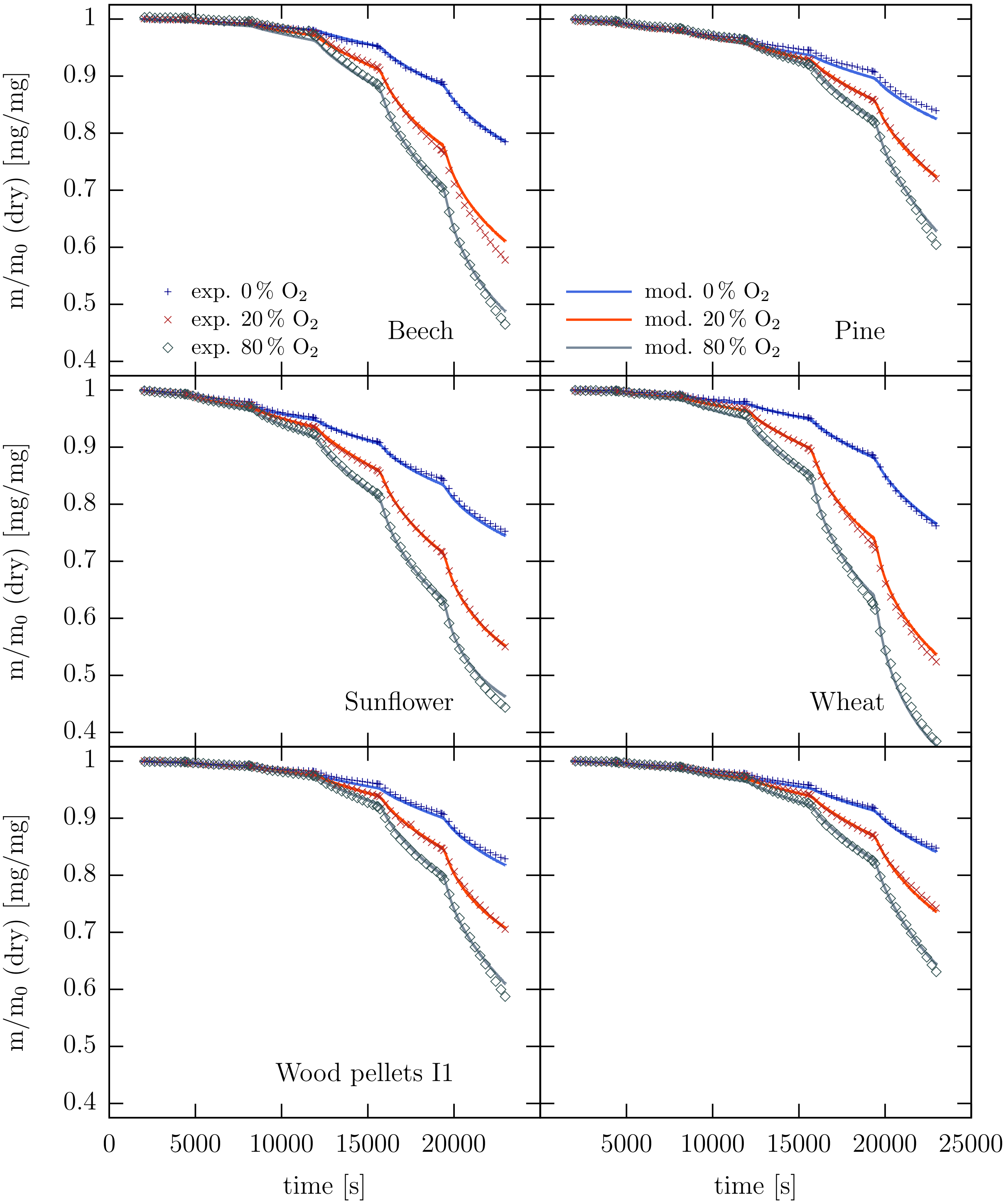

Figure 9: Oxidation model II: comparison of isothermal experiment and model, assuming separate oxidation kinetics of hemicellulose, cellulose, lignin and extractives. Kinetic parameters are listed in the main text

Table 2: Scaled root-mean-square deviations ($\delta_{S,\varphi}$) between modelled and measured data in oxidative atmosphere. "Isothermal" refers to the stepwise isothermal experiments, "ramp" to those at constant heating rate 5 K/ min.

Biomass	Model	$\delta_{\mathrm{S}}(m/m_0)$		$\delta_{\mathrm{S}}(dX/dt)$	
Isothermal		20 % O_2 [%]	80 % O_2 [%]	20 % O_2 [%]	80 % O_2 [%]
Beech	I	1.25	1.53	11.0	12.3
	II	1.84	0.91	10.3	12.4
Pine	I	5.55	4.27	12.3	10.6
	II	0.72	1.25	14.4	11.9
Sunflower	I	1.15	0.80	12.5	13.2
	II	0.73	0.81	12.2	12.4
Wheat	I	3.79	1.76	11.4	9.2
	II	1.87	1.29	13.1	12.0
Wood pellets I1	I	2.40	2.15	11.2	11.1
	II	0.88	1.32	10.4	12.5
Wood pellets I2	I	2.79	2.80	11.1	11.2
	II	2.46	1.53	15.8	10.4
5 K/ min ramp		10 % O_2 [%]	20 % O_2 [%]	10 % O_2 [%]	20 % O_2 [%]
Beech	I	2.65	2.77	7.35	7.00
	II	1.73	1.46	6.29	5.90
Pine	I	5.09	5.53	10.4	10.8
	II	3.03	3.26	5.29	6.11
Sunflower	I	3.43	3.84	9.69	9.52
	II	3.13	3.40	10.6	9.31
Wheat	I	2.89	2.80	6.30	6.04
	II	2.18	2.59	11.2	13.8
Wood pellets I1	I	3.97	3.91	9.79	9.70
	II	3.04	2.68	5.77	6.16
Wood pellets I2	I	4.29	4.55	11.0	11.1
	II	4.89	4.72	8.43	8.99

Use of K-content to determine cellulose pyrolysis kinetics

Inorganic elements are well-known to catalyze the pyrolysis of biomass.[20–22] Catalytic effects of potassium have been reported for cellulose[22–26] and hemicellulose components.[24,26] Our experiments were consistent with the literature, in that the temperature of peak pyrolytic decomposition rate scaled with the potassium content of the samples, Figure 10. The peak in pyrolysis decomposition rate is typically associated with the cellulose component.[20] A linear correlation can be found for the pre-exponential factor for celullose pyrolysis $k_{0,\mathrm{pyr,CELL}}$ to reproduce these temperatures ($E_{\mathrm{a,pyr,CELL}} = 185\,\mathrm{kJ/mol}$) as a function of the cellulose mass fraction w_{K} [kg kg^{-1}]:

$$k_{0,\mathrm{pyr,CELL}} = (9.34 \times 10^{15} \cdot w_{\mathrm{K}} + 2.37 \times 10^{12} \pm 2.29 \times 10^{12}) \cdot \mathrm{s}^{-1} \tag{8}$$

The correlation and the actual values used in the pyrolysis model are seen on the right side of Figure 10. Comparing the model predictions for the cellulose components with measured data for pure cellulose (Figure 11), it can be seen that the models predict a broader range

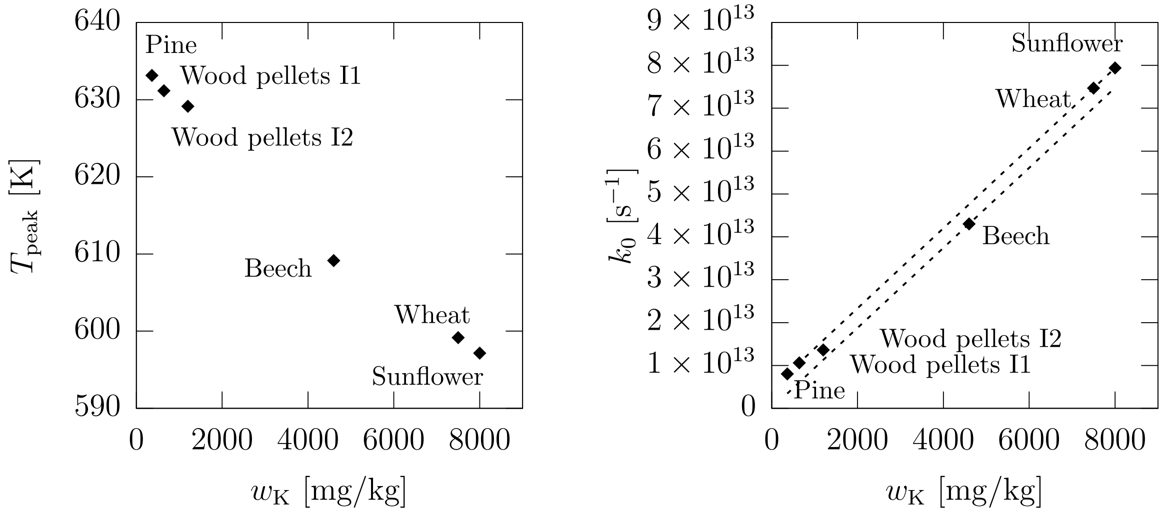

Figure 10: Peak pyrolysis rates and potassium content: The temperature of peak conversion rates T_{peak} correlates with biomass potassium content (left). This correlation can be used to estimate the interval of $k_{0,\mathrm{pyr,CELL}}$ (right, dashed lines), for an apparent activation energy of 185 kJ/mol. Points represent the values used in the pyrolysis models of the six biomasses.

of decomposition than that seen for isolated cellulose. The peaks for sunflower and wheat cellulose components appear at lower temperatures than that of pure cellulose, those of pine and the two wood pellet samples are delayed.

Modelled conversion of biomass components

Figures 12 through 17 show the cumulated conversion of extractives, hemicellulose, lignin, cellulose and char as predicted by the pyrolysis model (left), oxidation model I at 20 % oxygen (center) and oxidation model II at 20 % oxygen (right), as predicted for the stepwise isothermal experiments 423–523 K (compare main text)

The figures illustrate how the different components of the biomasses are gradually consumed in the isothermal experiments, starting with the most reactive fractions (extractives and hemicellulose). No consumption of char is predicted. Conversion of cellulose is weak for the pyrolysis cases, and only occurs in the final isothermal stages. The main difference

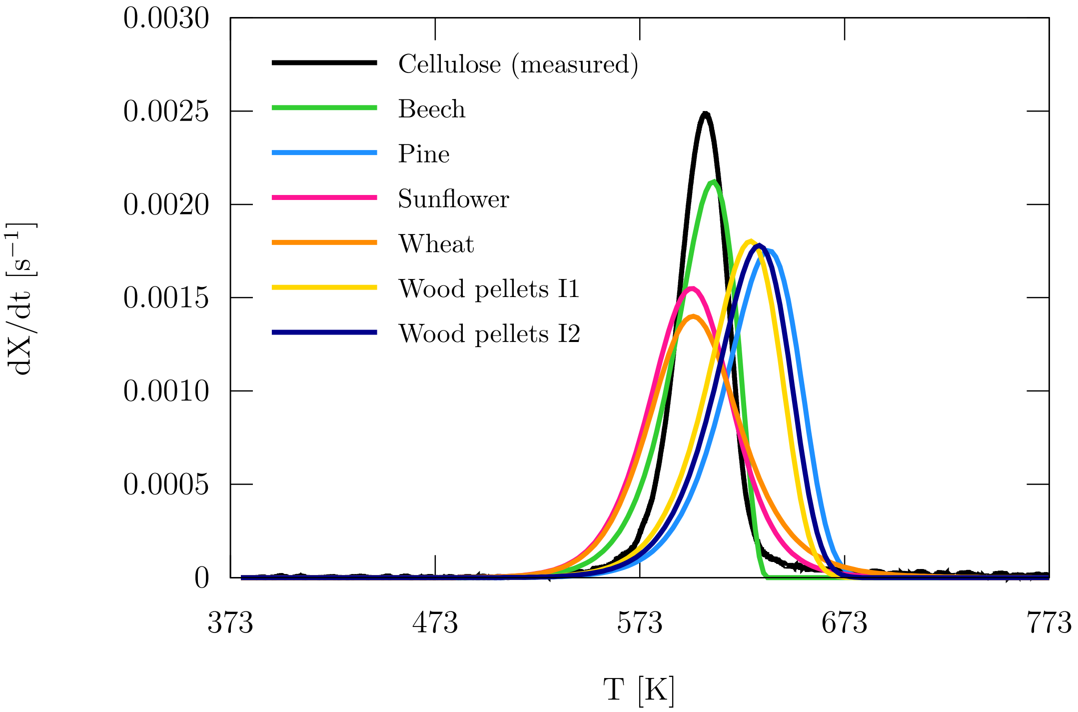

Figure 11: Pyrolysis models of the cellulose components for six biomasses, compared to measured data for pure cellulose pyrolysis

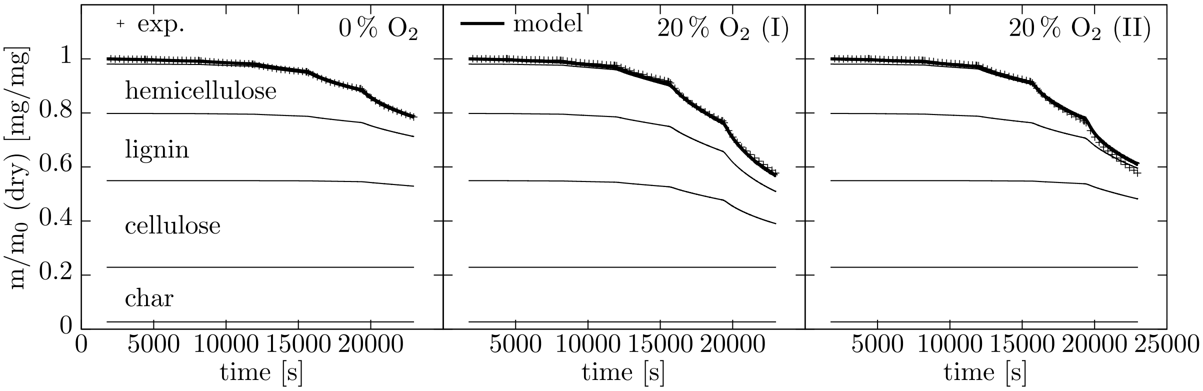

Figure 12: Beech: cumulated conversion of components during stepwise isothermal TGA experiments (423–523 K). Unlabeled fractions are ash (bottom) and extractives (top). Labels (I) and (II) refer to oxidation models I and II, respectively.

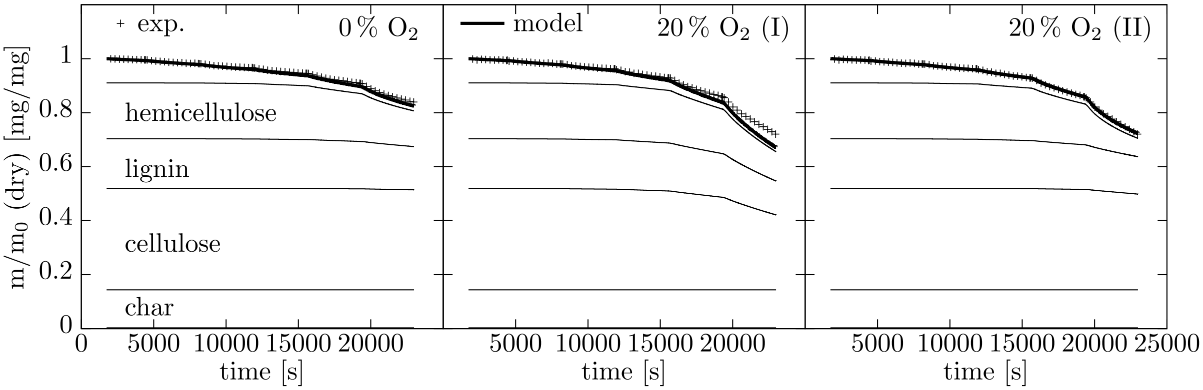

Figure 13: Pine: cumulated conversion of components during stepwise isothermal TGA experiments (423–523 K). Unlabeled top fraction is extractives, ash content is < 0.01. Labels (I) and (II) refer to oxidation models I and II, respectively.

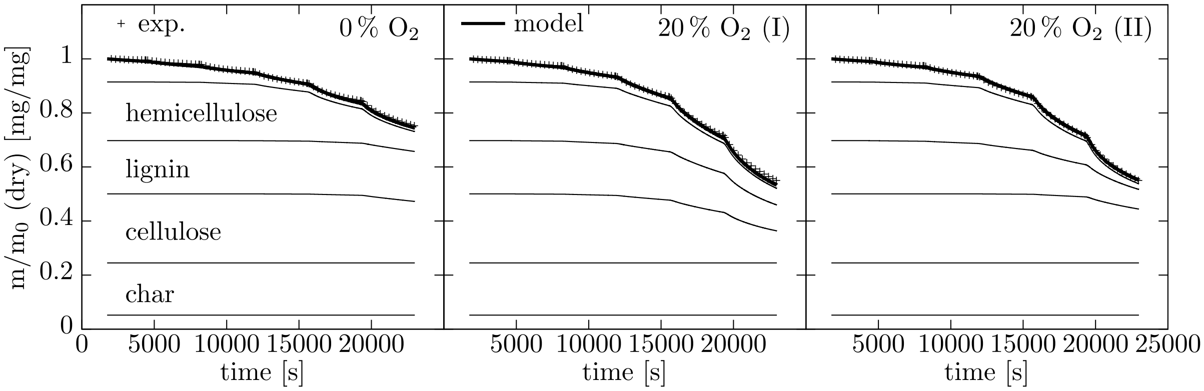

Figure 14: Sunflower: cumulated conversion of components during stepwise isothermal TGA experiments (423–523 K). Unlabeled fractions are ash (bottom) and extractives (top). Labels (I) and (II) refer to oxidation models I and II, respectively.

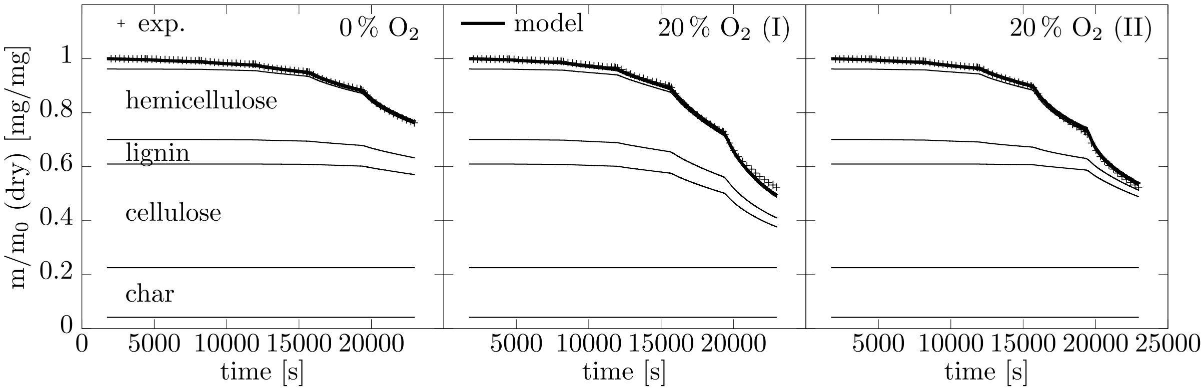

Figure 15: Wheat: cumulated conversion of components during stepwise isothermal TGA experiments (423–523 K). Unlabeled fractions are ash (bottom) and extractives (top). Labels (I) and (II) refer to oxidation models I and II, respectively.

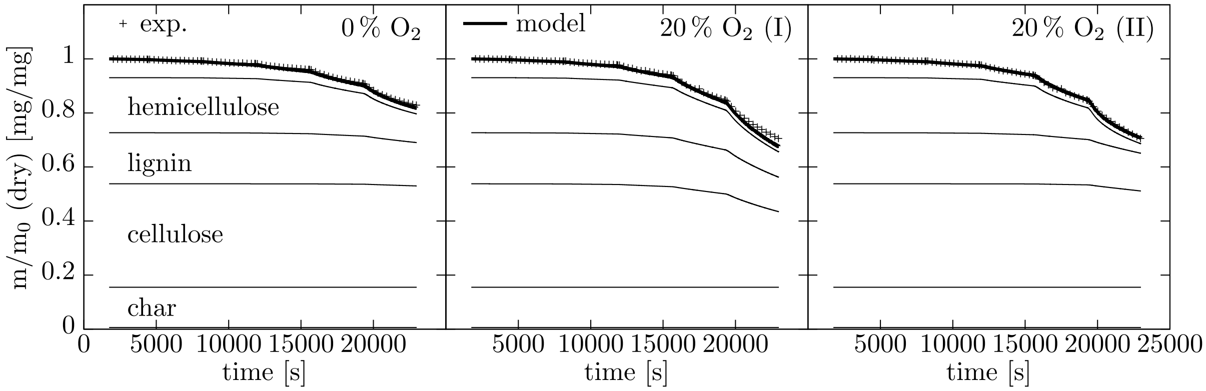

Figure 16: Wood pellets I1: cumulated conversion of components during stepwise isothermal TGA experiments (423–523 K). Unlabeled top fraction is extractives, ash content is < 0.01. Labels (I) and (II) refer to oxidation models I and II, respectively.

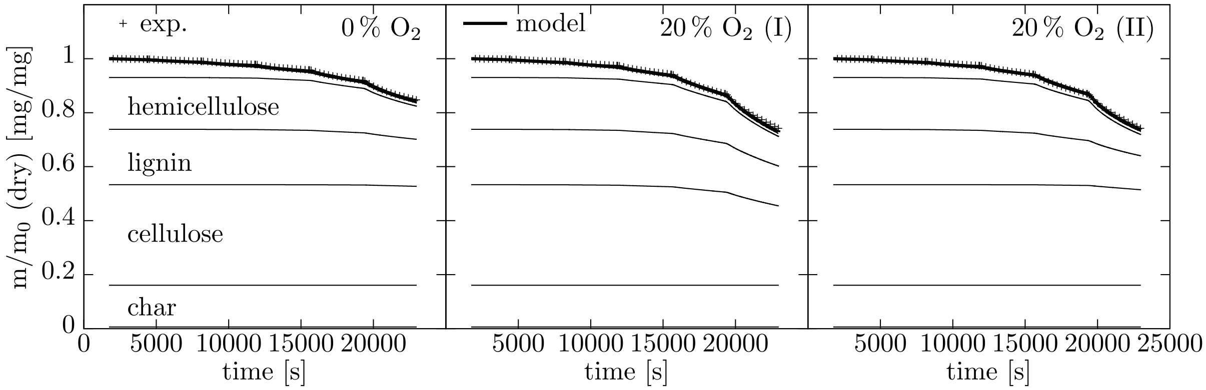

Figure 17: Wood pellets I2: cumulated conversion of components during stepwise isothermal TGA experiments (423–523 K). Unlabeled top fraction is extractives, ash content is < 0.01. Labels (I) and (II) refer to oxidation models I and II, respectively.

between oxidation model I and II is in the relative conversion of cellulose and hemicellulose. Model II predicts very little cellulose conversion (in agreement with the pure cellulose experiments the model is based on). Lignin conversion does not differ much between the two oxidation models, as the global oxidation kinetic parameters (model I) and those of the lignin component (model II) are very similar.

References

(1) Grønli, M.; Antal, M. J.; Várhegyi, G. A Round-Robin Study of Cellulose Pyrolysis Kinetics by Thermogravimetry. *Industrial & Engineering Chemistry Research* **1999**, *38*, 2238–2244.

(2) Grønli, M. G.; Várhegyi, G.; Blasi, C. D. Thermogravimetric Analysis and Devolatilization Kinetics of Wood. *Industrial and Engineering Chemistry Research* **2002**, *41*, 4201–4208.

(3) Anca-Couce, A.; Zobel, N.; Berger, A.; Behrendt, F. Smouldering of pine wood: Kinetics and reaction heats. *Combustion and Flame* **2012**, *159*, 1708–1719.

(4) Pyle, D. L.; Zaror, C. A. Heat transfer and kinetics in the low temperature pyrolysis of solids. *Chemical Engineering Science* **1984**, *39*, 147–158.

(5) Hayhurst, A. N. The kinetics of the pyrolysis or devolatilisation of sewage sludge and other solid fuels. *Combustion and Flame* **2013**, *160*, 138–144.

(6) Verein Deutscher Ingenieure VDI-Gesellschaft Verfahrenstechnik und Chemieingenieurwesen (GVC),, Ed. *VDI-Wärmeatlas*, 10th ed.; Springer Berlin Heidelberg, 2006.

(7) Sjöström, J.; Blomqvist, P. Direct measurements of thermal properties of wood pellets: Elevated temperatures, fine fractions and moisture content. *Fuel* **2014**, *134*, 460–466.

(8) Frank-Kamenetskii, D. A. *Diffusion and Heat Transfer in Chemical Kinetics*, 2nd ed.; Plenum Press, 1969; English translation by J. P. Appleton.

(9) Perzon, M. Emissions of organic compounds from the combustion of oats - a comparison with softwood pellets. *Biomass and Bioenergy* **2010**, *34*, 828–837.

(10) Branca, C.; Di Blasi, C. Global interinsic kinetics of wood oxidation. *Fuel* **2004**, *83*, 81–87.

(11) Font, R.; Conesa, J. A.; Moltó, J.; Muñoz, M. Kinetics of pyrolysis and combustion of pine needles and cones. *Journal of Analytical and Applied Pyrolysis* **2009**, *85*, 276–286.

(12) Shen, D. K.; Gu, S.; Luo, K. H.; Bridgwater, A. V.; Fang, M. X. Kinetic study on thermal decomposition of woods in oxidative environment. *Fuel* **2009**, *88*, 1024–1030.

(13) Conesa, J. A.; Domene, A. Biomasses pyrolysis and combustion kinetics through n-th order parallel reactions. *Thermochimica Acta* **2011**, *523*, 176–181.

(14) Branca, C.; Di Blasi, C. A unified mechanism of the combustion reactions of lignocellulosic fuels. *Thermochimica Acta* **2013**, *565*, 58–64.

(15) Benkorichi, S.; Fateh, T.; Richard, F.; Consalvi, J.-L.; Nadjai, A. Investigation of thermal degradation of pine needles using multi-step reaction mechanisms. *Fire Safety Journal* **2017**, *91*, 811–819.

(16) Safi, M. J.; Mishra, I. M.; Prasad, B. Global degradation kinetics of pine needles in air. *Thermochimica Acta* **2004**, *412*, 155–162.

(17) Amutio, M.; Lopez, G.; Aguado, R.; Artetxe, M.; Bilbao, J.; Olazar, M. Kinetic study of lignocellulosic biomass oxidative pyrolysis. *Fuel* **2012**, *95*, 305–311.

(18) Abreu Naranjo, R.; Conesa, J.; Foppa Pedretti, E.; Romero Romero, O. Kinetic analysis: Simultaneous modelling of pyrolysis and combustion processes of dichrostachys cinerea. *Biomass and Bioenergy* **2012**, *36*, 170–175.

(19) Niu, H.; Liu, N. Thermal decomposition of pine branch: Unified kinetic model on pyrolytic reactions in pyrolysis and combustion. *Fuel* **2015**, *160*, 339–345.

(20) Di Blasi, C. Modeling chemical and physical processes of wood and biomass pyrolysis. *Progress in Energy and Combustion Science* **2008**, *34*, 47–90.

(21) Anca-Couce, A. Reaction mechanisms and multi-scale modelling of lignocellulosic biomass pyrolysis. *Progress in Energy and Combustion Science* **2016**, *53*, 41–79.

(22) Saddawi, A.; Jones, J. M.; Williams, A. Influence of alkali metals on the kinetics of the thermal decomposition of biomass. *Fuel Processing Technology* **2012**, *104*, 189–197.

(23) Antal, M. J.; Varhegyi, G. Cellulose Pyrolysis Kinetics: The Current State of Knowledge. *Industrial & Engineering Chemistry Research* **1995**, *34*, 703–717.

(24) Jensen, A.; Dam-Johansen, K.; Wójtowicz, M. A.; Serio, M. A. TG-FTIR Study of the Influence of Potassium Chloride on Wheat Straw Pyrolysis. *Energy & Fuels* **1998**, *12*, 929–938.

(25) Eom, I.-Y.; Kim, J.-Y.; Kim, T.-S.; Lee, S.-M.; Choi, D.; Choi, I.-G.; Choi, J.-W. Effect of essential inorganic metals on primary thermal degradation of lignocellulosic biomass. *Bioresource Technology* **2012**, *104*, 687–694.

(26) Khazraie Shoulaifar, T.; DeMartini, N.; Karlström, O.; Hupa, M. Impact of organically bonded potassium on torrefaction: Part 1. Experimental. *Fuel* **2016**, *165*, 544–552.

July 2019

ForskEL project no. 12150/EUDP 64018-003

Final report: Flexible use of biomass on PF Fired power plants

Appendix I. List of student projects

1. Department of Chemical and Biochemical Engineering
Technical University of Denmark
Søltofts Plads, Building 229, DK-2800, Kgs. Lyngby, Denmark
2. Ørsted Bioenergy & Thermal power,
Kraftværksvej 53, DK-7000, Fredericia, Denmark

CHEC no. R1902

Student lis

Name	Title	Project type
Philipp Fritsch (TU Munich)	Sulphation of biomass ash deposits	MSc research project (exchange semester)
Mohammad Shabani Ghazvini	Sulphation of biomass ash deposits	MSc thesis
Akhilesh Nair	Tensile adhesion strength of biomass ash deposits	MSc special course
Tareq Abdulrahman	Ignition of biomass in power plant mills	Msc thesis